

Polarized spin transport in
Ferromagnetic material/Normal metal
bilayers driven by heat



DISSERTATION

ZUR ERLANGUNG DES DOKTORGRADES DER NATURWISSENSCHAFTEN

(DR. RER. NAT.) DER FAKULTÄT FÜR PHYSIK DER UNIVERSITÄT

REGENSBURG

vorgelegt von

Anatoly S. Shestakov

aus Krasnokamensk, Russland

im Jahr 2021

Promotionsgesuch eingereicht am:

Die Arbeit wurde angeleitet von: Prof. Dr. C. Back

Prüfungsausschuss: Vorsitzender: Prof. Dr. F. Evers

1. Gutachter: Prof. Dr. C. Back (TU München)

2. Gutachter: Prof. Dr. C. Strunk

weiterer Prüfer: Prof. Dr. D. Weiss

Datum Promotionskolloquium:

Contents

1	Introduction	1
2	Theory	4
2.1	Magnetic anisotropy	4
2.2	Ferromagnetic resonance (FMR) in thin films	6
2.2.1	Basics of FMR	6
2.2.2	Magnetic susceptibility	7
2.3	Magneto-optical Kerr effect (MOKE)	10
2.4	Family of spin-current-related effects	11
2.4.1	Charge current to spin current – the spin Hall effect (SHE)	11
2.4.2	Spin injection and accumulation in NM/FM systems	15
2.4.3	Spin filtering at the NM/FM interface	18
2.4.4	Spin Hall angle in FMR experiments with FM/NM bilayers	19
2.4.5	Charge current distributions in FM/NM stack	21
2.5	Conventional Nernst effects	23
2.5.1	Seebeck effect as the driving force of Nernst effects	23
2.5.2	The anomalous Nernst effect (ANE)	25
2.5.3	The planar Nernst effect (PNE) and anisotropic magnetothermopower (AMTEP)	26
2.6	Spincaloric effects	28
2.6.1	Thermal counterpart of SHE – the spin Nernst effect (SNE)	29
2.6.2	Theoretical aspects of the SNE	29
2.6.3	The spin Seebeck effect (SSE)	32
3	Experimental methods	37
3.1	Set-up №1 for measurements of TSSE	37
3.1.1	Definition of temperature gradients	38
3.1.2	Data processing	39
3.1.3	Offset voltage in TSSE measurements	41
3.2	Set-up №2 for measurements of TSSE	43
3.3	Set-up for measurements of SNE	44
3.3.1	TRMOKE set-up	44
3.3.2	Coplanar waveguide FMR	46
3.3.3	Example of a measured FMR curve	48
3.3.4	Sample geometries and production steps	49
3.3.5	Determination of the temperature of FM	52
3.3.6	Data processing	55
3.3.7	Modulation of damping technique in FMR experiments	55

4	TSSE measurements	59
4.1	Pt/Py/MgO sample	59
4.1.1	ANE induced artifact	59
4.1.2	TSSE-like artifact in the AMTEP signal induced by external magnetic field inhomogeneity	61
4.1.3	Interpretation of the experimental results	67
4.2	Pt/YIG/GGG sample	69
4.2.1	LSSE contribution to the measured signal	69
4.2.2	Discussion on possibility of the magnetic proximity effect	70
4.3	Py/MgO sample	71
4.3.1	Unriddling the magnetization vector rotation from AMTEP curves	75
4.4	Conclusion on the spin Seebeck effect	82
5	SNE measurements	86
5.1	Simulation of temperature distribution over the sample in view of different geometries	87
5.2	Experimental thermal magnetization dependencies and temperature distribution at the experimental FM/NM interfaces	93
5.3	Check of spin-accumulation by means of the SHE	97
5.3.1	Evaluation of spin Hall angles	102
5.4	Check of SNE	103
5.4.1	Conclusion and outlook on the SNE	109
	Appendix	111
A	Interdiffusion in FM/NM bilayer systems	111
A.1	General	111
A.2	Solution of Fick's second equation for a bilayer stack	112
A.3	Magnetic valence model for 3d-FM-containing alloys	113
A.4	Dependence of sample magnetization on diffusion length	114
A.5	Experimental interdiffusion in FM/NM bilayers	117
A.6	XPS concentration depth-profiling	120
A.7	Conclusion on interdiffusion model	124
	Bibliography	126
	List of abbreviations	137
	Acknowledgments	140

Chapter 1

Introduction

In the last decade computer microelectronics have approached physical limits of transistor sizes and the Moore's trend of the transistor number enhancement per microchip has slowed down. Heat produced by transistors is among the faced physical problems, while currents consumed by CPUs and GPUs amount to hundreds of Amperes, and the heat has manifested itself as the main performance-limiting factor for the market of mobile devices. The spin is another degree of freedom of electrons, i.e. an information channel. A very young branch of electronics¹, spin caloritronics [12], potentially addresses both an enhancement of the information density transported by the electron and simultaneously it can transform the Joule heat produced by electronic components into useful work.

The term "current" is usually understood as the conventional electron charge transfer \vec{j} , whereas the spin current \vec{j}_s is the transfer of spin angular momentum \vec{s} of electron. Moreover, the electron has a spin magnetic moment $\vec{\mu}_s$, which is coupled to \vec{s} via the gyromagnetic ratio γ :

$$\vec{\mu}_s = \gamma \vec{s}, \quad (1.1)$$

for this reason the spin current is sometimes called "magnetic current". Due to the interconnection, the spin current can influence magnetic properties of a substance, for example, it can switch the magnetization direction of a ferromagnet. Different examples of charge and spin transfer for electrons are depicted in Fig. 1.1. Conventional electric current is the flow of randomly polarized electrons so that net spin transfer \vec{j}_s is absent. Enhancing the polarization of the electric current one additionally gets spin transfer. A pure spin-current \vec{j}_s is observed when the current \vec{j}_\uparrow (spin-up electrons) moves into the direction opposite to the current \vec{j}_\downarrow (spin-down), with $|j_\uparrow| = |j_\downarrow|$, i.e. a pure spin current is the transfer of spin angular momentum with net charge current $j = 0$.

The spin current can be induced by different means: the spin Hall Effect (SHE) [122], the inverse spin galvanic effect (ISGE, also known as the Rashba-Edelstein effect) [52], spin pumping in ferromagnetic metal/non-magnetic metal (FM/NM) systems in ferromagnetic resonance (FMR) experiments [101, 140], spin Seebeck effect (SSE) [144, 147, 96], acoustic spin pumping [142, 141], spin-transfer torque (STT) in spin valves [126], spin Nernst effect (SNE) [99] etc..

Conventional thermoelectric (Seebeck family) and thermomagnetic (Nernst family) effects have been known for about two centuries and deal with the interaction of

¹more precisely a branch of spintronics [23]

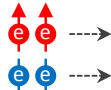

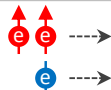





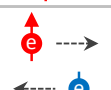

		Charge transfer	Spin transfer
Unpolarized current			0
Spin-polarized current			
Fully spin-polarized current			
Pure spin-current		0	

Figure 1.1: Different cases of charge and spin transfer for electrons

charge currents and heat. These effects find broad application as modern thermometers, power generators and coolers. The main issue with all thermoelectric/magnetic phenomena is those efficiency and sensitivity to the applied heat currents. The reason why charge-based electronics have got its important position in the modern life is that the electrical conductivity of solids spans more than 30 orders of magnitude offering an astronomical tuning range by different means. On the other hand, for the thermal conductivity the range barely makes 5 orders. While for metals the Wiedemann–Franz law is valid and the linear dependence between the thermal λ and electrical σ conductivities takes place at RT (see Dulong–Petit law for metals) due to the electron mechanism, for electrical insulators different mechanisms are responsible, such as the phonon contribution to the thermal conductivity. For the latter reason, there are no real thermal insulators in nature, causing strong technical limitations in the design of thermoelectric/magnetic devices. Even in perfect vacuum another heat flow mechanism, radiation, has a devastating impact to thermal insulation. For example the sun brings to the Earth up to 700 W/m^2 in a sunny day through the vacuum of 150 million km. The heat power collected on $2\text{-}3 \text{ m}^2$ is the same power that one uses to boil a teapot.

So far the most expedient of thermoelectric generators is based on the Seebeck generator². Its efficiency is characterized by the thermoelectric figure of merit $zT = \frac{\sigma S^2 T}{\lambda}$, where S is the conventional Seebeck coefficient, T is the temperature. According to the mentioned Wiedemann–Franz law, stating linear proportionality of σ and λ for electrically conducting materials, a separate tuning of σ and λ for maximization of zT is very limited. Semiconductors show the highest zT value due to an asymmetric band structure around the Fermi energy leading to higher S values. In turn, spin-based phenomena are practically uncoupled from the thermal conductivity of solids and, therefore, spin caloritronics may offer better ways to enhance the efficiency of thermoelectric devices.

Different applications for spin-caloric effects were proposed, illustrated by some examples:

²the structure is also known as Peltier element, where the Peltier effect is the effect reciprocal to the Seebeck effect

-
1. It was shown that the thermal spin-transfer torques (STT) can switch the magnetization in ferromagnetic-insulator-based (FMI) spin valves more efficiently than charge-current-induced torques [127];
 2. The longitudinal SSE (LSSE) [147] in combination with the inverse spin Hall effect (ISHE) converts a heat flow into an electric voltage proportional to the size of the ISHE detector. The structure of such a device is simpler than of the conventional thermopiles of Seebeck generators;
 3. Rotational engines driven by heat currents were proposed in [13]. In the device a domain wall existing between magnetic domains in a two-domain FM is driven by a spincaloric effect, leading to the magnetization change of the FM. The magnetization change leads to a change of the mechanical moment of FM via the Einstein-de-Haas/Barnett effect. As the result the FM rotates.

In this work we mostly focus on the detection of spincaloric effects, namely, the transverse spin Seebeck effect (TSSE) and the spin Nernst effect (SNE). In analogy to the families of conventional Nernst and Seebeck effects, the spincaloric effects are, so to say, the second order of infinitesimals in the sense that they are more challenging for detection as the non-thermal electronic effects. Already the pioneering effect of spin caloritronics, the TSSE, has faced great problems in interpretation of the experimental results, because a number of spurious conventional thermomagnetic effects influence the measured signals. Another spincaloric effect, the SNE, despite being officially observed [99], is still to be proof-checked in different materials and by different methods.

In the appendix we additionally discuss interdiffusion in metallic multilayers - another important aspect for the thermal measurements.

Chapter 2

Theory

The theoretical part can be separated in two logical blocks related to: a) the transverse spin Seebeck effect (TSSE); b) the spin Nernst effect (SNE).

The TSSE chapters include a discussion of the broad family of conventional charge Nernst effects that interrupt a straight forward interpretation of TSSE experimental results, magnetic anisotropy used for charge Nernst effects signals description, and finally the theoretical details of the TSSE.

The SNE chapters include ferromagnetic resonance (FMR) used to induce magnetization dynamics, magneto-optical Kerr effect (MOKE) used for magnetization dynamics detection, SHE theory with spin accumulation and spin injection in NM/FM bilayers as it is well established and strongly related to the SNE, and finally, the SNE theoretical aspects are briefly mentioned.

2.1 Magnetic anisotropy

Magnetic bodies often have preferred directions of magnetization, in other words, a magnetic anisotropy. In the general case different forces compete trying to orient the magnetic moment along the so-called easy directions. In order to find the easy direction at given conditions, one has to minimize the magnetic free energy U of a body. In many cases [58, 28], the magnetic free energy can be separated into the following parts:

$$U = U_Z + U_M + U_a, \quad (2.1)$$

where U_Z is the Zeeman energy, U_M is the demagnetizing energy (also known as the shape anisotropy energy), U_a is the term including the magnetocrystalline anisotropy and growth anisotropy. In the following we neglect inhomogeneities of the magnetization M and treat the sample magnetization as a single vector (macrospin approximation).

The Zeeman term equals to:

$$U_Z = -\mu_0 \vec{M} \vec{H} dV, \quad (2.2)$$

where μ_0 is the permeability of vacuum, \vec{H} is the external magnetic field, \vec{M} is the magnetization vector, V is the FM volume.

Shape anisotropy U_M

For ellipsoidal ferromagnets Kittel [58, 28] has introduced the following description:

$$U_M = \frac{1}{2} \mu_0 \vec{M} \hat{N} \vec{M} dV, \quad (2.3)$$

where \hat{N} is the demagnetizing tensor. Also cases of long thin cylinders and thin films can be approximated with this equation. The demagnetizing term is also often called shape anisotropy, as it induces easy magnetic directions depending on the shape of the sample. Intuitively, spherical ferromagnets show no shape anisotropy. Corrections to the Kittel's \hat{N} tensor in case of a parallelepipedal sample can be found in [2].

Anisotropy term U_a

U_a depends on the crystal symmetry and sample-growth conditions.

Uniaxial anisotropy

According to [58, 28], the in-plane density of magnetic free energy U in the presence of a uniaxial magnetic anisotropy (UMA) reads:

$$U_u = K_u \sin^2(\varphi_M - \varphi_{ua}), \quad (2.4)$$

where φ_M is the direction of the magnetization vector, φ_{ua} is the direction of the easy axis.

Cubic anisotropy

The in-plane density of the magnetic free energy U in the presence of UMA and CMA (cubic magnetic anisotropy) for a monodomain magnetization reads:

$$U_c = K_{c1}(\alpha_1^2 \alpha_2^2 + \alpha_2^2 \alpha_3^2 + \alpha_3^2 \alpha_1^2) + K_{c2} \alpha_1^2 \alpha_2^2 \alpha_3^2, \quad (2.5)$$

where α_i are the direction cosines of the magnetization. In the following, for simplicity, we neglect higher orders of the cubic anisotropy.

Interface anisotropy

In the vicinity of an interface hybridization of electrons of atoms of neighboring layers can occur. This causes a distortion of the electronic orbitals, and in combination with spin-orbit coupling leads to an effective anisotropy. The strength of this type of anisotropy is reciprocal to the FM thickness because only the atoms in the vicinity of the interface are involved. The anisotropy can be both in-plane and out-of-plane [97]. For some thin FM film interfaces like Co/Pt [107], Ni/Cu [57] the out-of-plane interface anisotropy is so strong that it overcomes the shape anisotropy field of FM, which is of 1 T order large.

Growth anisotropy

Anisotropy of thin FM film samples strongly depends on growth conditions. If a sample grows polycrystalline in absence of an external magnetic field it tends to be macroscopically isotropic, because the individual crystallites compensate each others magnetocrystalline anisotropy on average. If some non-zero field is present during the growth, the FM is likely to get an uniaxial anisotropy. This anisotropy can be removed by a post-annealing of FM. Additionally, the post-annealing can relax some mechanical stresses acquired during the growth due to the mismatch of lattice constants of grown film and substrate (practically up to about 15% mismatch is tolerable). The above described issues are particularly relevant for Permalloy films which we have used in the most of our experiments.

2.2 Ferromagnetic resonance (FMR) in thin films

2.2.1 Basics of FMR

In general, the magnetization is spatially non-uniform in sample. However, its behavior can be often adequately approximated by some averaged magnetization vector $\vec{M} = M\vec{m}$ (macrospin approximation), where \vec{m} is the unit vector of magnetization. Dynamics of the magnetization vector \vec{M} in the case of a FM with losses is described with the Landau-Lifshitz-Gilbert equation (LLG) [77, 28, 33]:

$$\begin{aligned} \frac{d\vec{m}}{dt} &= -\gamma\vec{m} \times (\mu_0\vec{H}_{\text{eff}}) + \alpha\vec{m} \times \frac{d\vec{m}}{dt} = \vec{T}_{\text{FL}} + \vec{T}_{\text{DL}}, \\ \vec{M} &= M\vec{m}, \end{aligned} \quad (2.6)$$

where α is the Gilbert damping factor, μ_0 is the permeability of vacuum, γ is the gyromagnetic ratio, \vec{T}_{FL} is the field-like torque, which defines the resonance frequency/resonance field, \vec{T}_{DL} is the damping-like torque, which defines the degree of losses in system, \vec{H}_{eff} is the effective magnetic field containing different contributions:

$$\vec{H}_{\text{eff}} = \vec{H}_{\text{ex}} + \vec{H}_{\text{dem}} + \vec{H}_{\text{ani}} + \vec{H}_{\text{ext}}, \quad (2.7)$$

here \vec{H}_{ex} is the exchange term, \vec{H}_{dem} is the demagnetizing term (shape anisotropy), \vec{H}_{ani} is the anisotropy term including all types of anisotropy except the shape anisotropy, \vec{H}_{ext} is the external applied magnetic field. For free electrons $\gamma = 176 \cdot 10^9, \frac{\text{rad}}{\text{T}\cdot\text{s}}$ and practically interesting materials like YIG and Py have values very close to it. In macrospin approximation the exchange term from \vec{H}_{eff} can be omitted, because this approximation explicitly assumes that all magnetic moments within the FM are parallel. In Fig. 2.1 a motion of \vec{M} according to the Eq. (2.6) is presented. Conventionally, \vec{H}_{eff} is directed along the z -axis. Once \vec{M} is not parallel to \vec{H}_{eff} , a counter-clockwise precession of \vec{M} driven by \vec{T}_{FL} starts with an ordinary frequency of

$$f = \frac{\omega}{2\pi} = \frac{\gamma}{2\pi}\mu_0 H_{\text{eff}}, \quad (2.8)$$

where ω is the angular frequency.

This kind of precession is also known as the Larmor precession, and in the case of lossless magnetic media \vec{M} precesses infinitely long around \vec{H}_{eff} . Introduction of

magnetic losses will exert \vec{T}_{DL} , which tends to align \vec{M} with \vec{H}_{eff} . Additionally, in a media with losses the resonance frequency is to be modified by a factor $\frac{1}{\sqrt{1+\alpha^2}}$. A media with amplification instead of damping can be described by a sign change of \vec{T}_{DL} , which is then called an anti-damping term.

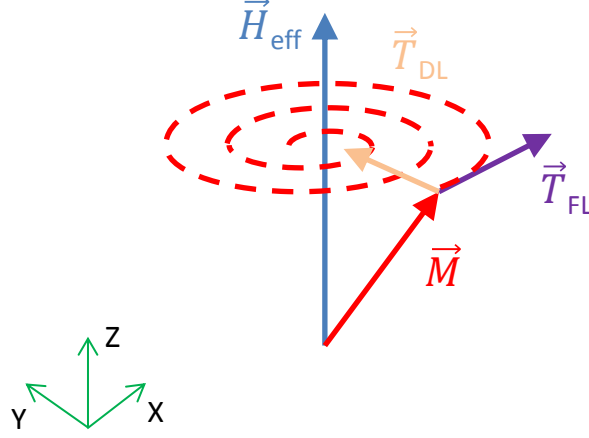


Figure 2.1: Precession dynamics of the magnetization \vec{M} in an external magnetic field \vec{H}_{eff} in terms of field-like and damping-like torques \vec{T}_{FL} and \vec{T}_{DL}

Setting $|M| = \text{const}$ strictly, we can write the following generalized forms for \vec{T}_{FL} and \vec{T}_{DL} :

$$\begin{aligned}\vec{T}_{\text{FL}} &= -\gamma\tau_{\text{FL}}\vec{m} \times \vec{\sigma}, \\ \vec{T}_{\text{DL}} &= -\gamma\tau_{\text{DL}}\vec{m} \times (\vec{m} \times \vec{\sigma}),\end{aligned}\tag{2.9}$$

where $\vec{\sigma}$ is a unit vector, τ_{FL} and τ_{DL} are the torque strengths in units of Tesla.

2.2.2 Magnetic susceptibility

When a small periodic excitation field $\vec{h} = \vec{h}_d e^{i\omega t}$ is applied perpendicular to the static field \vec{H}_{eff} , an oscillation of the magnetization around the equilibrium position starts in FM, where $\omega = 2\pi f$. At a certain frequency the magnetic system reaches FMR condition, see Eq.(2.8). In FMR experiments usually the frequency f is fixed and the applied field H_{ext} is swept in a certain range. The effective field H_{eff} , at which the resonance condition is fulfilled is called resonance field H_r .

In experiments the magnetic susceptibility is of particular interest, because it represents the amplitude of magnetization precession. As defined, the magnetic susceptibility is the relation between magnetization M and magnetic field strength H : $M = \chi H$. Parameters of corresponding susceptibility curves evaluated for the resonance conditions give insight into the physical processes of magnetic dynamics.

Solving the LLG equation (2.6) we can separate all torques acting on \vec{m} into dynamic and static ones [33]:

$$\begin{aligned}\vec{T}_s &= \gamma\vec{m} \times \mu_0\vec{H}_{\text{eff}} + \gamma\tau_{\text{DL},s}\vec{m} \times (\vec{m} \times \vec{\sigma}), \\ \vec{T}_d &= \gamma\vec{m} \times \mu_0\vec{h}_d e^{i\omega t} + \gamma\tau_{\text{DL},d}\vec{m} \times (\vec{m} \times \vec{\sigma})e^{i\omega t}.\end{aligned}\tag{2.10}$$

Under the action of the driving field \vec{h} the magnetization oscillates around an equilibrium direction \vec{m}_{eq} , which can be found from the condition:

$$\frac{\partial \vec{m}_{\text{eq}}}{\partial t} = \vec{T}_s = 0. \quad (2.11)$$

Once the equilibrium direction is found, we define a new local coordinate system $(\vec{x}', \vec{y}', \vec{z}')$ with $\vec{m}_{\text{eq}} = \vec{x}'$, which simplifies the solution of the LLG equation. The temporal magnetization dependence can be expressed as:

$$\vec{m}(t) = \vec{m}_{\text{eq}} + \Delta \vec{m}(t) = \begin{bmatrix} 1 \\ \Delta m_{y'}(t) \\ \Delta m_{z'}(t) \end{bmatrix} \quad (2.12)$$

with $\vec{m}_{\text{eq}} \cdot \vec{m}(t) = 0$.

Thus, the problem is reduced to two dimensions. We solve the LLG equation with complex magnetization in chosen form $\Delta \vec{m}(t) = \Delta \vec{m} e^{i\omega t}$ and leave only linear terms. The solution can be written via the dynamical susceptibility:

$$\begin{bmatrix} \Delta m_{y'}(t) \\ \Delta m_{z'}(t) \end{bmatrix} = \begin{bmatrix} \chi_{y'y'} & \chi_{y'z'} \\ \chi_{z'y'} & \chi_{z'z'} \end{bmatrix} \begin{bmatrix} d_{y'}(t) \\ d_{z'}(t) \end{bmatrix}, \quad (2.13)$$

where $d_{y'}(t) = (h_{y'} - \frac{\tau_{\text{DL,d}}}{\mu_0} \sigma_{z'}) e^{i\omega t}$ and $d_{z'}(t) = (h_{z'} - \frac{\tau_{\text{DL,d}}}{\mu_0} \sigma_{y'}) e^{i\omega t}$ are the driving torques. Note that the susceptibility terms have complex form $\chi_{ii} = \chi'_{ii} + i\chi''_{ii}$.

In general case the susceptibility is:

$$\chi_{\text{f}} = \frac{1}{N_{\text{f}}} \begin{bmatrix} \mathfrak{H}_0 + i \frac{\alpha\omega}{\mu_0\gamma} & -\mathfrak{H}_2 + \mathfrak{s} + i \frac{\omega}{\mu_0\gamma} \\ -\mathfrak{H}_2 - \mathfrak{s} - i \frac{\omega}{\mu_0\gamma} & \mathfrak{H}_1 + i \frac{\alpha\omega}{\mu_0\gamma} \end{bmatrix},$$

$$N_{\text{f}} = \mathfrak{H}_0 \mathfrak{H}_1 + \mathfrak{s}^2 - \mathfrak{H}_2^2 - (1 + \alpha^2) \left(\frac{\omega}{\mu_0\gamma} \right)^2 + i(\mathfrak{H}_0 + \mathfrak{H}_1) \frac{\omega}{\mu_0\gamma} \left(\alpha + \frac{2\mathfrak{s}}{\mathfrak{H}_0 + \mathfrak{H}_1} \right), \quad (2.14)$$

where $\mathfrak{H}_0, \mathfrak{H}_1, \mathfrak{H}_2$ are terms depending on the components of \vec{H}_{eff} and static field-like SOT (or TSOT), \mathfrak{s} is the term containing static damping-like SOT torque.

Here we consider an important configuration of a magnetic system for which the susceptibility can be expressed analytically. First, the demagnetizing energy of thin FM films often has dominating contribution in the magnetic energy, for example the demagnetizing field (shape anisotropy) $H_{\text{dem}} = \mu_0 M_s$ for Permalloy (Py) amounts to around 1 T. This field forces the magnetization to lie in the plane of FM (xy -plane). Layers adjacent to FM can exert forces on FM leading to an out-of-plane anisotropy (interface anisotropy) that counteracts the demagnetizing field. Both the shape and out-of-plane anisotropies have the same symmetry and for this reason they are often combined into the effective magnetization:

$$M_{\text{eff}} = M_s - \frac{2K_{\text{oop}}}{\mu_0 M_s}. \quad (2.15)$$

In-plane-isotropic FM is very often a reasonable assumption for Py as well. Also, the static damping-like SOT is usually very small, when compared to other terms and can be omitted. With this simplifications we obtain:

$$\mathfrak{H}_0 = H + M_{\text{eff}}, \quad \mathfrak{H}_1 = H, \quad \mathfrak{H}_2 = 0, \quad \mathfrak{s} = 0. \quad (2.16)$$

The resonance condition arises from minimization of the denominator N_f in Eq. (2.14). By neglecting all insignificant small terms, i.e. terms containing α and \mathfrak{s} , we get the so-called general Kittel formula:

$$\mathfrak{H}_0 \mathfrak{H}_1 - \mathfrak{H}_2^2 = \left(\frac{\omega}{\mu_0 \gamma} \right)^2. \quad (2.17)$$

Then we expand the \mathfrak{H}_0 and \mathfrak{H}_1 terms around the resonance field H_r , i.e. $\mathfrak{H}_i = \mathfrak{H}_{ir} + (H - H_r)$, where \mathfrak{H}_{ir} are the \mathfrak{H}_0 and \mathfrak{H}_1 at the resonance conditions. Using this expansions and neglecting quadratic terms in α and $\frac{2\mathfrak{s}}{\mathfrak{H}_0 + \mathfrak{H}_1}$ we obtain the following denominator:

$$N_f = (\mathfrak{H}_{0r} + \mathfrak{H}_{1r}) \left((H - H_r) + i \frac{\alpha_{\text{eff}} \omega}{\mu_0 \gamma} \right), \quad (2.18)$$

where α_{eff} is the effective damping factor with the damping-like SOT term of:

$$\alpha_{\text{eff}} = \alpha + \frac{2\mathfrak{s}}{\mathfrak{H}_{0r} + \mathfrak{H}_{1r}} \quad (2.19)$$

One should note that whereas the intrinsic damping parameter α is frequency-independent, the second term (SOT term) is not. Also we define here the FMR field-linewidth ΔH :

$$\Delta H = \frac{\alpha_{\text{eff}} \omega}{\mu_0 \gamma} \quad (2.20)$$

Expanding the numerator part of Eq.(2.14) similarly to the denominator, we get the susceptibilities:

$$\begin{aligned} \chi_{y'y'} &= \frac{\mathfrak{H}_{0r}}{\Delta H (\mathfrak{H}_{0r} + \mathfrak{H}_{1r})} \frac{\Delta H (H - H_r) - i(\Delta H)^2}{(H - H_r)^2 + (\Delta H)^2} = A_{y'y'} [F_A(H) - iF_S(H)], \\ \chi_{y'z'} = -\chi_{z'y'} &= \frac{\omega / (\mu_0 \gamma)}{\Delta H (\mathfrak{H}_{0r} + \mathfrak{H}_{1r})} \frac{(\Delta H)^2 + i\Delta H (H - H_r)}{(H - H_r)^2 + (\Delta H)^2} = A_{y'z'} [F_S(H) + iF_A(H)], \\ \chi_{z'z'} &= \frac{\mathfrak{H}_{1r}}{\Delta H (\mathfrak{H}_{0r} + \mathfrak{H}_{1r})} \frac{\Delta H (H - H_r) - i(\Delta H)^2}{(H - H_r)^2 + (\Delta H)^2} = A_{z'z'} [F_A(H) - iF_S(H)], \end{aligned} \quad (2.21)$$

where $F_S(H)$ and $F_A(H)$ are the symmetric and antisymmetric Lorentzian functions:

$$\begin{aligned} F_S(H) &= \frac{(\Delta H)^2}{(H - H_r)^2 + (\Delta H)^2}, \\ F_A(H) &= \frac{\Delta H (H - H_r)}{(H - H_r)^2 + (\Delta H)^2}. \end{aligned} \quad (2.22)$$

In case of pure in-plane or out-of-plane driving field \vec{h} applied, only the $\chi_{y'y'}$ or $\chi_{z'z'}$ are expected to be measured. However, due to imperfect match of the sample and RF-line impedances, dependance of impedance of other parts of setup on the magnetic field and other reasons, the measured FMR curve will always be a mixture of symmetric and antisymmetric Lorentzian functions with weighting coefficients different from those in Eq.(2.21):

$$p_{\text{abs}}(H, H_r, \Delta H) = A(F_S(H) \cos(\epsilon) + F_A(H) \sin(\epsilon)), \quad (2.23)$$

where ϵ is some phase, A is some absorption amplitude. By fitting experimental p_{abs} FMR curves we can extract needed H_r and ΔH and estimate FM-media parameters from those.

2.3 Magneto-optical Kerr effect (MOKE)

In 1877 John Kerr has observed polarization plane rotation of light reflected from the polished iron pole of an electromagnet [28, 7]. The sense of rotation was dependent on the magnetization direction. For 3d FMs the maximum of visible light Kerr rotation lies at 1.5 eV. This means that the effect is stronger for the red light than for the blue light.

Depending on the orientation of light incidence plane with respect to the magnetization of the reflecting surface three configurations are possible, see Fig. 2.2. In transverse (T) configuration only a change of the reflectance coefficient is observed. For both polar (P) and longitudinal (L) configurations the rotation of the polarization plane is observed. The polar Kerr effect scales with the $\cos \theta$ and the longitudinal one with the $\sin \theta$, where θ is the angle of incidence. In our experiments we use normal incidence of light, thus the polar Kerr effect is dominant. We register the M_z component of the magnetization via the Kerr rotation angle $\theta_K \propto M_z$.

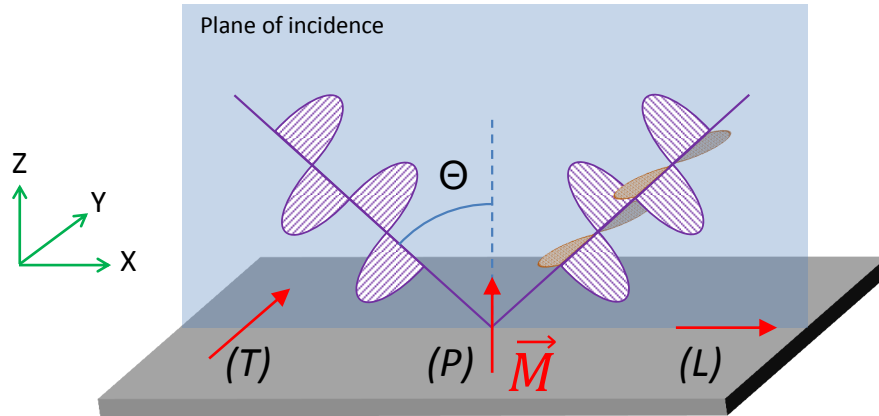


Figure 2.2: MOKE configurations: (T) - transverse, (P) - polar, (L) - longitudinal with respect to the orientation of the magnetization vector \vec{M} to the light incidence plane.

The MOKE is of particular interest, as it gives a possibility of local FMR measurements with resolution below $1 \mu\text{m}$. These kind of measurements are advantageous towards the SNE measurements, because large thermal gradients can be produced on the micrometer scale, leaving the temperature of heater relatively low, avoiding problems related to the interdiffusion and electromigration (see Appendix A.1).

2.4 Family of spin-current-related effects

Starting from the discovery of the giant magnetoresistance (GMR) [8, 15] in 1988, the interest to the spin of electrons as a new controllable quantity has started to increase and a new field of electronics, spintronics has been launched. The effect found its application in constructing a very sensitive magnetic field sensors, particularly as the read head of HDDs. The spin valve structure, which underlies the GMR effect is also used in non-volatile random-access memory, the magnetoresistive RAM (MRAM). Further research in the field led to the discovery of the tunnel magnetoresistance (TMR) [102, 100] in a structure, similar to the spin valve, where the metal between two FMs is changed to a thin insulator.

One of the newest effects of spintronics, the spin Hall effect (SHE), was discovered experimentally only a decade ago and received a great attention as it can generate a spin current without use of a ferromagnetic metal (FM), only a normal metal (NM) with a large spin-orbit coupling is needed.

This chapter we start from the description of the charge-to-spin transformations via the SHE. We briefly describe different mechanisms responsible for the SHE and discuss a principal problem of its separation from the inverse spin Galvanic effect (ISGE, also known as the Rashba-Edelstein effect) in experimental data. After this we introduce a phenomenological drift-diffusion model extended to spin currents, which is used for the interpretation of experimental results. Following this formalism we show the appearance of a spin accumulation at the boundaries in NM. In case if a FM is attached to the NM, the accumulated spin momentum will be transferred from the NM to the FM. The efficiency of the spin transfer is limited by the spin-filtering of interface, which we briefly explain. Then we discuss a possibility to evaluate the efficiency of SHE, the spin Hall angle (SHA), via the modulation of damping (MOD) technique. And finally, we sketch an idea of charge current distribution in the FM/NM stack and factors that influence the distribution.

2.4.1 Charge current to spin current – the spin Hall effect (SHE)

The SHE is the generation of a spin-current \vec{j}_s transverse to the conventional charge current \vec{j} under applied electric field \vec{E} in a NM, see Fig.2.3(a). The conventional current \vec{j} is being scattered in NM and electrons with opposite spin-polarization are moving into the opposite directions transverse to the initial direction of \vec{j} . Such a spatial separation of the oppositely polarized electrons is nothing else but a pure spin current \vec{j}_s . At the boundaries the spin current is blocked and a spin accumulation, similar to the charge accumulation for the conventional Hall effect, is formed. Note, due to symmetry the spin current is also formed along the y-direction.

Reciprocal to the SHE, the inverse spin Hall effect (ISHE), is the generation of \vec{j} under inhomogeneous spatial spin-distribution [39, 114, 76]. The ISHE has found a broad application as a detector of spin-currents and today it is a robust and simple method for electrical sensing of spin currents [76].

Similarly, a thermal counterpart of SHE the spin Nernst effect (SNE) is the production of spin current j_s transverse to an applied thermal gradient $\vec{\nabla}T$, see Fig.2.3(b). Here, we only emphasize the similarity of the SNE to the SHE and that the physics underlying the SNE is closely related to that of the SHE. We will return

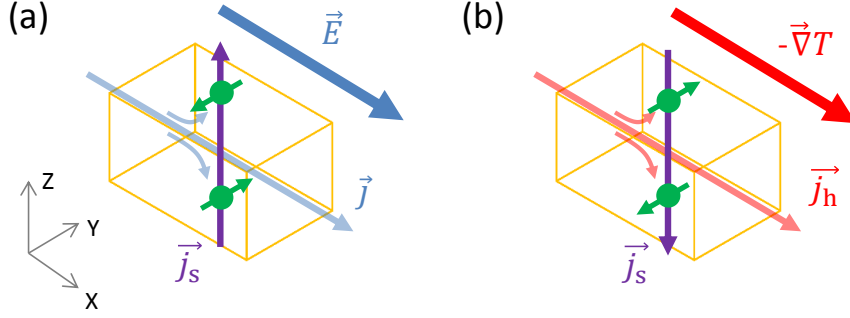


Figure 2.3: a) Spin Hall Effect (SHE). The polarization $\vec{\sigma}$ (shown with green arrows) of electrons is perpendicular to both \vec{j} and \vec{j}_s . b) spin Nernst Effect (SNE). Note that the heat current \vec{j}_h is directed opposite to the thermal gradient $\vec{\nabla}T$.

to the SNE in a few chapters, and now will focus on the SHE.

The SHE was predicted by Dyakonov and Perel [39] in 1971. First experimental proof was provided by Kato [74] in 2004, who observed the spin accumulation at the edges of a semiconductor sample via the optical Kerr rotation. The SHE is important for practical applications due to the fact, that for spin-current production one can use nonmagnetic (NM) materials and no magnetic field is needed. Before the discovery of the SHE, the spin injection from ferromagnetic (FM) material was used for spin current production.

The modern SHE theory is strongly bounded to earlier developed theory of the AHE [44]. Despite the existence of established models, the SHE brought a new level of theoretical complexity, while the spin, in comparison to the charge, is generally not a conserved quantity.

Dyakonov and Perel first reported a phenomenological description [40] derived from the symmetry considerations for the spin-charge coupled drift-diffusion equation. This model is well justified for weak spin-orbit coupling (SOC). Models based on this formalism are often used to fit experimental results. Details of the drift-diffusion model are presented later in the text.

Formally, the spin current formed by the SHE is written:

$$j_x^z = \sigma_{yx}^z E_x, \quad (2.24)$$

where E_x is applied electric field and σ_{yx}^z is spin Hall conductivity (SHC) consisting of three contributions, intrinsic $\sigma_{yx}^{z-\text{int}}$, skew scattering $\sigma_{yx}^{z-\text{skew}}$ (Mott-like), and side-jump $\sigma_{yx}^{z-\text{sj}}$:

$$\sigma_{yx}^z = \sigma_{yx}^{z-\text{int}} + \sigma_{yx}^{z-\text{skew}} + \sigma_{yx}^{z-\text{sj}}, \quad (2.25)$$

An experimentally measured (effective) SHC is coupled to the the spin accumulation and therefore its value depends on the measuring method, be it FMR-based or non-local measurements, and actual value of σ_{yx}^z need be recalculated from the experimental one.

Similarly to the electrical conductivity in the AHE models, the taxonomy of SHC is based on its dependence on the Bloch state transport lifetime τ . The skew scattering has τ^1 dependance, while the intrinsic and side-jump SHC contributions have the τ^0 dependance. Due to the latter fact, a separation of the intrinsic and side-jump conductivities is not trivial.

Skew scattering mechanism

Skew scattering is an asymmetric scattering, its basic idea was described by Mott [103, 105] in 1930s. Randomly polarized electrons acquire a certain polarization during the scattering event from an atom (with a strong SOC), and the polarization is dependent on the scattering direction, see Fig.2.4. In a frame centered on the electron, the electric field of atom \vec{E} is seen by the electron as a magnetic field $\vec{B} = [\vec{E} \times \vec{v}]$, where \vec{v} is the electrons velocity vector. The field \vec{B} polarizes initially randomly oriented spins of electrons. Electrons deflected to the left become spin-down polarized and the electrons deflected to the right of the atom spin-up polarized. Heavier elements show larger \vec{E} due to the larger proton number Z . This description is somewhat oversimplified, for a more in-depth quantum description see [128, 129].

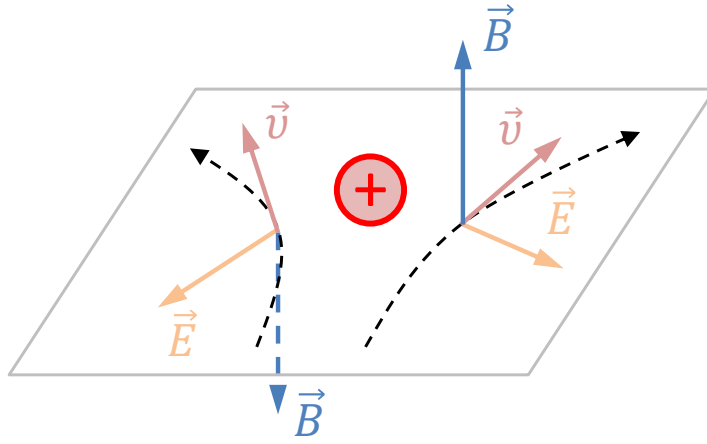


Figure 2.4: Skew scattering of an electron on an impurity atom.

The skew scattering contribution to the SHC is purely extrinsic and due to τ^1 dependance, it dominates in nearly perfect crystals.

Side-jump mechanism

Semiclassically, the side-jump contribution can be considered as a Gaussian wave-packet scattered from a spherical impurity with SOC. The wave-packet with incident wave-vector \vec{k} will be displaced transverse to its initial direction. This mechanism was first mentioned in [128, 129], but taken in a more detailed consideration only later in [14].

In materials with a strong SOC the side-jump contribution can be further separated into:

- Intrinsic-side-jump. The spin-orbit coupled wave-packet is scattered on the scalar potential without SOC.
- Extrinsic-side-jump. The non-spin-orbit coupled wave-packet is scattered from the spin-orbit coupled disorder.

Particularly the intrinsic-side-jump is believed to be dominant for application-important materials such as Pt and Ta.

Intrinsic mechanism

The intrinsic SHC is a contribution in pure ideal crystal appearing due to the Berry phase phenomena [20]. This phase is the addition to the dynamical phase of quantum systems. It is accumulated as the quantum system adiabatically transported around a circuit C and depends only on the geometry of the circuit C . It is related to the topological property known as anholonomy (dependence of state of physical system on the path taken in order to achieve it) and it is known in classical systems from the problems related to the Foucault pendulum. The Berry phase phenomenon of great importance in the field of magnetism.

To predict SHE values of a given sample composition the theorists use the Boltzmann [56] and Kubo Formalisms [48]. The Boltzmann model allows to calculate only the skew scattering contribution (valid for dilute alloys) for the SHE conductivities, whereas the Kubo formalism takes into account the strong SOC coherent effects of the band structure and covers all contributions to transverse conductivities. Moreover, the theory of spin pumping (SP) was developed for the FM/NM systems with oscillating magnetization [139]. For a more profound and comprehensive discussion on the SHE we refer to the review [122].

In SHE experiments unavoidably another spin-current-inducing effect occurs, the inverse spin galvanic effect (ISGE, also known as the Rashba-Edelstein effect). Both effects have similar angular dependance, thus it is challenging to separate one from another.

Inverse spin galvanic effect

ISGE is the generation of spatially homogeneous non-equilibrium spin polarization by a charge current, whereas the SHE leads to the spin accumulation only at the boundaries of the solid. ISGE is observed in systems with broken inversion symmetry where a shift of spin-up sub-band toward spin-down sub-bands in momentum k -space goes along with the spin-flip scattering asymmetry [52].

Two cases of the broken symmetry that lead to the spin splitting are known: the Dresselhaus [37] and the Rashba [112] spin splittings. The Dresselhouse splitting is related to the bulk inversion asymmetry (being inherent crystallographic property), whereas the Rashba splitting is related to the structure inversion asymmetry (appears in multilayer structures with unequal interfaces). For the NM/FM systems usually only the Rashba spin splitting is relevant, while materials with bulk inversion asymmetry are very rare.

Simplifying, the ISGE can be imagined as an analogue to the spin-orbit coupling of an electron with orbital momentum l that moves in the electric field \vec{E} of a nucleus. Due to relativistic effects, the electric field transforms into an effective magnetic field acting on the spin of the electron, thus coupling orbital and spin moments. If now the electric fields in a crystal have a broken symmetry, e.g. at the interface where the ligand fields for example may have a preferred axis out-of-plane, the conduction electrons experience a net electric field perpendicular to the interface. The field "seen" by electrons is $B_{\text{SO}} = -\frac{\hbar}{2mc^2} \vec{k} \times \vec{E}$, where m is the electron mass, c is the speed of light in vacuum, and \vec{k} is the wave-vector of electron. Then, if spin relaxation is taken into account, the electron spins align with the average Rashba field.

Due to the coupling of electron spin and \vec{m} , a torque will be exerted on \vec{m} [91]:

$$\vec{T}_{\text{SO,R}} = \frac{m\delta_{\text{ex}}}{e\hbar E_{\text{F}}} \alpha_{\text{R}} (\vec{m} \times (\vec{z} \times \vec{j})), \quad (2.26)$$

where $\delta_{\text{ex}} = \frac{J_{\text{ex}}\hbar M_{\text{s}}}{2\gamma}$, E_{F} is the Fermi energy, α_{R} is the Rashba constant describing the strength of the SOC. From this torque one can extract the Rashba field entering the LLG equation:

$$\mu_0 \vec{H}_{\text{R}} = \frac{\alpha_{\text{R}}}{2\mu_{\text{B}} M_{\text{s}}} P(\vec{z} \times \vec{j}), \quad (2.27)$$

where μ_{B} is the Bohr magneton, $P = \frac{\delta_{\text{ex}}}{E_{\text{F}}}$ is the spin polarization of the current. This Rashba field (a shift in the resonance field following from the LLG equation) is not to be confused with the relativistic Rashba magnetic field B_{SO} mentioned earlier in the text.

It was shown [123] that the Rashba field-like torque is inversely proportional to the FM layer thickness. Thus, the Rashba effect can not be neglected in experiments with ultrathin FM samples.

2.4.2 Spin injection and accumulation in NM/FM systems

Spin currents flowing in NM lead to spin accumulation in the vicinity of NM boundaries with a decay length λ_{s} called spin-diffusion length. If a FM is attached to the NM the spin current will be injected into the FM producing spin-orbit torques (SOTs). If simultaneously FMR is induced in the FM, the torque influences magnetization dynamics, see Fig. 2.1. In a reciprocal case, the FMR precession injects spin currents into the NM, a phenomenon called spin pumping (SP).

Drift-diffusion formalism

One of the formalisms for the description of the spin current is the drift-diffusion model. The model is applicable if the system is much larger than the mean free path (MFP) of electrons, and it is widely used for interpretation of most of the SHE experiments.

For conventional charge current the following set of equations is used:

$$\begin{aligned} -|e| \frac{\partial n}{\partial t} + \nabla j &= 0 \\ j_i &= \sigma E_i + |e| D \frac{\partial n}{\partial x_i} = \sigma (\nabla \mu_i), \end{aligned} \quad (2.28)$$

where n is the electron density, j_i is the charge current in direction i , $\sigma = \frac{e^2 \tau n}{m}$ is the electrical conductivity, μ is the effective electrical potential, and $D = \frac{v_{\text{F}}^2 \tau}{2}$ is the diffusion coefficient, m is the effective electron mass, v_{F} is the Fermi velocity and τ is the momentum relaxation time. The first expression is the continuity equation, whereas the second describes the charge drift induced by the electric field and diffusion phenomena.

For the spin current in NM another set of equations is used:

$$0 = \frac{\hbar}{2} \left(\frac{\partial s_j}{\partial t} + \frac{s_j}{\tau_s} \right) + \frac{\partial j_{ij}^s}{\partial x_i}, \quad (2.29)$$

$$j_{ij}^s = \frac{\hbar}{2} \left(-\mu' E_i s_j - D \frac{\partial s_j}{\partial x_i} \right), \quad (2.30)$$

where τ_s is the spin relaxation time, related to the spin diffusion length $\lambda_s = \sqrt{D\tau_s}$, μ' is the mobility and not the chemical potential, the bottom indexes of j_{ij}^s describe the spatial flow direction and the spin polarization direction. In NM the spin accumulation is $s_j = n_{+j} - n_{-j}$, where $n_{\pm j}$ is the number of electrons with spin polarization in $\pm j$ -direction. The associated spin momentum is then $\frac{\hbar}{2}s$.

The spin relaxation is usually modeled with the Elliott-Yafet spin-lattice relaxation [42, 154] where the idea is as follows: for each electron momentum scattering there is a probability P at which additionally the spin switches, so that $\tau_s = P \cdot \tau$, where τ is the average time between momentum scattering events.

The first term in (2.30) describes a drift of electrons with certain polarization and it is often referred as a "polarized current", while the second term is the diffusion of the spin without the charge redistribution and is often referred as "pure spin current". In comparison to the charge current, the spin current drift-diffusion model has an additional degree of freedom and spin is not a conserved quantity.

The drift-diffusion formalism only describes spin and charge distributions. In the following considerations the charge current distribution and the conductivity are assumed homogeneous, which is not true in the general case. For simplicity a homogeneous, but smaller than the bulk electrical conductivity value is used to fit experimental data.

The drift-diffusion equations for the FM are out of scope of this work, but we will mention that those have to be modified [61]. The first difference is that the electron current in FM is modeled with the two channel model (spin-up and spin-down electrons with respect to the magnetization \vec{m}). Second, Eq. (2.29) needs to be extended with two additional terms, which describe the precession of the spin accumulation around the local magnetization and its damping. However, in metallic FMs total damping of the non-collinear spin accumulation happens within a few lattice translation periods as the spin current enters the FM. Due to this reason the mentioned terms are often dropped and the damping of spin accumulation is included into the boundary condition at the NM/FM interface.

The charge current in FM is $j = j^\uparrow + j^\downarrow$. The electrical conductivity is then $\sigma = \sigma_\uparrow + \sigma_\downarrow$ and spin conductivity is $\sigma_s = \sigma_\uparrow - \sigma_\downarrow$. The spin polarization is defined as $P_\sigma = \frac{\sigma_s}{\sigma}$ and it is aligned with the magnetization direction.

Due to the SOC phenomenon, charge and spin currents are coupled. The charge current produces a transverse spin current due to the SHE. The reciprocal phenomenon (ISHE) can be described by exactly the same formalism. The transformation efficiency of one current into the other is described with a constant θ_{SH} called the spin Hall angle (SHA) and its value lies in the range $0 < \theta_{\text{SH}} < 1$. The connecting equation reads [38]:

$$\begin{aligned} j_i &= j_i^0 + \frac{2|e|\hbar}{\hbar} \theta_{\text{SH}} \epsilon_{ijk} j_{jk}^{s,0}, \\ j_{ij}^s &= \frac{\hbar}{2|e|} \theta_{\text{SH}} \epsilon_{ijk} j_k^0, \end{aligned} \quad (2.31)$$

where ϵ_{ijk} is the Levi-Civita symbol, j_i^0 and $j_{ij}^{s,0}$ are the charge and spin currents without spin-orbit coupling, respectively. Spin current polarization $\vec{\sigma}$ is perpendicular to both charge current and spin current directions. Using the Eqs. (2.31) we can write the general form of equations for the charge and spin current:

$$j_i = \sigma E_i + |e| D \frac{\partial n}{\partial x_i} - \theta_{\text{SH}} |e| \epsilon_{ijk} \left[\mu' E_j s_k + D \frac{\partial s_k}{\partial x_j} \right], \quad (2.32)$$

$$j_{ij}^s = \frac{\hbar}{2} \left(-\mu' E_i s_j - D \frac{\partial s_j}{\partial x_i} - \frac{\theta_{\text{SH}}}{|e|} \epsilon_{ijk} \left[\sigma E_k + |e| D \frac{\partial n}{\partial x_k} \right] \right). \quad (2.33)$$

The terms in the square brackets in (2.32) are the AHE (a comprehensive review can be found in [106]) and ISHE parts, whereas for Eq. (2.33) both terms are referred in the literature as the SHE terms.

Now, let us imagine a NM with a homogeneous charge current in x direction. Due to the symmetry of the system, the spin current will be induced into the y and z directions by means of the SHE. Without the loss of generality we consider the spin accumulation along the the z axis. Solving Eq. (2.29) together with Eq. (2.33) we get the following spin accumulation distribution:

$$s_y(z) = \frac{\lambda_s \theta_{\text{SH}} j_x}{|e| D} \frac{\sinh\left(\frac{z}{\lambda_s}\right)}{\cosh\left(\frac{w}{2\lambda_s}\right)} \quad (2.34)$$

where w is the width of NM film. An example of the spin profile $s_y(z)$ is shown in Fig. 2.5. As can be seen from Eq. (2.34) the size of the spin accumulation region depends on the spin diffusion length λ_s .

If a FM is attached on the top of the NM the spin accumulation will be partially transported into the FM inducing the spin transfer torque (STT). The component transverse to the magnetization \vec{m} is absorbed. The transported angular momentum therefore influences the magnetization dynamics of the FM.

It is important to mention that the spin transfer to the FM is in general not complete due to a phenomenon called spin filtering. As a consequence the effective SHA is reduced.

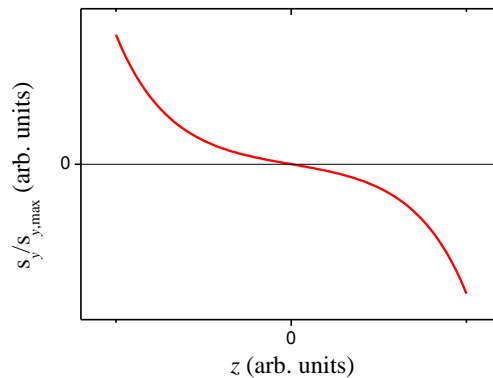


Figure 2.5: An example spin accumulation at the boundary of FM/NM according to Eq. (2.34)

2.4.3 Spin filtering at the NM/FM interface

The SHE induces a spin accumulation in NM, and the magnetization dynamic is influenced by the spin angular momentum transferred to the FM. The momentum transfer might be not complete and it depends on the orientation of the magnetization \vec{m} and spin accumulation direction.

The drift-diffusion model works well down to nm-thick samples. In the general case, the electronic band structure changes abruptly at the NM/FM interface and therefore makes it impossible to use the drift-diffusion formalism at the interface. However, this problem can be overcome by introduction of a quantum mechanical boundary condition between NM and FM [19]. The interface can be considered as a resistor characterized by a scattering matrix that connects states n of the distribution function in the NM to the states m in the FM.

In FM we have a preferred direction: parallel and antiparallel to \vec{m} , whereas for the NM no such a preferred direction exists and the spin current polarization can be directed arbitrarily. Therefore, to investigate the transfer/reflection of the spin current on the interface one needs to consider the directions parallel and transverse to the \vec{m} .

The initial spin state can be written as $a|\uparrow\rangle + b|\downarrow\rangle$, with complex amplitudes a and b . The transverse component of the initial spin state is given by a^*b , the reflected part of the transverse component is $(r^\uparrow)^*r^\downarrow$, the transmitted part is $(t^\uparrow)^*t^\downarrow$. **The parallel part** is described by the two-current model, where the interface is characterized by a finite conductance for majority and minority charge currents:

$$\begin{aligned} j^\uparrow &= G^\uparrow \Delta\mu^\uparrow, \\ j^\downarrow &= G^\downarrow \Delta\mu^\downarrow, \end{aligned} \quad (2.35)$$

where G^\uparrow and G^\downarrow are the spin-dependent interface conductivities, $\Delta\mu^\uparrow$ and $\Delta\mu^\downarrow$ are the respective drops in quasichemical potentials [3]. The spin current is built up by the difference between the two charge currents. The interface conductivities are given by [19]:

$$G^{\uparrow(\downarrow)} = \frac{e^2}{h} \left[M - \sum_{nm} |r_{nm}^{\uparrow(\downarrow)}|^2 \right] = \frac{e^2}{h} \sum_{nm} |t_{nm}^{\uparrow(\downarrow)}|^2, \quad (2.36)$$

where $r_{nm}^{\uparrow(\downarrow)}$ and $t_{nm}^{\uparrow(\downarrow)}$ are the reflection and transmission probabilities for up-spins (down-spins) at the interface, M is the number of conducting channels in the NM.

While the transfer of the parallel part of the spin angular momentum through the interface is intuitively clear, the **transverse part** transfer is a quantum phenomenon and has no classical analogs, see Fig. 2.6.

The **transverse** spin transfer as for the **parallel part** is defined by the reflection and transmission coefficient. However, unexpected effects appear, let's consider three limiting cases:

1. Full reflection for one of the spin populations and full transmission for the other. As the result the transverse component of spin angular momentum will be completely absorbed at the interface and both reflected and transmitted parts of the momentum will not contain the transverse components. Due to this property, this phenomenon is called the spin filtering [133].

2. Full transmission of both spin populations. In this case the transverse component is fully transmitted to the FM without a loss at the interface.
3. Full reflection of both spin populations. In this case no transverse component is lost as well, however the transverse part might undergo a rotation.

The $1 - (r^\uparrow)^* r^\downarrow$ value describes the amount of the transverse momentum that reaches the interface. The quantity called the spin mixing conductance (SMC) can be introduced:

$$G^{\uparrow\downarrow} = \frac{e^2}{h} \left[M - \sum_{nm}^M |(r_{nm}^\uparrow)^* r_{nm}^\downarrow|^2 \right], \quad (2.37)$$

In literature one can find different designations for the SMC, here we define notations that we use further in the text:

$$[G^{\uparrow\downarrow}] = \frac{1}{\Omega}, \quad \tilde{G}^{\uparrow\downarrow} = \frac{G^{\uparrow\downarrow}}{A_{\text{int}}}, \quad [\tilde{G}^{\uparrow\downarrow}] = \frac{1}{\Omega m^2}$$

where A_{int} is the area of NM/FM interface.

The full boundary condition for the spin current at NM/FM interface reads:

$$\begin{aligned} \vec{j}^s = & [-(G^\uparrow + G^\downarrow)\Delta\vec{\mu}_s \cdot \vec{m} + (G^\uparrow - G^\downarrow)\Delta\mu] \vec{m} + \\ & + \text{Re}\{G^{\uparrow\downarrow}\}(2\Delta\vec{\mu}_s \times \vec{m}) \times \vec{m} - \text{Im}\{G^{\uparrow\downarrow}\}(2\Delta\vec{\mu}_s \times \vec{m}), \end{aligned} \quad (2.38)$$

The first two terms describe the parallel part of the spin current with the drops in the quasichemical spin $\Delta\vec{\mu}_s$ and charge $\Delta\mu$ potentials. The second pair of terms describes the transverse part, where the double cross product gives the part of $\vec{\mu}_s$ that is transverse to the \vec{m} and simultaneously lies in the plane spanned by the \vec{m} and $\vec{\mu}_s$ (i.e. the incoming transverse part). The incoming transverse part is reduced by the amount of backscattered transverse spins without rotation (real part of the SMC). For the backscattered spins the rotated part is perpendicular to both \vec{m} and the incoming transverse part (imaginary part of the SMC).

In the context of interface conductivities a value called the Sharvin conductivity is introduced $G_{\text{SH}} = \frac{e^2}{h} M$. The value describes the conductivity of interface for the perfectly transparent contacts and it is the upper limit for all spin-dependent conductivities.

2.4.4 Spin Hall angle in FMR experiments with FM/NM bilayers

Once the spin angular momentum is transferred from NM to FM, a torque acting on the magnetization \vec{m} is produced. The parallel part of the transferred spin does not produce a torque on \vec{m} and the angular momentum is transferred to the lattice [61]. In turn, the transverse part of the spin angular momentum is transferred predominantly to \vec{m} . As the electron enters FM, the transverse spin part starts to precess in the exchange field of the FM and it relaxes after a few lattice translation periods of the FM [133]. Additionally, rotation of the reflected part of the transverse part exerts the torque on the magnetization as well.

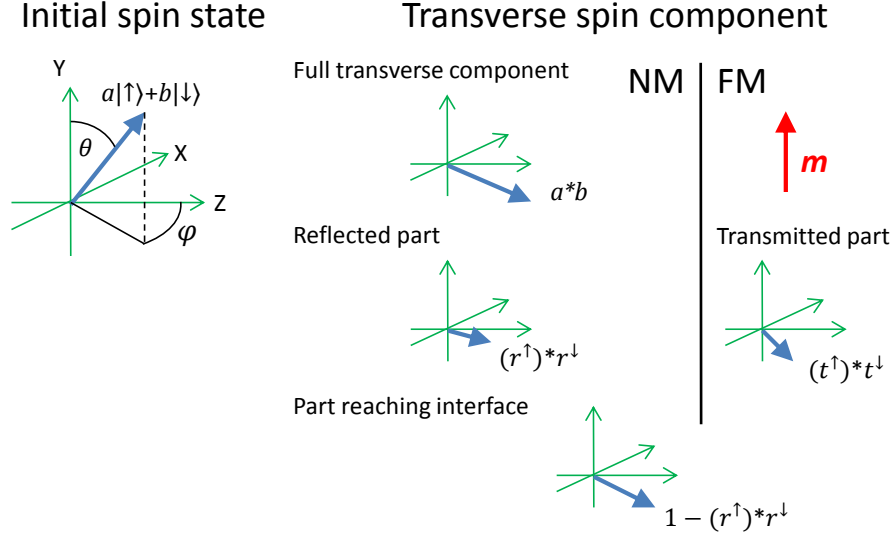


Figure 2.6: Spin filtering at the NM/FM interface. The phenomenon is relevant only for the transverse spin component (with respect to \vec{m}).

Using the drift-diffusion model for the SHE in NM/FM bilayers one gets the following expressions for the field-like and damping-like torques acting on the \vec{m} [61]:

$$\begin{aligned} \vec{T}_{\text{FL}} &= -\gamma\tau_{\text{FL}}\vec{m} \times \vec{\sigma}, & \tau_{\text{FL}} &= \frac{h}{2|e|M_s d_{\text{FM}}}\eta_{\text{FL}}\theta_{\text{SH}}j, \\ \vec{T}_{\text{DL}} &= -\gamma\tau_{\text{DL}}\vec{m} \times (\vec{m} \times \vec{\sigma}), & \tau_{\text{DL}} &= \frac{h}{2|e|M_s d_{\text{FM}}}\eta_{\text{DL}}\theta_{\text{SH}}j, \end{aligned} \quad (2.39)$$

where d_{FM} is the FM thickness, τ_{DL} and τ_{FL} are the corresponding torque strengths in units of Tesla, η_{DL} and η_{FL} are the spin injection efficiencies, the values lie in the interval $[0,1]$. From the expressions one sees, that the effect on thin FM is stronger than on thicker ones. Also, the comparison of the expression for Rashba torque Eq.(2.26) and Eq.(2.39) for the SHE-induced torque shows the principal problem to separate those contributions due to the shared symmetry. However, the knowledge of the SMC can give an upper limit for the SHE-induced torque [33].

Since the STT is not complete due to the spin filtering phenomena and the interaction of reflected spin accumulation from the boundaries of NM, the effective SHA is defined as $\theta_{\text{eff}} = \eta_{\text{DL}}\theta_{\text{SH}}$. The injection efficiency from the drift-diffusion model reads:

$$\begin{aligned} \eta_{\text{DL}} &= \left(1 - \frac{1}{\cosh\left(\frac{d_{\text{NM}}}{\lambda_s}\right)}\right) \frac{|\tilde{G}_r^{\uparrow\downarrow}|^2 + \text{Re}\left(\tilde{G}_r^{\uparrow\downarrow}\right) \tanh\left(\frac{d_{\text{NM}}}{\lambda_s}\right)^2}{|\tilde{G}_r^{\uparrow\downarrow}|^2 + 2\text{Re}\left(\tilde{G}_r^{\uparrow\downarrow}\right) \tanh\left(\frac{d_{\text{NM}}}{\lambda_s}\right)^2 + \tanh\left(\frac{d_{\text{NM}}}{\lambda_s}\right)^4}, \\ \eta_{\text{FL}} &= \left(1 - \frac{1}{\cosh\left(\frac{d_{\text{NM}}}{\lambda_s}\right)}\right) \frac{\text{Im}\left(\tilde{G}_r^{\uparrow\downarrow}\right) \tanh\left(\frac{d_{\text{NM}}}{\lambda_s}\right)^2}{|\tilde{G}_r^{\uparrow\downarrow}|^2 + 2\text{Re}\left(\tilde{G}_r^{\uparrow\downarrow}\right) \tanh\left(\frac{d_{\text{NM}}}{\lambda_s}\right)^2 + \tanh\left(\frac{d_{\text{NM}}}{\lambda_s}\right)^4}, \\ \tilde{G}_r^{\uparrow\downarrow} &= \tilde{G}^{\uparrow\downarrow} \frac{2\lambda_s \tanh\left(\frac{d_{\text{NM}}}{\lambda_s}\right)}{\sigma_{\text{NM}}^0}, \end{aligned} \quad (2.40)$$

where σ_{NM}^0 is the bulk electrical conductivity of NM. The first multiplier in both efficiencies comes from the drift-diffusion model within the NM, whereas the second multiplier is due to the NM/FM interface transparency. The first multiplier reduces the efficiency if d_{NM} is not significantly larger than the spin-diffusion length λ_{s} . This happens due to the reflection and backflow of the spin current from the boundary opposing to the NM/FM interface. As the rule of thumb, the NM thickness should be $\geq 2\lambda_{\text{s}}$, to avoid strong reduction of the SHE efficiency [33].

For the evaluation of experimental data the approximation $|\tilde{G}^{\uparrow\downarrow}|^2 \approx \text{Re}(\tilde{G}^{\uparrow\downarrow})^2$ seems reliable enough, because $\text{Im}(\tilde{G}^{\uparrow\downarrow})$ is about one order of magnitude smaller than $\text{Re}(\tilde{G}^{\uparrow\downarrow})$ for metal/metal systems [159]. The SMC cannot be measured directly and a series of thickness-dependent measurements has to be done to extract it. In order to avoid a series of measurements we use for our experimental data an expression obtained for the Pt/Py system by [4]:

$$\eta_{\text{DL}} = \frac{2 \sinh^2\left(\frac{d_{\text{NM}}}{2\lambda_{\text{NM}}}\right)}{\cosh\left(\frac{d_{\text{NM}}}{\lambda_{\text{NM}}}\right) \left[1 + \frac{\lambda_{\text{Py}} \rho_{\text{NM}}}{\lambda_{\text{NM}} \rho_{\text{Py}}} \frac{\tanh\left(\frac{d_{\text{NM}}}{\lambda_{\text{NM}}}\right)}{\tanh\left(\frac{d_{\text{Py}}}{\lambda_{\text{Py}}}\right)}\right]}, \quad (2.41)$$

where λ_{Py} and λ_{NM} are the spin diffusion lengths of Py and NM, ρ_{Py} and ρ_{NM} are the resistivities of Py and NM. The spin diffusion lengths from literature are cited in Table 5.10.

2.4.5 Charge current distributions in FM/NM stack

In order to evaluate the strength of the SOTs one needs to know the current flowing through the NM I_{NM} , being only a fraction of a total current I_{stack} flowing through FM/NM stack. More specifically, one needs to know the current density j_{NM} . Starting from a simple model where the FM and NM can be treated as two resistors connected in parallel, we obtain a fraction k of I_{NM} in the I_{stack} :

$$k = \frac{I_{\text{NM}}}{I_{\text{stack}}} = \frac{1}{1 + \frac{\rho_{\text{NM}} d_{\text{FM}}}{\rho_{\text{FM}} d_{\text{NM}}}}, \quad (2.42)$$

where d_{FM} and d_{NM} are the thicknesses of FM and NM layers, ρ_{FM} and ρ_{NM} are the electrical resistivities of FM and NM layers.

For macroscopically large and homogeneous samples the Drude theory can be used to describe the conductivity. The theory assumes that electrons move freely between scattering events. Scattering leads to the randomization of the motion with conservation of the electron velocity. The average distance that an electron travels between scattering events is called the mean free path (MFP, usually labeled with λ).

For thin films the bulk values of resistivities cannot be used anymore if the thickness of film is below or comparable with the electron MFP. At this point interfaces start to play a significant role for scattering events. Moreover, the current distribution in thin film starts to be inhomogeneous.

Models based on the Boltzmann equation were established in order to describe the thickness dependence of thin film conductivity and current distribution within it.

The first developed Fuchs-Sondheimer model [49, 132] takes into account scattering at metal/substrate and metal/vacuum interfaces. In this model the interfaces are assumed to be perfectly flat. Electrons are reflected from the interface either specular or diffusive (somewhat similar to the optical Lambertian reflection). In the model the degree of specular/diffusive reflection is a tunable parameter. Logically, the diffusive scattering reduces the conductivity of thin films stronger because electrons can be reflected backwards. For purely specular-reflecting interfaces the conductivity is not changed, whereas for purely diffusive-reflecting interfaces it is significantly reduced already for $4 - 5\lambda$ -thick films and amounts to $\approx 70\%$ of bulk value at film thicknesses $= 1\lambda$. However, the hypothesis with perfectly flat interfaces is somewhat a bold assumption and the Fuchs-Sondheimer model was modified with inclusion of interface roughness [130]. The roughness leads to a strong enhancement of the diffusive scattering probability, making it almost 100% for non-epitaxially grown samples (roughness > 0.5 nm). In case of the purely diffusive scattering at the interface, the maximal density of the current is found in the middle of a film with its reduction towards the interfaces (about 30% deviation for film thickness $= 1\lambda$).

Next extension to the Fuchs-Sondheimer model is the Mayadas-Shatzkes model [92]. It includes scattering at grain boundaries for polycrystalline samples. This is relevant for samples grown in sputtering chambers, the average grain size is often estimated to be equal to the film thickness up to a certain thickness when it saturates [116]. The grain boundaries are modeled as the vertical planes with a certain reflection probability from it, which leads to a further reduction of the film conductivity. If reflection happens in 50% of cases, the conductivity amounts to $\approx 35\%$ of the bulk value for 1λ -thick polycrystalline films. The current distribution stays similar to the Fuchs-Sondheimer model with fully diffusive scattering.

And the last to mention: so far we were talking about the conductivity of vacuum/metal/insulating substrate structure. But for the vacuum/FM/NM/insulating substrate the FM/NM interface plays an additional role for the current distributions. The interface is transparent for the electrons to some extent. Thus, a layer with a larger MFP pumps the second layer with electrons enhancing the current density in the vicinity of the interface as shown in [33].

In experiments we use FM/NM/insulating substrate stacks with metal layer thicknesses below 2λ . All samples show large surface roughness of 1-1.5 nm, which assume similar interface roughnesses of the stack. Due to all mentioned reasons, we use electrical and thermal conductivity values reduced by factor ≥ 2 for metals as compared to the bulk conductivity, see simulations in Ch. 5.1.

2.5 Conventional Nernst effects

Nernst (the author of the third law of thermodynamics) was breeding fishes in a pond near his cottage. - Why do you bother with them? - asked his acquaintance. - Even a poultry breeding seems to be more interesting. - I bred animals which are in thermodynamic equilibrium with the environment. - replied Nernst. - Breeding homeotherms just means warming the Universe at your expense.

In this chapter we describe the conventional Nernst effects, because those are required for interpretation of the spin Seebeck effect experiments.

Among conventional Nernst effects are the ordinary Nernst effect, the Anomalous Nernst effect (ANE), the Anisotropic magnetothermopower (AMTEP) and the Planar Nernst effect (PNE). All these effects are thermomagnetic analoga of the Hall and magnetoresistive effects. The connection of the mentioned thermomagnetic effects to electromagnetic effects is presented in Table 2.1.

Electromagnetic effect		Thermomagnetic effect
ordinary Hall effect	\longleftrightarrow	ordinary Nernst effect
anomalous Hall effect (AHE)	\longleftrightarrow	anomalous Nernst effect (ANE)
ordinary anisotropic magnetoresistance (AMR)	\longleftrightarrow	anisotropic magnetothermopower (AMTEP)
planar Hall effect (PHE)	\longleftrightarrow	planar Nernst effect (PNE)

Table 2.1: Correspondence table between electromagnetic and thermomagnetic effects

A usual way to describe the Nernst effects is to start from description of a certain electromagnetic phenomenon and then extend it on to the corresponding Nernst effect. Such an approach is valid, because in fact, Nernst effects are combinations of the mentioned electromagnetic effects with the conventional Seebeck effect [78].

2.5.1 Seebeck effect as the driving force of Nernst effects

The Seebeck effect is the phenomenon describing the appearance of an electric current caused by a thermal gradient. Two mechanisms are responsible for the Seebeck effect: the charge carrier diffusion and the phonon drag.

Charge carrier diffusion

First, we discuss the case of charge carrier diffusion. Let us imagine a piece of a metallic solid one side of which has higher temperature (hot side) than the other side (cold side). What happens with the electronic structure of the metal? In Fig. 2.7 we

present Fermi-Dirac (F-D) distributions at different temperatures T for some metal with characteristic Fermi temperature $T_F = 10^5$ K. As the temperature of the solid state body elevates from 0 K, the slope of the F-D distribution of electrons in the region of the Fermi energy E_F changes from infinite (grey line with sharp corners) to finite (red, black and blue lines with rounded corners) [77]. The step is steep, because the deviation in energy of electrons due to the thermal term $k_B T$ is very small in comparison to the Fermi energy $E_F = k_B T_F$, where k_B is the Boltzmann constant. For many metals the Fermi temperature ranges from 10^4 to $2 \cdot 10^5$ K [77, 5].

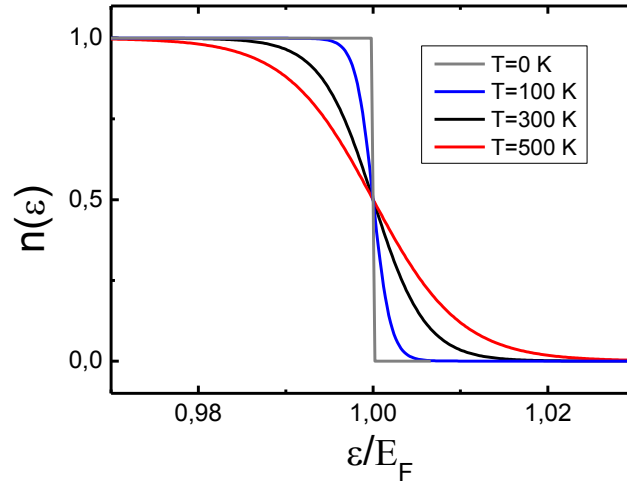


Figure 2.7: Fermi-Dirac distributions of electrons for some metal set at different ambient temperatures $T = 0, 100, 300, 500$ K. As the Fermi temperature of the metal we take a common value $T_F = 10^4$ K.

In the hot region the energy levels above the Fermi level are more populated than in the cold region, while the energy levels below the Fermi level are less populated. Due to this fact, opposing concentration gradients of high- and low-energy electrons appear, leading to diffusion of electrons. Thus, opposed diffusional flows of cold electrons from the cold region and of hot electrons from the hot region appear. Following the Mott formalism [31],

$$GS = \frac{k_B}{-e} \int \frac{E - \mu}{k_B T} \sigma(E) \left(-\frac{df(E)}{dE} \right) dE, \quad (2.43)$$

where G is the electrical conductance, $\sigma(E)$ is the energy-dependent conductivity, $f(E)$ is the F-D distribution, S is the Seebeck coefficient, μ is the chemical potential. If those flows have significantly different conductivities, one gets a substantial effective current flow. This leads to accumulation of charges on opposite sides of the sample. These charges produce an electric field that counteracts further charge accumulation. At some moment a steady-state voltage is formed. It is proportional to the temperature difference between opposite sides, and to the S coefficient. According to the free electron model together with the Mott formalism and Sommerfeld expansion, all metals are expected to have a negative Seebeck coefficients $S = -e L_0 T \frac{\partial}{\partial E} \ln \sigma(E)|_{E_F}$, where L_0 is the Lorenz number. However, the free electron model does not take into account the complexity of real metals.

Larger Seebeck coefficients S are observed for semiconductors, while those conductivities have stronger temperature dependence. $10 \mu\text{V}/\text{K}$ is pretty usual S value for metals, while for semiconductors values as high as $1 \text{ mV}/\text{K}$ are common.

Phonon drag

Another contributor to the Seebeck effect - the phonon drag - is strong for temperatures T close to $\frac{1}{5}$ of the Debay temperature Θ_D [90], [78]. Usually, $\frac{1}{5}\Theta_D$ -value lies far below RT. At these temperatures oscillations of the crystalline lattice are large and electron-phonon scattering starts to affect electron movement, contributing to the Seebeck coefficient. At higher temperatures phonon-phonon interaction becomes very strong, and the phonon drag contribution to the Seebeck effect is greatly suppressed [90].

2.5.2 The anomalous Nernst effect (ANE)

The anomalous Nernst effect (ANE) [43, 68, 17, 117, 94] is a phenomenon well known for more than a century, similar to the Hall effect. For convenience of explanation, we will start from the description of the ordinary Hall effect [59].

When an electric current of density j is applied to the sample in a certain direction, say the x-direction, and simultaneously an external magnetic field \vec{B} perpendicular to the current (conventionally along the z-direction) is applied, the charge carriers q experience the Lorentz force [46] $\vec{F}_{y-L} = q\vec{v} \times \vec{B}$, see Fig. 2.8(a). This force is perpendicular to both \vec{B} and \vec{j} , and drive electric charges q in y-direction. The charges are accumulated at the boundaries of the sample (in case of open circuit condition at the y-boundaries) producing an electric field E_y which counteracts infinite charge accumulation.

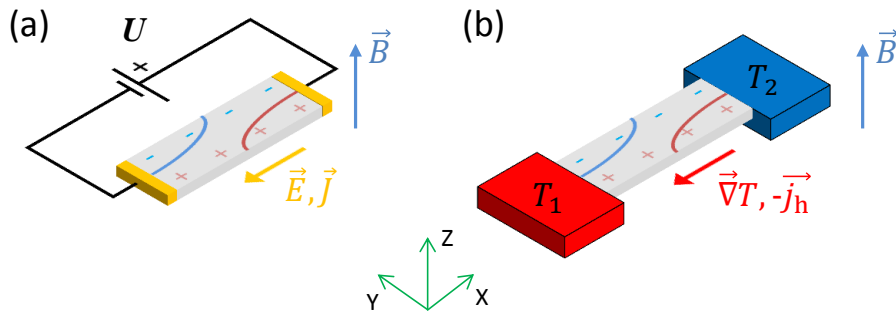


Figure 2.8: (a) The Hall Effect. Magnetic field \vec{B} is applied in z-direction. Electric field \vec{E} applied in x-direction produces an electric current of density \vec{j} . Due to the Lorentz force, electric charges (blue line is for negative charges trajectory and red line is for positive charges) are deflected in y-direction. Electric charges are accumulated at the y-boundaries of the sample (open circuit geometry). (b) The Nernst effect. Magnetic field \vec{B} is applied in z-direction, thermal gradient $\vec{\nabla}T$ - in x-direction ($T_1 > T_2$). Due to the conventional Seebeck effect, electric current in x-direction is formed, leading to an effective Hall effect.

Next, if a sample additionally possesses FM properties, an effect stronger than the Hall effect is observed, namely, the anomalous Hall effect (AHE), first described

in [60]. The AHE and the SHE are two closely related phenomena, with the same three mechanisms responsible for it, see Eq. (2.25) in Ch. 2.4.1.

Substitution of the electric field E_x with a thermal gradient $\vec{\nabla}T$ (Nernst effect in Fig.2.8(b)) leads to the formation of a thermally driven electric current by means of the conventional Seebeck effect. This thermally induced current, in turn, leads to the formation of a Hall effect in case of a non-magnetic material. To be more precise - the resulting signal is the difference of Hall signals produced by cold and hot carriers. This thermomagnetic effect was first observed by Nernst and Ettingshaus [43] and is named after them (often shortened to just Nernst effect). In analogy to the AHE, a stronger thermomagnetic effect is observed in FM - the Anomalous Nernst effect (ANE).

$$\vec{E}_{\text{ANE}} = \alpha \vec{\nabla}T \times \mu_0 \vec{H}, \quad (2.44)$$

where α is a material constant, μ_0 is the permeability of vacuum. From the famous constitutive relations of electromagnetism $\vec{B} = \mu_0 H$ for vacuum.

2.5.3 The planar Nernst effect (PNE) and anisotropic magnetothermopower (AMTEP)

The anisotropic magnetothermopower (AMTEP) and the closely related planar Nernst effect (PNE) [6, 117, 94, 111, 80] are the thermal analogues of the anisotropic magnetoresistance (AMR) and the Planar Hall effect (PHE), respectively. Both AMTEP and PNE can be expressed with the same mathematical framework. AMTEP is the voltage drop measured along the applied thermal gradient $\vec{\nabla}T$ and PNE is the voltage drop measured perpendicular to $\vec{\nabla}T$.

A usual way to describe the AMTEP and PNE is to start from the description of the anisotropic magnetoresistance (AMR, ordinary magnetoresistance) introduced by Thompson [138]. The AMR is a phenomenon that describes the difference of the electric resistivity in parallel and perpendicular to the magnetization direction in a conductive ferromagnet. Due to the spin-orbit coupling the overlap of atom orbitals changes as the magnetization \vec{M} rotates. As a result, the electron scattering cross section is influenced and, therefore, the electric conductivity changes. Typically, the conductivity is higher when the magnetization \vec{M} is perpendicular to the electric current \vec{J} .

We assume an electric current density j_x directed along the x-axis (Fig. 2.9). Following the formalism of [137], we introduce components of the electric field E_{\parallel} and E_{\perp} parallel and perpendicular to \vec{M} :

$$\begin{aligned} E_{\parallel} &= \rho_{\parallel} j_x \cos \varphi, \\ E_{\perp} &= \rho_{\perp} j_x \sin \varphi, \end{aligned} \quad (2.45)$$

where φ is the angle between \vec{M} and x-axis, ρ_{\parallel} and ρ_{\perp} are the resistivities parallel and perpendicular to the \vec{M} , respectively. Projections of these electric field components onto the x-axis are:

$$\begin{aligned} E_{x,\parallel} &= E_{\parallel} \cos \varphi = \rho_{\parallel} j_x \cos^2 \varphi, \\ E_{x,\perp} &= E_{\perp} \sin \varphi = \rho_{\perp} j_x \sin^2 \varphi. \end{aligned} \quad (2.46)$$

Both projections lead to an electric field longitudinal to j

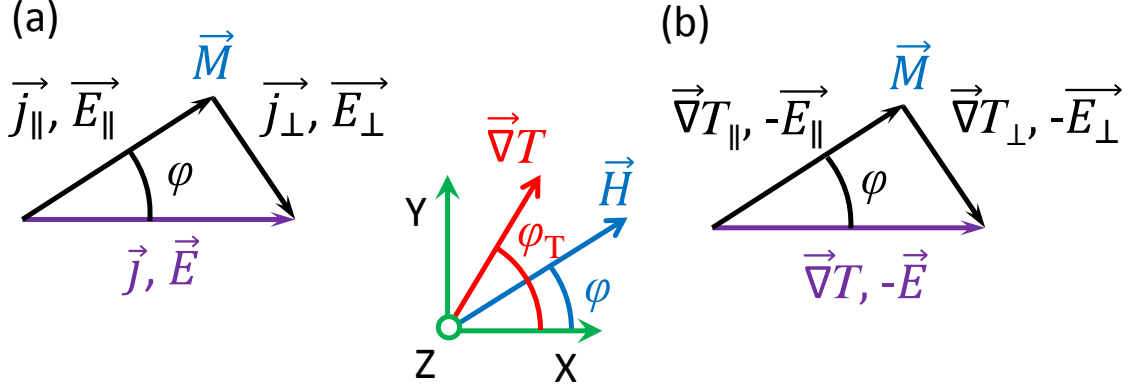


Figure 2.9: (a) When an electric current of density j is driven through a ferromagnetic conductor along the x-axis, the electric resistances \parallel and \perp to \vec{M} are different due to the AMR. The different electric fields parallel and perpendicular to \vec{M} result in different electric fields along the x- and y-direction strongly depending on the angle between the electric current \vec{j} and \vec{M} . (b) Thermal analogue to (a): a temperature gradient is the driving force of an electric current along the x-axis. Due to the anisotropic orbitals of atoms, the parallel and perpendicular Seebeck coefficients S_{\parallel} and S_{\perp} differ from each other. Thus, the measured voltage depends on the direction of the magnetization.

$$E_x = E_{x,\parallel} + E_{x,\perp} = (\rho_{\parallel} \cos^2 \varphi + \rho_{\perp} \sin^2 \varphi) j_x. \quad (2.47)$$

Using well known trigonometric equations $\sin^2 \varphi = 1 - \cos^2 \varphi$ and $\cos^2 \varphi = \frac{1 + \cos 2\varphi}{2}$ one can derive the longitudinal AMR:

$$E_x = \left(\frac{\rho_{\parallel} + \rho_{\perp}}{2} + \frac{\rho_{\parallel} - \rho_{\perp}}{2} \cos 2\varphi \right) j_x. \quad (2.48)$$

In a similar way we obtain an expression for the transverse electric field E_y :

$$E_y = E_{y,\parallel} + E_{y,\perp} = (\rho_{\parallel} - \rho_{\perp}) \cos \varphi \sin \varphi j_x. \quad (2.49)$$

With $\cos \varphi \sin \varphi = \frac{1}{2} \sin 2\varphi$,

$$E_y = \frac{\rho_{\parallel} - \rho_{\perp}}{2} \sin 2\varphi j_x. \quad (2.50)$$

The last equation describes the transverse AMR, also known as the planar Hall effect (PHE) [80].

Now, if we substitute the current density j_x with a thermal gradient ∇T_x along the x-axis, the ordinary Seebeck effect (see Ch. 2.5.1) generates an electric current in the x-direction. Consequently, the AMR and the PHE are involved. Thus, we can use the same mathematical framework for the description of such an anisotropic effect. For a longitudinal-to-thermal-gradient measurement (open circuit geometry) the anisotropic magnetothermopower (AMTEP, the thermomagnetic counterpart of the AMR) leads to an electric field along the x-axis:

$$E_{\text{AMTEP}-x} = - \left(\frac{S_{\parallel} + S_{\perp}}{2} + \frac{S_{\parallel} - S_{\perp}}{2} \cos 2\varphi \right) \nabla T_x. \quad (2.51)$$

For a transversal-to-thermal-gradient measurement the planar Nernst effect (PNE, thermomagnetic counterpart of the PHE) induces an electric field along the y-axis:

$$E_{\text{PNE-}y} = -\frac{S_{\parallel} - S_{\perp}}{2} \sin 2\varphi \nabla T_x \quad (2.52)$$

For directions of a thermal gradient $|\nabla T|$ different from the x- and y-axes one gets a superposition of the AMTEP and PNE signals. For measurements in the AMTEP configuration (along the x-axis) Eq. (2.51) transforms into

$$E_{\text{AMTEP-}x} = -(S_+ + S_- \cos 2\varphi) |\nabla T| \cos \varphi_T, \quad (2.53)$$

where $S_+ = \frac{S_{\parallel} + S_{\perp}}{2}$, $S_- = \frac{S_{\parallel} - S_{\perp}}{2}$, φ_T is the angle between $|\nabla T|$ and the x-axis. Similarly, Eq. (2.52) transforms into

$$E_{\text{PNE-}y} = -S_- \sin 2\varphi |\nabla T| \cos \varphi_T \quad (2.54)$$

Now, we need to find an expression for the AMTEP measured along the y-axis. Taking into account that angles are defined with respect to the x-axis, a phase shift of 90° has to be introduced:

$$\begin{aligned} E_{\text{AMTEP-}y} &= -(S_+ + S_- \cos(2(\varphi - 90^\circ))) |\nabla T| \cos(\varphi_T - 90^\circ) = \\ &= -(S_+ - S_- \cos(2\varphi)) |\nabla T| \sin \varphi_T. \end{aligned} \quad (2.55)$$

By combining Eq. (2.54) and (2.55) and applying the trigonometric equality $\sin(\alpha - \beta) = \sin \alpha \cos \beta - \cos \alpha \sin \beta$ the final expression for the electric field along the y-axis is obtained:

$$E_y = -(S_+ \sin \varphi_T + S_- \sin(2\varphi - \varphi_T)) |\nabla T| \quad (2.56)$$

In the case of an arbitrary direction of the thermal gradient $\vec{\nabla} T$, it is not very correct to refer to the electric field E_y as the PNE. In the following, we mostly refer to both AMTEP and PNE as just AMTEP, since this name more generally describes the phenomena. Note, some authors use the abbreviation AMTP instead of AMTEP.

2.6 Spincaloric effects

Spin caloritronics [12] is a very young branch of spintronics which appeared just recently, however a great amount of work has already been done in the field and the relevant phenomena can be roughly separated into the following three classes:

1. independent electron effects in metallic magnets, which are the generalization of the collinear magnetoelectronics. The effects are described by the two-current model, where the minority and majority of spin carriers flow in parallel channels with different resistance dependent on the spin direction. The model, first introduced by Mott in 1936 [104], is applied in the bulk of a FM as well as for the interfaces between FMs and NMs, also with tunneling barriers where

at least one metal is magnetic. Particularly, the spin-dependent Seebeck effect [124] belongs to this class, and this effect should not be confused with the spin Seebeck effect (SSE, also referred by some as the spin wave or magnonic Seebeck effect), which belongs to the class of collective effects.

2. collective dynamics effects based on the magnetic order parameters that couple to single particle spins via the spin-transfer torque (STT) and spin pumping. At elevated temperatures the phonons, magnons and electron-hole excitations coexist and carry heat. Most non-equilibrium states are well explained in terms of a weakly interacting three-reservoir model, in which phonons, magnons and electrons are all at their own equilibria and have different temperatures. The coupling of different modes can lead to such phenomena like the phonon-drag effect on the thermopower at low temperatures. Phonons and electrons are relatively strongly coupled in comparison to their coupling to the spin;
3. relativistic effects, thermoelectric generalization of relativistic correction of such effects as the AMR, AHE, and SHE, i.e. the corresponding AMTP, ANE and SNE.

In the following subchapters we focus on the theory of transverse SSE (TSSE) and the SNE.

2.6.1 Thermal counterpart of SHE – the spin Nernst effect (SNE)

The spin Nernst effect (SNE, also known as thermo-spin Hall effect) is the thermal counterpart of the SHE, see Fig. 2.3(b). Namely, it is the generation of spin-current \vec{j}_s transverse to an applied temperature gradient $\vec{\nabla}T$, an effect which has been, until recently, investigated only by theorists [26, 86, 136, 150]. A first experimental observation of SNE effect has just been published [99]. The effect was experimentally found in Pt/YIG with the technique refereed by the authors as the spin Nernst magneto-thermopower (SNMTP). The authors found that the SNE magnitude is comparable to the magnitude of the SHE, but has a sign opposite to it. This technique is very similar to the recently discovered spin Hall magnetoresistance (SMR) [25].

In contrast to the SNMTP technique, we use in our experiments the modulation of damping technique (MOD) [33] in order to detect the SNE. This technique has already proven to be a reliable tool for the detection of spin currents in the SHE experiments and it is in fact a less ambiguous method for the interpretation of spin current detection in comparison to transport measurements, which are more prone to side effects. However, according to [99], the lower limit of spin current detection sensitivity for the SNMTP method is by orders of magnitude better than of the MOD technique.

2.6.2 Theoretical aspects of the SNE

In analogy to SHC in Eq. (2.24), the Spin Nernst conductivity (SNC) is introduced by [26, 86]:

$$j_x^z = -\alpha_{yx}^z \nabla T_x. \quad (2.57)$$

The name spin Nernst conductivity is somewhat misleading, since its unit of measurement is $\text{AK}^{-1}\text{m}^{-1}$, the name is just coined due to its affinity to the spin Hall conductivity. And similarly to Eq.(2.25), the SNC can be subdivided into the intrinsic, the skew scattering, and the side-jump conductivities:

$$\alpha_{yx}^z = \alpha_{yx}^{z\text{-int}} + \alpha_{yx}^{z\text{-skew}} + \alpha_{yx}^{z\text{-sj}}. \quad (2.58)$$

According to the Mott relation at 300 K [136, 150] the SNC amounts to:

$$\alpha_{yx}^z = -\frac{e}{h} \int d\varepsilon \frac{df(\varepsilon, \mu, T)}{d\mu} \sigma_{yx}^z(\varepsilon) \frac{\varepsilon - \mu}{T}. \quad (2.59)$$

As it is obvious from the equation, the asymmetry of $\sigma_{yx}^z(\varepsilon)$ in the vicinity of the Fermi level is the key property to achieve a large SNC. This means, that materials, which are good for SHE experiments are not necessarily good for SNE experiments.

In analogy to the SHA, one can introduce the spin Nernst angle (SNA):

$$j_x^z = -\theta_{\text{SN}} \sigma S \nabla T_x. \quad (2.60)$$

where θ_{SN} is the SNA, σ is the electrical conductivity, and S is the conventional Seebeck effect coefficient. As the SHA, the SNA is a dimensionless quantity, and connection of the SNA to the SHA reads as the

$$\frac{\theta_{\text{SH}}}{\theta_{\text{SN}}} = -S \frac{\sigma_{yx}^z}{\alpha_{yx}^z}. \quad (2.61)$$

One of the first theoretical works [26] on the SNE is conducted for a Hall-bar structure with the Rashba spin-orbit interaction (SOI) with external magnetic field included. The authors use the formalism of the tight binding model and the Landau-Buttiker formula, which states, that the conventional Nernst effect shows maxima when the Landau levels cross the Fermi levels. In turn, the SNE shows non-zero oscillatory behavior in the vicinity of the Landau levels only when the SOI is not 0. Also, the authors underline that strong electrical fields suppress SNE.

The conventional Seebeck and Nernst effects are known for a stronger sensitivity to the details of the electron DOS than the electrical conductivity. Similarly, the SNE shows significantly more complicated dependence, than the SHE. But, in contrast to the charge Nernst effects, which are in fact combinations of the conventional Seebeck effect with a corresponding charge Hall effect, the SNE is not simply a combination of the Seebeck effect and the SHE. Authors [136] show that the SNE conductivity consists of two parts - electrical and thermal $\alpha_{yx}^z = \alpha_{yx}^{sc,z} + \alpha_{yx}^{sq,z}$, where the electrical part is in fact a SHE effect induced by the conventional Seebeck effect, and the thermal part is determined by the electronic structure variation in the vicinity of the Fermi energy.

Liu and Xie [86] exploit similar ideas to [26], but with external magnetic field switched off. They showed that the SNE is generated even if the Seebeck effect is 0 (the electrical part in [136]). Unexpectedly, it is found that the disorder in the system might enhance the SNE coefficient.

An intrinsic (topological) SNE was evaluated in single-layer and bilayer graphene in [41]. The presence of the SOC in graphene leads to the appearance of a band gap,

and the SNC has peaks in the vicinity of the boundaries of valence and conductivity bands, everywhere else it rapidly goes to 0.

Tauber et al. [136] use DOS calculations together with the semi-classical linearized Boltzmann equation to investigate the extrinsic skew scattering mechanism of the SNE. A Cu host with 1% dilution by Au, Bi, and Ti atoms is simulated, because these impurity metals show distinct features in their local DOS. The authors found large SNA for CuAu, which lies in the range from -0.72 to -0.28 , and predicted $1 \cdot 10^9$ A/m² spin current density production at $5 \cdot 10^7$ K/m temperature gradient applied. Reduction of the dilution level by 10 times (down to 0.1 at. %) can theoretically enhance the spin current by 10 times. Controversially, it is shown that the SNE conductivity (for skew scattering) is proportional to the temperature in comparison to the observations in [86]. In contrast to the SHE, the SNE in the CuAu alloy is high due to the lower scattering (impact of the longitudinal conductivity). The theoretical work has encouraged us to produce Cu_{1-x}Au_x samples for experimental SNE investigation. According to the work, lower dilution levels are preferred for a higher SNE. However, we were able to produce controllably only 1-2% dilutions of Au atoms in the Cu host.

Wimmer et al. [150] use the Kubo-Středa formalism for the calculation of the same metallic system as the previous authors [136]. This formalism has already been proven to be useful for the AHE and SHE calculations, and in comparison to the Boltzmann equation formalism (exploited by [136]), which gives access only to the skew scattering, the Kubo-Středa formalism accounts for all possible contributions. It can be applied to disordered, pure systems, and concentrated alloys. Wimmer et al. report on about two times higher values for the thermal part of the spin Nernst conductivity and 14 times higher values for the electrical part than Tauber et al.'s study. It is shown for the Cu_xAu_{1-x} system that by far the strongest contribution to the SNE is skew scattering. Additionally to the divergence of the SNE in the low dilution limit $x \rightarrow 0$ shown by [136], Wimmer et al. demonstrate that the SNE diverges as well in the case $x \rightarrow 1$.

The problem of the sensitivity of spin phenomena to the thermal gradients was underlined by Long et al. [87]. They tried to find theoretically a system with higher SNE sensitivity. The authors report that Ag(111) with skew scattering off impurities on its surface leads to a gigantic SNE. Previously shown coefficients of 20-30 A/Km for spin Nernst conductivity in Cu_{0.99}Au_{0.01} [136, 150] can be enhanced by an order of magnitude in 10-monolayer thick of Ag(111) with a 1% Cr or Pb adatoms on its surface. Authors underline that the way to enhance the SNE is to introduce an asymmetry of the SHC energy dependence around the Fermi energy. The possibility used in their work is the resonant impurity scattering-off on d-impurities introduced by Fert and Levy [45]. Another suggestion to enhance the SNE is to introduce Kondo impurities.

The authors of [54] have modeled the spin-orbit torque (SOT) and the thermal spin-orbit torque (TSOT) with the Kubo Formalism for a FePt/Pt sample. They aimed to estimate a possibility to switch the direction of the magnetization of FM. The authors have estimated, that the thermal gradient needed to accomplish this task amounts to $2 \cdot 10^9$ K/m. Such a large thermal gradient is technically challenging, and in practice gradients one order of magnitude smaller are used.

2.6.3 The spin Seebeck effect (SSE)

The transverse spin Seebeck effect (TSSE)

In 2008 an indication to a phenomenon - the spin Seebeck effect was published by Uchida et al. [144]. Experiments were conducted on the following system: a ferromagnetic (FM) conductive thin film of permalloy (Py) was grown on an insulating sapphire substrate, see Fig. 2.10(a). At the opposite sides of the Py film, thin stripes of Pt were deposited. A heat source and heat sink attached to the FM produce heat flow and a thermal gradient ∇T perpendicular to the Pt stripes. An external magnetic field H is applied in the plane of sample. The voltage signal V proportional to ∇T is measured on each Pt strip. Note, that the sign of the measured voltage depends on whether one or another Pt strip is chosen. Additional measurements with the Pt strips placed at different positions of the Py film reveal that the voltage drop V changes gradually along the Py film reaching 0 in the middle of it. Also, the V signals scales lineary with ∇T . These experimental voltage readings were explained as detection of the spin current \vec{j}_s produced by the heat flow. The detection is performed via inverse spin Hall effect (ISHE) [39, 76, 114] in the Pt strip:

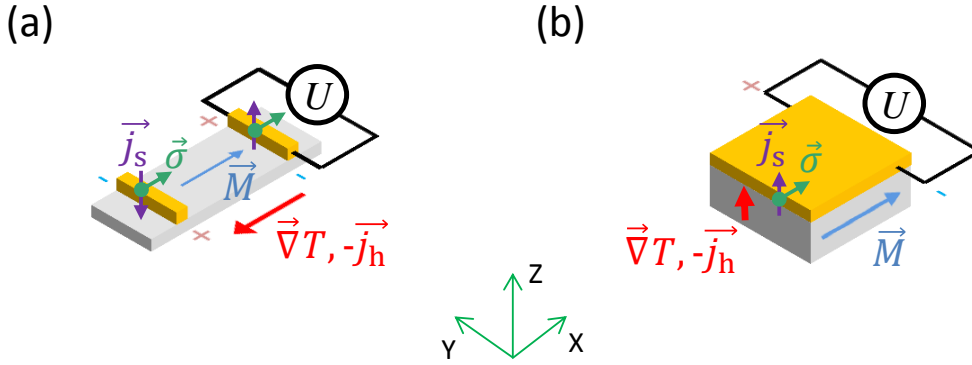


Figure 2.10: Spin Seebeck effect (SSE). (a) Transverse SSE: due to a thermal gradient ∇T applied along the x-axis, a spin current \vec{j}_s arises in FM (grey area) and flows into NM (yellow area) attached to it. The spin current has polarization $\vec{\sigma}$ that coincides with the magnetization \vec{M} direction. Via the ISHE \vec{j}_s is transformed into an electric field perpendicular to both \vec{j}_s and ∇T . (b) Longitudinal SSE: a thermal gradient ∇T is parallel to spin current \vec{j}_s . Similarly to the TSSE, the NM layer transforms \vec{j}_s into an electrical field \vec{E} .

$$\vec{E}_{ISHE} = D_{ISHE} \vec{j}_s \times \vec{\sigma}, \quad (2.62)$$

where D_{ISHE} is the ISHE efficiency, $\vec{\sigma}$ is the spin polarization vector. D_{ISHE} shows higher values in the noble heavy metals due to the spin-orbit coupling. Following this equation at the given geometry, the voltage drop is proportional to $\cos(\Theta)$, where Θ is the angle between ∇T and \vec{M} .

The discovery of this effect was followed by further measurements in a variety of materials: in the half-metallic Heusler compound Co_2MnSi [17], in the ferromagnetic semiconductor GaMnAs [70, 71, 131], in the FM insulator $\text{LaY}_2\text{Fe}_5\text{O}_{12}$ [146].

Later, the authors referred to the described measuring geometry as the conventional or transverse spin Seebeck effect (TSSE), underlining that the spin current flows perpendicular to the thermal gradient.

The longitudinal spin Seebeck effect

In contrast to the initial TSSE geometry, measurements in FM/NM systems, where \vec{j}_s is parallel to the thermal gradient (longitudinal spin Seebeck effect geometry), were conducted [147], see Fig. 2.10(b). First measurements were performed in the Pt/YIG/GGG stack.

This observation showed that the measured voltage signal V is proportional to $\vec{\nabla}T$ and has a dependence on the external magnetic field obeying Eq.(2.62). Measurements were also conducted in a few other materials [95, 143, 121].

LSSE measurements are limited to electrically insulating materials, because otherwise the anomalous Nernst effect masks it in the experimental signal (see Ch. 2.5.2). LSSE and ANE share same angular dependence and Nernst coefficient usually larger than LSSE.

Theoretical description of the spin Seebeck effect

The first attempt to describe theoretically the nature of the measured signal was made already by Uchida et al. in their pioneering work on the TSSE [144]. Authors assumed that the spin-dependent chemical potentials μ_\uparrow and μ_\downarrow have different temperature dependencies. More precisely, the so called "entropy terms" $\frac{\partial\mu_\uparrow}{\partial T}$ and $\frac{\partial\mu_\downarrow}{\partial T}$ are not equal, leading to spin Seebeck coefficient $S_s = \frac{1}{e}(\frac{\partial\mu_\uparrow}{\partial T} - \frac{\partial\mu_\downarrow}{\partial T})$. This description needs to be distinguished from the spin-dependent Seebeck effect [124], where "diffusional terms" are used for the description of the phenomenon. Later the description of SSE via chemical potentials was neglected, because the conduction electron's spin-flip diffusion lengths λ in Py is of several nm order, which contradicts to the experimental observations of voltage signals on the mm-scale.

Experiments of Jaworski et al. [70] on GaMnAs film-samples reveal that the TSSE signal does not originate from the macroscopic longitudinal spin current. This was shown with the help of a scratch perpendicular to the thermal gradient $\vec{\nabla}T$ separating GaMnAs film into two electrically insulated pieces. The measured TSSE signal remained unchanged after the scratch was made. This indicated the importance of the substrate, specifically, the phonon interactions. Further experiments with the GaMnAs system at low temperatures [71] showed similarities between the TSSE and thermal conductivity amplitudes in the range of the Umklapp-process temperatures [77]. These findings in combination with the experiments on insulating FM have supported the phonon-based suggestion, practically excluding conduction electrons of FM from the consideration.

Next, Xiao et al. [153] proposed a **magnon-mediated mechanism** (magnon heat current) based on the difference between the temperatures of the conduction electrons in NM and magnons in the FM underneath, see Fig.2.11(a). The in-equilibrium magnon temperature arises from the neighboring part of FM with the higher temperature. The temperature difference between magnon and electron systems can be found [153, 118] as follows:

$$\Delta T_{\text{me}} = \frac{V_{\text{sat}} \pi M_{\text{S}} V_{\text{a}} t_{\text{NM}}}{g_{\text{r}} \gamma k_{\text{B}} e \Theta_{\text{SH}} \rho_{\text{Pt}} \lambda \tanh t_{\text{NM}} / 2\lambda}, \quad (2.63)$$

where V_{sat} is the difference in SSE signal when external magnetic field direction is switched, V_{a} is the magnetic coherence volume, t_{NM} is the thickness of the NM-detector, g_{r} is the real part of the spin mixing conductance, γ is the gyromagnetic ratio, k_{B} is the Boltzmann constant, e is the electron's elementary charge, Θ_{SH} is the spin Hall angle, ρ_{Pt} is the resistivity of NM-detector, and λ is the spin diffusion length.

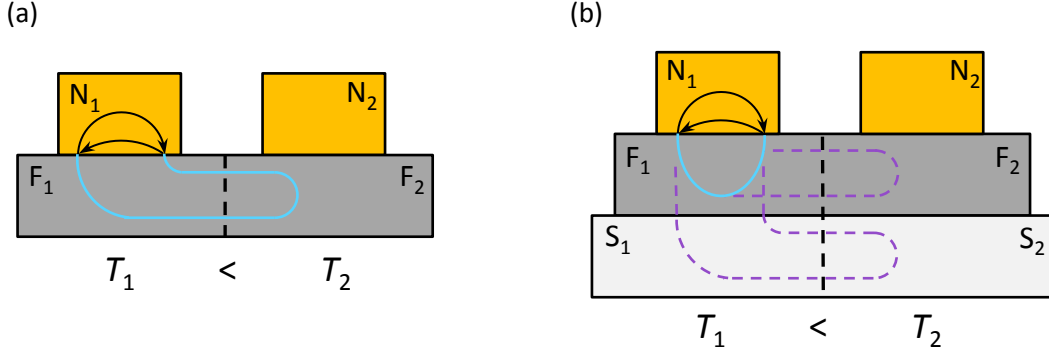


Figure 2.11: Mechanisms of the SSE. (a) Magnon-mediated mechanism. (b) Phonon-dragged SSE. N is a nonmagnetic metal, F is a ferromagnet, S is a substrate. N, F and S are divided into regions with different temperatures. The solid black lines with arrows are electron propagators, the solid blue lines are magnon propagators, the dashed purple lines are phonon propagators.

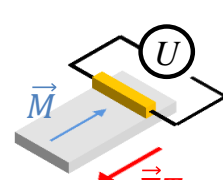
However, this mechanism is unable to explain the Umklapp-process-based TSSE signal enhancement.

A second mechanism was proposed by Adachi et al. [1] in analogy with the phonon-drag in the conventional Seebeck effect. Magnons of one part of FM are dragged via the **magnon-phonon interaction** into the neighboring FM part, causing a magnon temperature imbalance there, see Fig.2.11(b). This mechanism can explain the Umklapp-process-based TSSE enhancement, since phonons are involved.

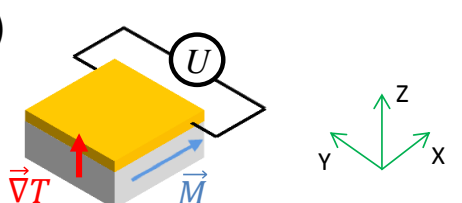
Experiments on acoustic spin pumping in NM/FM/acoustic actuator systems [142, 141] are proving the importance of the phonon-magnon coupling by the appearance of an ISHE voltage signal when MHz-range acoustic resonances are generated.

Interestingly, the authors showed two simultaneous contributions to the SSE signal. First is the mentioned above MHz phonon-magnon interaction in FM that lead to inequilibrium magnon temperature with following injection of spin current into NM. For their sample the de Broglie wavelengths of magnons and phonons were close to each other in the MHz range leading to effective phonon-magnon interaction. The second contribution came from heating of the acoustic actuator and the detected ISHE voltage signal was of the opposite sign with respect to the MHz-range-induced one. RT phonons are of the THz-range in which the phonon-electron scattering in NM appears. This leads to an imbalance in electron and magnon temperatures and spin current is ejected from the NM into the FM.

Controversy on the transverse spin Seebeck effect

(a)  symmetry with respect to the external magnetic field

		in-plane temperature gradient		
		AMTEP	proximity AMTEP	TSSE
NM FMM	symmetric	FM metal with magnetic anisotropy	FMM with magnetic anisotropy and spin polarisation in the NM	?
	antisymmetric	no charge transfer in the FMI		
NM FMI	no effect			

(b)  out-of-plane temperature gradient

		out-of-plane temperature gradient		
		ANE	proximity ANE	LSSE
NM FMM	conducting material		spin polarisation in the NM	spin injection
	no charge transfer in the FMI			
NM FMI				

(c) in-plane temperature gradient + unintended out-of-plane temperature gradient

		ANE	proximity ANE	LSSE	AMTEP	proximity AMTEP	TSSE
		NM FMM	unintended out-of-plane temperature gradient		unintended out-of-plane temperature gradient and spin polarisation in the NM	unintended out-of-plane temperature gradient	FM metal with magnetic anisotropy
no charge transfer in the FMI			no charge transfer in the FMI				
NM FMI							

Figure 2.12: Table of spurious effects in TSSE measurements. (a) (b) (c)

Since the first observation of the TSSE in 2008 many other scientific groups worldwide tried to reproduce these measurements. Most of them faced problems of reproducibility.

There are a few effects to mention, which might interfere the measurements. All these effects are carefully collected by Meier et al. [96], see Tables in Fig. 2.12.

First is the AMTEP (described in Ch. 2.5.3), see table in Fig. 2.12(a). This effect produces a voltage signal that adds up to the TSSE signal. However, this effect is easy to filter out, because it is symmetric to the external magnetic field H , while the TSSE is antisymmetric.

Some NM like Pd, Sc, Pt are very close to satisfy the Stoner criterion [28]. In vicinity of FMs such materials interact with the magnetic moments of FM and can fulfill the Stoner criterion. In this case a few atomic monolayers of NM become also FM. This effect is called magnetic proximity effect (MPE) [83, 69]. Thus, a spurious AMTEP in NM can appear, which is important for ferromagnetic insulator (FMI)/NM samples. However, as mentioned before, AMTEP is easy to filter out due to its symmetry with respect to the magnetic field.

Next, there are effects, that might be induced by the unintended out-of-plane thermal gradient, see Fig. 2.12(b). Among those are ANE (see Ch. 2.5.2) and LSSE, which are antisymmetric to the external magnetic field making difficulties in interpretation of the TSSE signal in conductive FMs [96].

In the case of the NM/FMI system one may assume that the ANE is not induced in the FMI, because the ANE is a feature of the conductive materials. But, again the MPE leads to the formation of a few FM atomic layers in NM and to the appearance of the ANE in NM.

Few sources of unintended out-of-plane ∇T were reported: a heat sink formed by the voltmeter measuring probes [94], surface-to-surface heat radiation coupling of sample surface to the surroundings in the measurement set-up [117].

The effects based on the out-of-plane gradient can be filtered out by comparison of voltage signals for ∇T with opposite sign and fixed temperature at position of the NM detector strip [117].

In the experimental part of this work we show additional effects that hamper the interpretation of the TSSE measurements.

Chapter 3

Experimental methods

3.1 Set-up №1 for measurements of TSSE

With this set-up we examine Pt/Py/MgO and Pt/YIG/MgO samples in Ch. 4.1 and 4.2 respectively.

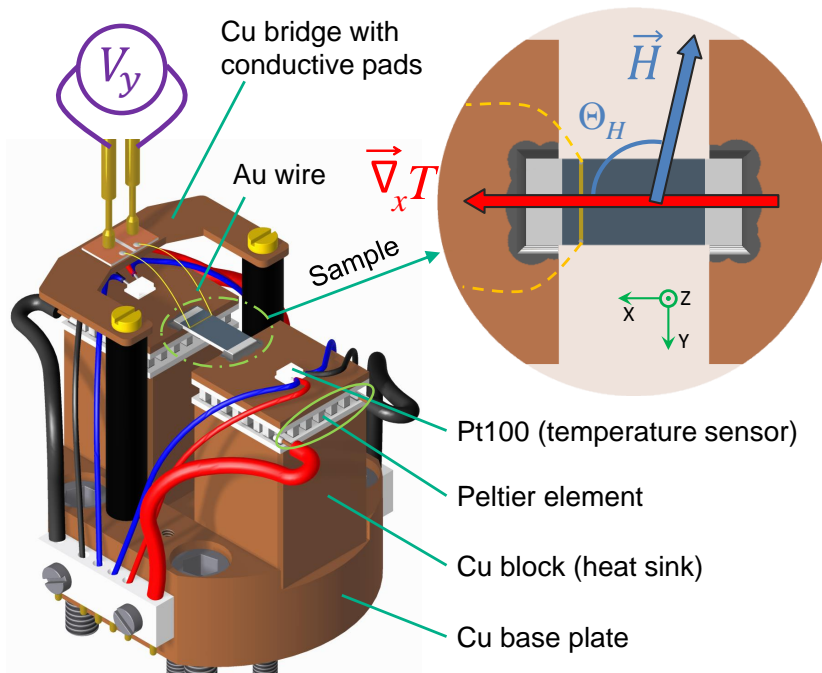


Figure 3.1: Sample holder: two Cu blocks are attached to a common Cu base plate, and carry the Peltier elements with Pt100 temperature sensors attached to them (these sensors measure the temperatures T_1 and T_2 , see Ch. 3.1.1). Close-up: the sample is connected by thermally conductive glue to the Cu interfaces of the Peltier elements, which produce the temperature gradient $\vec{\nabla}_x T$. The external magnetic field \vec{H} is applied in the x-y plane with the angle Θ_H in reference to the x-axis.

In Fig. 3.1 the sample holder is shown. A Cu base plate holds two Cu blocks (heat sinks). Peltier elements are attached to each Cu block. The sample is glued onto the Cu pads, which are mounted as heat sinks onto the Peltier elements. The Peltier elements provide a controlled temperature gradient in the sample plane along the x-axis (see close-up in the inset in Fig. 3.1). The temperatures of the Peltier elements

are measured with Pt100 temperature sensors.

The examined samples have the following composition: substrate/FM/Pt strip, where the Pt strip is exploited for spin-current measurements via the ISHE, see Ch. 2.4.1 for the effect description. The temperature value at the position of the Pt strip T_{str} is used as the base temperature. For details concerning the determination of T_{str} and the temperature difference on the sample ΔT_x , see Ch. 3.1.1.. 20 μm thin Au wires are glued to the ends of the Pt strip detector to provide electrical contacts to a nanovoltmeter. Opposite ends of the Au wires are glued to conductive pads of a Cu bridge, where a voltage signal gets picked up by two spring contacts. The conductive pads are electrically isolated one from another and from the Cu bridge as well.

Measurements are performed in a vacuum chamber (see Fig. 3.2) at a base pressure $2 \cdot 10^{-6}$ mbar to prevent influence of convection and thermal conductivity of air. Each measured voltage signal is averaged over 8 measurements. The external magnetic field is produced by Helmholtz coils for the Pt/Py sample ($H = -44.. +44$ Oe) and by a electromagnet with iron yoke for the Pt/YIG sample ($H = -1120.. +1120$ Oe). Both magnets can be rotated around the fixed measuring chamber. The magnetic field is applied in the x-y plane of the samples with angles in steps of 30° ($\Theta_H = 0^\circ, 30^\circ, \dots, 360^\circ$, see close-up in Fig. 3.1) with respect to the x-axis.

3.1.1 Definition of temperature gradients

The effective temperature difference on the sample ΔT_x can be evaluated:

$$\Delta T_x = (1 - 2\alpha_t)(T_1 - T_2), \quad (3.1)$$

where T_1 is the temperature measured with the Pt100 sensor on the Cu interface of the Peltier element that is closer to the Pt strip of the sample (on Fig. 3.3 left heat sink with Pt 100 sensor on it), T_2 is the temperature measured on the second Peltier element, α_t is a dimensionless coefficient that describes temperature "losses" $\alpha_t(T_1 - T_2)$ on each of the glue interfaces between Peltier elements and sample. To find α_t we conduct measurements with 2 additional thermocouples of type K and at ambient pressure (opened vacuum chamber), because: the vacuum chamber is not suited for additional electrical outputs; wires of thermocouples can rupture the 20 μm -thick Au wires. Thermocouples are placed on top of the sample in the points $T_{1\text{thc}}$ and $T_{2\text{thc}}$ shown in Fig. 3.3. The difference between the temperatures measured by these thermocouples gives us $\Delta T_x = T_{1\text{thc}} - T_{2\text{thc}}$. We assume that the temperature changes linearly with distance from a point with temperature $T_{1\text{thc}}$ to a point with temperature $T_{2\text{thc}}$. Thus:

$$T_{\text{str}} = T_{1\text{thc}} - \Delta T_x \frac{l_{\text{str}}}{l}, \quad (3.2)$$

where l_{str} is the distance from the point with $T_{1\text{thc}}$ to the position of the Pt strip, l - distance between the point with $T_{1\text{thc}}$ and the point with $T_{2\text{thc}}$. Since we fix certain T_{str} and ΔT_x in our measurements, we need to know at which temperatures both Peltier elements should be kept. These temperatures can be calculated as follows:

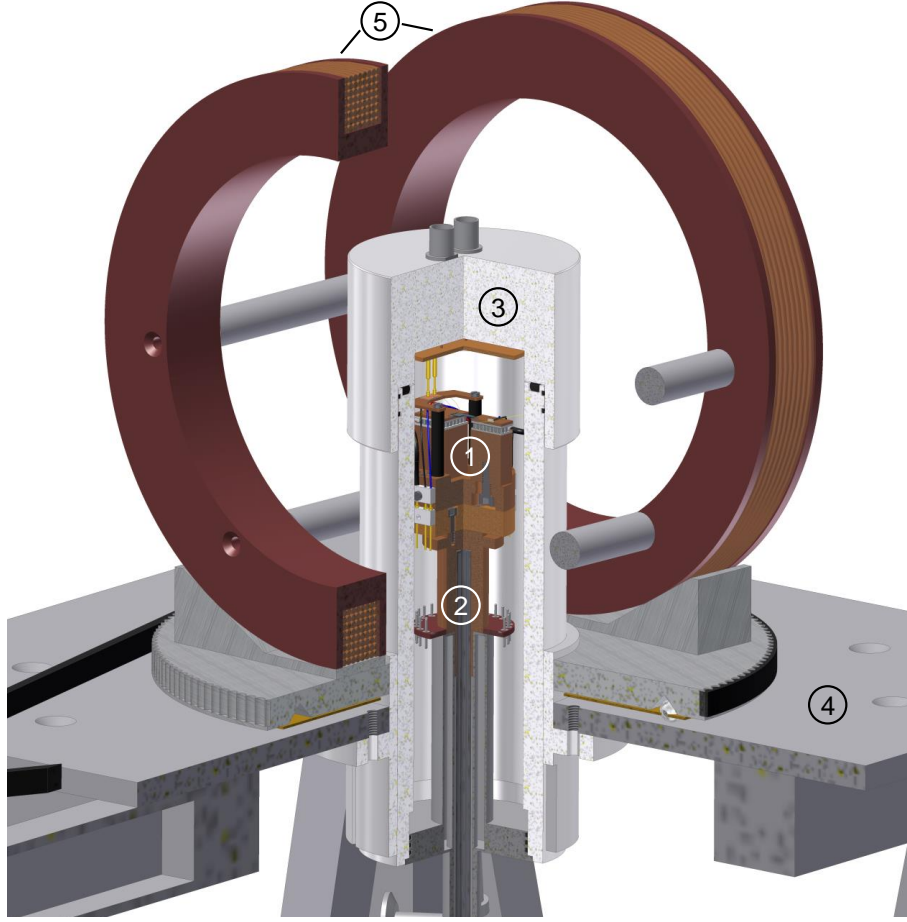


Figure 3.2: Set-up: The sample holder (1) rests on a pillar (2) and is placed in the middle of the vacuum chamber (3) without any contact to its walls. The vacuum chamber is mounted onto a table (4) and fixed rigidly. Helmholtz coils (5) (or alternatively an electromagnet with iron yoke, not shown here) surround the vacuum chamber and are able to rotate around it. Additionally, an Al shield (not shown here) covers the whole set-up. This shield is used to decrease external temperature variations as well as electro-magnetic noise during the measurements.

$$\left. \begin{aligned} T_1 &= T_{\text{str}} + \Delta T_x \left(\frac{l_{\text{str}}}{l} + \frac{\alpha_t}{1 - 2\alpha_t} \right) \\ T_2 &= T_{\text{str}} - \Delta T_x \left(\frac{l - l_{\text{str}}}{l} + \frac{\alpha_t}{1 - 2\alpha_t} \right) \end{aligned} \right\} \quad (3.3)$$

3.1.2 Data processing

Pt/Py/MgO sample

In Fig. 3.4 we show a typical set of the experimental voltages $V_y(H)$ (green lines) measured across the Pt strip of a Pt/Py sample. The red dots shown on the left and on the right side of each green curve represent two averaged values of $V_y(H)$: for the H ranges $-44..-40$ and $40..44$ Oe, respectively. From these two values we find the mean value $A(\Theta_H)$ and the difference value $\Delta(\Theta_H)$.

The peaks visible in the $V_y(H)$ curves as well as the $\sin 2\Theta_H$ dependence of

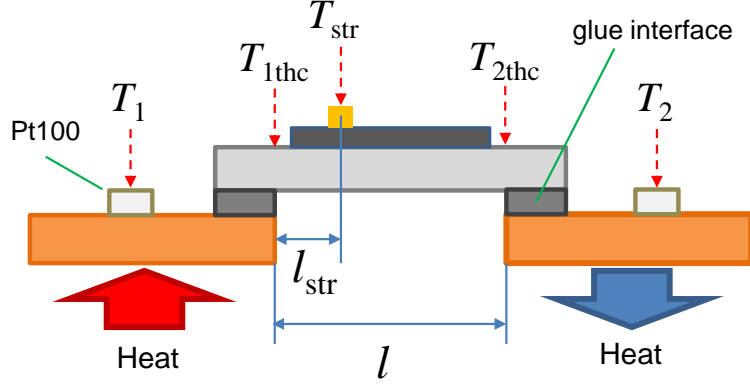


Figure 3.3: Definition of certain temperatures: T_1 and T_2 are the temperatures of the Peltier elements measured by temperature sensors Pt100; T_{str} is the temperature at the position of the Pt strip; T_{1thc} and T_{2thc} are the temperatures at the edges of the suspended part of the sample, $\Delta T_x = T_{1thc} - T_{2thc}$.

$A(\Theta_H)$ are related to the AMTEP, for details see Ch. 2.5.3. With modification of the Eq. (2.56), the transverse voltage, associated with the AMTEP traces, can be described as:

$$V_y(H) - V_{\text{offset}} = A_0(\Delta T_x) \sin 2\Theta_0(H), \quad (3.4)$$

where Θ_0 is the angle between the temperature gradient $\vec{\nabla}_x T$ and the magnetization vector \vec{M} , which corresponds to $2\varphi - \varphi_T$ from Eq. (2.56) with $\varphi_T = 0$; A_0 is the AMTEP amplitude, which corresponds to $-S_-$ from Eq. (2.56); V_{offset} is the voltage signal produced in the Au wires due to the conventional charge Seebeck effect, but unrelated to the $-S_+ \sin \varphi_T$ term from Eq. (2.56), because for TSSE set-up №1 $\varphi_T = 0$. The details on the offset voltage are given in next subsection - 3.1.3. The peaks in $V_y(H)$ are caused by the alignment procedure of the magnetization \vec{M} parallel to the magnetic easy axis of the Py film [94]. The easy axis of the sample has an angle of $\varphi \approx 35^\circ$ with respect to the x-axis of the sample. For angles of the sweeping field $\Theta_H = 30^\circ, 60^\circ, 210^\circ, 240^\circ$ we observe the smallest peaks in the AMTEP curves since the easy axis is close to the direction of the sweeping field \vec{H} . When values of H are large enough to saturate the sample, the magnetization direction angle Θ_0 is very close to the angle Θ_H of the applied magnetic field. In this case the mean values A follow the $\sin 2\Theta_H$ dependence as can be seen for the blue dashed line.

The difference signal $\Delta(\Theta_H)$ has a $\cos \Theta_H$ dependence (see inset in Fig. 3.4). Its amplitude Δ_0 can be interpreted as a mixture of TSSE and ANE signals, where the ANE is produced by a spurious out-of-plane temperature gradient $\vec{\nabla}_z T$ [117], see also end of Ch. 2.6.3.

Pt/YIG/GGG sample

The experimental voltage sets $V_y(H)$ (green line) for a Pt/YIG sample are presented in Fig. 3.5. Fig. 3.5(a) represents the $V_y(H)$ signals for the case of idle Peltier elements (current is off). These voltage signals have a loop-like hysteretic artifact, which is produced by the iron yoke electromagnet. This artifact starts to vanish when the iron yoke of the electromagnet is saturated ($|H| > 900$ Oe) and it is not

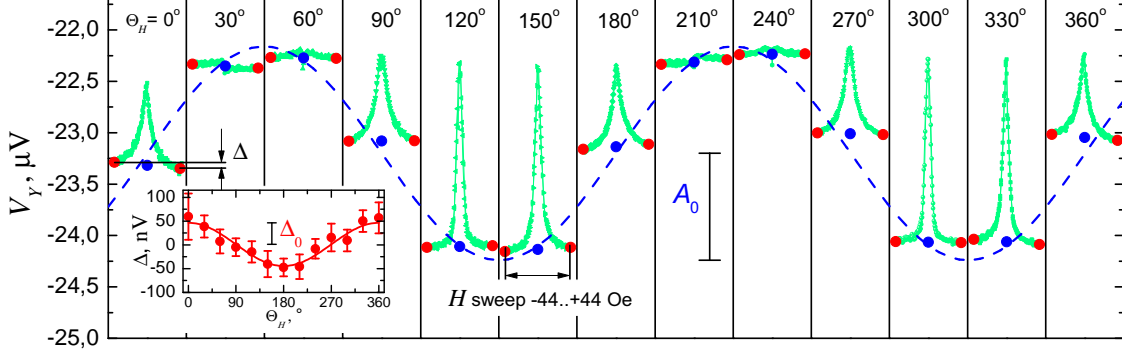


Figure 3.4: Set of transverse voltages $V_y(H)$ (green traces) of Pt/Py sample for temperature difference $\Delta T_x = 28$ K ($\sim \nabla_x T = 4.7$ K/mm), base temperature $T_{\text{str}} = 360$ K and different Θ_H . The average values A (blue dots and blue dashed line) follow a $\sin 2\Theta_H$ dependence with amplitude A_0 as expected from the contribution of the AMTEP. The difference values Δ (inset, red dots) show a $\cos \Theta_H$ dependence with amplitude Δ_0 . This $\cos \Theta_H$ dependence could be associated with both TSSE and ANE.

related to the YIG magnetization process, because the coercive field of YIG does not exceed 200 Oe [96]. The difference signal $\Delta(\Theta_H)$ (small inset) is calculated analogously to the one for the Pt/Py sample in Fig. 3.4 with the only difference that the minuend is the voltage signal averaged over $H = -1120..-1050$ Oe and the subtrahend - over $H = 1050..1120$ Oe. The obtained $\Delta(\Theta_H)$ signal barely contains any $\cos \Theta_H$ contribution. The $\cos \Theta_H$ -fit is shown by the red line in the small inset of Fig. 3.5(a) and its amplitude amounts to 6 ± 4 nV.

In the following, we subtract voltage sets $V_y(H)$ with Peltier elements turned off from measured $V_y(H)$ sets with Peltier elements turned on. An example of such a corrected voltage set is shown in Fig. 3.5(b). This voltage set is measured for $\Delta T_x = 0$ K and $T_{\text{str}} = 387$ K. The average voltage offset of $V_y(H)$ appears because of the charge Seebeck effect (details are in subsection 3.1.3). The deviation from the average offset-position shows stochastic slow drift of $V_y(H)$ with a maximum amplitude of ± 350 nV. The difference signal $\Delta(\Theta_H)$ shows a weak $\cos \Theta_H$ dependence (red line in the inset), which might be related to the LSSE signal (or also to ANE, when MPE in NM is involved) produced by an unintended out-of-plane temperature gradient [96].

3.1.3 Offset voltage in TSSE measurements

For the Pt/Py sample the functional dependence of V_{offset} is given by:

$$V_{\text{offset}} = \alpha_1 \Delta T_x + \alpha_2 \Delta T_x (T_{\text{str}} - T_{\text{room}}), \quad (3.5)$$

where T_{room} is room temperature (RT), α_1 and α_2 are the effective first and second order coefficients of the conventional charge Seebeck effect. According to our measurements at $T_{\text{room}} \approx 296$ K, $\alpha_1 = -0.53$ $\mu\text{V}/\text{K}$ and $\alpha_2 = -4.6$ nV/K^2 . In this case the coefficients α_1 and α_2 are not only usual thermoelectric coefficients, but thermoelectric coefficients of the Py/Ag interface (coefficients of the first and the second order) multiplied by the geometrical mismatch coefficient $\frac{l_{x-m}}{l}$, where l_{x-m} is

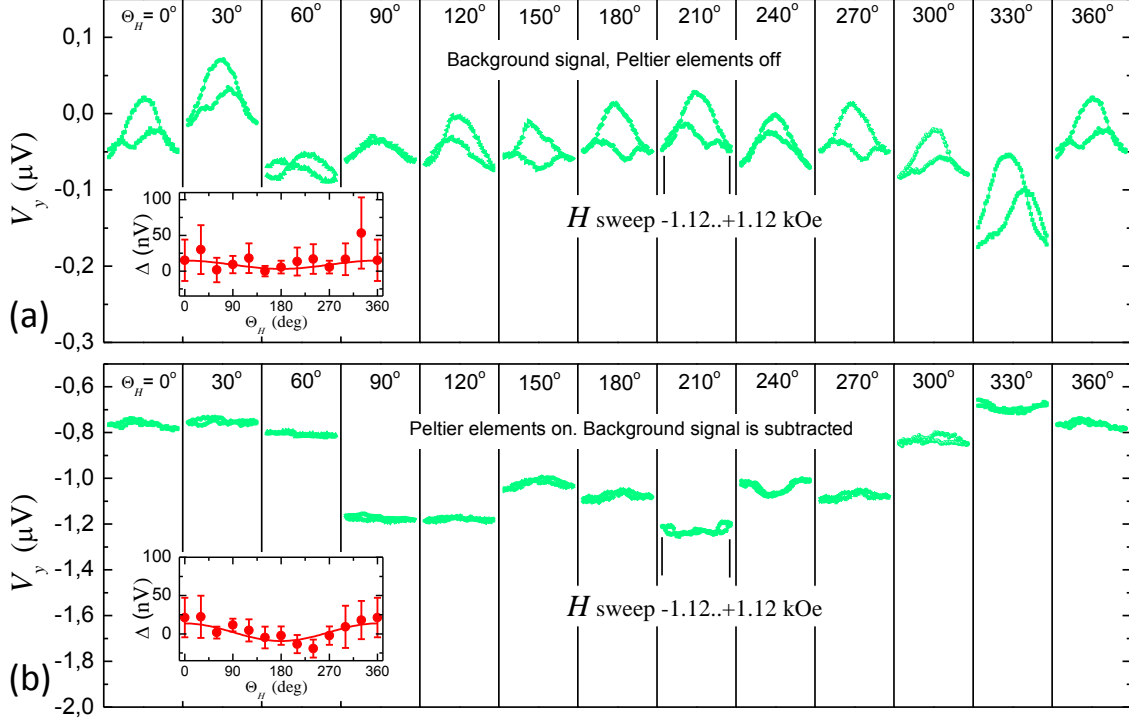


Figure 3.5: Sets of transverse voltages $V_y(H)$ (green traces) for the Pt/YIG sample. (a) measurements with Peltier elements turned off: temperature difference $\Delta T_x = 0$ K, base temperature $T_{\text{str}} = 295$ K (RT). (b) corrected $V_y(H)$ data (data set from (a) is subtracted from raw $V_y(H)$ experimental data) for temperature difference $\Delta T_x = 0$ K, base temperature $T_{\text{str}} = 387$ K, and different Θ_H . The difference values Δ shown in the inset (extracted the same way as for the Pt/Py sample from Fig. 3.4) possess a weak $\cos \Theta_H$ dependence with amplitude $\Delta_0 = 11 \pm 4$ nV. This $\cos \Theta_H$ dependence could be associated with LSSE or ANE contributions.

the x-projection of the distance between the centers of the glue drops that connect the Au wires with the Pt strip (see Fig. 3.6), l is the length of the suspended part of the sample (see Fig. 3.3). According to the several sources [81, 152, 34], the first order Seebeck coefficient of Py/Ag amounts to $-19.5 \mu\text{V}/\text{K}$. Assuming $l = 6$ mm, we get $l_{x-m} = 0.16$ mm, which is a reasonable value.

We consider a Py/Ag interface since Ag is the main component of the glue that connects the Au wires with the Pt strip of the sample and since the glue spots are distributed not only over the Pt strip, but also over the Py film. We take into account only the Py/Ag interfaces for estimation of the thermoelectric coefficients as the Pt/Ag interfaces stay at the same temperature and produce no thermoelectric voltage. The thermoelectric voltage produced by the Au/Ag interface is at least 2 orders of magnitude smaller than the voltage produced by the Py/Ag interface [81, 152, 34]. All other pairs of electrical interfaces, starting from the Cu bridge and finishing by the direct contacts of the nanovoltmeter, do not produce thermoelectric voltage, since all pairs stay at the same temperatures.

For the Pt/YIG sample the offset voltage is of the following functional dependence:

$$V_{\text{offset}} = \alpha_3(T_{\text{str}} - T_{\text{room}}), \quad (3.6)$$

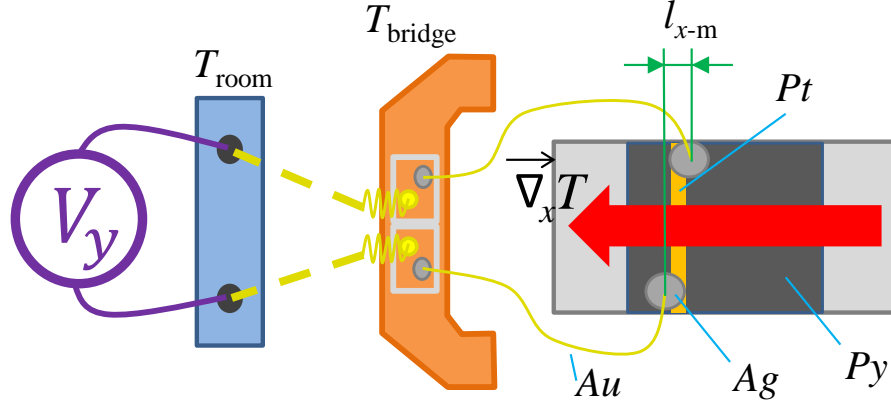


Figure 3.6: Appearance of a thermoelectric signal in Au wires for the Pt/Py sample. The ends of the Au wires that are connected to the voltmeter are kept at temperature T_{bridge} which is close to room temperature T_{room} . Opposite ends are glued to the Pt strip. A small x-coordinate mismatch l_{x-m} of the centers of the glue drops in the presence of a temperature gradient $\vec{\nabla}_x T$ leads to the temperature mismatch of these ends of the Au wires.

where α_3 is the first order Seebeck coefficient of the Pt/Ag interface multiplied by some factor that takes into account inhomogeneities in temperature distribution over the Pt strip. In the case of the Pt/YIG sample the distribution of the Ag-based glue is not important, as YIG is an insulator, thus the YIG/Ag Seebeck coefficient is 0. We find $\alpha_3 = 14 \pm 0.5$ nV/K. Because the Pt/Ag Seebeck coefficient equals to $6.5 \mu\text{V/K}$, the inhomogeneity factor in α_3 is about 0.002.

3.2 Set-up №2 for measurements of TSSE

A collaborative research on a Py/MgO system was conducted using the set-up of the Bielefeld group [113], see Fig. 3.7.

The set-up exploits Peltier elements for heating and cooling purposes. As a key feature, this set-up allows the in-plane rotation of a thermal gradient $|\nabla T|$ and, thus, also the angle-dependent investigation of the anisotropic magnetothermopower (AMTEP) and planar Nernst effect (PNE).

The set-up realizes an in-plane rotation of $|\nabla T|$ by four independently heated sample holders (Fig. 3.7(a)). The sample is clamped at the center of the sample holders and the application of different x- and y- temperature differences leads to a superpositioned net thermal gradient along φ_T . Each pair of opposing poles produces a magnetic field in the direction of the poles axis. Superposition of two perpendicular magnetic fields provides a rotatable in-plane magnetic field along φ . All four cores are connected via a toroidal yoke (not shown in Fig. 3.7(a)). The magnetic field produced by each pair of opposing poles is separately calibrated with a Hall probe. The values of the magnetic coil currents are used in the experiments to determine the magnetic fields.

To reduce parasitic effects induced by unintended out-of-plane $|\nabla T_z|$, the heat is transferred into the sample using an upper and a lower half of the sample holder (Fig. 3.7(b)). This was already used in the set-ups in [94, 96] and proved to successfully reduce unintended out-of-plane thermal gradients. PT1000 elements are glued at the

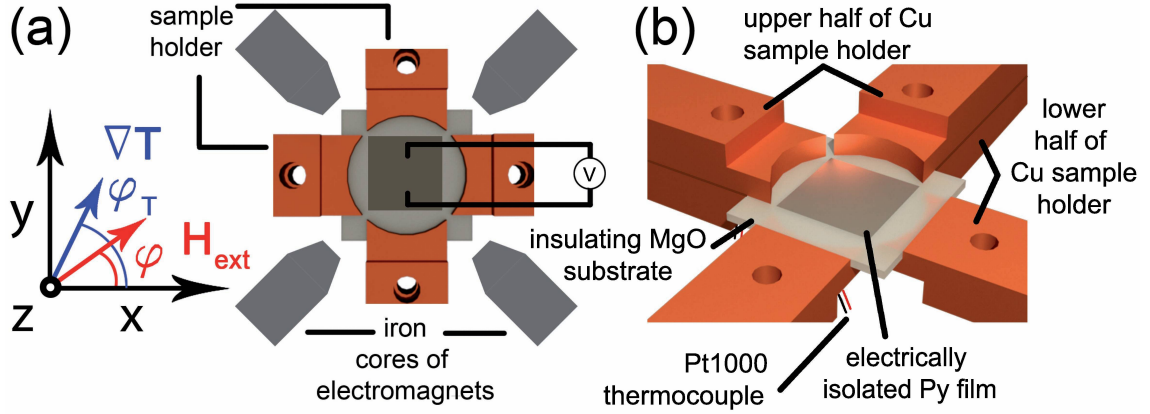


Figure 3.7: (a) The sample is clamped without thermal grease between four circularly shaped copper holders, which can be heated independently. Thus, the variation of different applied ∇T_x and ∇T_y results in a rotated net $|\nabla T|$. Due to its centered deposition, the Py film is electrically insulated from the sample holder. Two pairs of electromagnets rotated by $\pm 45^\circ$ with respect to the x-axis supply a rotatable in-plane magnetic field based on the superposition of the fields of both magnetic axes. (b) Each sample holder consists of a lower and upper half to reduce unintended out-of-plane thermal gradients in the sample. The temperatures are detected via PT1000 elements attached at ≈ 2 mm next to the sample.

backsides of each sample holder to detect the temperatures of the sample holders. A voltmeter is mechanically connected to the FM surface with Au gold tips.

3.3 Set-up for measurements of SNE

The heart of the set-up for SNE measurements is the time-resolved magneto-optic Kerr effect (TRMOKE) spectroscope. We start with a description of TRMOKE and continue with an explanation of coplanar waveguides (CPWs) and the FMR curve fit-procedure in finer detail. The description of the SNE sample production steps is followed by an explanation of FM temperature measurement technique with the use of FMR. And finally we describe the application of the MOD technique for the SNE experiments and discuss a criterion of the SNE detection.

3.3.1 TRMOKE set-up

For the SNE-related FMR measurements we use a complex set-up for time-resolved MOKE measurements (TRMOKE), see Fig.3.8. The set-up allows to study the out-of-plane magnetization dynamics $m_z(t)$ of a sample via the polar MOKE in a stroboscopic manner with picosecond resolution. For probing, we exploit a Ti:Sa laser with a wavelength of 800 nm.

The sample is placed onto a piezo stage, which allows lateral scans of the sample for a $30 \times 30 \mu\text{m}^2$ area. For focusing on the sample surface we use an objective lens with a magnification factor of 100 and numerical aperture of 0.9. The spatial resolution is limited by the diffraction of the laser light and amounts to $\approx 0.5 \mu\text{m}$ (for $\lambda = 800$ nm). For lateral navigation a bright field LED source with a wavelength of 532 nm is set to illuminate the sample surface. The reflected light is collected with

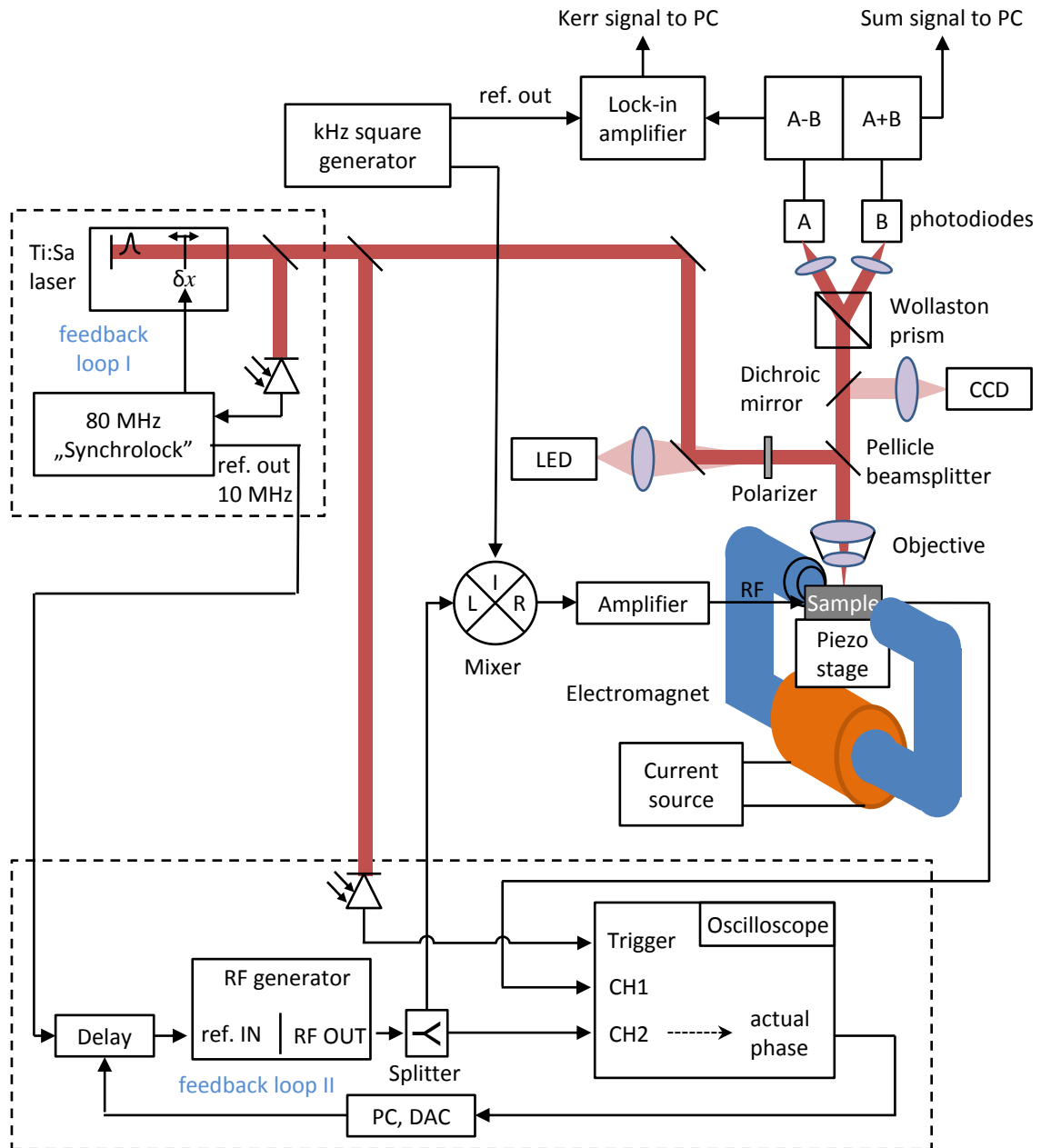


Figure 3.8: TRMOKE set-up. For description see text

an objective lens and then reflected by a dichroic mirror and sent to a CCD camera. The focal planes of laser light and LED light are adjusted to match each other.

A rotatable electromagnet produces sweeps of external in-plane static magnetic field \vec{H}_{ext} . A Hall probe is glued on one of the electromagnet poles in order to measure the magnitude of \vec{H}_{ext} . Prior to FMR measurements, the Hall probe is calibrated with an additional Hall probe placed in the middle of electromagnet's gap.

Laser light falls normally to the sample surface and reflects onto a Wollaston prism that separates the incoming light into two orthogonal polarisation components. The incidence light polarisation is preset in the way that if no Kerr rotation happens, the beam separates into two components equal in magnitude (adjusted with the help of a polarizer). The separated components are then sent to a balanced photodetector. The change in the polarisation angle of the reflected light leads to the $2\theta_K$ signal on the photodetector. The sum signal, also known as the "Topography", and the difference "Kerr" signal are acquired by a PC.

The probing light is formed by a Ti:Sa laser. Laser pulses of 150 fs duration are sent with a repetition rate f_{rep} of 80 MHz. The RF driving magnetic field frequencies f in the experiments are multiple of f_{rep} . In this way MOKE probing secures the same phase of magnetic oscillations. To ensure synchronization of the system, a feedback and stabilization loop are employed. First, the laser system has a "synchrolock" module with its feedback loop that adjusts the length of the laser cavity in order to set f_{rep} exactly to 80 MHz. The synchrolock provides a 10 MHz synchronization signal that feeds the reference input of a RF generator. Before reaching the reference input of the RF generator, the 10 MHz signal is delayed with an adjustable phase shifter "delay". Thus, the phase between magnetic dynamics and laser probing can be chosen. The generated RF signal is split in two: one is sent to the sample, another is sent to the second channel of a fast oscilloscope. The oscilloscope is triggered with the laser pulses and in this way the RF signal actual phase is defined. This phase is sent to the PC where it is compared to a certain value fixed for the experiment. Then a correction signal is generated and sent to the delay module for tuning of the phase.

In general, the measured Kerr signal is very small. In order to improve the signal-to-noise ratio we use a lock-in amplifier [134]. The RF signal is multiplied with the square wave signal of $f_{\text{mod}} = 6.6$ kHz, therefore at each half-period of the modulating signal we switch the phase of the RF signal by 180° . As a consequence, the Kerr signal changes its sign. The modulated Kerr signal is sent through the lock-in amplifier, denoised and rectified there, and after this saved on the PC.

The described optical measuring method has some advantages in application to the SNE: 1) the spatial resolution below $1 \mu\text{m}$ allows to produce huge thermal gradients on a very small distance, thus dramatically reducing problems related to the interdiffusion and electromigration in FM/NM structures, see Appendix A.1; 2) it allows to avoid many possible spurious signals in comparison to transport measurements (SMR-like set-up for SNE measurements [99]).

3.3.2 Coplanar waveguide FMR

For generation of an oscillating driving field \vec{h} in FMR experiments we use a coplanar waveguide (CPW). A CPW is known for its wide bandwidth and compatibility with

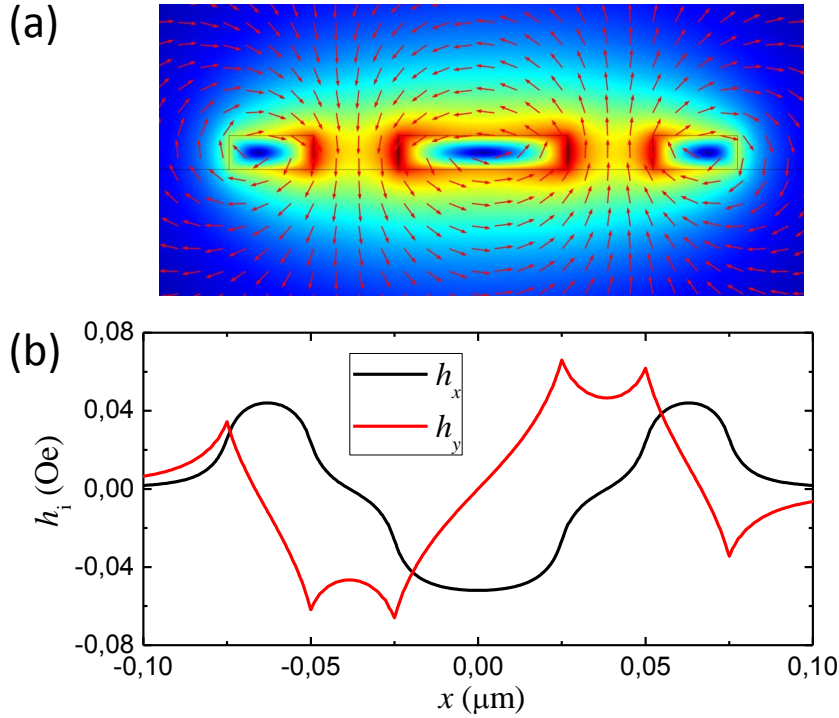


Figure 3.9: COMSOL simulations of the driving magnetic field \vec{h} in the cross-section of a CPW. (a) The Magnitude of \vec{h} in rainbow scale (blue for the smallest, red for the highest). Arrows show the direction of \vec{h} in a point of interest. Left and right rectangles are the ground lines of the CPW and the middle rectangle the signal line. (b) h_x and h_y the in-plane and out-of-plane components in dependence of the x-coordinate.

standard microwave generators and RF lines. The geometry of the CPW can be easily tuned for a certain sample structure. A CPW consists of a signal line in the middle and two ground lines. We simulate the \vec{h} field distribution of the CPW with COMSOL, see Fig. 3.9. In the gaps between the signal line and ground lines \vec{h} is mostly directed out-of-plane and on top of the lines \vec{h} is mostly in-plane. Depending on a certain needed excitation field direction a FM film can be placed either in the gap or on the top of the line. One important property of FMR excitation needs to be considered: the magnitude of FMR is $\propto \sin \alpha$, where α is the angle between \vec{H}_{ext} and \vec{h} . In our experiments we apply in-plane \vec{H}_{ext} . Thus, the in-plane \vec{h} efficiency of FMR is angle-dependent and maximal FMR is induced when $\vec{h} \perp \vec{H}_{\text{ext}}$, whereas the out-of-plane \vec{h} efficiency is close to maximal and is independent from the azimuthal angle of \vec{H}_{ext} . For the last reason we place FM structures in the gap of the CPW.

As the RF line has an impedance of 50 Ohm, we adjust the CPW geometry in order to match the mentioned impedance value. The CPW lines are wired to the RF line with a wedge-bonder. The bonder wires have to be as short as possible and symmetric in order to reduce their effect on the impedance of the system.

Calculations of \vec{h} shown in Fig. 3.9 are made for a DC current. However, in the experimental set-up we apply AC currents of GHz range. Due to the skin effect [28, 46] the GHz-currents are no more homogeneous over the cross-section of CPW lines. This leads to a partial deviation in the \vec{h} distribution with some enhancement of the out-of-plane component. For 10 GHz the skin depth of Au and Cu is about

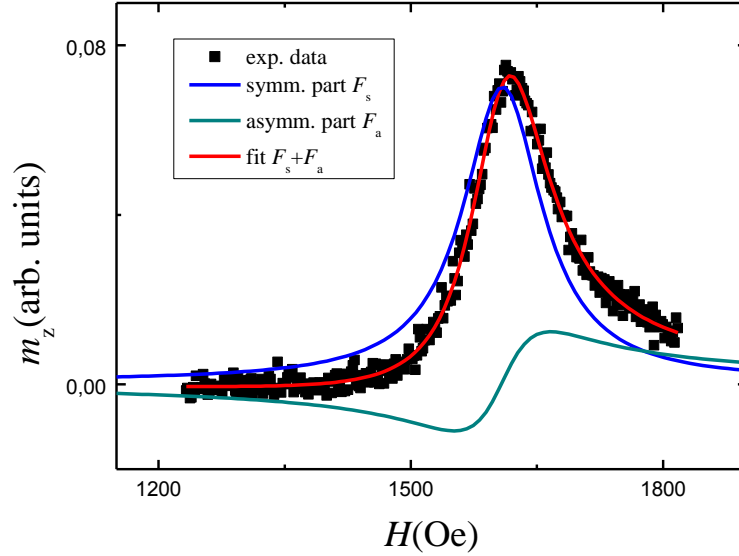


Figure 3.10: Example of raw TRMOKE/FMR data. The experimental data is fitted with Eq. (3.7). The symmetric and antisymmetric Lorentzian components are additionally presented.

600 nm. For the experiments we designed the CPW to be 200 nm thick to suppress this effect.

3.3.3 Example of a measured FMR curve

The measured raw data from TRMOKE (see an example in Fig. 3.10) can be fitted with

$$m_z(H, H_r, \Delta H, \Theta) = A[\cos(\Theta')F_S(H) + \sin(\Theta')F_A(H)], \quad (3.7)$$

where $\Theta' = \Theta + \text{const}$ is a certain phase that depends on the pre-installed phase Θ described before, A is some magnitude. The experimental curve can at will be made either purely symmetric (F_S) or purely antisymmetric (F_A) by adjusting Θ , for definition of the F_S and F_A see Eqs. 2.22. After the fit procedure the parameters of interest H_r and ΔH are extracted. Those values are used for the estimation of the SOT and TSOT, see Ch. 3.3.7 concerning the MOD technique.

The FMR parameters such as the gyromagnetic ratio γ and Gilbert dissipation parameter α can be extracted from the frequency dependencies of H_r and ΔH , respectively. Combining the FMR resonance condition from Eq.(2.17) with terms from Eq. (2.16), where we substitute the external field value H_{ext} with the resonant value H_r , we get an explicit resonance condition:

$$\frac{\omega}{\gamma} = (\mu_0 H_r)^2 + \mu_0^2 H_r M_{\text{eff}}, \quad (3.8)$$

where M_{eff} is the effective magnetization of the sample including the out-of-plane anisotropy, see Eq.(2.15); $\omega = 2\pi f$ is the angular frequency, H_r is the FMR resonance field. The H_r frequency dependence is fitted with Eq. (3.8), see Fig. 3.11 (a). ΔH is fitted with a linear function

$$\Delta H = \frac{\alpha_{\text{eff}} \omega}{\mu_0 \gamma}, \quad (3.9)$$

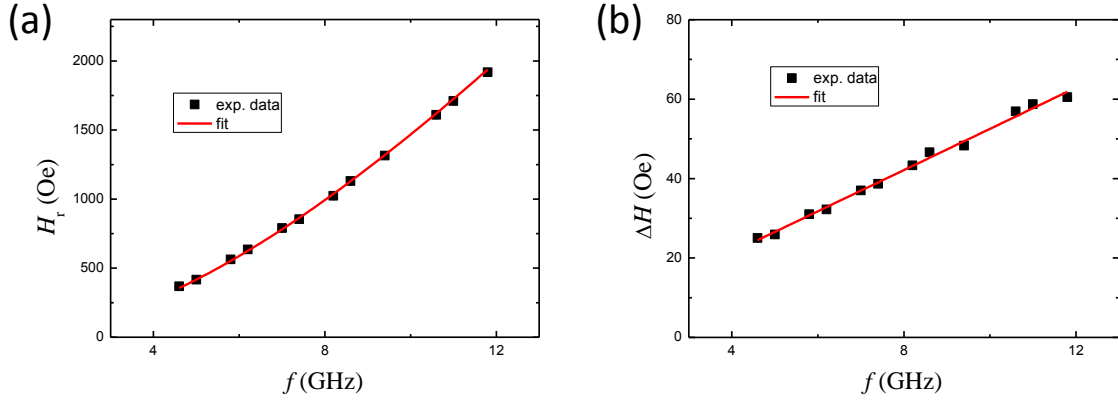


Figure 3.11: Example of parameters extracted from FMR measurements. (a) Resonance field H_r in dependence on the frequency, fitted with Eq.(3.8). (b) FMR linewidth ΔH in dependence on the frequency, fitted with Eq.(3.9).

see Fig. 3.11 (b). We use this fit procedures in the Appendix for FM film characterization.

3.3.4 Sample geometries and production steps

To investigate thermal phenomena on the μm -scale a nanometer-thick membrane substrate is often exploited. Thin membranes have very low thermal conductivity making it possible to produce gigantic thermal gradients. The studied SNE samples consist of three main components: 1) a heater to induce an in-plane thermal gradient; 2) a NM/FM stack, where NM subjected to the in-plane thermal gradient induces a spin current in the FM layer; 3) a coplanar waveguide (CPW) to induce the FMR in the FM.

Here we present production steps of two geometries for the SNE measurements. One of them has a traditional square-wave-like shape of the heater, which is placed aside the FM, whereas another one has shovel-like shape and is placed underneath the FM. Both have their physical cons and pros: magnetic stray-field strength, inductive loop size, which influences a danger of heater explosion during the RF generator switching on due to inductive disturbances, thermal gradient homogeneity and amplitude, and others, all discussed in detail in Ch. 5.1. Another important aspect is the production difficulty, following the principle that the less number of production steps is the less sample defect probability.

Geometry 1 production

In Fig.3.12 production steps for two different samples with Pt and $\text{Pt}_{0.98}\text{Mn}_{0.02}$ as a NM layer are shown. We used 50 nm-thick Si_3N_4 membrane (sand color in figure) substrates with $50 \times 50 \mu\text{m}^2$ lateral size. The production process includes the following steps:

1. Deposition of Pt heater

- (a) Cr(5)/Au(50) bilayers of alignment crosses (light brown, shown only in top view) are deposited by thermal evaporation at a pressure level of 10^{-6}

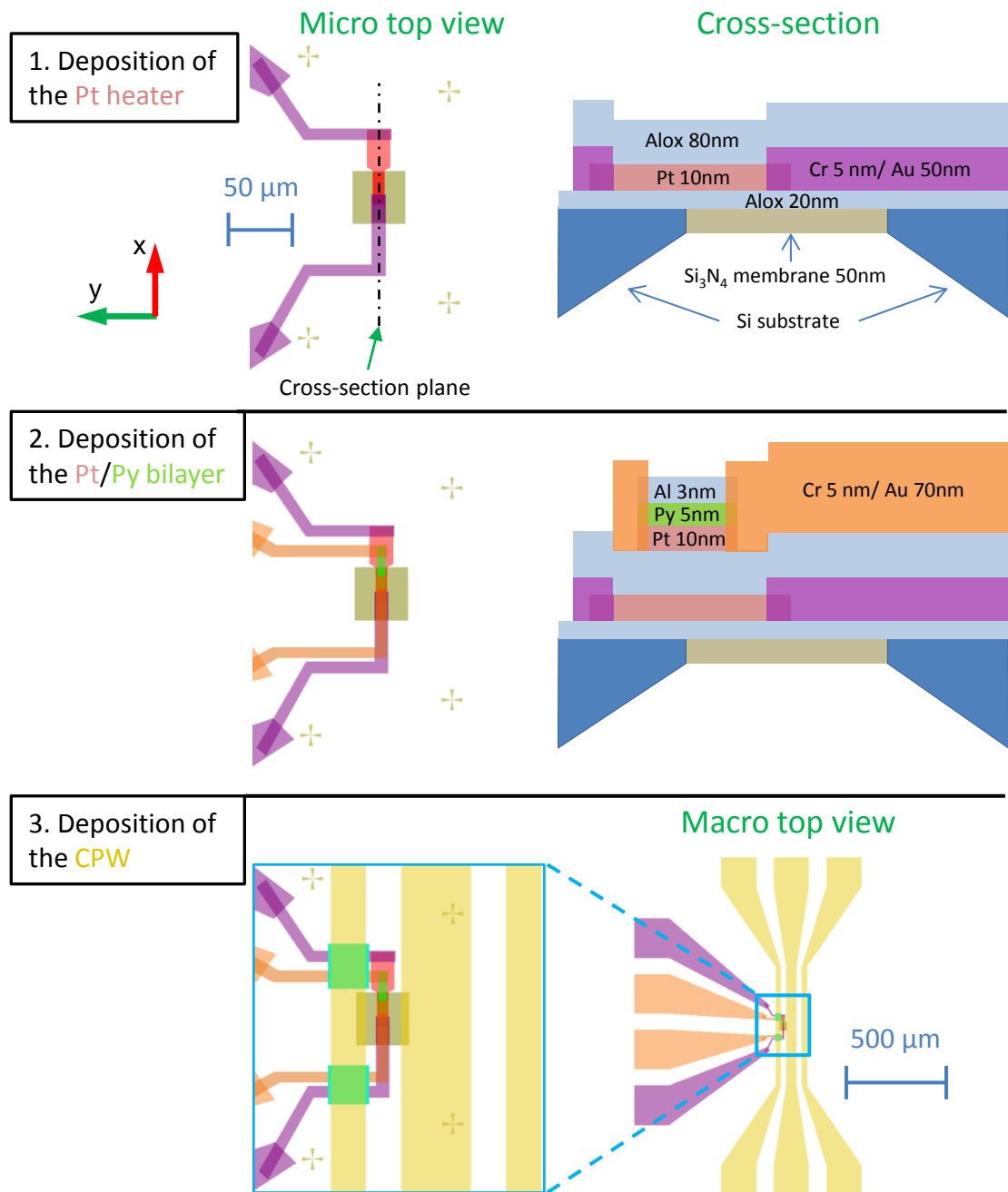


Figure 3.12: Sample production steps in geometry 1: (1) Deposition of the Pt heater (red) on the Si_3N_4 membrane (sand) substrate. Alignment crosses are shown in brown. Contacts of the heater are marked in violet. Alumina layer (light blue) for electrical insulation is placed. (2) Deposition of the non-magnetic/ferromagnetic (NM/FM) stack. Pt (or $\text{Pt}_{0.98}\text{Mn}_{0.02}$)/Py/Al stack (also referred to as NM/FM stack) is presented in red/green/light blue, respectively. Contacts of the NM/FM stack are marked in orange. (3) Deposition of the coplanar waveguide antenna (CPW, yellow color). Cross-linked PMMA (mint green) is deposited between CPW and contacts of the heater and NM/FM stack for electrical insulation. CPW antenna area is about $1.7 \times 0.8 \text{ mm}^2$

mbar. We use Cr as an adhesion layer. Additionally, 30 sec of Ar-etching is used prior to the metallization for better adhesion. Planar geometries are drawn with e-beam lithography on positive PMMA resist. In the following, we imply that each metallization step is preceded by positive PMMA e-beam lithography and Ar-etching.

- (b) We deposit a 20 nm Alumina (Al_2O_3 , light blue in figure) layer for additional electrical insulation of the adjacent layers from the semi-conductive Si substrate. Atomic layer deposition (ALD, [108]) technique is exploited for this step.
- (c) A 10 nm-thick Pt heater (red color) is deposited using electron beam evaporation at a pressure level of 10^{-6} mbar. At this step we avoid Ar-etching because it enhances surface roughness, which potentially leads to inhomogeneities of the temperature gradient.
- (d) Cr(5)/Au(50) heater electrical contacts (violet) are deposited with the thermal evaporation at a pressure level of 10^{-6} mbar.
- (e) 80 nm of Alumina (light blue) is deposited using the ALD technique to insulate the heater structures from the NM/FM structures.

2. Deposition of the Pt(or $\text{Pt}_{0.98}\text{Mn}_{0.02}$)/Py detector-bilayer

- (a) The NM/FM stack is placed without breaking the vacuum: Pt 10 nm (red color) with electron beam evaporation, 5 nm of Py (green color) with thermal evaporation, and 3 nm of Al (light blue) capping layer with thermal evaporation. In case of the $\text{Pt}_{0.98}\text{Mn}_{0.02}$ sample, the $\text{Pt}_{0.98}\text{Mn}_{0.02}$ is deposited in the MBE, with subsequent breaking of vacuum before deposition of Py and Al. The Al capping layer is converted into 3.8 nm of Alumina due to exposure to air. At this step the Ar-etching is not applicable, because it induces high surface roughness, which is critical for interface effects of the NM/FM structure.
- (b) Cr(5)/Au(70) bilayer - electrical contacts of NM/FM stack (orange color) deposited with thermal evaporation at a pressure level of 10^{-6} mbar. For the Pt sample the contacts are shifted to 12 μm from the membrane edge, while for $\text{Pt}_{0.98}\text{Mn}_{0.02}$ to 6 μm , due to its influence on the thermal gradient strength, as is discussed in Ch. 5.1.

3. Deposition of cross-linked PMMA and CPW

- (a) A trapezoid of cross-linked PMMA (mint green color) above the contacts of heater and NM/FM stack is made in order to insulate the last two from the CPW. The trapezoid height is about 300 nm and the angle at the base is about 10 deg.
- (b) A Cr(5)/Au(150) bilayer - CPW (yellow color) is deposited with thermal evaporation at a pressure level of 10^{-6} mbar.
- (c) A water solution of NaOH is used to remove Alumina at the broadest part of the heater contacts in order to improve the bonding of samples to the sample holder. A 30- μm Al wire bonder is used.

Geometry 2 production

This geometry is used with the $\text{Cu}_{0.98}\text{Au}_{0.02}$ alloy as the NM layer, see Fig. 3.13.

Many of the production steps are similar to those for the geometry 1.

1. Deposition of the Au heater
 - (a) Alignment cross deposition is similar to the step 1.(a) of geometry 1.
 - (b) Alumina insulation layer deposition is similar to step 1.(b).
 - (c) A Cr(5)/Au(30) 0.5 μm -broad meander-structure heater (red) is deposited using thermal evaporation at a pressure level of 10^{-6} mbar.
 - (d) A Cr(5)/Au(100) heater contacts (violet) are also deposited using thermal vapor deposition.
2. Deposition of the $\text{Cu}_{0.98}\text{Au}_{0.02}$ /Py detector-bilayer
 - (a) The NM/FM stack of the following composition: 5 nm $\text{Cu}_{0.98}\text{Au}_{0.02}$ (red), 10 nm Py (green color), 3 nm Al (light blue) capping layer, all are deposited *in situ* at a pressure level of 10^{-10} mbar in the MBE. The Al capping layer is converted into 3.8 nm of Alumina by exposure to air. At this step Ar-etching is avoided as it causes high surface roughness that is critical for interface effects of the NM/FM structure.
 - (b) Similar to 2.(b) of geometry 1, Cr(5)/Au(70) bilayer - contacts of the NM/FM stack (orange color) are deposited with thermal evaporation.
3. Deposition of cross-linked PMMA and CPW. This step copies step 3 for geometry 1.

A physical comparison of the sample geometries is presented in the experimental part Ch. 5.1. Some technical details of geometry 2 are worth mentioning.

1. In the last step of the CPW lithography, we have encountered a problem with mechanical tensions produced on the membrane by the PMMA resist layer, which led in some cases to the membrane rupture. The cross-linked PMMA from the previous step shows different degree of thermal expansion in comparison with fresh PMMA resist during its drying. Different geometries of heater contacts are also of some importance, but less relevant.
2. The loop of the heater contacts has to be kept as small as possible to reduce induced voltages by switching-on of the RF field of the CPW. Too large loops (especially when placed under the CPW) lead to explosion of the heater.

3.3.5 Determination of the temperature of FM

During the SNE measurements it is necessary to know the temperature distribution in order to estimate the temperature gradient across the FM. The FMR measurements give such a possibility.

The main value that changes with the temperature is M_{eff} . We express a temperature dependence of the magnetization as following:

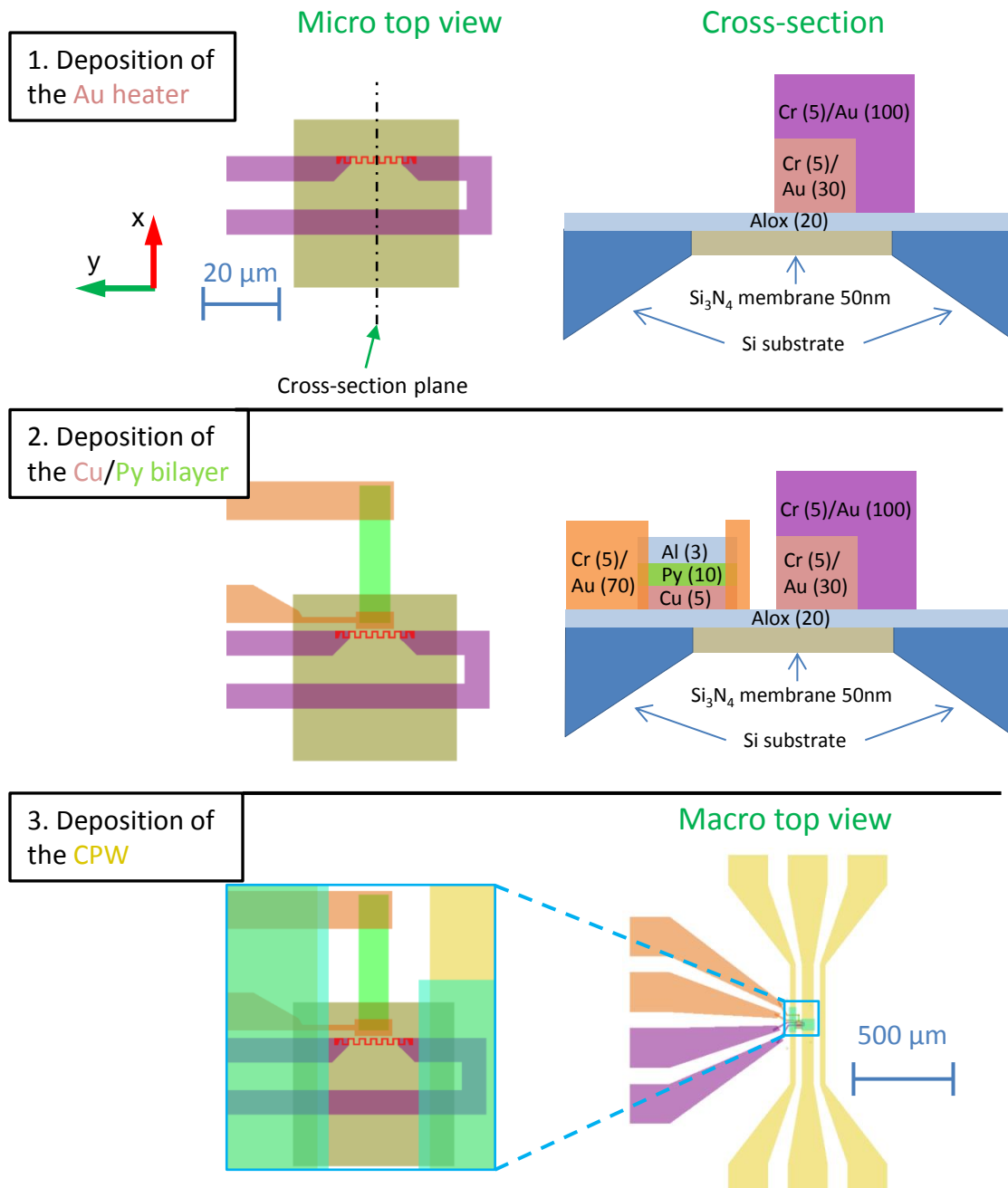


Figure 3.13: Sample production steps in geometry 2: besides the heater structure and its position the production steps are similar to those in Fig. 3.12.

$$M_{\text{eff}}(T) = M_{\text{eff}}(T_b) + \Delta M_{\text{eff}}(\Delta T), \quad (3.10)$$

where $T = T_b + \Delta T$ is the local temperature of FM, T_b is the base temperature of the sample holder, and ΔT is the enhancement of temperature in comparison to the base temperature.

After substitution of Eq.(3.10) into Eq.(3.8), rearrangements of terms and division by $H_r(T)$ one gets an expression for the magnetization deviation:

$$\mu_0 \Delta M_{\text{eff}}(\Delta T) = \left(\frac{2\pi f}{\gamma} \right)^2 \frac{1}{\mu_0 H_r(T)} - \mu_0 H_r(T) - \mu_0 M_{\text{eff}}(T_b) \quad (3.11)$$

In practice, the Bloch's law approximation for FM magnetization temperature dependence is used:

$$M_S(T) = M_S(0K) \left[1 - \left(\frac{T}{T_C} \right)^{3/2} \right], \quad (3.12)$$

where M_S is the saturation magnetization, T_C is the Curie temperature. The Curie temperature T_C of Py is 843 K for bulk [28], and according to the performed SQUID measurements (in Ch. 5.2) it is at least above 500 K for our thin film samples. According to the data from the Appendix, the safe temperature limit in terms of interdiffusion is below 450 K and is not exceeded in our SNE experiments. Thus, we can use a linear approximation for the change of magnetization. Assuming only a linear temperature dependence:

$$\mu_0 \Delta M_{\text{eff}}(\Delta T) = M_{\text{lin.T}} \Delta T, \quad (3.13)$$

we rewrite Eq.(3.11) as:

$$\Delta T = \frac{1}{M_{\text{lin.T}}} \left(\left(\frac{2\pi f}{\gamma} \right)^2 \frac{1}{\mu_0 H_r(T)} - \mu_0 H_r(T) - \mu_0 M_{\text{eff}}(T_b) \right) \quad (3.14)$$

Thus, knowing the resonance field $H_r(T)$ at elevated temperature T from FMR measurements, the magnetization of FM at the base temperature $M_{\text{eff}}(T_b)$ and the linear coefficient of change of magnetization $M_{\text{lin.T}}$, we can measure the local temperature distribution of a FM film. In experiments we induce a temperature enhancement with currents applied to the heater and define $T(I)$ dependencies.

In Fig.3.14 an example magnetization dependence of a Pt/Py sample on T is shown. The slope $M_{\text{lin.T}}$ of a linear fit (red line in plot) is performed for a temperature range of 295-450 K. The upper limit is chosen as 450 K in view of the starting interdiffusion of NM and FM layers. In Appendix in Fig.A.5a for a PtMn/Py/Al sample one can see, that after a temperature of about 450 K a significant change of magnetization starts due to the layer interdiffusion.

In Fig.3.15 one can see a modeled behavior from Eq.(3.14). For 10 GHz we obtain ≈ 1 K per 1 Oe shift. Also, the higher the resonance frequency the more pronounced is the change of H_r with the temperature.

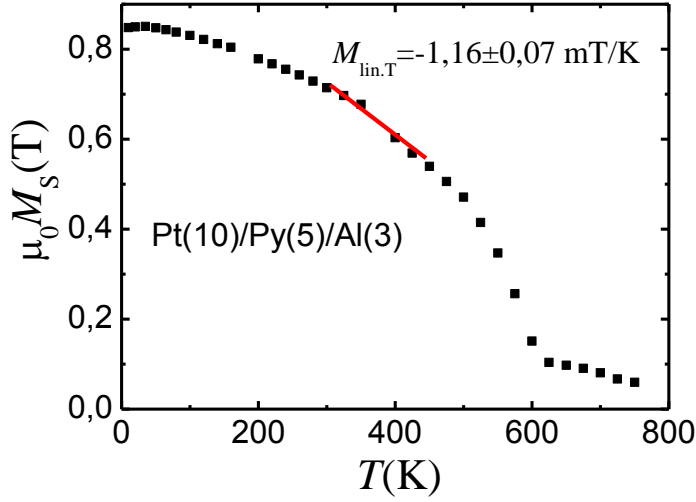


Figure 3.14: Temperature dependence of the saturation magnetization measured with SQUID. A linear fit of the parameter $M_{\text{lin.T}}$ (see Eq.(3.13)) is performed in a temperature range of 295–450 K. Above 450 K not only the reduction of saturation magnetization is observed while approaching the Curie temperature, but also a reduction due to the interdiffusion of NM and FM layers, see Appendix.

3.3.6 Data processing

Here we describe the modulation of damping (MOD) technique [122, 33, 135] often exploited for detection of the spin currents injected in a FM. The MOD technique has already found a broad acknowledgment in the field of the SHE and we will extend it to the field of the SNE.

3.3.7 Modulation of damping technique in FMR experiments

The SOT induces both field-like and damping-like torques in FM. Both can be extracted and evaluated from a experimental FMR data.

As shown in Eq.(2.19) the SOT damping-like torque brings an additional term to the intrinsic FMR damping parameter α . For in-plane isotropic FM the damping-like torque evaluated from a change of FMR linewidth reads [4, 85]:

$$\mu_0 \delta \Delta H = \frac{\omega}{\gamma} \frac{2s}{\mu_0 (\mathfrak{H}_{0r} + \mathfrak{H}_{1r})} = \frac{\omega}{\gamma} \frac{-\tau_{\text{DL}} \sin \varphi}{\mu_0 \left(H_r + \frac{M_{\text{eff}}}{2} \right)}, \quad (3.15)$$

where φ is the angle between m_{eq} and the x-axis. Therefore, the maximal effect is achieved when the external magnetic field is parallel to the spin current polarisation σ , which is parallel to the y-axis of our samples as described in the previous chapters.

Additionally to the damping, the magnetization equilibrium direction slightly shifts from the purely in-plane orientation to the out-of-plane one. However, this shift is usually negligibly small and the effect on the resonant field is:

$$\mu_0 \delta H_r = (\tau_{\text{FL}} + \mu_0 H_y^{\text{Oe}}) \sin \varphi, \quad (3.16)$$

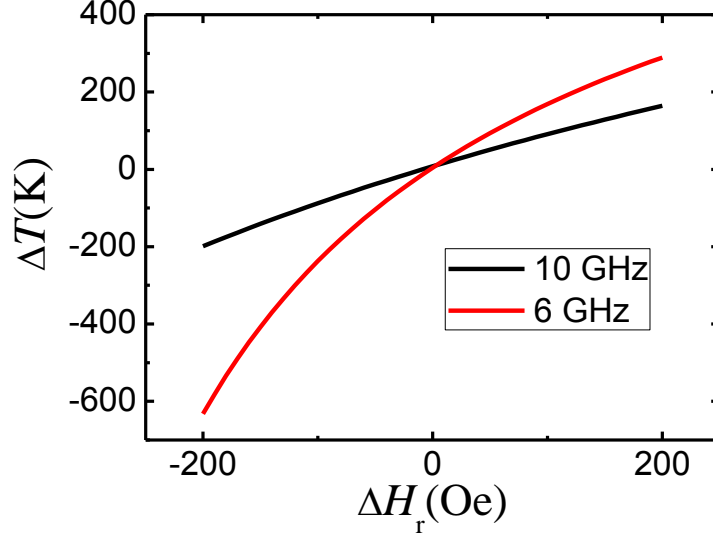


Figure 3.15: Dependencies according to Eq.(3.14) calculated at 6 and 10 GHz, where $\Delta H_r(T) = H_r(T) - H_r(T_b)$. Parameters in the model are set to: $\gamma = 1.76 \cdot 10^{11} \frac{1}{\text{s}\cdot\text{T}}$, $\mu_0 M_{\text{eff}}(T_b) = 0.85 \text{ T}$, $M_{\text{lin.T}} = 1.16 \text{ mT/K}$.

where τ_{FL} is the field-like torque strength, H_y^{Oe} is the Oersted magnetic field induced by the charge current flowing in NM of the FM/NM structure or also in the heater, depending on the geometry, as shown in Ch. 5.1. A precise estimation of H_y^{Oe} often brings some difficulties, because the exact current density distribution in FM/NM depends on the resistivity of NM and FM, and also possible structural inhomogeneities in NM cause a change in the distribution of the induced Oersted field, see Ch. 2.4.5.

MOD is a good method for the estimation of SOTs in materials with relatively low damping; it is proven to be a reliable tool for the SHE experiments. However, in confined FM one needs to be careful with interpretation of the damping data, because an overlap of multiple dynamic magnetization modes can lead to an additional deviation of the linewidth. According to [33] 7% deviation was reported in such a case. To minimize the effect of the edge modes on measurements one must make measurements exactly in the middle of FM.

MOD in application to the SNE experiments

For the SNE measurements we expect to have three contributions to the FMR linewidth:

$$\begin{aligned} \Delta H &= \Delta H_{\text{intr}} + \Delta H_{\text{intr,therm}} + \Delta H_{\text{SNE}}, \\ \Delta H_{\text{intr,therm}} &\propto \Delta T \propto I_{\text{heater}}^2, \\ \Delta H_{\text{SNE}} &\propto \nabla T \sin(\varphi) \propto I_{\text{heater}}^2 \sin(\varphi), \end{aligned} \quad (3.17)$$

where ΔH_{intr} is the term due to the intrinsic damping of FM, $\Delta H_{\text{intr,therm}}$ is the enhancement of the intrinsic linewidth due to the heating of FM, ΔH_{SNE} is the term that describes the effect of TSOT induced by the SNE, and φ is the angle between $\vec{\nabla}T$ and \vec{m}_{eq} . Thus, switching the angle between external field \vec{H}_{ext} direction and $\vec{\nabla}T$ by 180° one can change the sign of ΔH_{SNE} contribution to the FMR linewidth,

see conceptual consideration in Fig. 3.16. As we need the highest possible $\vec{\nabla}T$, we have chosen membrane samples. This makes a change of the direction of $\vec{\nabla}T$ impossible, thus only the change of \vec{H}_{ext} direction is an option to convey the SNE measurements. From this we conclude that the way to detect the SNE in the MOD experiments is to analyze changes in magnitude of the quadratic term of ΔH as the field \vec{H}_{ext} is reversed. In the experimental data called "SNE configuration" we designate **+H** and **-H** cases when the field \vec{H}_{ext} is parallel and antiparallel to the y -axis, respectively. $\vec{\nabla}T$ is directed along the x -axis. The term ΔH_{SNE} corresponds to the one in Eq.(3.15) and contains $H_r + M_{\text{eff}}/2$ in denominator. Strictly speaking, this has to introduce disturbances in the expected quadratic current dependence of the SNE, since both terms are temperature-dependent. However: a) as H_r grows with temperature, while M_{eff} is reducing, the changes in the denominator are partially compensated; b) In our experiments in the positions of measurements the changes of M_{eff} are below 10%, therefore, we neglect these perturbations to the quadratic current dependencies.

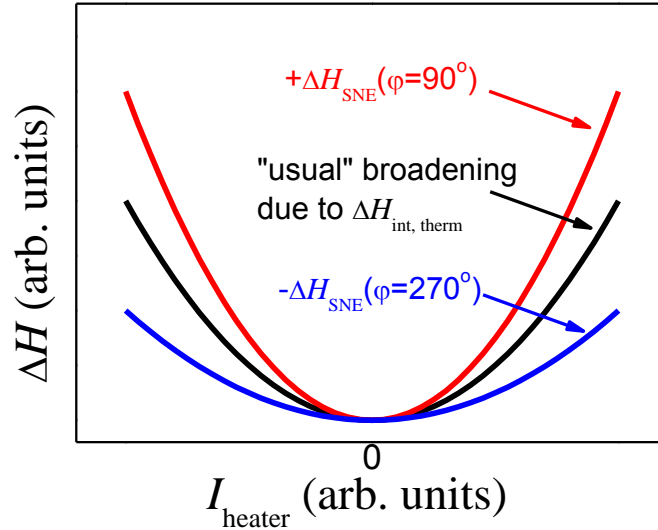


Figure 3.16: Schematic description of the expected thermal influence on the linewidth in SNE experiments. Temperature is approximately proportional to the square of the I_{heater} . The linewidth ΔH (in the absence of SNE) is roughly proportional to the temperature change.

Additionally, we conduct measurements called "SNE $_{\perp}$ configuration" with \vec{H}_{ext} directed parallel and antiparallel to the x -axis and designate those again **+H** and **-H**, respectively. Here, ∇T is oriented along the x -axis as before. In these orientations we do not expect to detect the SNE-induced torques. Thus, ΔH_{SNE} is supposed to be 0.

During the SNE measurements we fit the $H_r(I_{\text{heater}})$ and the $\Delta H(I_{\text{heater}})$ dependencies with the quadratic function $y = A + Bx + Cx^2$. For $\Delta H(I_{\text{heater}})$ fits we fix the slope B to 0.

The SNE $_{\perp}$ configuration is always measured later than the SNE configuration. This is important for the discussion of sample deterioration due to interdiffusion and electromigration.

Current measurements are performed in the order 0, +1, -1, +2, -2 and so on, to

reduce the systematic error due to the possible sample deterioration. For the same reason the field \vec{H}_{ext} directions are switched for each new current value. In this way a drift in the linear components B is significantly reduced.

Connection schemes for SHE and SNE measurements

Both sample geometries described in Ch.3.3.4 are possible to use for SHE and SNE measurements depending on the connection scheme of electrical contacts, see an example for the geometry 1 in Fig. 3.17. Prior to the SNE measurements we conduct SHE measurements in order to check the quality of the interface and detectability of spin currents.

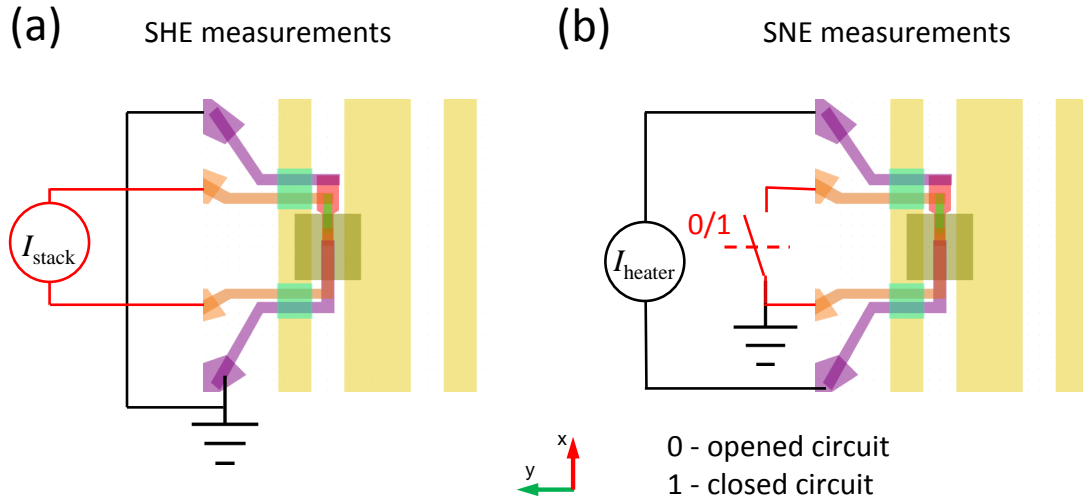


Figure 3.17: Connection schemes for the sample geometry 1. a) SHE configuration for check of interface quality. The FM/NM stack is powered with the I_{stack} , whereas the heater is grounded. b) SNE configuration. FM/NM stack can be closed or opened. The heater is powered with the I_{heater} .

For the case of the SNE measurements in Fig. 3.17(b) the question whether the FM/NM should be opened or closed might be disputable at first glance. On the one hand, closing/opening the circuit can "switch off/on" the ΔH_{SNE} term in the MOD measurements, thus providing another method for the SNE MOD detection besides the switching of the magnetic field direction. On the other hand, following [99] if the wiring between the spin detecting terminals is longer than the spin diffusion length λ , the magnetic circuits are always open with respect to the spin current, and thus make no impact on the SNE detection. We have checked the last statement in our experiments and we do not observe any detectable difference in the experimental data for opened/closed FM/NM stack circuit. Another aspect to consider is the danger of induced surge voltages in the opened circuit due to the effect of the CPW, especially during switching on and off of RF generator. This danger is even higher for the sample geometry 2, because it has larger electrical loop. In the light of the surge voltages, we have chosen in our experiments the electrically closed (but spin current/magnetically open) circuit connection scheme.

Chapter 4

TSSE measurements

As described in Ch. 2.6.3 and shown in Fig.2.12, different effects influence the TSSE measurements. Some of the effects can be filtered out via the use of experimental set-ups allowing rotation of the external magnetic field H . Other effects are induced by unintended out-of-plane thermal gradients, which appear due to the thermal coupling of the sample surface to the set-up environment. In many of the very first TSSE studies [144, 70, 146] the in-plane temperature difference ΔT_x was varied and not much attention was focused on the temperature T_{str} at the position of the detector strip. However, with variation of T_{str} at fixed ΔT one can estimate and exclude the influence of the out-of-plane gradient [117]. In our measurements we rotate the field \vec{H} and vary the values of T_{str} and ΔT . In this way we can exclude all spurious contributions to the TSSE shown in the table in Fig.2.12. Here we present our experimental findings for different sample compositions and contribute to the table of spurious effects with artifacts induced by small perturbations of the external magnetic field.

4.1 Pt/Py/MgO sample

A 20 nm thick permalloy (Py) film with area of 6 mm \times 4 mm is deposited onto a 0.5 mm thick MgO substrate (area of 10 mm \times 4 mm) using sputter deposition as shown in Fig.3.1(a). To detect the expected pure spin current via the inverse spin Hall effect (ISHE) Ch. 2.4.1) a 10 nm thick Pt strip is deposited in-situ through a shadow mask onto the Py film ensuring a clean Py/Pt interface. For the Py/Pt sample measurements we use TSSE set-up №1 described in Ch. 3.1. A similar structure was investigated in the pioneering work on the spin Seebeck effect[144].

4.1.1 ANE induced artifact

In Fig.4.1(a) we re-plot the experimental difference signal amplitude Δ_0 (defined in Ch. 3.3.2) for a similar Py/Pt sample that was published in [117]. These measurements have been performed for fixed temperature differences $\Delta T_x = -25, 0, +25$ K (gradients $\nabla_x T = -4.2, 0, 4.2$ K/mm) and as a function of base temperature T_{str} . The slope of the Δ_0 lines of fixed temperature differences $\Delta T_x = -25, 0, +25$ K (dashed lines in Fig.4.1(a)) was explained in [117] as a contribution of ANE produced by a spurious $\vec{\nabla}_z T$ gradient due to surface-to-surface radiation heat transfer between the sample and the vacuum chamber ($\nabla_z T \propto (T_{\text{room}} - T_{\text{str}})^2$, where T_{room} is

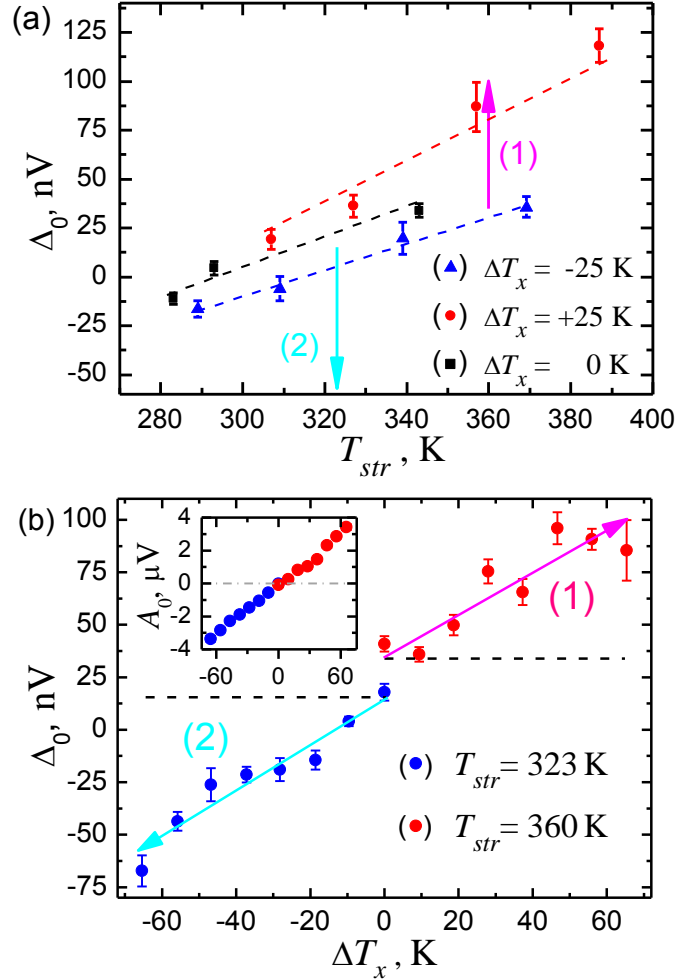


Figure 4.1: (a) Dependence of the difference signal amplitude Δ_0 on the base temperature T_{str} for fixed temperature differences $\Delta T_x = -25, 0, 25$ K ($\sim \vec{\nabla}_x T = -4.2, 0, 4.2$ K/mm respectively) taken from [117]. (b) Dependence of the amplitude of the difference signal Δ_0 on the temperature difference ΔT_x for fixed base temperatures $T_{str} = 323$ K (blue dots and light blue arrow) and 360 K (red dots and magenta arrow). The data shown in (b) is represented in (a) as the numbered arrows 1 (magenta) and 2 (light-blue). The inset represents the dependence of the AMTEP magnitude A_0 on ΔT_x .

the ambient temperature in the laboratory). At first sight, the shifts of the "undisturbed" line for $\Delta T_x = 0$ K (up for a positive temperature gradient and down for a negative one) are expected to be related to TSSE. However, after having performed control measurements on the samples, where we have replaced the Pt detector strip with a Cu strip we found that the vertical shift is not related to the TSSE (Cu is not expected to give a measurable ISHE signal contribution), but at this point its origin was an open question [117].

To clarify the nature of these shifts, we compare the data to additional measurements of Δ_0 for a fixed T_{str} and varying ΔT_x (see Fig. 4.1(b)). Here, we use $T_{\text{str}} = 360$ K and $T_{\text{str}} = 323$ for the strip being located at the hot and being located at the cold side, respectively. The inset in Fig. 4.1(b) proves that no in-plane temperature gradient is generated at the point $\Delta T_x = 0$ K, since the AMTEP amplitude $A_0(\Delta T_x = 0$ K) is equal to 0 V within the uncertainty range meaning that no in-plane temperature gradient is generated. Note that the black dashed lines in Fig. 4.1(b) indicate that $\Delta_0(\Delta T_x = 0$ K) is not equal to 0 V for both $T_{\text{str}} = 360$ K and $T_{\text{str}} = 323$ K. This is caused by an ANE signal, since the base temperatures T_{str} differ from T_{room} (compare to the line for $\Delta T_x = 0$ K in Fig. 4.1(a)). The experimental data shown in Fig. 4.1(b) is also represented in Fig. 4.1(a) as the numbered arrows. We note that the data agrees with the previously observed experimental findings: Δ_0 increases with positive temperature gradients and decreases with negative temperature gradients.

Next we take a more precise look at the evolution of the $\Delta(\Theta_H)$ traces (its definition is depicted in Ch. 3.1.2) as a function of ΔT_x . Fig. 4.2 reveals a new, non cosine-like contribution to the $\Delta(\Theta_H)$ signal. This contribution becomes even more obvious for larger temperature gradients $\nabla_x T$. In the following we will show that it can be explained in terms of an antisymmetric AMTEP-based artifact due to extremely small static parasitic magnetic fields \vec{H}_p .

4.1.2 TSSE-like artifact in the AMTEP signal induced by external magnetic field inhomogeneity

Simulation model

To simulate the AMTEP curves we need to know the equilibrium angle of the magnetization Θ_0 (see Eq. (3.4)) for every value of the sweeping field H . The angle Θ_0 can be found by minimization of the magnetic free energy in presence of the uniaxial magnetic anisotropy (Ch. 2.1). The model in Fig. 4.3 for calculation of the free energy includes an in-plane uniaxial magnetic anisotropy (UMA) with angle φ , sweeping field \vec{H} with angle Θ_H and parasitic static magnetic field \vec{H}_p with angle α . The effective magnetic field \vec{H}_Σ with angle Θ_Σ is found as a vector sum of \vec{H} and \vec{H}_p . All angles are counted with respect to the x-axis direction.

The magnetic free energy reads then as:

$$U = -M_0 H_\Sigma \cos(\Theta - \Theta_\Sigma) + K \sin^2(\Theta - \varphi), \quad (4.1)$$

where the first term is the Zeeman energy, the second term represents the magnetocrystalline anisotropy energy, M_0 is the saturation magnetization, K is the constant describing the strength of the UMA and Θ is an arbitrary angle between the magnetization vector \vec{M} and the temperature gradient $\vec{\nabla}_x T$.

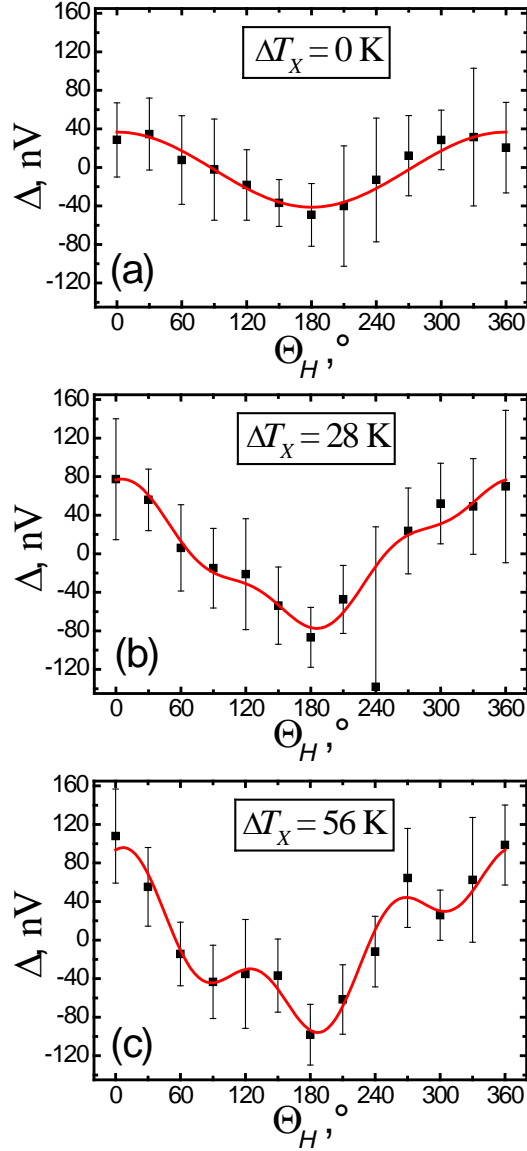


Figure 4.2: Difference signals $\Delta(\Theta_H)$ for fixed base temperature $T_{\text{str}} = 360$ K and temperature differences: (a) $\Delta T_x = 0$ K ($\nabla_x T = 0$ K/mm); (b) $\Delta T_x = 28$ K ($\nabla_x T = 4.7$ K/mm); (c) $\Delta T_x = 56$ K ($\nabla_x T = 9.5$ K/mm). With higher temperature differences ΔT_x a non cosine-like behavior appears. The red line is a fit function in Eq. (4.3) described in detail below.

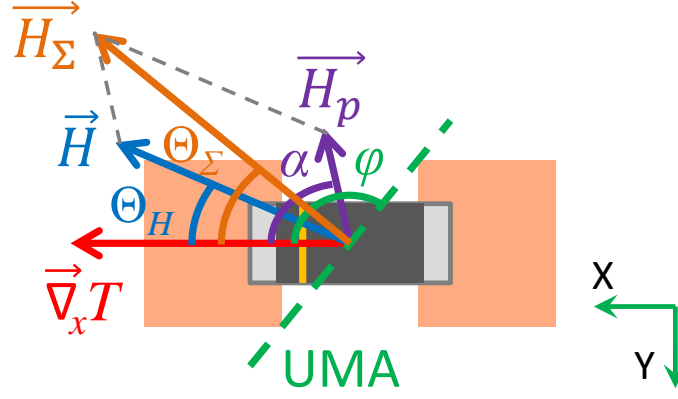


Figure 4.3: Definition of the coordinate system. The axis of the UMA is defined through the angle φ , the direction of the sweeping field \vec{H} through the angle Θ_H , the direction of the parasitic static magnetic field \vec{H}_p through the angle α and the direction of the effective magnetic field \vec{H}_Σ (vector sum of \vec{H} and \vec{H}_p) through the angle Θ_Σ . The temperature gradient $\vec{\nabla}T$ is parallel to the x-axis.

In our model we exclude the demagnetization energy, since its in-plane contribution for our geometry is two orders of magnitude smaller than the energy of the magnetocrystalline anisotropy of our sample. We calculate the demagnetization factors according to [2] that leads to an effective in-plane demagnetization factor $(N_x - N_y)/4\pi$ of the order of 10^{-6} (effective in-plane demagnetizing field ≈ 0.01 Oe).

The equilibrium angle Θ_0 can therefore be found as a root of the derivative of the magnetic free energy U (Eq. (4.1)) :

$$0 = H_\Sigma \sin(\Theta_0 - \Theta_\Sigma) + \frac{H_a}{2} \sin 2(\Theta_0 - \varphi), \quad (4.2)$$

where $H_a = \frac{2K}{M_0}$ is the effective UMA field. The subsequent calculation includes the following steps:

1. The parameters $\Theta_H, H_p, \alpha, H_a, \varphi$ are kept fixed. For each value of the sweep field H (with a certain step in the range $[H_{\max}; -H_{\max}]$, where H_{\max} is the maximum value of the sweep field) we compute the effective magnetic field \vec{H}_Σ (with its angle Θ_Σ) as a sum of the sweep field \vec{H} and the parasitic field \vec{H}_p , see Fig. 4.3. After this step we know the dependencies $H_\Sigma(H)$ and $\Theta_\Sigma(H)$;
2. We solve Eq.(4.2) numerically for the variable Θ_0 . This equation is solved for each value of H . After this step the dependence $\Theta_0(H)$ is known;
3. Inserting the computed dependence $\Theta_0(H)$, the experimental values $A_0(\Delta T_x)$ and V_{offset} into Eq.(3.4) we build our calculated curve $V_{y\text{calc}}(H)$, which we can compare with the experimentally determined $V_y(H)$. Determination of the V_{offset} is described in Ch. 3.1.3.
4. We repeat steps 1.-3. for $\Theta_H = 0^\circ..360^\circ$. Finally, we calculate the AMTEP artifact difference signal $\Delta_{\text{calc}}(\Theta_H) = V_{y\text{calc}}(\Theta_H, -H_{\max}) - V_{y\text{calc}}(\Theta_H, H_{\max})$.

Fig. 4.4(a) shows that the calculated AMTEP curves without the offset voltage ($V_{y\text{calc}}(H) - V_{\text{offset}}$) shift and become asymmetric as the parasitic field \vec{H}_p appears and increases. The curves become actually antisymmetric for moderately high values of H_p (> 2 Oe). We should note that a change of symmetry appears only if \vec{H}_p is not parallel to \vec{H} , otherwise only a shift of the AMTEP curves can be observed. However, a difference signal $\Delta_{\text{calc}}(\Theta_H) \neq 0$ caused by the parasitic field must be introduced in any way, since $V_{y\text{calc}}(H_{\text{max}}) \neq V_{y\text{calc}}(-H_{\text{max}})$ due to the induced shift. Fig. 4.4(b) presents the AMTEP artifact difference signals $\Delta_{\text{calc}}(\Theta_H)$, related to the curves from Fig. 4.4(a). The artifact's magnitude obviously scales with the parasitic field value H_p and in the absence of a parasitic field the difference signal $\Delta_{\text{calc}}(\Theta_H)$ does not appear.

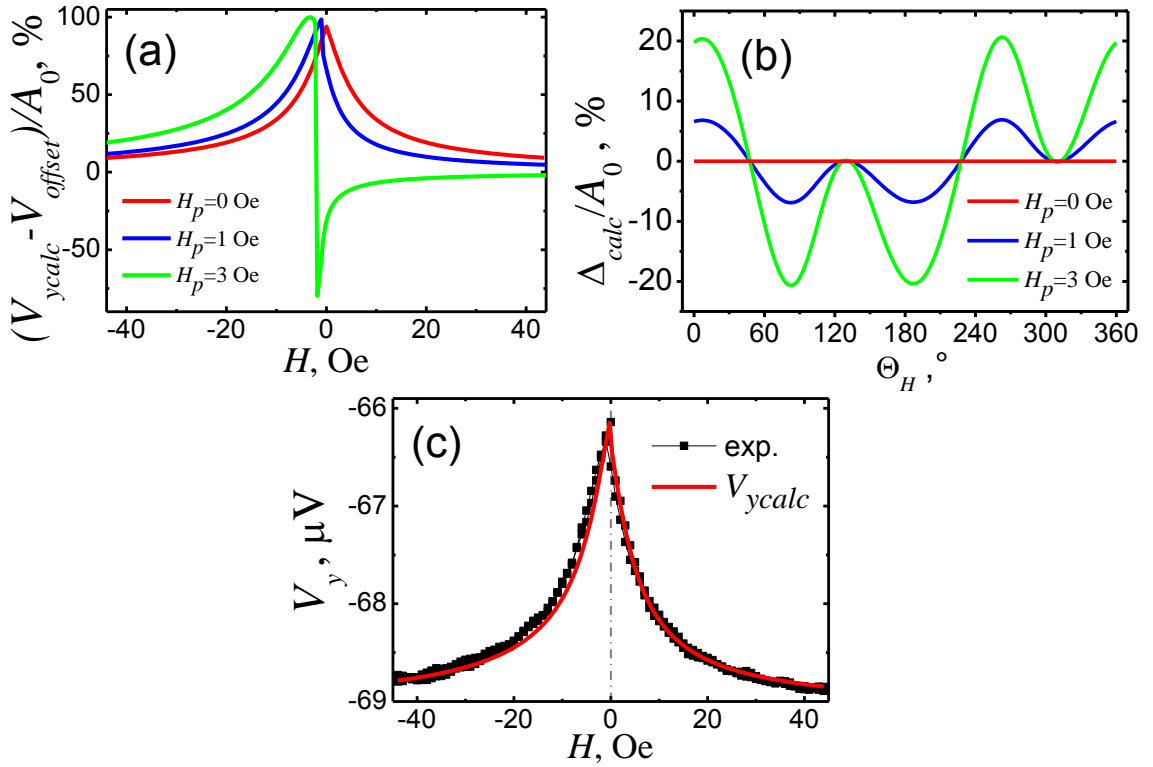


Figure 4.4: Appearance of an asymmetry in the AMTEP curves: (a) Calculated AMTEP curves $(V_{y\text{calc}}(H) - V_{\text{offset}})/A_0$ for $\Theta_H = 0^\circ$ and $H_p = 0, 1, 3$ Oe; (b) Calculated difference signals $\Delta_{\text{calc}}(\Theta_H)$ related to $V_{y\text{calc}}(H)$ from figure (a); (c) Experimental curve $V_y(H)$ for $T_{\text{str}} = 360$ K, $\Delta T_x = 65$ K ($\sim \nabla_x T = 11$ K/mm), $\Theta_H = 0^\circ$ and calculated curve $V_{y\text{calc}}(H)$ for $H_p = 0.28$ Oe (the measured parasitic field in the current set-up).

The good match of the experimental data $V_y(H)$ with the calculation $V_{y\text{calc}}(H)$ for $H_p = 0.28$ Oe (the value of the parasitic field found in our set-up) can be seen in Fig. 4.4(c). We use parameters of our set-up from Table 4.1 for all calculations in Fig. 4.4.

¹Since we average the experimental V_y data points from ± 40 to ± 44 , a range of $H = -42 \dots +42$ Oe is used for the simulation of $\Delta_{\text{calc}}(\Theta_H)$

Parameter	Value	Unit
H_p	0.28	Oe
α	-51	°
H_a	4.5	Oe
φ	35	°
H range	-44...+44 ¹	Oe

Table 4.1: Parameters of experimental TSSE set-up №1 (see Ch. 3.1) used for AMTEP artifact calculation.

Verification of the simulation model

To verify the accuracy of the computational model we perform additional measurements with a large static parasitic magnetic field (several 10s of Oe). In this case the AMTEP curves are expected to be antisymmetric. A small permanent magnet was glued to the wall on the outside of the vacuum chamber at the same height with the sample. The value and direction of the magnetic field at the position of the sample are determined with a Hall probe. One of the measurements for $H_p = 19 \pm 2$ Oe, $\alpha = -80 \pm 3^\circ$, $T_{\text{str}} = 323$ K and $\Delta T_x = 28$ K is exemplarily shown in Fig. 4.5. Fig. 4.5(a) and Fig. 4.5(b) present a comparison of the calculated dependencies $V_{y\text{calc}}(H)$ with the experimental $V_y(H)$ for angles of the sweeping field $\Theta_H = 0^\circ$ and 90° . Fig. 4.5(c), in turn, presents a comparison of the calculated dependence $\Delta_{\text{calc}}(\Theta_H)$ with the experimental $\Delta(\Theta_H)$. The calculated traces $V_{y\text{calc}}(H)$ and $\Delta_{\text{calc}}(\Theta_H)$ nearly perfectly reproduce the experimental traces $V_y(H)$ and $\Delta(\Theta_H)$, respectively. A very small difference between $\Delta_{\text{calc}}(\Theta_H)$ and $\Delta(\Theta_H)$ due to contributions of ANE and (potentially) TSSE signals to the experimental data is barely visible, since their magnitudes are smaller by 2 orders than the artifact's magnitude.

Parasitic difference signal Δ_{calc} for the actual parameters of the set-up

In Fig. 4.6 we present the calculated difference signal $\Delta_{\text{calc}}(\Theta_H)$ (normalized by A_0) for the parameters from Table 4.1. $\Delta_{\text{calc}}(\Theta_H)$ is in a good agreement with the experimental curve $\Delta(\Theta_H)$ shown in Fig. 4.2(c) for a large temperature difference of $\Delta T_x = 56$ K. The divergence of $\Delta(\Theta_H)$ in Fig. 4.2 from $\Delta_{\text{calc}}(\Theta_H)$ is caused by an additional cosine contribution of the ANE signal (with magnitude of ≈ 35 nV) to the experimental data $\Delta(\Theta_H)$.

Since we use numerical calculations, we cannot extract a functional dependence from $\Delta_{\text{calc}}(\Theta_H)$. However, using a fit function:

$$\Delta(\Theta_H)_{\text{fit}} = \Delta_{\text{AMTEP}} \cos \Theta_H + E \sin(\Theta_H + \phi_1) \cos(2\Theta_H + \phi_2) \quad (4.3)$$

we can match our calculations Δ_{calc} with less than 10% error, $R^2 = 0.99$. Here $\Delta_{\text{AMTEP}} = 4A_0(\Delta T_x) \cdot \frac{H_p}{H_{\text{max}}} \sin(-\alpha)$ is the amplitude of the cos-like part of the artifact, where H_{max} is the maximum value of the applied magnetic field; $E = 4A_0(\Delta T_x) \frac{H_p}{H_{\text{max}}}$ is the amplitude of the non-cos-like part of the artifact; phase $\phi_1 = 0^\circ$; phase $\phi_2 = -\alpha$. The fit function (4.3) describes the behavior of the difference signal $\Delta_{\text{calc}}(\Theta_H)$ very well until the conditions $\frac{H_p}{H_{\text{max}}} \ll 1$ and $\frac{H_a}{H_{\text{max}}} \ll 1$ are satisfied. The anisotropy field H_a and its orientation angle φ keep the shape of the calculated curve nearly undisturbed, until $\frac{H_a}{H_{\text{max}}} \ll 1$. The larger $\frac{H_a}{H_{\text{max}}}$ becomes, the more the parameters Δ_{AMTEP} , E , ϕ_1 and ϕ_2 deviate from the values defined above. After a

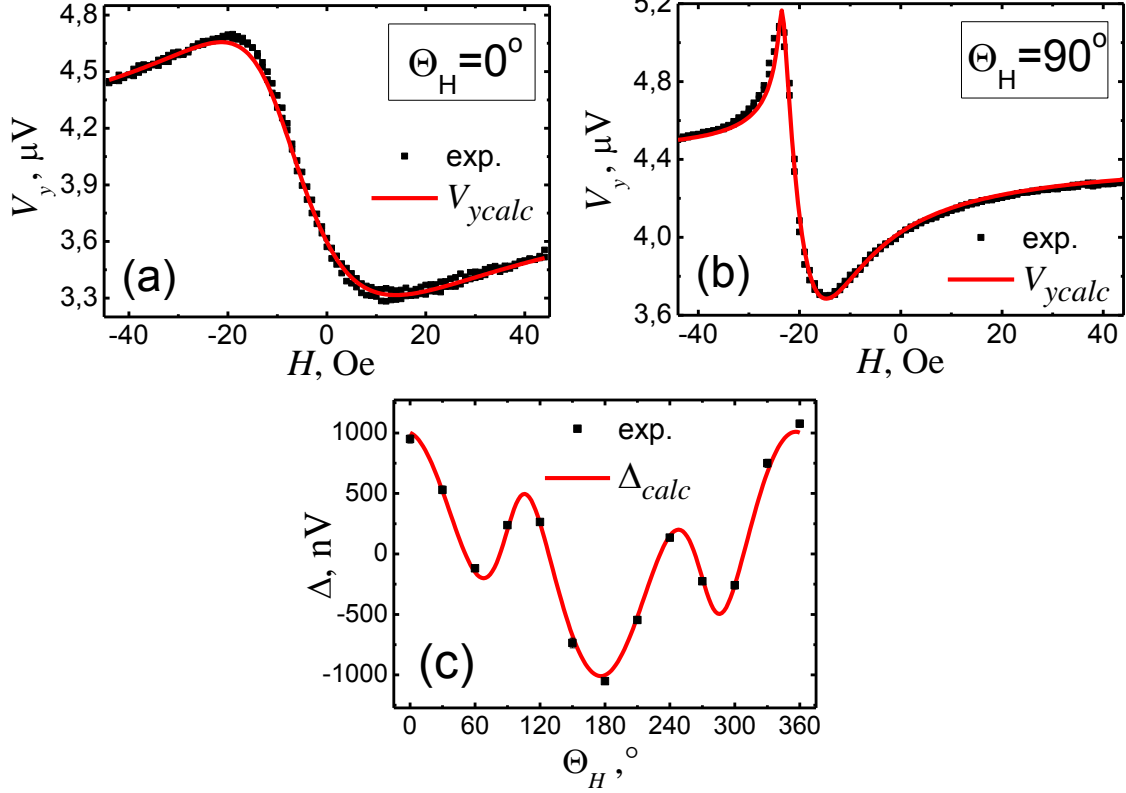


Figure 4.5: Experiments with large static parasitic magnetic field $H_p = 19 \pm 2$ Oe with angle $\alpha = -80 \pm 3^\circ$ for $T_{\text{str}} = 323$ K and $\Delta T_x = 28$ K ($\sim \nabla_x T = 4.7$ K/mm). Experimental $V_y(H)$ in comparison with calculated $V_{y\text{calc}}(H)$: (a) Angle of the sweeping magnetic field $\Theta_H = 0^\circ$; (b) $\Theta_H = 90^\circ$. (c) Experimental $\Delta(\Theta_H)$ in comparison with calculated artifact $\Delta_{\text{calc}}(\Theta_H)$.

certain point ($\frac{H_a}{H_{\text{max}}} \approx \frac{1}{2}$) the difference signal $\Delta_{\text{calc}}(\Theta_H)$ gets peaks, its shape changes strongly and it cannot be described with function (4.3) anymore. The angle α of a parasitic magnetic field strongly defines the phase ϕ_2 and the amplitude Δ_{AMTEP} : when $\vec{H}_p \parallel \vec{\nabla}_x T$ ($\alpha = 0^\circ$) $\Delta_{\text{AMTEP}} = 0$ V; when $\vec{H}_p \perp \vec{\nabla}_x T$ ($\alpha = 90^\circ$) Δ_{AMTEP} has a maximum value. When $\frac{H_p}{H_{\text{max}}} \gg 1$ the shape of the difference signal $\Delta_{\text{calc}}(\Theta_H)$ transforms from function (4.3) into $-\sin(\Theta_H + \phi_2)$. As shown in the inset of Fig. 4.6, $\Delta_{\text{calc}}(\Theta_H)$ contains a significant cosine-like contribution that can be mistaken for a TSSE or ANE contribution.

The shape of the AMTEP artifact $\Delta_{\text{calc}}(\Theta_H)$ does not depend on ΔT_x , but its magnitude scales linearly with ΔT_x . In this sense, the cosine-part of the artifact Δ_{AMTEP} has absolutely the same behavior as the TSSE. It shows the same angular dependence as TSSE and both effects are proportional to the temperature gradient $\nabla_x T$. The ANE, in turn, shares with the TSSE only the angular dependence.

Since we found a new fit function (4.3), we can use it to fit the experimental difference signals $\Delta(\Theta_H)$. We only replace Δ_{AMTEP} in (4.3) by Δ_0 , which in case of the experimental data contains three contributions:

$$\Delta_0(T_{\text{str}}, \Delta T_x) = \underbrace{\propto T_{\text{str}}^2}_{\Delta_{\text{ANE}}(T_{\text{str}})} + \underbrace{\propto \Delta T_x}_{\Delta_{\text{AMTEP}}(\Delta T_x) + \Delta_{\text{TSSE}}(\Delta T_x)}, \quad (4.4)$$

where Δ_{AMTEP} is the cosine-part of the AMTEP artifact, Δ_{ANE} the contribution of

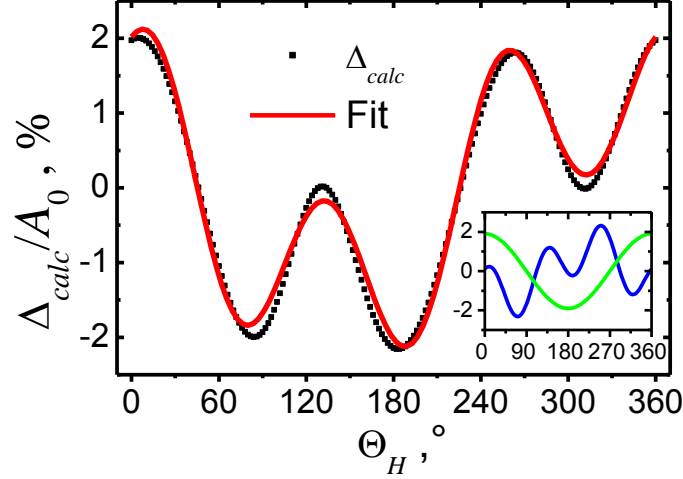


Figure 4.6: $\Delta_{\text{calc}}(\Theta_H)$ computed for the parameters of the experimental set-up (see Table 4.1). The red line is a fit to equation (4.3). Artifacts of $\approx 2\%$ of the AMTEP amplitude A_0 are found. The inset presents the extracted fitted parts of the $\Delta_{\text{calc}}(\Theta_H)$ signal: $\Delta_{\text{AMTEP}} \cos(\Theta_H)$ (green line) and $E \sin(\Theta_H + \phi_1) \cos(2\Theta_H + \phi_2)$ (blue line). The fit curve deviates from $\Delta_{\text{calc}}(\Theta_H)$ by less than 10% of its amplitude, $R^2 = 0.99$.

the ANE due to a spurious out-of-plane temperature gradient $\vec{\nabla}_z T$, and Δ_{TSSE} the contribution of the TSSE due to the applied in-plane thermal gradient. The phases ϕ_1 and ϕ_2 in (4.3) are extracted from the $\Delta_{\text{calc}}(\Theta_H)$ in Fig. 4.6 (which is computed for actual set-up parameters, see Table 4.1) and are then kept constant in (4.3) for fitting the experimental data.

4.1.3 Interpretation of the experimental results

The vertical shift of the line for $\Delta T_x = 0$ K in Fig. 4.1(a) corresponding to the temperature difference ΔT_x change is mostly caused by the AMTEP artifact. It can finally be proven by the data in Fig. 4.7. The experimental data points are calculated by subtracting the ANE contribution $\Delta_{\text{ANE}} = \Delta_0(\Delta T_x = 0 \text{ K})$ from the experimental amplitude $\Delta_0(\Delta T_x)$, see Eq. (4.4) (i.e. these points contain a mixture of possible TSSE signal magnitude Δ_{TSSE} and cosine-part of AMTEP artifact Δ_{AMTEP}). The normalized amplitude of the calculated cosine-part of the AMTEP artifact amounts to $\Delta_{\text{AMTEP}}/A_0 = 1.9\%$ (green line). This value is in good agreement with the experimental value $(\Delta_0 - \Delta_{\text{ANE}})/A_0$ of $2 \pm 0.5\%$ (magenta line and shaded area). This means, that the maximum possible contribution of the TSSE inside the error bars is $< \pm 0.3$ nV/K ($\sim \pm 2 \cdot 10^{-12}$ V.m/K in terms of the temperature gradient), which leads to ± 20 nV for the maximum achieved temperature differences $\Delta T_x = \pm 65$ K. Comparing this value with the value 250 nV/K reported in Uchida et al. [144] one sees a discrepancy of 3 orders of magnitude.

Sources of the parasitic field and methods to suppress it

We have examined possible sources of parasitic magnetic fields in our set-up and found that the parasitic field $H_p = 0.28$ Oe is caused by external magnetic fields

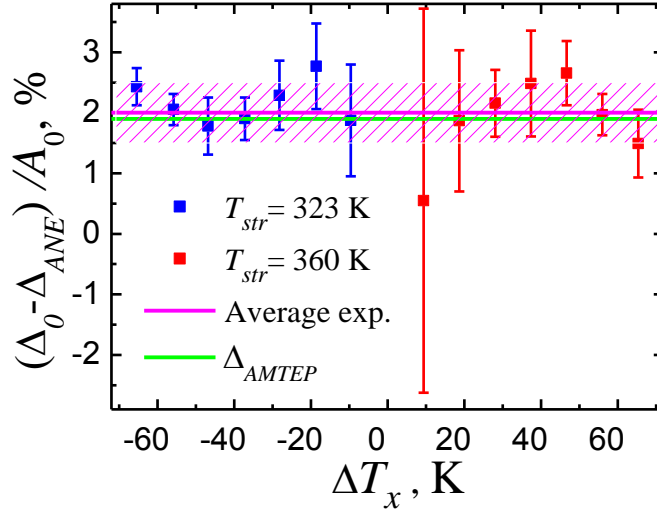


Figure 4.7: Comparison of the experimental level $(\Delta_0 - \Delta_{ANE})/A_0$ (blue and red points, magenta line with shaded area presents the averaged experimental data) with the normalized calculated AMTEP artifact Δ_{AMTEP}/A_0 (green line). Large deviations of the experimental points from the average value in the region of small differences ΔT_x are connected to small values of the $\Delta_0 - \Delta_{ANE}$ and are proportionally impacted by noise.

existent in the laboratory. We have also examined the magnetic field contribution from the Peltier elements and verified that it produces only an insignificant field of 0.03 Oe maximum.

There are few possibilities to suppress the cos-part of the AMTEP artifact:

1. Increasing of the maximum value of the sweep field H_{\max} , as the equilibrium angle Θ_0 will then be closer to the angle of the sweep field Θ_H . According to our calculations, the level of the artifact could be reduced from 2% of the AMTEP amplitude A_0 (equal to 70 nV for the highest temperature gradients $\nabla_x T = \pm 11$ K/mm) to 0.06% (equivalent to 2 nV \ll than noise level of 20 nV) by increasing the H_{\max} from 44 Oe to 2000 Oe. The level of the artifacts is inversely proportional to the H_{\max} . Unfortunately, in our set-up we have no possibility to produce high magnetic fields larger than 50 Oe.
2. Keeping the sweep field \vec{H} parallel to the parasitic field \vec{H}_p and rotating the sample together with the applied in-plane temperature gradient $\vec{\nabla}T$. In this case the symmetry of the AMTEP traces is not disturbed, but a horizontal shift of traces equal to the value H_p appears. After this shift is subtracted, no AMTEP artifact in the difference signal $\Delta(\Theta_H)$ will be observed. However, rotation of the vacuum chamber in our case is not feasible.
3. Keeping the parasitic field \vec{H}_p parallel to the applied in-plane temperature gradient $\vec{\nabla}T$. With this alignment the cos-part of the AMTEP artifact will be strongly suppressed. The lower is the ratio $\frac{H_a}{H_{\max}}$ and the closer is φ to $n \cdot 90^\circ$ (where n is integer), the stronger the suppression is. However, the non-cos-part of the AMTEP artifact will be not suppressed in this way.

4. Suppressing H_p using additional compensating magnetic field. This is the best solution, because no source of artifacts is introduced in the set-up.

Conclusion on Py/Pt sample measurements

In this study we have shown that in conductive FM samples a small parasitic static magnetic field below 1 Oe (of the order of the earth's magnetic field) can produce an AMTEP artifact with an amplitude of 10-100 nV that contains a TSSE-like contribution. This artifact has the same order of magnitude as the previously found source of misinterpretations in the TSSE experiments - the ANE due to out-of-plane temperature gradient. But in contrast to the ANE-based parasitic effects, the new artifact does depend on the applied in-plane temperature gradient. This fact makes it more difficult to separate from possible TSSE signal, and, consequently, it has to be thoroughly taken into account. We have found that the investigated parasitic effect also gives us the missing explanation for the vertical shift observed in [117]. Finally, no TSSE signals larger than the noise level of 20 nV have been detected in permalloy thin films. This upper error level is 3 order of magnitude lower than in the first report on the TSSE [144].

4.2 Pt/YIG/GGG sample

A 24 nm thick Yttrium iron garnet ($Y_3Fe_5O_{12}$, YIG) film is deposited on a Gadolinium gallium garnet ($Gd_3Ga_5O_{12}$, GGG) (111)-oriented single crystal substrates with 5 mm width and 9 mm length by pulsed laser deposition (PLD) [27] from a stoichiometric polycrystalline target. The PLD technique allows production of thin YIG films with the low Gilbert damping constant [62].

After a vacuum break and cleaning with ethanol in an ultrasonic bath a 10 nm thin Pt strip was deposited by DC magnetron sputtering in an Ar atmosphere of $1.5 \cdot 10^{-3}$ mbar through a 100 μm wide split-mask on one sample side of the YIG film.

Our YIG sample shows a coercive field close to 100 Oe and an effective saturation magnetization of $M_{\text{eff}} = 190 \text{ emu/cm}^3$ ($\mu_0 M_{\text{eff}}$ of about 239 mT). This M_{eff} value is somewhat higher than the bulk saturation magnetisation of YIG ($\mu_0 M_{\text{eff}}$ of about 163 mT), what can be explained by the influence of the out-of-plane anisotropy.

For Pt(10)/YIG(24)/GGG sample we perform measurements with fixed T_{str} and varying ΔT_x with TSSE set-up №1, described in Ch. 3.1. Instead of the Helmholtz coils in Ch. 3.1 we use an iron yoke electromagnet with field magnitude up to 1120 Oe.

4.2.1 LSSE contribution to the measured signal

As it was mentioned in Ch. 2.6.3 and in Fig. 2.12(b), ferromagnetic insulators (FMI) have fewer sources of misinterpretation in TSSE experiments. For those the spurious effects are produced solely by the unintended out-of-plane gradients, namely LSSE and ANE. The LSSE is expected to be present always, while ANE appears only when a magnetic proximity effect appears in the NM detector strip.

The experimental difference signal amplitude Δ_0 is shown in Fig. 4.8. The extraction procedure for this signal is explained in Ch. 3.1.2. The plot contains 3

data sets with $\Delta T_x = -40, 0, 40$ K ($\sim \vec{\nabla}_x T = -5.7, 0, 5.7$ K/mm, respectively). The base temperature T_{str} is varied in a range from 20 to 110° C. When the temperature gradient is varied and at the given T_{str} we see no difference between experimental points within error bars of ± 5 nV, meaning no measurable TSSE contribution. All three traces show an increase of Δ_0 magnitude with T_{str} : up to 10 nV for maximal 110° C (90 ° C temperature difference with respect to room temperature). The negative slope of Δ_0 is in agreement with the observations in [96, 147]. We attribute this signal to the influence of the LSSE signal induced by an unintended out-of-plane temperature gradient. The unintended temperature gradient appears because of the surface-to-surface radiation between the chamber walls and the sample surface (same as for Pt/Py sample written in Ch. 4.1.1).

In the next step we calculate the difference in temperatures of magnon and electron systems ΔT_{me} via Eq.2.63, where V_{sat} corresponds to the measured Δ_0 . All YIG parameters, except M_S are taken from [118]. A resistivity $\rho_{\text{Pt}} = 40\mu$ Ohm · cm is used for the calculation. For $\Delta_0 = 10$ nV we obtain a value $\Delta T_{me} = 0.1\mu$ K, which is of the same order as in [96].

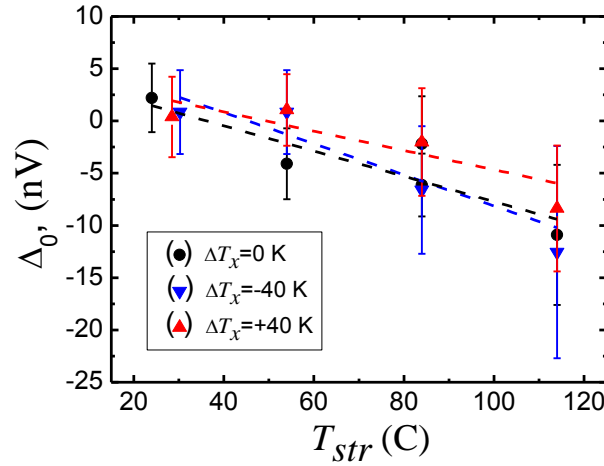


Figure 4.8: Pt(10)/YIG(24)/GGG sample. Dependence of the difference signal amplitude Δ_0 on the base temperature T_{str} for fixed temperature differences $\Delta T_x = -40, 0, 40$ K ($\sim \vec{\nabla}_x T = -5.7, 0, 5.7$ K/mm respectively).

4.2.2 Discussion on possibility of the magnetic proximity effect

Another possible explanation for the Δ_0 shift in Fig.4.8 is the ANE contribution induced by the unintended out-of-plane temperature gradient. Neither YIG (dielectric material) nor Pt (non-magnetic material) are expected to show any ANE contribution. However, observations of magnetic proximity effect (MPE) induced in Pt on ferromagnetic metal (FM) [88] and ferromagnetic insulator (FMI) [89, 53, 88, 83] were reported. This effect might lead to the appearance of an ANE effect in Pt, which is difficult to separate from LSSE contribution, while both have the same angular and out-of-plane temperature gradient dependencies.

X-ray magnetic circular dichroism (XMCD) is an often employed technique to investigate MPE. However, XMCD data for the Pt/YIG interface seem contradictory

[89, 53]. Authors of [89] found an induced average magnetic moment per atom in Pt to be $0.054 \mu_B$ at 300 K and $0.076 \mu_B$ at 20 K. But authors of [53] have measured only $0.003 \pm 0.001 \mu_B$ per Pt atom at RT. DFT simulations of the Pt/YIG interface give values $0.07 \mu_B$ for Pt(100)/YIG(100) and $0.03 \mu_B$ for Pt(111)/YIG(111) [83].

Additionally to the MPE, the SHE, ISHE, spin-mixing conductance, and magnetocaloric effect in the Pt/YIG system are shown to be strongly dependent on the treatment of the interface and vary from sample to sample. The strength of the MPE changes dramatically with the surface variation between different YIG samples [88]. Annealing, ion milling, or wet chemical cleaning can significantly influence ISHE and the spin-mixing conductance [72]. Annealing the YIG film prior to Pt film deposition leads to a change of the strength of the LSSE [75]. These findings highlight the importance of the interface structure for the magnetic properties of the Pt/YIG system.

Finally, XMCD investigation of our sample made by the Bielefeld group show a large error in the estimation of the magnetic moment in Pt. Thus, we can not make a conclusion on the presence or absence of MPE in the sample.

4.3 Py/MgO sample

In this Chapter we present a collaborate work on a Py/MgO sample conducted on set-up of a Bielefeld group. A detailed description of the set-up can be found in Ch. 3.2.

Electric measurements are conducted along the y-axis of a sputter deposited Py thin film ($5 \times 5 \text{ mm}^2$, 18 nm thick) on MgO(001). A voltmeter is connected mechanically to the Py surface via Au tips.

The main goal of the measurements was to prove the functionality of the set-up towards TSSE measurements. In TSSE measurements a NM-detector strip is exploited to detect spin-currents via the ISHE. Thus, the TSSE is not expected to be detected in the bare FM. However, the detections of TSSE in such case were reported in GaMnAs [70] and in Py [145]. This phenomenon was explained by the authors as the "self-ISHE" of FM, meaning that the FM works as its own spin current detector.

Our measurements on the Py/MgO sample with the Au tip contacts reveal voltage traces of very peculiar shape. Some odd mixture of effects, including TSSE, was assumed as the starting hypothesis to explain it. However, after detailed analysis, these traces were attributed to another AMTEP artifact.

In this chapter we follow the designation for AMTEP signal used in Ch. 2.5.3 and specifically Eq. (2.56). We conduct 2 types of measurements: 1) with rotation of magnetic field \vec{H} direction at fixed thermal gradient $\vec{\nabla}T$ direction; 2) vice versa.

Changing the magnetic field direction

In the first series of measurements, the Py/MgO sample was kept at a constant temperature difference of $\Delta T_x = 30 \text{ K}$, so that the cold side was kept at 293 K and the hot side at 323 K. Field-sweep measurements were recorded for $0^\circ \leq \varphi \leq 360^\circ$ and six exemplary chosen curves in the range of $0^\circ \leq \varphi \leq 180^\circ$ are shown in Fig. 4.9(a-f). The measured voltage difference V_y saturates for high magnetic fields but shows differently shaped extrema, depending on φ . Figure 4.9(a) for $\varphi = 0^\circ$ shows a

similar data set as Fig. 4.9(e) for $\varphi = 180^\circ$ with the appearance of a minimum and a maximum. Increasing φ to 20° (Fig. 4.9(b)) changes the signal in the low magnetic field regime into a minimum for both branches with lower intensity but similar shape. For $\varphi = 40^\circ$ (Fig. 4(c)) the intensity of these minima increases until for $\varphi = 70^\circ$ (Fig. 4.9(d)) the curves change their shape into a minimum and maximum again. But in contrast to Fig. 4.9(a) both branches have the same progression, thus, the magnetization reversal process is independent of the sweep direction of the magnetic field. For $\varphi = 130^\circ$ (Fig. 4.9(e)) large, clearly separated maxima can be observed, that in the case of $\varphi = 180^\circ$ (Fig. 4.9(f)), form a similar curve as for $\varphi = 0^\circ$. For angles larger than $\varphi = 180^\circ$ the curves repeat those from the range $0^\circ \geq \varphi \geq 180^\circ$.

Not only the shape of the curves but also the saturation voltage depends on φ . All saturation voltages $V_{\text{sat}} = V_y$ (for $|H| \geq 140$ Oe for each φ were averaged (similar to the average signal $A(\Theta)$ described in Ch.3.1.2 for the set-up №1) and plotted vs. φ forming V_{sat} trace, see Fig. 4.9(g). Apart from the offset level, V_{sat} shows a clear $\sin 2\varphi$ dependence, which is a clear sign of the AMTEP signal. V_{sat} oscillates around an offset voltage of $\approx -15.0 \mu\text{V}$, which originates from the ordinary thermovoltage, which is described in Eq. (2.56) by S+. Small deviations of V_{sat} from the fit can be found around $\varphi = 90^\circ, 270^\circ$, but the analysis of $V_{\text{sat}} - V_{\sin 2\varphi}$ reveals no systematical higher order measurement artifacts.

The V_y trace in Fig. 4.9(a) has, for the initially expected AMTEP signal, a very unusual behavior: it is antisymmetric (the AMTEP is symmetric with respect to magnetic field) and changes sign of the asymmetry depending on the sweep direction. The small magnitudes of both sweep-up and sweep-down curves for $\varphi = 20^\circ, 70^\circ$ indicate the presence of magnetic easy axes in these directions [94].

As it was discussed in Ch. 2.6.3 and shown in Table in Fig. 2.10, measured V_y traces in TSSE experiments are usually separated into a symmetric and antisymmetric part. A systematically observed antisymmetric part with $\cos \varphi$ dependence will indicate an ANE induced by an unintended out-of-plane ∇T_z . However, using this method for the data in Fig. 4.9 we do not find any systematic dependence of the antisymmetric contribution. Therefore, we can exclude any unintended out-of-plane ∇T_z for the set-up, as authors [94, 96] do for their thermal set-ups, where unintended out-of-plane thermal gradients are strongly suppressed.

Changing the thermal gradient direction

As the next series of measurements, the angle of the thermal gradient φ_T (see Fig. 3.7) was increased in steps of 15° , and sweep measurements were conducted at $\varphi = 0^\circ$. In Fig. 4.10(a-f) each curve again shows a saturation voltage for high magnetic fields and two extrema close to each other at around 0 Oe. For the data in Fig. 4.10(a) the voltage measurement is carried out perpendicular to the thermal gradient, thus, the signal is expected to originate from the pure PNE ($E_y(\nabla T_x)$, Eq. (2.52)). In Fig. 4.10(c) the voltage measurement is conducted parallel to the thermal gradient because it was rotated to $\varphi_T = 90^\circ$. Here, the voltage signal is expected to be produced purely by the AMTEP, since this effect needs a longitudinal ∇T ($E_y(\nabla T_y)$, Eq. (2.55)). But only the last mentioned signal has a more or less symmetric shape, whereas both of them have to be symmetric.

The results for $0^\circ < \varphi_T < 90^\circ$ consist of a superposition of the PNE and the AMTEP, since for these φ_T the ∇T consists of a x- and y-component, in the following we refer to all these signals as AMTEP as this name well represents the nature of the

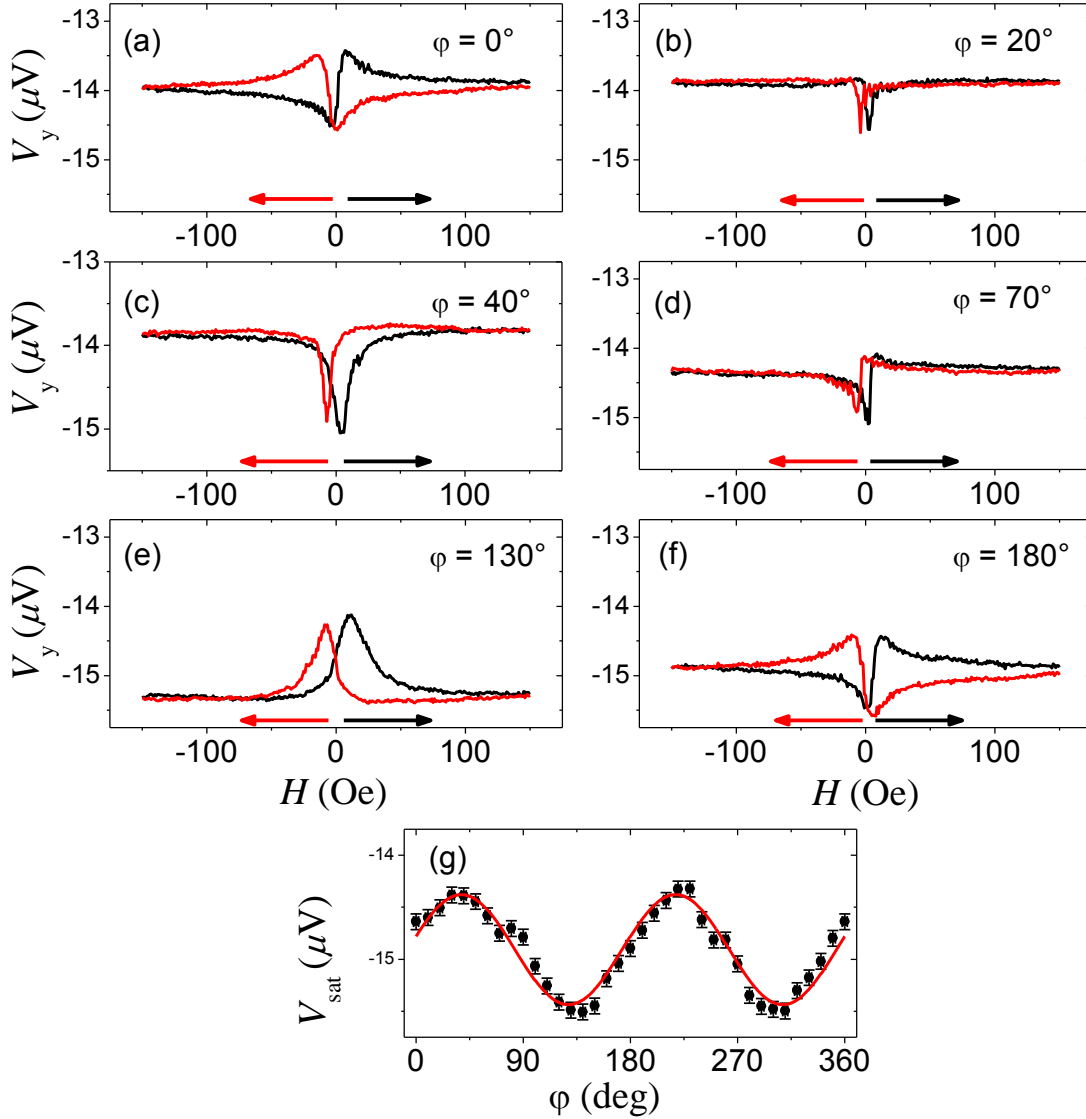


Figure 4.9: (a–f) Measurement of V_y against the magnetic field in the Py/MgO sample. The temperature difference $\Delta T = 30$ K is kept constant along the x-direction ($\varphi_T = 0^\circ$). The in-plane angle φ of the external magnetic field was varied. The data for $\varphi \geq 180^\circ$ repeat the data in a range of $\varphi = 0^\circ$ to 180° . (g) The voltage V_{sat} for each φ was averaged in the range of $140 \text{ Oe} \leq |H| \leq 150 \text{ Oe}$ and plotted against φ , showing the theoretical $\sin 2\varphi$ dependence (Eq. (2.56)).

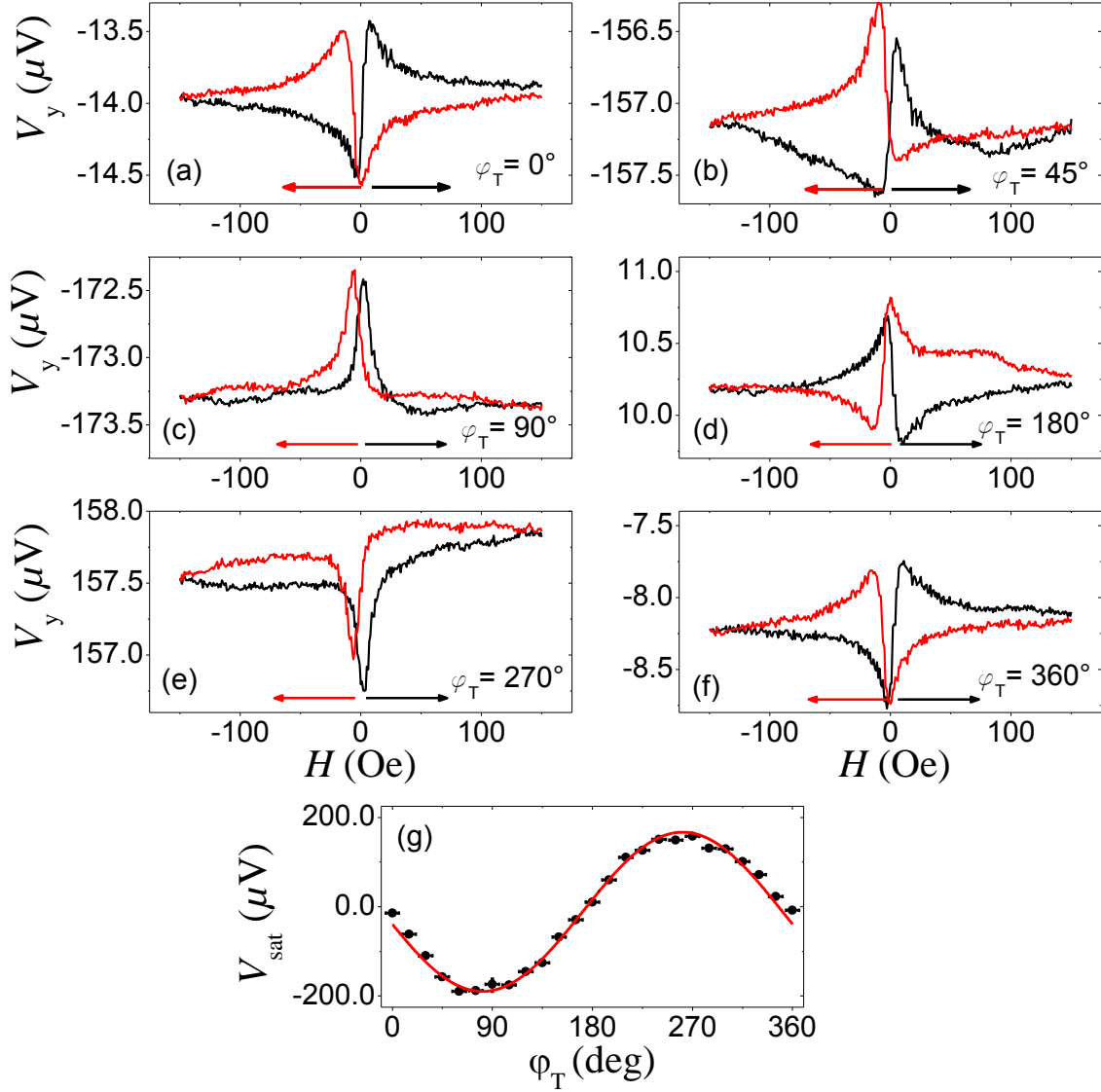


Figure 4.10: (a–f) Electric signal V_y as a function of the magnetic field for the Py/MgO sample with φ set to 0° and various φ_T . The insets indicate the directions φ_T of the thermal gradients. The sample is kept at the base temperature of 308 K with $\Delta T = 30$ K. (g) The voltage V_{sat} is averaged as described for Fig. 4.9(g) and plotted against φ_T . The data show a $\sin \varphi_T$ dependence attributed to S_\perp (see Eq.(2.56)).

effect. A qualitative change in the signal can also be observed in the voltage features for low magnetic fields. Figure 4.10(a) shows the same signal progression as in Fig. 4.9, reaching a minimum before crossing 0 Oe. Increasing φ_T now suppresses this minimum before the zero crossing point until for $\varphi_T = 90^\circ$ only two sharp maxima are shaped. Due to the rotation of ∇T the relative orientation of \vec{M} with respect to ∇T changes for different φ_T , thus, leading to changing contributions of the pure PNE and AMTEP to the measured voltage signal.

Figure 4.10(g) shows the saturation voltages of Fig. 4.10(a-f) vs. φ_T . In contrast to Fig. 4.9(g), where the oscillation of $V_{\text{sat}}(\varphi)$ is only due to the PNE part, Fig. 4.10(g) identifies the contribution of the ordinary, magnetic field independent Seebeck effect $V_{\text{sat}}(\varphi_T)$, expressed by S_\perp in Eq. (2.56) (remembering that $S_+ = \frac{S_\parallel + S_\perp}{2}$ and $S_- = \frac{S_\parallel - S_\perp}{2}$). Since V_y is measured, the rotation of ∇T leads to a $\sin \varphi_T$ shaped projection of ∇T on the y-axis, resulting in a sine-shaped V_y signal. The nonmagnetic Seebeck signal is three orders of magnitude higher than the one of the PNE, while the magnetic field dependent part of the AMTEP is expected to be of the same order of magnitude as the PNE.

4.3.1 Unriddling the magnetization vector rotation from AMTEP curves

The appearance of two magnetic easy axes (MEA, $\varphi = 20^\circ, 70^\circ$) in Fig. 4.9 can be explained by the superposition of a uniaxial (UMA) and a fourfold in-plane cubic magnetic anisotropy (CMA). A UMA can be attributed to, e.g., surface steps [24], oblique growth [109], substrate shape [79] or dangling bonds [32]. For example, Fe/MgO(001) systems were used to manipulate the UMA in terms of strength and orientation with different deposition techniques [158, 157] showing the likelihood of forming a UMA during the deposition of thin films, not only for Fe/MgO(001) but also for Py thin films on different substrates [73, 82]. Due to the crystalline symmetry of cubic magnetic films, a CMA is expected to be present for cubic systems [158, 157].

The magnetic field dependent voltages in Fig. 4.9 and 4.10 have partially asymmetric behavior, although AMTEP traces are known to be symmetric to the magnetic field in case of a present UMA [6, 117, 94, 111, 131]. To resolve this situation different simulations are conducted and described in the following.

In Eq.(2.56) it is implicitly assumed that the magnetization vector \vec{M} coincides with the magnetic field \vec{H} which means that $\varphi_{M0} = \varphi$, where φ_{M0} is the angle of equilibrium position of \vec{M} . This assumption works well when the applied magnetic field is at least one order of magnitude stronger than the magnetic anisotropy and any parasitic field \vec{H}_p contribution in the system [58] $|H| \gg C_i K_i / M_s, |H_p|$, where K_i is some anisotropy constant with the dimension of J/cm³, M_s is the saturation magnetization and C_i is a dimensionless constant of the order of unity (depends on the present type of anisotropy: uniaxial/cubic/hexagonal or other). However, this assumption is fulfilled only for external magnetic fields greater than 100 Oe (saturation of V_y signal in Fig. 4.9 and 4.10). Thus, an adequate model for calculation of φ_{M0} for lower magnetic fields is needed in order to reproduce the field sweeps of the experimental AMTEP traces.

First of all, we rewrite Eq.(2.56):

$$E_y = -S_- \sin(2\varphi - \varphi_T) |\nabla T| \quad (4.5)$$

where we have neglected the summand with S_+ , since it does not depend on \vec{H} and produces only an offset of the field sweep traces. Then remembering that the measured voltage is $V_y = -E_y d$ (where d is distance between the measurement contacts) and that in general $\varphi_{M0} \neq \varphi$, we get the following expression for the AMTEP field dependent traces V_y :

$$V_y(H) = dS_- |\nabla T| \sin(2\varphi_{M0}(H) - \varphi_T). \quad (4.6)$$

In further calculations we show normalized AMTEP traces (i.e. we take $dS_- |\nabla T| = 1$).

As a suggestion for the rotation of \vec{M} during the field sweep, being later proven by **model C** (see below), the shape of the experimental curves can be understood with the help of the sweep-up trace shown in Fig. 4.11. According to Eq.(4.6) the maximum and minimum of the V_y signal appear for $\varphi_{M0} = 45^\circ, 225^\circ$ and $\varphi_{M0} = 135^\circ, 315^\circ$, respectively (gray dashed lines in Fig. 4.11(b)). Point "0" is the fully saturated state of the sample, when \vec{M} is aligned with the field \vec{H} (corresponds to negative values of H). When the absolute field value H is decreased, \vec{M} tends to rotate away from the direction of the external magnetic field and \vec{M} passes through the direction of minimum "1" (despite it is expected to rotate in opposite direction, closer towards MEA1). When the magnetic field switches its direction (towards the red dashed arrow) and increases its absolute value, \vec{M} passes through the maximum position "2" trying to align with the magnetic field in direction "3".

Model A - classical theoretical anisotropy model

Here we write the energy equation for combined in-plane uniaxial and cubic magnetic anisotropies (UMA and CMA, respectively):

$$U = -M_S H \cos(\varphi_M - \varphi) + K_u \sin^2(\varphi_M - \varphi_{ua}) + \frac{K_c}{4} \sin^2 2(\varphi_M - \varphi_{ca}), \quad (4.7)$$

where the first term is the Zeeman energy, the second and the third terms represent the magnetocrystalline uniaxial and cubic anisotropy energies, M_S is the saturation magnetization, K_u and K_c are the constants describing the strength of the UMA and CMA with angles φ_{ua} and φ_{ca} , respectively, and φ_M is an arbitrary direction of the magnetization vector \vec{M} .

The demagnetization energy is excluded, since its in-plane contribution for the given geometry is negligible. Calculation of the demagnetization factors according to [2] leads to an effective in-plane demagnetization factor $(N_x - N_y)/4\pi$ of the order of 10^{-6} (effective in-plane demagnetizing field ≈ 0.01 Oe).

Using reasonable values of $\mu_0 M_S = 1$ T, $K_c = 5 \cdot 10^4$ erg/cm³ [155], $K_u = 2 \cdot 10^4$ erg/cm³ [47, 120], $\varphi_{ca} = 0^\circ$ and $\varphi_{ua} = 45^\circ$ and assuming magnetic field H set to zero, the free magnetic energy angular distribution is plotted in Fig. 4.12. As it can be seen, the magnetic easy axes are aligned to the previously mentioned directions of 20° and 70° . However, with application of this model only symmetric AMTEP traces

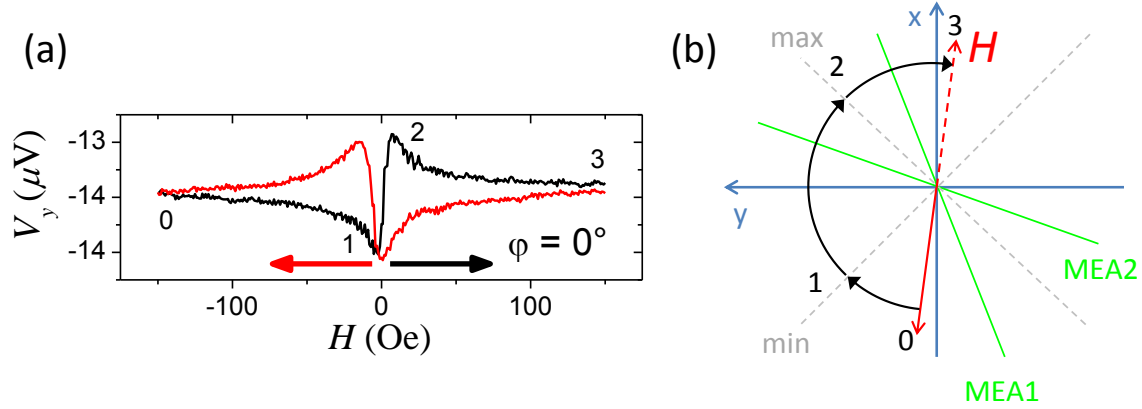


Figure 4.11: Explanation of the experimental field sweeps: (a) The experimental sweep up trace for φ and $\varphi_T = 0^\circ$ passes through 4 specific positions; (b) \vec{M} reversal in relation to the experiment at $\varphi = 0^\circ$. The solid red line corresponds to the orientation of \vec{M} at high negative magnetic fields \vec{H} and the dashed red line - to the positive. MEA1 and MEA2 (green lines) are magnetic easy axes situated around 20° and 70° , respectively. The gray dashed lines "min" and "max" correspond to the minimum and maximum of the AMTEP signal, respectively. Shown rotation from "0" to "3" is somewhat "unnatural", while it is expected that \vec{M} would orient along closest to the easy magnetic axis MEA1 as the external magnetic field \vec{H} reduces to 0 Oe.

can be obtained (see Fig. 4.4 for $H_p = 0$ Oe), because \vec{M} switches between directions "1" and "2" immediately via multidomain state after inverting \vec{H} (described below in model B Fig. 4.13(b)). A multidomain state exists only in an extremely narrow range around $H = 0$ Oe, which is a reasonable assumption for Py thin films.

Model B - simulation of multidomain state

A more elaborate research with keeping the magnetic prehistory of the sample (hysteresis phenomenon), using multidomain state and including modeling of finite temperatures as well as UMA and CMA was performed in MuMax³ [148], see Fig. 4.13. In this model it is not possible to conduct simulations for large sample areas (5×5 mm²), because of the cell number limitation of MuMax³. Instead, an area of 1×1 μm was used. The reduction of area leads to an enhanced contribution of demagnetization energy to anisotropy by 3 orders of magnitude. To make this contribution negligible, M_S has to be reduced twice in comparison to the Py value and the anisotropy constants are enlarged by an order of magnitude in comparison to model A. The sweep region was expanded to $[-1000, 1000]$ Oe. Thus, this model only gives a qualitative description.

The simulated voltage trace in Fig. 4.13(a) gives an antisymmetric trace, but yet the transition of \vec{M} in Fig. 4.13(b) significantly differs from the supposed one shown in Fig. 4.11(b). \vec{M} rotates in the direction "1" in Fig. 4.13(b) which corresponds to MEA1, when the field sweep goes up (absolute value H goes down). Then \vec{M} switches its direction by 180° via a multidomain state (the region between "1" and "2" in Fig. 4.13(a); position "1" is related to $H \approx 0$ Oe) into "2". The minimum of the voltage trace does occur not because of passing through the minimum direction

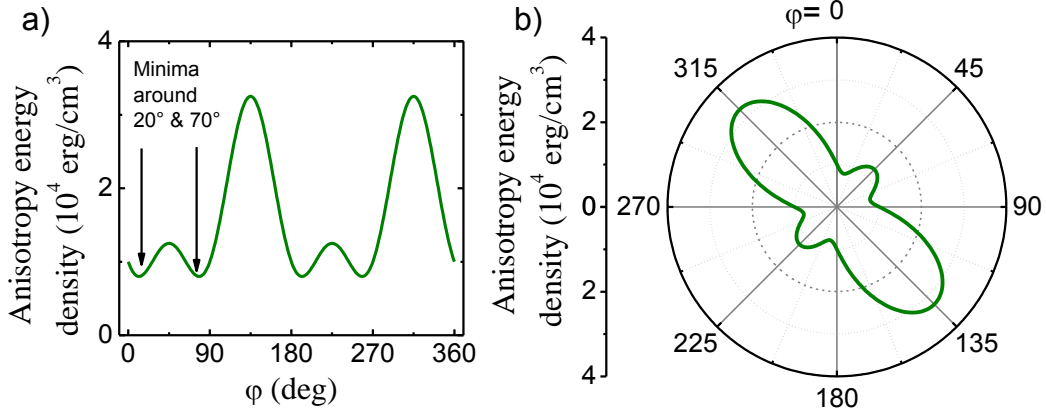


Figure 4.12: a) Energy angular dependence according to Eq.(4.7) with parameters $\mu_0 M_S = 1$ T, $K_c = 5 \cdot 10^4$ erg/cm³, $K_u = 2 \cdot 10^4$ erg/cm³, $\varphi_{ca} = 0^\circ$ and $\varphi_{ua} = 45^\circ$. Magnetic easy directions are situated around $\varphi_{\min 1} = 20^\circ$ and $\varphi_{\min 2} = 70^\circ$; b) Representation of the energy landscape in polar coordinate system.

at 135° , but because of the multidomain state, which tends to reduce the absolute value of \vec{M} (AMTEP signal is $\propto |\vec{M}|^2$). Next, when \vec{H} switches its direction and increases its value, \vec{M} tends to align with the external magnetic field (point "3"). Such an asymmetric behavior in systems with CMA, low M_S and large magnetic anisotropy was already observed in other AMTEP experiments [111, 131].

Model C - influence of electromagnet calibration method

Next, we take a more precise look to the parameters of **model A**, namely the directions of UMA and CMA. The fact that the magnetic hard directions $45, 135, 225, 315^\circ$ coincide with the directions of the magnetic caps of the electromagnet (see Fig. 3.7(a)) hints to a magnetic anisotropy which rather comes from the electromagnet system itself than from the sample. In case of a perfect geometry of the magnet a pure CMA could be expected only due to its symmetry. Since all four caps of the electromagnet are connected via the toroidal magnetic core, slightly different distances between the opposing magnetic cores and/or inhomogeneities in the yoke can introduce an additional contribution of UMA, just because one magnetic pair might be more preferable for the magnetic flux than the other one. Magnetic hard directions of CMA coincide with the magnetic poles of the magnet, since even when only one pair is used, there is always some remanence in the second pair. Thus, the fields of both pairs always have to be summed up, so that the superpositioned field direction always tends to align somewhere between the pole directions.

In this model a parasitic field H_p due to the magnetic yoke is assumed. The set-up's magnetic field was initially calibrated in the following manner: a magnetic field of each pair of opposing poles (B_{+45° and B_{-45° components) was measured as a function of magnetizing current, while the current through the other pair was set to 0. After the field calibration the current values $I_{+45^\circ}, I_{-45^\circ}$ were used in the experiments to evaluate the total field $B(I_{+45^\circ}, I_{-45^\circ}) = \sqrt{B_{+45^\circ}^2(I_{+45^\circ}) + B_{-45^\circ}^2(I_{-45^\circ})}$. However, since x- and y- magnetic poles share the same toroidal yoke the magnetic state of one pair may be sensitive to the state of the second one.

In fact, this leads to the "strange" magnetic anisotropy. In Fig. 4.14(a) we show

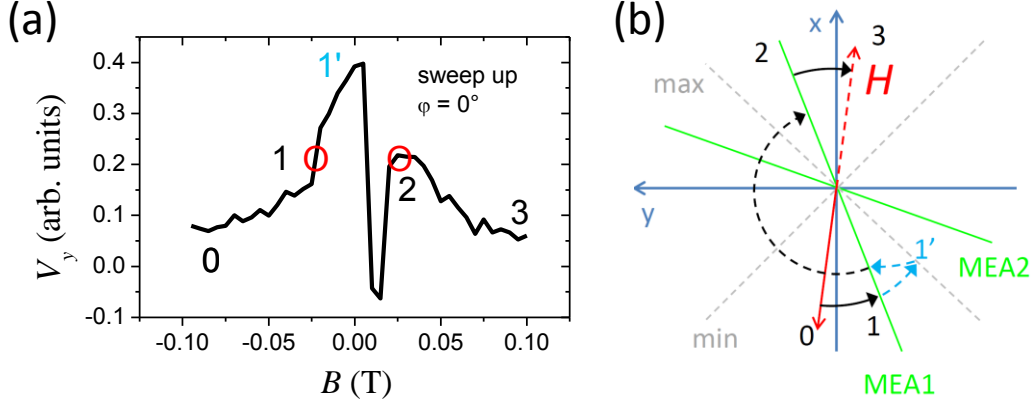


Figure 4.13: MuMax³ simulation for the sweep up curve: a) normalized voltage sweep up curve for $\varphi = 0^\circ$. The minimum of the voltage trace occurs because of the multidomain state, which tends to reduce the absolute value of \vec{M} (AMTEP/PNE signal is $\propto |\vec{M}|^2$); b) \vec{M} behavior during field sweep up for $\varphi = 0^\circ$. \vec{M} rotates in the direction "1", which corresponds to MEA1, when the field sweep goes up. Then \vec{M} switches its direction by 180° via a multidomain state (position "1" is related to $H \approx 0$ Oe) into "2". Next, when \vec{H} switches its direction and increases its value, \vec{M} tends to align with the external magnetic field (point "3").

paths of magnetic fluxes producing magnetic fields B_{+45° and B_{-45° in position of the sample. In Fig. 4.14(b) the schematic current dependence of these fields is depicted in assumption that the magnetizing current through the opposing set of magnetic poles is set to 0. In Fig. 4.14(e) a close-up in the region of the origin is presented.

Despite the fact that the magnetic easy axes are situated close to the directions $\varphi = +20, +70^\circ$, we assume that the remanent magnetization in $\varphi = -45^\circ$ direction is stronger than for $\varphi = +45^\circ$. Thus, the magnitude of $B_{+45^\circ}(I_i = 0)$ is larger than for $B_{-45^\circ}(I_i = 0)$.

To qualitatively explain magnetic behavior of the system, we choose 3 orientations of the resulting magnetic field B , $\varphi = 0, 20, 40^\circ$. In Fig. 4.14(e) we normalize the corresponding I_i abscissa values for each magnetic pair by the maximal sweep current $I_{i-\max(\varphi)}$. Making this we ensure that each abscissa point simultaneously represents the momentary produced magnetic fluxes of each pair of the poles.

For $\varphi = 0^\circ$, the $B_i(I_i)$ traces for both pairs of poles are parallel, but the remanent magnetizations $B_i(I_i = 0)$ and coercive current values I_{c-i} (points "1" and "2" in Fig. 4.14(e)) differ for different pairs. This leads to the following behavior of the magnetization vector \vec{M} of the sample: for large negative I_i values the ratio of $|B_i/B_j|$ is very close to 1 (point "0") and \vec{M} is oriented in the direction $\varphi = 180^\circ$. When the sweep reaches position "1", $B_{+45^\circ} = 0$ and \vec{M} orients in the direction $\varphi = 135^\circ$. Next, when the sweep reaches position "2" $B_{-45^\circ} = 0$ and \vec{M} orients in the direction $\varphi = 45^\circ$. Then, as the amplitudes of both B_i components increase, \vec{M} rotates towards $\varphi = 0^\circ$. In this way we obtain already discussed asymmetric voltage trace in Fig. 4.14(c) for $\varphi = 0^\circ$.

For $\varphi = 40^\circ$ the field component B_{+45° is very large in comparison to simultaneously applied B_{-45° . The B_{-45° trace is effectively "stretched" (by mentioned

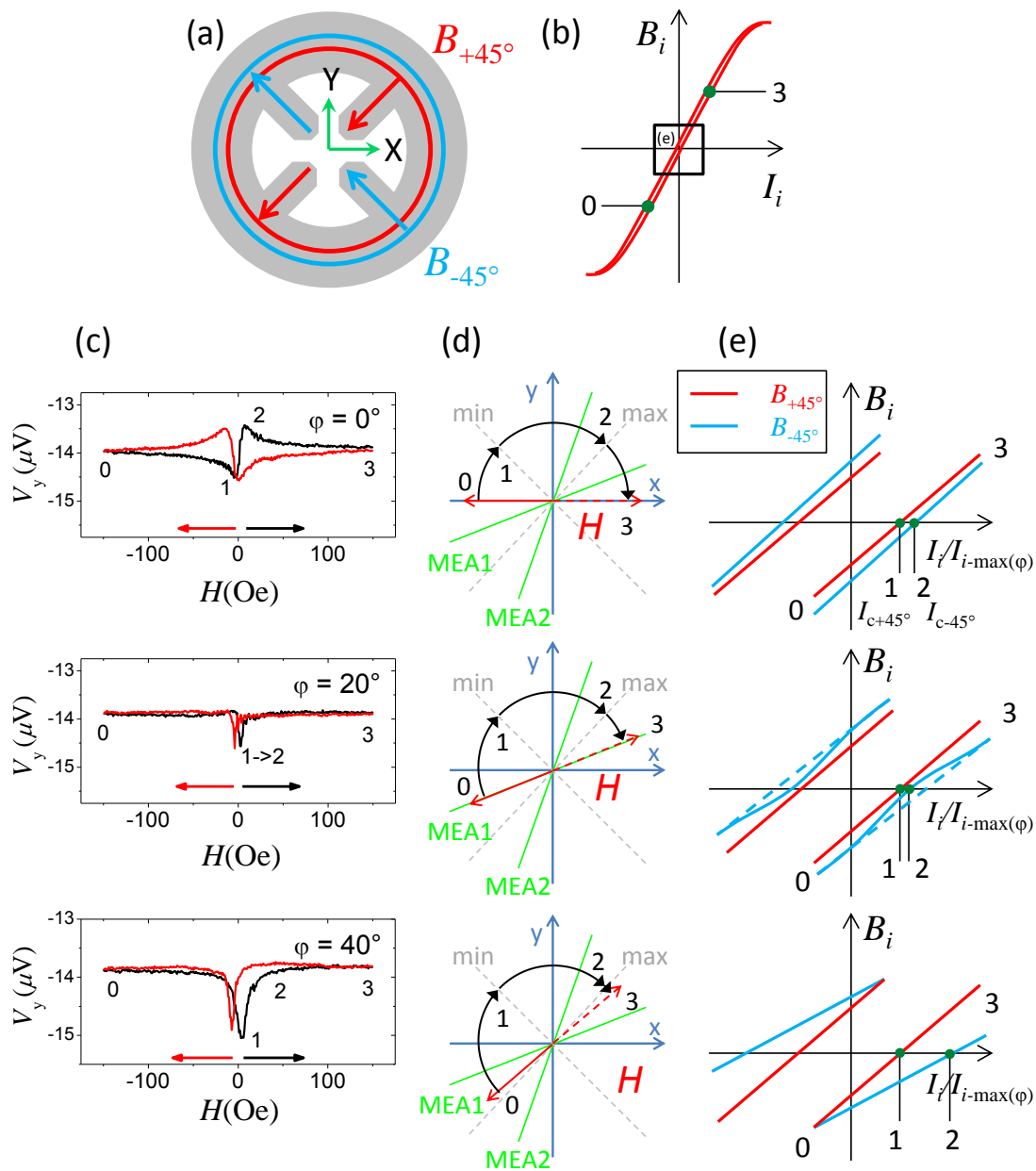


Figure 4.14: To the explanation of the observed magnetic anisotropy. (a) Magnetic fluxes in the yoke of the set-up. (b) Hysteresis loops of each pair of magnetic poles. (c) Experimental $V_y(H)$ voltage traces for different angles φ of applied magnetic field. Note, that here we interchangeably use H and B for magnetic field, because for air those are linearly connected via $B = \mu_0 H$. (d) Rotation of the magnetization vector \vec{M} during field sweep. (e) Magnetic fields B_i of pairs of the electromagnet induced by corresponding coil currents I_i , enlarged region from (b). Points "1" and "2" are related to the current values I_{c+45° and I_{c-45° , which correspond to the coercive fields of magnetic poles.

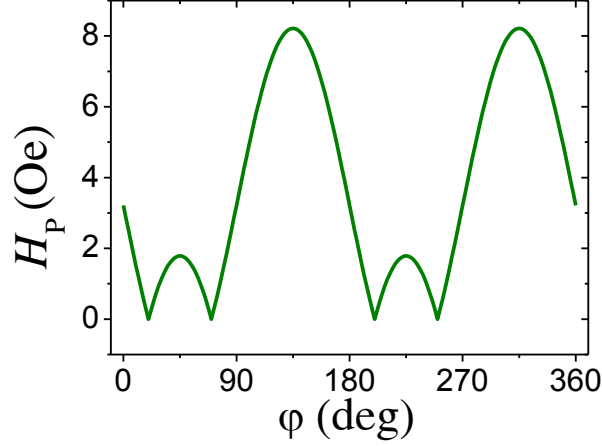


Figure 4.15: $|H_p(\varphi)|$ according to Eq.(4.8): $H_{p\max} = 7.5$ Oe, $\varphi_{\min1} = 20^\circ$, $\varphi_{\min2} = 70^\circ$. The angular dependence resembles that from Fig. 4.12.

I_i normalization), shifting the position of point "2" (coercive current I_{c-45°). This makes the evolution from min to max voltage values (directions "1" and "2", respectively) relatively slow.

For $\varphi = 20^\circ$ field sweep we get another mechanism counteracting the mentioned "stretching". The flux in the yoke induced by B_{+45° facilitates the orientation of magnetic domains in the low-current region, effectively reducing I_{c-45° (coercive field of the "-45" pair of poles is reduced due to the crosstalk of the yoke). This brings points "1" and "2" close together, leading to a faster evolution from min to max voltage V_y in Fig. 4.14(c),

Taking into account the above considerations, the effective parasitic magnetic field (produced by the crosstalk in the electromagnet) can be written as

$$|H_p(\varphi)| = |H_{p\max}| |\sin(\varphi - \varphi_{\min1}) \sin(\varphi - \varphi_{\min2})|, \quad (4.8)$$

with $H_{p\max}=7.5$ Oe as the modulus of parasitic field, $\varphi_{\min1} = 20^\circ$ and $\varphi_{\min2} = 70^\circ$. $H_p(\varphi)$ is oriented along

$$\varphi_p(H, \varphi) = \varphi \pm 180^\circ \left(\frac{H_{\max} + H}{2H_{\max}} \right), \quad (4.9)$$

where H_{\max} is the maximal amplitude of the produced magnetic field during the sweep (-150 Oe \rightarrow 150 Oe). $|H_p(\varphi)|$ (see also simulated trace in Fig. 4.15) takes into account the anisotropic character of the magnet system (amplitude of anisotropy). Its angular dependence behaves very similar to the energy angular dependence of **model A** shown in Fig.4.12. The angular dependence $\varphi_p(H)$ describes a forced rotation of \vec{M} due to the inequality of the hysteretic loops for different pairs of the magnetic poles. The sign of the phase shift (+ or -) is chosen so that \vec{M} rotates in the direction of the closest minimum of the AMTEP signal +135/-45 deg. (Fig.4.11(b)).

The subsequent calculation for each sweep measurement at a specific angle φ includes the following steps:

1. The parameters $H_{p\max}$, φ_T , φ , $\varphi_{\min1}$, $\varphi_{\min2}$ are kept fixed. First, $|H_p(\varphi)|$ is calculated. For each value of the sweep field H , $\varphi_p(H)$ is determined;

2. In Eq. (4.1) H is substituted with $H_\Sigma(H)$ and φ with $\varphi_\Sigma(H)$, where H_Σ is the magnitude of the superimposed magnetic fields H and H_p and φ_Σ is its superimposed angle. $K_c = 5 \cdot 10^4$ erg/cm³, $K_u = 0$ erg/cm³, $\varphi_{CA} = 0^\circ$ are used. In order to find $\varphi_{M0}(H)$ the derivative of Eq. (4.1) is taken and its root is determined. This procedure is done for each value of H . After this step the $\varphi_{M0}(H)$ dependence is known.
3. After inserting the computed dependence $\varphi_{M0}(H)$ into Eq.(4.6) the normalized curve $V_y(\varphi_\Sigma(H))$ (with $dS_- |\nabla T| = 1$) can be constructed and compared with the experimentally determined data.

Calculated traces are presented in Fig. 4.16 and 4.17. The simulated voltage signals for $\varphi = 20^\circ, 70^\circ$ in Fig. 4.16(b,d) coincide, whereas in the experiment corresponding traces do not. Furthermore, the simulated traces show no shift between the sweep-up and sweep-down traces for this angles. All simulated sweep-up and sweep-down traces in Fig. 4.17 appear to be mirror reflections of each other with respect to the $H = 0$ point. The experimental curves in Fig. 4.17 (b-e) in the same time have significant disturbances, which are explainable due to the stochastic drift of the nanovoltmeter signal. Drifts of 300 nV are usual for nanovoltmeters.

All in all, the simulations fit the experimental data decently, despite the use of a relatively simple *ad hoc* model.

Methods to suppress the electromagnet's self-interference artifact

There are at least 2 ways to avoid the described magnetic artifact:

1. Use two separated electromagnets with no common yoke. This will sufficiently suppress the crosstalk between magnetic poles.
2. Use other calibration technique for the magnetic poles. The magnetic fields produced by each pair of poles have to be measured during the experiments, then compared to the required values, corrected, then again compared and so on in an iterative manner till a permissible precision is reached. This adds a complexity to the electromagnet's control and somewhat enhances the experiment time.

Conclusion on the Py/MgO sample

The oddness of the observed V_y signals is qualitatively well explained by the AMTEP behavior in Py influenced by the cross-talk effect in the electromagnet.

At some circumstances this oddness in the AMTEP signal can lead to false extraction of apparent TSSE signal. However, detailed measurements with rotated \vec{H} leave no space for such misinterpretation.

4.4 Conclusion on the spin Seebeck effect

At the present time, most research groups consider the absence of the TSSE effect or at least that the signal is beyond measuring capabilities of their equipment. TSSE measurements show a bad reproducibility and a strong dependence on certain properties of the set-up. Finally, experimental results that were declared as

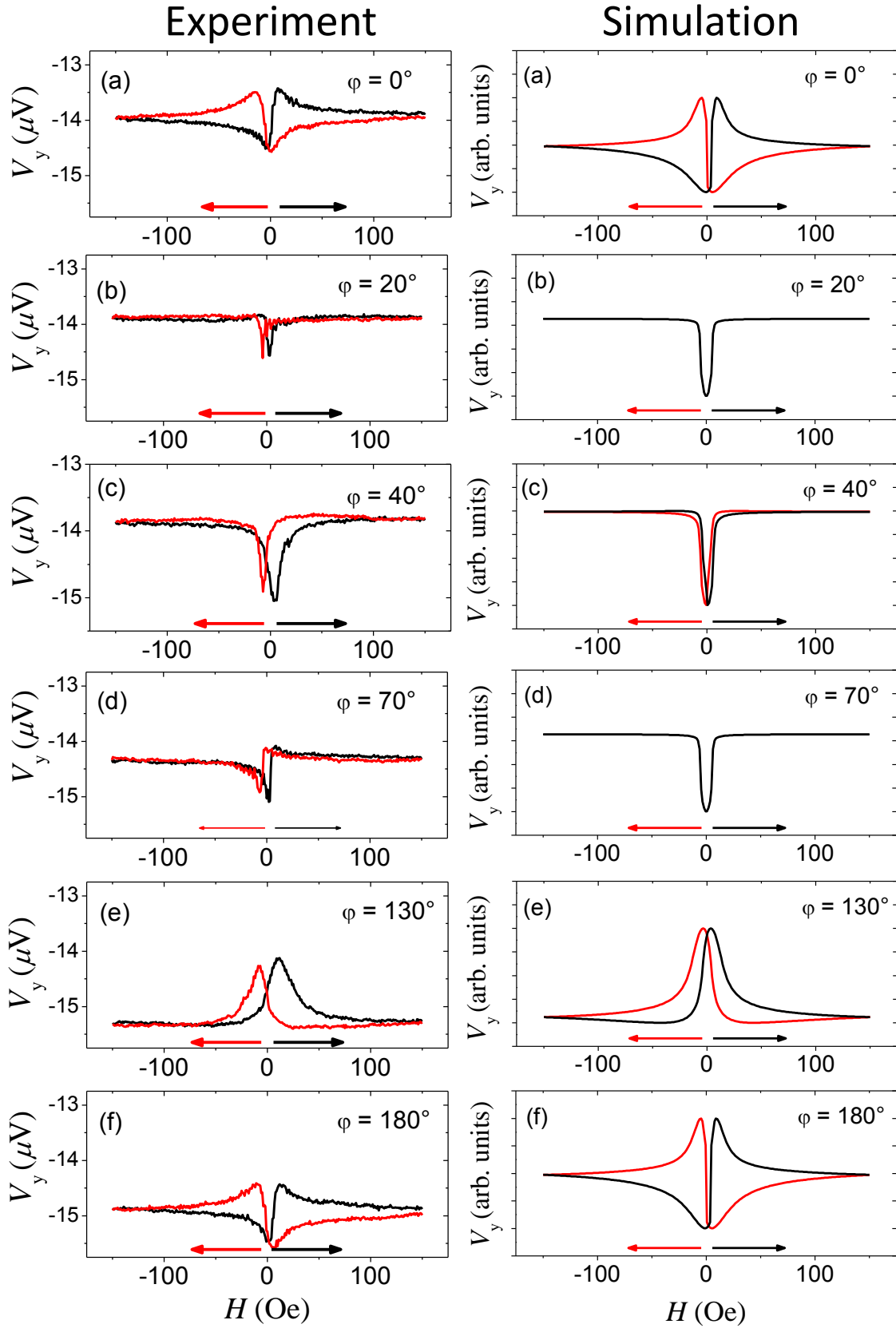


Figure 4.16: Simulations based on the **model C** for different angles φ in comparison to the experimental data from Fig. 4.9. Simulations fit well the experimental data for different angles of the external magnetic field φ .

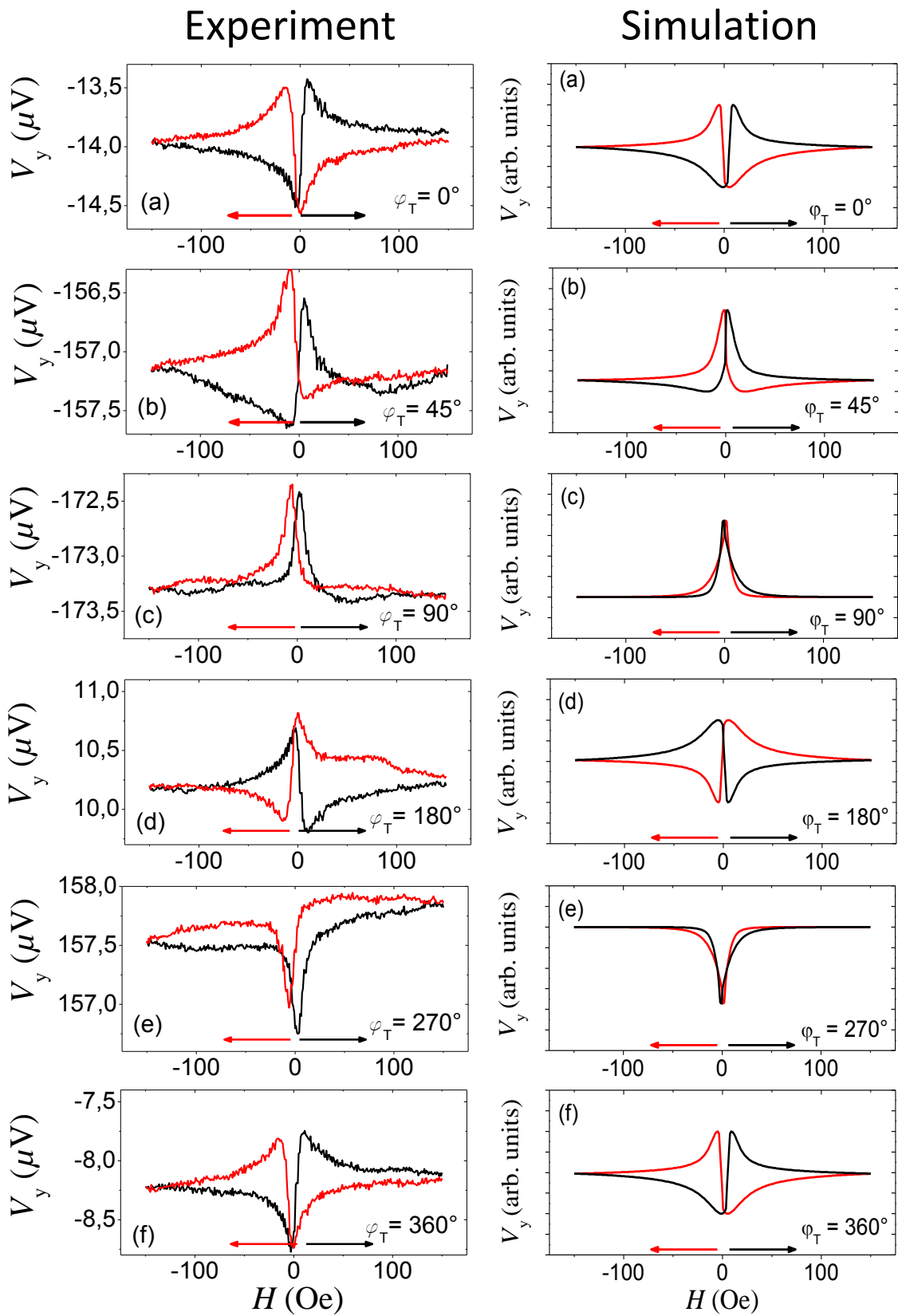


Figure 4.17: Simulations based on the **model C** for different angles φ_T in comparison to the experimental data from Fig. 4.10.

the manifestation of the TSSE can be mostly explained as a number of spurious effects gathered by Meier et al. [96] in Tables in Fig.2.12. Those effects are predominantly evoked by the combination of the unintended out-of-plane temperature gradient in the set-up with one of the conventional Nernst effects. We contribute to the list of spurious effects with the phenomena evoked by the interference on the magnetic side of the set-up: an external weak static magnetic field that leads to distortion in AMTEP, which accompanies TSSE measurements in conductive FM; a self-interference in the electromagnet of the set-up that also leads to a distortion of the AMTEP signals.

Though the TSSE-crusade failed trying to find the TSSE, it attracted a great attention to the field of spin Caloritronics. Different effects were investigated, including the LSSE that appears as a sturdy phenomenon. Conclusively, the spin Seebeck effect does exist, yet not in the initial form but in the LSSE.

Chapter 5

SNE measurements

At the moment, there is a very few information regarding the SNE in certain materials, the most of works are theoretical. $\text{Cu}_x\text{Me}_{1-x}$ systems, where Me is some metal, were simulated [136, 150] with the help of different formalisms. Specifically, the $\text{Cu}_{0.99}\text{Au}_{0.01}$ system shows fairly large SNC values.

Meanwhile, Pt is a standard material for SHE measurements and there is an assumption¹ that a small amount of Mn will make the electron DOS of Pt more asymmetric, thus, enhancing the SNE magnitude.

In our experiments we exploit MOKE-measured FMR with use of the MOD technique in order to detect the SNE. The lower sensitivity level of our setup to the spin currents is about $1 \cdot 10^9$ A/m², which is expected to be generated in the $\text{Cu}_{0.99}\text{Au}_{0.01}$ alloy at a temperature gradient of $5 \cdot 10^7$ K/m. Such a high value of thermal gradient is technically challenging for a few-micrometer-large samples, because the materials might destroy due to high resultant temperatures. Another SNE detection technique based on transport measurements [99] (the authors refer to it in analogy to the SMR as the SNMTP - the spin Nernst magmeto-thermopower), shows SNE-related voltage signature already at the $5 \cdot 10^3$ K/m thermal gradients. Despite transport measurements being more sensitive to the thermal gradients, the MOD technique is a more direct method to detect spin currents, because it has a smaller number of spurious contributions to the measured signal. Thus, the MOD-measured SNE suggests less problems with interpretation of the measurements.

Summarizing, we prepared the following samples for the SNE measurements:

- the $\text{Cu}_{0.98}\text{Au}_{0.02}$ alloy as the SNE strength for it was already calculated [136, 150] and it is fairly large;
- Pt as it is a standard material for SHE measurements and its usefulness for the SNE experiments has to be checked;
- the $\text{Pt}_{0.98}\text{Mn}_{0.02}$ alloy due to the Mn specific band structure in the vicinity of the Fermi level, which might enhance the SNE.

In this chapter we follow a certain path. First we provide simulations of heat and stray magnetic fields produced in two different arrangements of samples. Then

¹Author is sincerely grateful to Nguyen H. Long and Yuriy Mokrousov from Peter Grünberg Institut and Institute for Advanced Simulation, Forschungszentrum Jülich for a fruitful discussion of theoretical aspects of the SNE and suggestions for the experimental sample compositions

we present the temperature dependencies of the magnetization for different samples, which we use for the estimation of temperatures from FMR data. The experimental temperature profiles are compared to the simulated ones. Next, we conduct SHE measurements in order to verify the quality of FM/NM interfaces and prove the detectability of spin currents in different samples. And finally, we conduct SNE measurements and complete this chapter with a conclusion and an outlook.

5.1 Simulation of temperature distribution over the sample in view of different geometries

In this chapter we perform finite elements method (FEM) simulations of the temperature distribution over the sample surface using COMSOL Multiphysics [67]. In the following, we compare simulations and experimental data. We model the membrane part of the device and 5- μm -surroundings of the membrane, see Fig.5.1(b) for the SNE geometry 1 and Fig.5.3(b) for the SNE geometry 2. For the detailed layer structure of samples we refer to Ch. 3.3.4.

In general, metal layers thicker than tens of nm have electrical and thermal conductivity lying very close to the bulk conductivity, whereas insulators have significant deviation from the bulk values even for thicknesses above 100 nm. This fact is based on the following physical properties of materials: 1) the thermal conductivity of metals consists of a phonon and an electron contribution with domination of the electron mechanism at RT (Wiedemann-Franz law, [77]), whereas for insulators only the phonon mechanism [77] matters; 2) the electron mean free path (MFP) is usually shorter than the phonon mean free path (the electron MFP lies in a range of 1-10 nm [51] and the phonon MFP is of order 100 nm at RT [18]). Therefore, the thermal conductivity of thin film insulators is affected at significantly larger thicknesses than for metals.

The MFP is defined via the time between scattering events. Scattering mechanisms include incoherent (surface roughness, impurities, defects of crystal structure) and coherent (destructive interference) effects. As scattering phenomena include a huge variety of possible mechanisms, resistivity values can be extremely sample-dependent, which implies that conductivity values from literature are to be used circumspectively.

In the current simulations we use thermal and electrical conductivity values smaller than for bulk for all materials except for Au, because the Au layer thicknesses for our samples are larger or comparable with the MFP of electron [51]. The resistivities of the Pt, Cu and Py layers are set a few times higher than their bulk values, see Table 5.3, in further chapters on the SHE angle. The thermal conductivity for alumina and silicon nitride are reduced three times as compared to the bulk values.

We expect the safe limit of the applicable temperatures for the investigated NM/FM stacks to be below 450-500 K, because at higher temperatures the interdiffusion phenomena significantly changes the properties of the stack. For more details about interdiffusion processes in FM/NM stacks see Appendix A.1. Additionally, one should differentiate the homogeneous heating of NM/FM stack (provided by an external heat source) from the Joule heating produced by the electric current passing through the NM/FM. In the former case one has only a diffusive regime of

chemical mixing, while for the latter a drift phenomenon additionally occurs, leading to an electromigration effect which appears at current densities j of the order of $10^{11} - 10^{12}$ A/m² [84, 11, 63]. Thus, the upper safe limit of applicable temperatures will be even lower than the 450 K-level mentioned above.

In the next two subchapters we simulate and compare thermal capabilities of two different geometries for the SNE experiments. These results are followed by another subchapter where we analyze an influence of current-induced magnetic fields and laser beam heating on the SNE experiments.

Geometry 1, Pt_{0.98}Mn_{0.02}(10)/Py(5) and Pt(10)/Py(5) samples

A detailed description of the geometry 1 layer structure can be found in Ch. 3.3.4.

The COMSOL simulation in Fig. 5.1(c) shows the maximal temperature distribution close to the gold contact ($x = -6.5$ μm for Pt_{0.98}Mn_{0.02}(10)/Py(5)²) of the NM/FM structure, which occurs due to the significant cooling effect of the thick gold contacts. The highest temperature gradient, in turn, is observed closer to the edge of the membrane (1/6 length of the suspended NM/FM stack part).

One can evaluate the temperature enhancement, produced by the heater in the following way: from a thermodynamical point of view, $\Delta T = \beta P$, where P is the Joule heat produced by the heater and β is some linear coefficient of dimension $\frac{\text{Ks}}{\text{J}}$ related to the heat-capacitance; from the electrodynamic point of view, the Joule heat is $P = RI^2$, where I is the electric current. Combining both views, one gets:

$$\Delta T = \beta RI^2. \quad (5.1)$$

The quadratic dependence of ΔT on current is very often considered during the analysis of SHE experimental data. However, the resistance R of an electric device also depends on the temperature, and the applicability of the quadratic fit for the SNE experiments need to be prove. We model resistance with a linear dependence on the temperature difference:

$$R(\Delta T) = R_0(1 + \alpha_R \Delta T), \quad (5.2)$$

where ΔT is the deviation from the base temperature of the substrate (RT), R_0 is the resistance of the heater at RT, α_R is the linear temperature coefficient of the resistivity (TCR). Inserting Eq. (5.2) in Eq. (5.1), we get the following iterative dependance

$$\Delta T_{n+1} = \beta R_0(1 + \alpha_R \Delta T_n)I^2, \quad (5.3)$$

which leads to an exponential solution:

$$R(I) = R_0 + \gamma \exp(vI), \quad (5.4)$$

where γ and v are constants depending on α_R and R_0 .

The simulated current dependencies of the heater resistance R , the maximal temperature T_{max} over the NM/FM bilayer and the maximal temperature gradients ∇T_{max} , all for the sample geometry 1 are presented in Fig. 5.2. In Fig. 5.2(a) we fit

²the Pt(10)/Py(5) sample has comparable results with the only difference that the suspended (means heated) part of the FM/NM stack is 13 μm long, instead of 6.5 μm for the Pt_{0.98}Mn_{0.02}(5)/Py(10) sample.

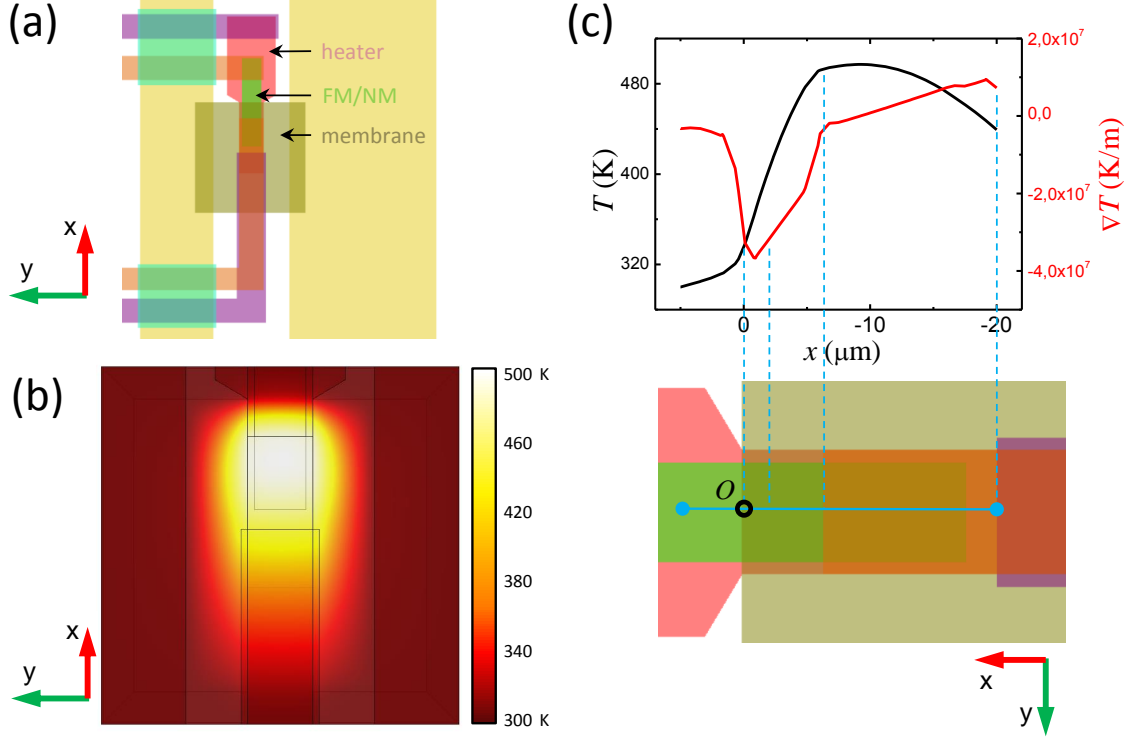


Figure 5.1: COMSOL simulation for geometry 1 of the SNE device for the $\text{Pt}_{0.98}\text{Mn}_{0.02}(10)/\text{Py}(5)$ sample. (a) Top view of the geometry 1 (for details of the layer structure see Ch. 3.3.4) and corresponding (b) COMSOL simulation for a-spatial temperature T distribution at the heater current $I_{\text{heater}} = 14$ mA. (c) Temperature T and temperature gradient ∇T distribution along the middle line of the FM/NM stack (light blue). The origin point O is placed on the membrane edge. The maximal temperature gradient ∇T is situated at $\approx 1 \mu\text{m}$ from the edge of the membrane.

the simulated resistance trace R with an exponential function (5.4), the resulting coefficient of determination is $R^2 = 0.99992$. Next, we analyze the highest reached temperature $T_{\text{max}} = 300 \text{ K} + \Delta T$ and the highest temperature gradient ∇T_{max} against the applied heater current I_{heater} in Fig. 5.2(b). We fit these dependencies with the quadratic function $y = uI^2 + y_{\text{offset}}$ (which is conventionally used in SHE measurements) and with combined expo-quadratic function $y = w \exp(v\Delta I)I^2 + y_{\text{offset}}$, where $u, w, v, y_{\text{offset}}$ are some fit parameters. For fits of T_{max} we set $y_{\text{offset}} = 300 \text{ K}$ (RT in simulations) and for ∇T_{max} $y_{\text{offset}} = 0$. One can see that the following function (hereinafter "expo-quadratic") fits the COMSOL simulation better than the quadratic function alone. Discrepancy between quadratic and expo-quadratic function becomes significant at high values of ΔT , but still for the geometry 1 the quadratic fit is a good assumption.

Geometry 2, $\text{Py}(10)/\text{Cu}_{0.98}\text{Au}_{0.02}(5)$ sample

In Fig. 5.3(c), no maximum feature in the temperature gradient ∇T distribution is observed over the FM/NM stack for geometry 2. In fact, ∇T is very homogeneous over the FM/NM stack in comparison to geometry 1 in Fig. 5.1(c). Also, one can see a drastic temperature change over a narrow gap (thermally low conductive layers

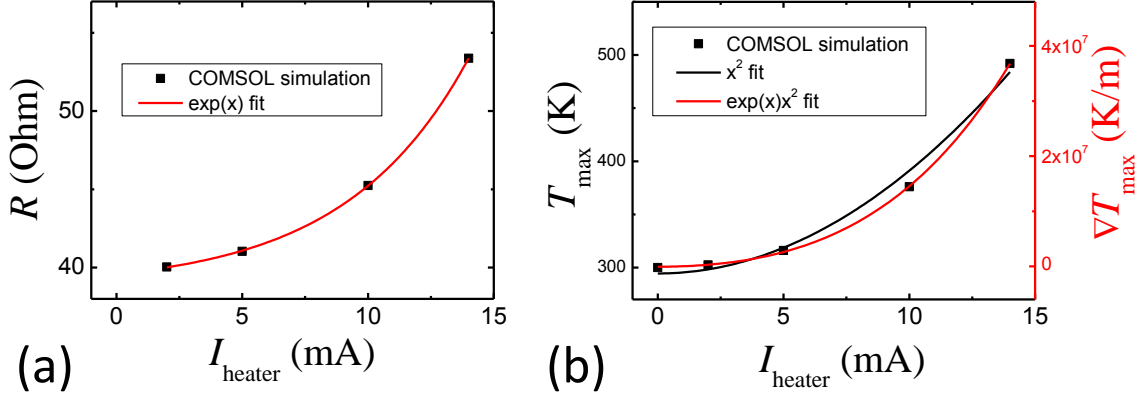


Figure 5.2: COMSOL simulation for the geometry 1 of SNE devices, $\text{Pt}_{0.98}\text{Mn}_{0.02}(10)/\text{Py}(5)$ and $\text{Pt}(10)/\text{Py}(5)$ samples. (a) Resistance R of the heater against the applied current I_{heater} (black dots) and its fit with an exponential function (red line). (b) Maximal reached temperatures T_{max} (black dots) and temperature gradient ∇T_{max} (red axis on the right) in dependence on the I_{heater} . Dependencies are fitted with the quadratic function (black line) and expo-quadratic function (red line).

of Si_3N_4 and alumina) between the heater and FM/NM structure with Au contact over it. This significantly (up to 20%) reduces the practically achievable maximal temperature gradients over the FM/NM stack.

In Fig 5.4(a) we present $R(I)$ and its fit with Eq. (5.4), similar to Fig. 5.2(a) for geometry 1. As for geometry 1, the fit is nearly perfect with $R^2 = 0.993$. In Fig 5.4(b) we simulate maximal values $T_{\text{max}}(I)$ and $\nabla T_{\text{max}}(I)$ over the FM/NM structure. Traces are fitted with the same quadratic and expo-quadratic functions as for geometry 1. The maximal reached gradient amounts to $6 \cdot 10^7$ K/m, close to the value for geometry 1. The discrepancy of the quadratic fit compared to the expo-quadratic is larger than for geometry 1 and the expo-quadratic function fits the simulation data significantly better. This fact is related to higher temperatures of the Au heater in geometry 2 and the Pt heater, leading to a higher relative change of the resistance R . The maximal temperature of the Au heater is 1.87 times higher than the maximal temperature of the FM/NM stack. For geometry 1 the maximal temperature of the Pt heater is the same as the maximal temperature of FM/NM. In fact, higher temperatures of the heater for geometry 2 might mean lower stability of the device due to electromigration. Thus, the practical maximal temperature gradients are lower than for geometry 1.

The highest temperature gradient for geometry 1 reaches $4 \cdot 10^7$ K/m, being not very far from the absolute limit for MOKE measurements at RT. Keeping in mind 450 deg C as the highest allowed temperature for the FM/NM stack, considering the optical resolution of $0.5 - 1 \mu\text{m}$ and minimizing the FM lateral size to the limit of $1 - 2 \mu\text{m}$ one cannot achieve gradients higher than $2 \cdot 10^8$ K/m. Generally, a quadratic fit $\Delta T(I^2)$ is reasonable for most of the SHE experiments, as SHE measurements are usually conducted on a well-cooled thick substrate. In the following SHE and SNE experiments we use the quadratic fit, because the moderate level of difference between quadratic and expo-quadratic fits is masked by the measurement inaccuracy.

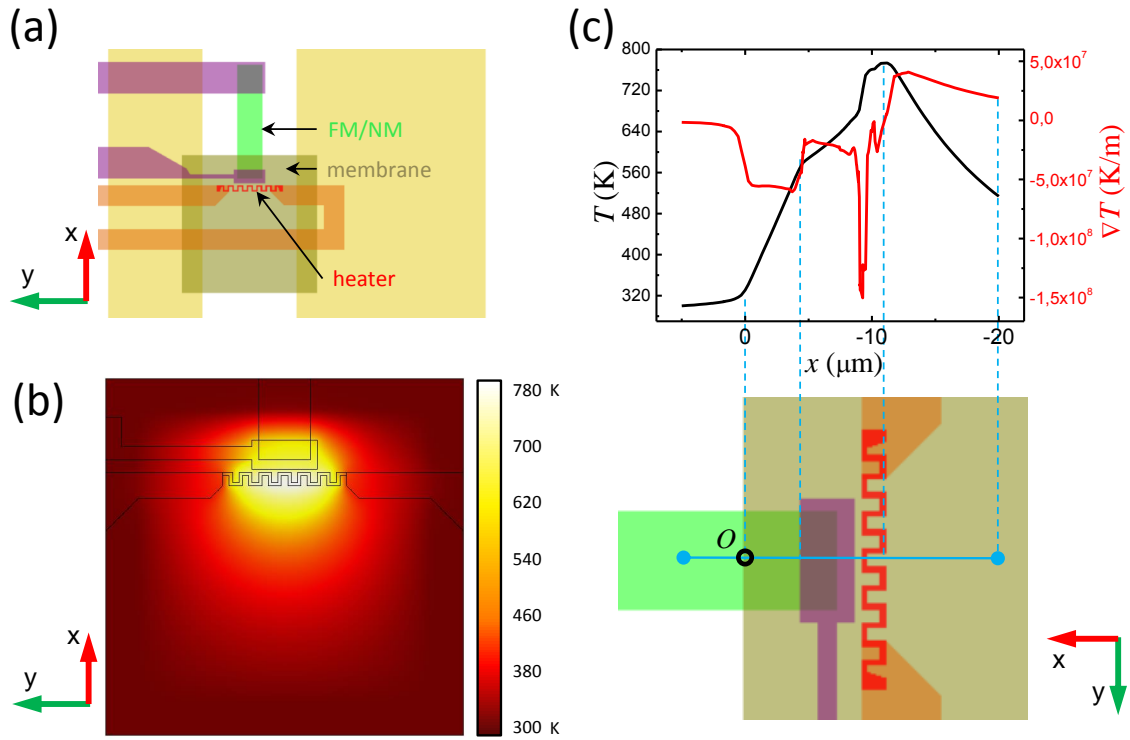


Figure 5.3: COMSOL simulation in geometry 2 of a SNE device for a $\text{Py}(10)/\text{Cu}_{0.98}\text{Au}_{0.02}(5)$ sample; heater current $I_{\text{heater}} = 9 \text{ mA}$. In all pictures the x-axis is directed along the FM/NM stack. (a) Top view of geometry 2 (for details of the layer structure see Ch. 3.3.4) and (b) COMSOL simulation of the spatial temperature T distribution. (c) Temperature T and temperature gradient ∇T distribution along the middle line of the FM/NM stack (light blue). The origin point O is placed at the membrane edge.

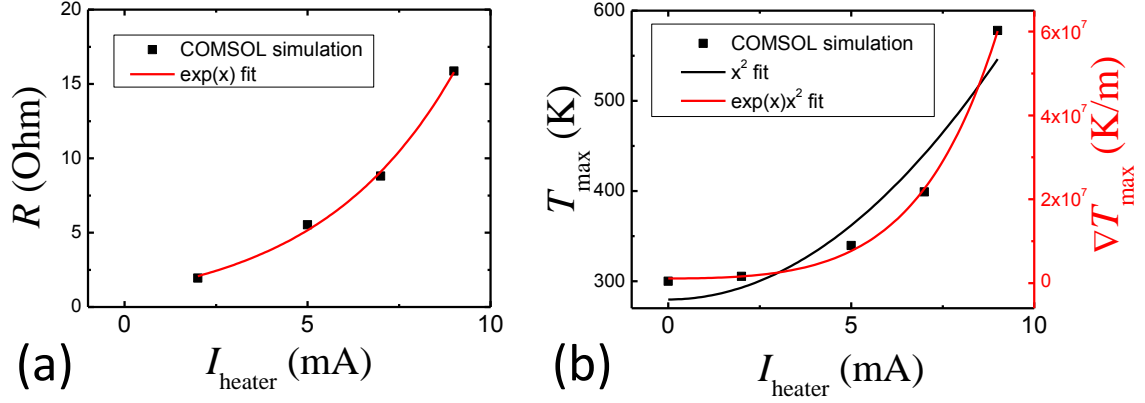


Figure 5.4: COMSOL simulations of geometry 2 of SNE devices for a Py(10)/Cu_{0.98}Au_{0.02}(5) sample. (a) Resistance R of the heater element against the applied current I_{heater} (black dots) and its fit with exponential function (red line). (b) Maximal reached temperatures T_{max} (black dots) and temperature gradient ∇T_{max} (red axis on the right) vs. I_{heater} . Dependencies are fitted with a quadratic function (black line) and expo-quadratic function (red line).

Current through heater

Geometry	H_x^{Oe}/I , Oe/mA	H_y^{Oe}/I , Oe/mA	H_z^{Oe}/I , Oe/mA
1	0, for the whole FM	0.62, for $y = 0 \mu\text{m}$	0, for $y = 0 \mu\text{m}$
2	0.0008, $x = \text{SNE spot}$	0, for the whole FM	0.144, $x = \text{SNE spot}$

Current through NM of FM/NM stack

Geometry	H_x^{Oe}/I , Oe/mA	H_y^{Oe}/I , Oe/mA	H_z^{Oe}/I , Oe/mA
1&2	0, for the whole FM	0.79, for $y = 0 \mu\text{m}$	0, for $y = 0 \mu\text{m}$

Table 5.1: Stray magnetic field values divided by current values at the points of interest for SHE and SNE measurements, as extracted from COMSOL simulations. The position "SNE spot" is the position where the SNE measurements are performed, see Ch. 5.4.

Additional simulations

The stray magnetic field H^{Oe} produced by a current passing through the heater or NM of FM/NM structure is simulated and evaluated. For comparison with the experimental data we divide the field values H^{Oe} by the relevant current values I . The origin point O is placed at the edge of the membrane and marked as a black circle in Figs. 5.1(c) and 5.3(c). The data for both geometries are collected in Table 5.1. These values are required for the interpretation of the experimental SHE and SNE data obtained later in the text.

The heating induced by the laser beam of the MOKE set-up is simulated. The modeled laser-heating area is a circle of $0.5 \mu\text{m}$ in diameter with homogeneous laser power distribution, $10 \mu\text{m}$ apart from the edge of the membrane. Assuming 100% absorption of $\approx 500 \mu\text{W}$ laser power we get a temperature enhancement of about 20 K. However, according to calculations made with the help of the reflectance calculator [151] the absorption coefficient for geometry 1 is 61% and for geometry 2 is 24%. Also, not all the energy is transformed into heat, but also into magnetization dynamics. Thus, we do not expect an additional temperature enhancement to exceed

Sample	$M_{\text{eff}}(T=300\text{K})$ (T)	$\mu_0 M_{\text{lin},T}$ (mT/K)
Py(10)/Cu _{0.98} Au _{0.02} (5)	0.62	-1.67 ± 0.07
Py(5)/Pt _{0.98} Mn _{0.02} (10)	0.72	-0.94 ± 0.14
Py(5)/Pt(10)	0.71	-1.16 ± 0.07

Table 5.2: Measured room-temperature magnetization $M_{\text{eff}}(T=300\text{K})$ and linear temperature coefficient of the magnetization $M_{\text{lin},T}$, SQUID data.

10 K, and this value will not qualitatively change the thermal gradient distributions obtained in previous simulations.

Summarizing, geometry 2 has a homogeneous thermal gradient over the NM/FM bilayer and a smaller stray in-plane magnetic field in comparison to geometry 1, but the maximal theoretical thermal gradient is smaller. Geometry 2 has disadvantages in terms of the maximal achievable temperature gradient caused by the small thermal conductivity of Si₃N₄ in the gap between the heater and FM/NM structure. Another issue is the somewhat large electrical loop formed by the heater and its feed line. This loop works as the inductive receiver of CPW-line energy. Starting from a certain level of the RF-generator power the switch-on process leads to excessive heating and explosion of the heater. The area of the heater loop has to be minimized in order to avoid heater explosions. The only doubtless advantages of geometry 2 are the significantly smaller number of production steps and smaller stray in-plane field. And finally, the assumption of a quadratic dependance of the temperature generated by the heater current is shown to be adequate to a certain extent in the SNE experiments.

5.2 Experimental thermal magnetization dependencies and temperature distribution at the experimental FM/NM interfaces

Here we present the magnetization M_{eff} and the linear temperature coefficient of the magnetization $M_{\text{lin},T}$ in dependence on temperature of FM measured with the SQUID technique [28], see Fig. 5.5³. With the values provided, we are able to estimate the temperature of FM from FMR data via Eq. (3.14). The temperature dependencies for Py(5)/Pt_{0.98}Mn_{0.02}(10) and Py(5)/Pt(10) are very similar, whereas the Cu_{0.98}Au_{0.02}(5) sample shows a somewhat faster decaying magnetization. We average the linear temperature coefficient of the magnetization $M_{\text{lin},T}$ for $T = 270 - 450$ K. These averaged values together with $M_{\text{eff}}(T=300\text{K})$ are presented in Table 5.2.

We choose this specific range of temperatures for averaging of the linear coefficient $M_{\text{lin},T}$ because of the interdiffusion effects that start after 450 K (for details we refer to Fig. A.5(a) in Appendix A.1). All investigated samples possess a thermal magnetization coefficient $M_{\text{lin},T}$ of about 1 mT/K. As one can see from Fig. 5.5, changes of M_{eff} in the mentioned range can be considered as linear, thus temperatures evaluated from our linear model in Ch. 3.3.5 are expected to be adequate.

³Author is grateful to Arpita Mitra (University of Leeds, W.Yorkshire, UK) who had conducted the SQUID measurements

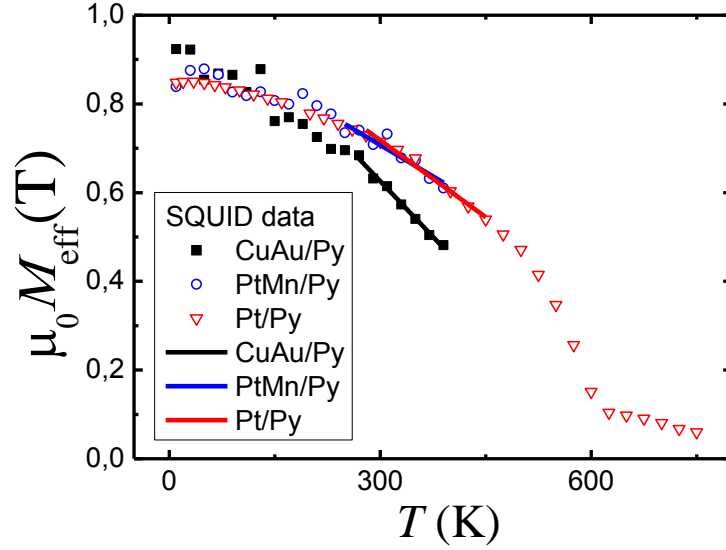


Figure 5.5: Magnetization M_{eff} temperature dependencies for different samples, SQUID data. Points represent measured values, lines are linear fits for the evaluation of the linear temperature coefficient of the magnetization $M_{\text{lin},T}$ in a temperature range of 270 – 450 K.

Experimental temperature profiles in the FM/NM stack

Here we quantify spatial temperature profiles over the FM/NM stacks. The profiles are evaluated for both cases when current passes through the heater and through the FM/NM stack. First, we have measured FMR curves in different points along the x-axis (light blue line in Fig. 5.1(c) and Fig. 5.3(c)) and extracted resonant fields H_r . FMR data was measured twice: for some non-zero value of I and for $I = 0$. Next we made the following procedure:

1. $H_{r\text{-aver}}$ is found as the average of $H_r(x)$ values for $I = 0$;
2. The difference $\Delta H_r(x) = H_r(x)(I \neq 0) - H_r(x)(I = 0)$ is calculated;
3. Modified resonant fields $H_{r\text{-mod}}(x) = H_{r\text{-aver}} + \Delta H_r(x)$ are calculated.
4. Then, using Eq. (3.14) and $M_{\text{lin},T}$ value from Table 5.2 $H_{r\text{-mod}}(x)$ is recalculated into the temperature differences $\Delta T(x)$ over FM, where $\Delta T(x) = T(x) - T_{\text{RT}}$, $T_{\text{RT}} = 300^\circ \text{K}$.

This procedure helps to reduce the influence of inhomogeneities of a FM layer on the evaluation of temperatures. Inhomogeneities in H_r ($I = 0$) up to 3% are observed. FMR data were collected at frequency of 10 GHz.

With the current I_{heater} passing through the heater we investigate both geometries. In Fig. 5.6(a) a $\Delta T(x)$ plot for the $\text{Cu}_{0.98}\text{Au}_{0.02}(5)/\text{Py}(10)$ sample (geometry 2) shows a very good quantitative match of COMSOL simulation and experimental points indicating fairness of conductivity values used in the simulation.

For the $\text{Pt}_{0.98}\text{Mn}_{0.02}(5)/\text{Py}(10)$ sample (geometry 1) the COMSOL simulation data in Fig. 5.6(b) match well the experimental points in the vicinity of the membrane edge (-2 to +3 μm region), but has a qualitative discrepancy for the points

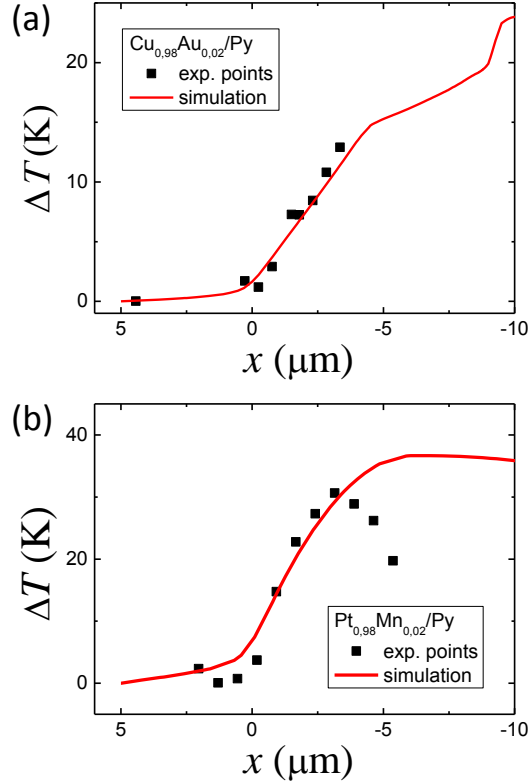


Figure 5.6: Experimental (black dots) and simulated (red lines) $\Delta T(x)$ temperature dependencies for the current I_{heater} applied to the heater structure. Temperatures are evaluated via Eq. (3.14) with use of parameters from Table 5.2, FMR data are measured at 10 GHz. (a) $\text{Cu}_{0.98}\text{Au}_{0.02}(5)/\text{Py}(10)$ sample, geometry 2. Simulated trace (red line) is similar to that in Fig. 5.3(c). Measurements are performed at current $I_{\text{heater}} = 3.24$ mA, current density $j_{\text{heater}} = 2 \cdot 10^{11}$ A/m². (b) $\text{Pt}_{0.98}\text{Mn}_{0.02}(5)/\text{Py}(10)$ sample, geometry 1. Simulated trace is similar to one from Fig. 5.1(c). $I_{\text{heater}} = 4.23$ mA, $j_{\text{heater}} = 3.5 \cdot 10^{10}$ A/m².

far from the membrane edge (-3 to -5 μm region). The experimental data show an extremum at 3 μm , while the simulation has a smooth character over the FM/NM stack. Possible reasons for that are:

- laser-beam-induced heating;
- inhomogeneities in the FM layer produced by electromigration and interdiffusion;
- not exact thermo- and electrical conductivity values in simulations.

For the Pt(10)/Py(5) sample we checked the temperature distribution $\Delta T(x)$ for the current I_{stack} sent through the FM/NM stack. Simulation and experimental data are presented in Fig. 5.7. The COMSOL trace match the experimental points qualitatively well. In the region far from the membrane edge (-6 to -13 μm) the experimental data show higher temperatures than the simulation. This might be related to the partial interdiffusion or electromigration, because M_{eff} drops due to these processes, leading to an overestimation of the temperatures derived from Eq. (3.8). The other two reasons listed above might also be responsible for the not perfect match of the simulation and the experiment.

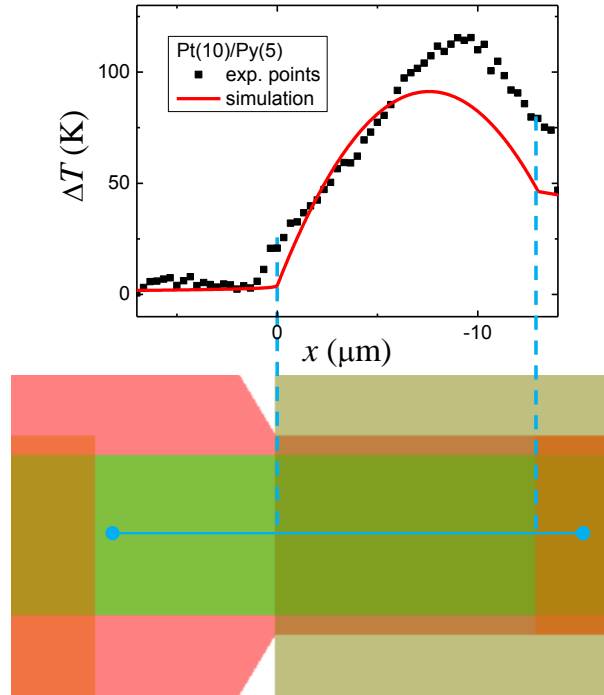


Figure 5.7: $\Delta T(x)$ dependencies for Pt(10)/Py(5) sample with current $I_{\text{stack}} = 5$ mA passing through the NM/FM stack. Current density j_{NM} passing through the NM layer amounts to $4.3 \cdot 10^{10}$ A/m. Please refer to Ch. 5.3 for the determination of the current density j_{NM} .

5.3 Check of spin-accumulation by means of the SHE

In a FM/NM stack current flows not only through the NM, but also through the FM. Depending on thicknesses and electrical conductivities of the FM and NM layers, this might lead to a significant underestimation of the spin Hall angle (SHA). From Eq.(2.42) for the model of two parallel resistances one can estimate a fraction k of I_{NM} current in the total current I_{stack} .

In the following, for binary NM alloys $\text{Pt}_{0.98}\text{Mn}_{0.02}$ and $\text{Cu}_{0.98}\text{Au}_{0.02}$ we use resistivities of the main component (Pt and Cu, respectively), as these alloys supposedly satisfy the low-dilution limit condition. In Table 5.3 we present data for the used resistivities. These resistivities deviate from bulk values 4-10 times, because the thicknesses of films are below the MFP of electron. One should carefully use the resistivity values for thin films, because those are very sensitive to condition and method of thin film production.

Material	ρ ($\mu\Omega\cdot\text{cm}$)	reference
Pt(10)	46	[115]
Py(5)	86	[29]
Py(10)	72	[29]
Cu(5)	12	[50]

Table 5.3: Resistivity data for Pt, Py and Cu thin layers

Using the values from Table 5.3 we calculate k and present the resulting values in Table 5.4. The calculated k values give 21 – 26% reduction of the estimation of the current I_{NM} . A correct evaluation of the k coefficients is necessary for precise estimation of the actual SHA values.

Sample	k
Py(5)/ $\text{Pt}_{0.98}\text{Mn}_{0.02}$ (10) and Py(5)/Pt(10)	0.79
Py(10)/ $\text{Cu}_{0.98}\text{Au}_{0.02}$ (5)	0.74

Table 5.4: Calculated k values for used FM/NM stacks

For all samples we have experimentally evaluated the SHE on the part of the FM/NM stack outside of the membrane. This part of the stack in the following is referred to as the "cold side", and the membrane part as the "hot side". For the $\text{Pt}_{0.98}\text{Mn}_{0.02}$ (5)/Py(10) sample we have additionally measured the SHE on the hot side. For geometry 1 ($\text{Pt}_{0.98}\text{Mn}_{0.02}$ (5)/Py(10) and Pt(5)/Py(10) samples) the hot side measurement point is situated at 1/6 distance of suspended length of FM ($\approx 1 \mu\text{m}$), where the highest temperature gradient is expected according to the COMSOL simulations.

In the following, to the magnetic field \vec{H} oriented in the positive direction of y-axis we refer as to "+ \mathbf{H} " state and oriented in negative direction as to "- \mathbf{H} "

Py(10)/ $\text{Cu}_{0.98}\text{Au}_{0.02}$ (5) sample (geometry 2)

For the $\text{Cu}_{0.98}\text{Au}_{0.02}$ (5)/Py(10) sample the experimental data measured at the cold side is shown in Fig. 5.8. Data sets for H_r and ΔH are fitted with linear functions

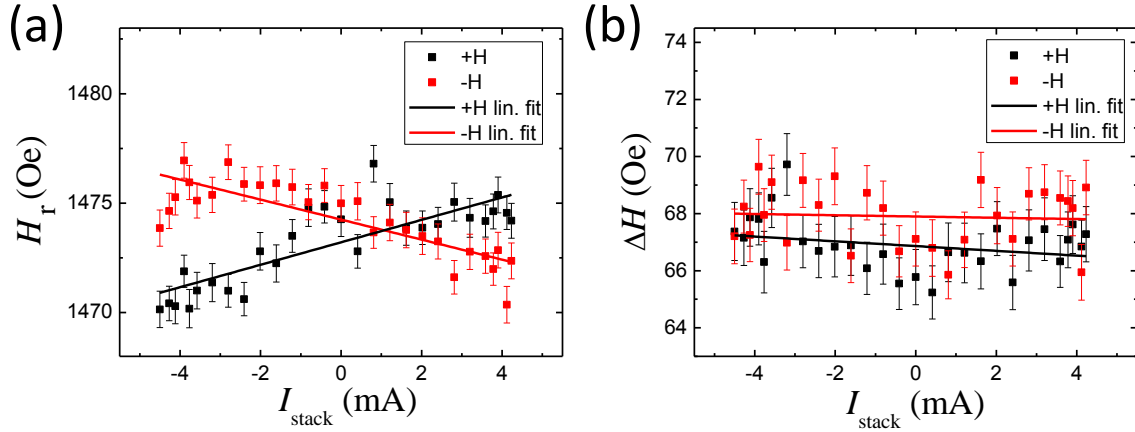


Figure 5.8: SHE data for $\text{Cu}_{0.98}\text{Au}_{0.02}(5)/\text{Py}(10)$ stack (geometry 2) at maximal applied current density of $4.4 \cdot 10^{10} \text{ A/m}^2$. Measurements are performed on the cold side of the NM/FM stack. (a) Resonant field H_r . (b) The FMR linewidth ΔH . All data sets are fitted with linear function and the fit parameters are gathered in Table 5.5.

$y = A + Bx$, and the extracted parameters A and B are presented in Table 5.5. For the resonant field H_r the intersection point of the $+\mathbf{H}$ and the $-\mathbf{H}$ traces is shifted to the right. Difference in y-intercept values A for H_r set is $1 \pm 0.3 \text{ Oe}$, which is outside the 3σ criterion. This difference can not be explained by the stray field induced by current passing through the NM layer. A possible explanation is a impedance change in the RF-line due to the reverse magnetization of its parts exposed to the magnetic field of the electromagnet. The slope B of H_r , in turn, is related to the stray magnetic field induced by the current I_{NM} flowing in the NM. The change of sign of the slope B when switching from the $+\mathbf{H}$ to the $-\mathbf{H}$ direction is, clearly, due to the change of field direction with respect to the I_{NM} . Taking into account the k factor, COMSOL simulations (the H_y^{Oe}/I value from Table 5.1) predict a value of $0.79 \text{ Oe/mA} - 0.74 = 0.58 \text{ Oe/mA}$, which is very close to the average experimental B $0.49 \pm 0.05 \text{ Oe/mA}$. The mismatch is explainable by incorrect resistance values for Cu used in the COMSOL simulation, while its MFP is 39.9 nm [51] meaning extreme resistivity sensitivity to the thickness in the range of 5 nm .

The offset level A in the ΔH data shows some discrepancy between $+\mathbf{H}$ and $-\mathbf{H}$ data sets, which is most probably due to the change of the RF-line impedance; the difference amounts to $1 \pm 0.4 \text{ Oe}$. The slope B for ΔH is 0 within error bars, meaning no measurable SHE effect for this sample.

Measured value	Field direction	A (Oe)	B (Oe/mA)
Resonant field H_r	$-\mathbf{H}$	1474.25 ± 0.15	-0.46 ± 0.05
	$+\mathbf{H}$	1473.2 ± 0.15	0.51 ± 0.05
Linewidth ΔH	$-\mathbf{H}$	67.9 ± 0.18	-0.02 ± 0.06
	$+\mathbf{H}$	66.86 ± 0.19	-0.08 ± 0.06

Table 5.5: SHE measurements. Fit parameters for the $\text{Cu}_{0.98}\text{Au}_{0.02}(5)/\text{Py}(10)$ sample

Py(5)/Pt_{0.98}Mn_{0.02}(10) sample (geometry 1)

The Pt_{0.98}Mn_{0.02}(5)/Py(10) sample was investigated on the hot side (distance from the membrane edge $x = 1.3 \mu\text{m}$) and on the cold side ($x = -1.9 \mu\text{m}$), see Fig. 5.9. There are clear qualitative differences in the trace shapes for the resonant fields H_r and linewidth ΔH , when the measurement side is changed. For the cold side the dependencies have linear character and for the hot side an additional quadratic contribution due to enhanced temperatures (up to $+34^\circ \text{C}$) is present. Therefore, it is logical to fit the cold side data with a $y = A + Bx$ function and the hot side data with $y = A + Bx + Cx^2$ functions. The experimental fit parameters A , B , and C are listed in Table 5.6.

The linear part B of H_r originates mostly from the stray magnetic field of the current I_{NM} and the parabolic part C originates from the heating induced by the total current I_{stack} .

For H_r on the hot side the average slope B amounts to $0.95 \pm 0.10 \text{ Oe/mA}$, whereas **for H_r on the cold side** to $0.72 \pm 0.06 \text{ Oe/mA}$. The slope B is not expected to be side-dependent, since the current in NM is assumed to be the same. However: 1) some inhomogeneities in the NM layer may lead to a variation in the current distribution; 2) the FM/NM interface inhomogeneities might lead to a difference in spin-filtering of the interface, thus different field-like SOT contributions to the resonant fields; 3) resistance temperature dependence leads to deviations of Δ from quadratic dependence, as discussed in Ch. 5.1, and as result the linear component B get fit artifacts. The average B for both sides is $0.83 \pm 0.06 \text{ Oe/mA}$. The simulated value equals to $0.79 \text{ Oe/mA} \cdot 0.79 = 0.62 \text{ Oe/mA}$. The discrepancy between experiment and simulation is explainable by extra contributions of the field-like torques in Eqs. (2.39), (2.26) induced by SHE and ISGE.

The linewidth ΔH for both cold and hot side has distinctly a regular linear current dependency, which confirms the influence of the SHE on the magnetization precession. The spin Hall angle (SHA) is estimated below.

Hot side

Measured value	Field direction	A (Oe)	B (Oe/mA)	C (Oe/mA ²)
Resonant field H_r	-H	1276.4 ± 0.7	0.90 ± 0.14	1.32 ± 0.05
	+H	1277.0 ± 0.6	-0.99 ± 0.14	1.41 ± 0.05
Linewidth ΔH	-H	73.8 ± 1.4	1.1 ± 0.3	0.47 ± 0.10
	+H	78.4 ± 0.6	-1.14 ± 0.12	0.24 ± 0.04

Cold side

Measured value	Field direction	A (Oe)	B (Oe/mA)	C (Oe/mA ²)
Resonant field H_r	-H	1258.1 ± 0.3	0.76 ± 0.09	0
	+H	1258.8 ± 0.3	-0.68 ± 0.08	0
Linewidth ΔH	-H	67.8 ± 0.4	-1.10 ± 0.11	0
	+H	67.2 ± 0.6	1.04 ± 0.10	0

Table 5.6: SHE experimental data. Fit parameters for Pt_{0.98}Mn_{0.02}(10)/Py(5) sample

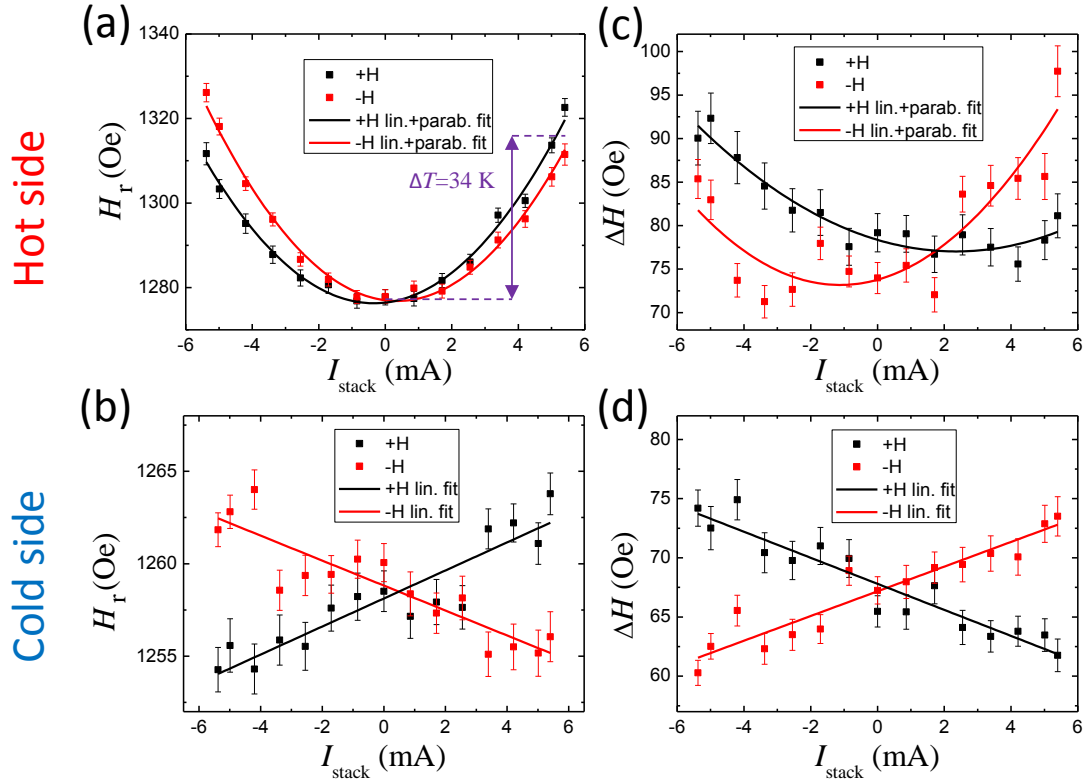


Figure 5.9: SHE data for Py(5)/Pt_{0.98}Mn_{0.02}(10) stack (geometry 1) for the hot side (membrane part) and for the cold side (bulk part) of the FM/NM stack and the maximal applied current density j_{NM} of $5.5 \cdot 10^{10}$ A/m². (a) Hot side resonant field H_r . Temperature enhancement ΔT above RT is evaluated via Eq.(3.14) with use of the experimentally defined parameters in Table 5.2. (b) Cold side resonant field H_r . (c) Hot side FMR linewidth ΔH . (d) Cold side FMR linewidth ΔH . All data sets are fitted with quadratic functions and the fit parameters are collected in Table 5.6.

Py(5)/Pt(10) sample (geometry 1)

The Py(5)/Pt(10) sample is investigated on the cold side, see Fig. 5.10. The resonant field H_r shows some parabolic behavior compared to the cold side data for the Py(5)/Pt_{0.98}Mn_{0.02}(10) sample. The reason is the two times higher maximal current density j_{NM} , which leads to a measurable temperature enhancement ($\approx 4^\circ\text{C}$). The H_r dependency is fitted with a quadratic polynomial, see Table 5.7. As for the previous sample, the linear part B in resonant field H_r originates mostly from the stray magnetic field of the current I_{NM} and the parabolic part originates from the heating induced by the total current I_{stack} .

The slope value B for H_r averaged over the $+\mathbf{H}$ and $-\mathbf{H}$ data sets amounts to 0.87 ± 0.07 Oe/mA. The simulated B value from Table 5.1 equals to $0.79 \cdot 0.79$ Oe/mA = 0.62 Oe/mA. The discrepancy between the simulation and the measurements is again explainable by extra contributions of the field-like torques induced by SHE and ISGE.

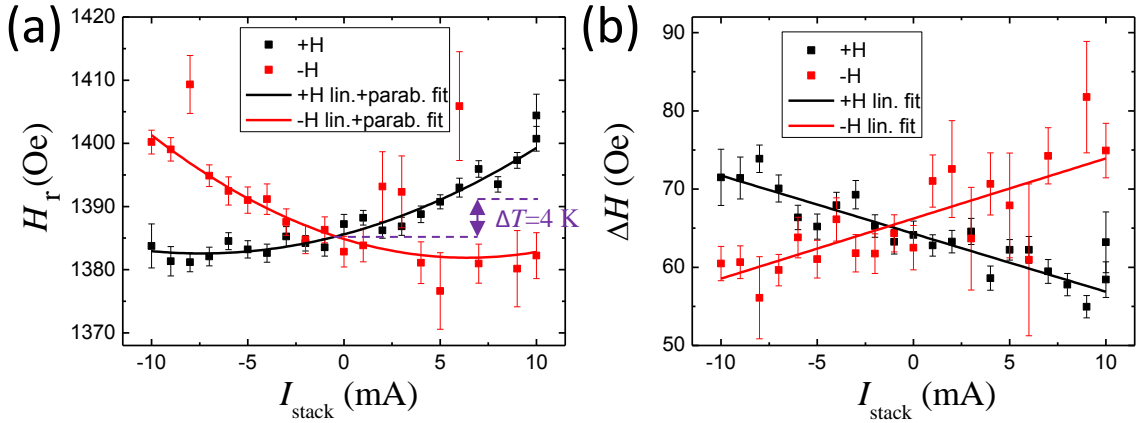


Figure 5.10: SHE data for Py(5)/Pt(10) stack (geometry 1) for the cold side of the FM/NM stack. (a) Resonant field H_r . Temperature enhancement ΔT above RT is evaluated via Eq.(3.14) with use of the experimentally defined parameters in Table 5.2. (b) FMR linewidth ΔH . All data sets are fitted with quadratic functions and the fit parameters are gathered in Table 5.6. The maximal reached current density j_{NM} amounts to $1 \cdot 10^{11}$ A/m².

The linewidth ΔH in Fig. 5.10(b) barely shows a parabolic contribution, and we fit it with a linear function. The linear coefficient B for the linewidth is confidently outside the error bars stating an influence of the SHE.

Measured value	Field direction	A (Oe)	B (Oe/mA)	C (Oe/mA ²)
Resonant field H_r	$-\mathbf{H}$	1384.9 ± 1.1	-0.92 ± 0.15	0.07 ± 0.2
	$+\mathbf{H}$	1385.6 ± 0.5	0.82 ± 0.06	0.055 ± 0.011
Linewidth ΔH	$-\mathbf{H}$	66.2 ± 0.8	0.77 ± 0.13	0
	$+\mathbf{H}$	64.3 ± 0.4	-0.74 ± 0.06	0

Table 5.7: SHE experimental data. Fit parameters for the Py(5)/Pt(10) sample

5.3.1 Evaluation of spin Hall angles

The effective SHA θ_{eff} can be found from the experimental data using:

$$\theta_{\text{eff}} = \eta_{\text{DL}} \theta_{\text{SH}} = \frac{j_s}{j_{\text{NM}}} = \frac{d_{\text{FM}} \mu_0 M_s (2H_r + M_{\text{eff}}) \gamma \Delta H_{\text{SHE}}}{\omega \hbar j_{\text{NM}}} \quad (5.5)$$

where η_{DL} is the spin injection efficiency, d_{FM} is the FM film thickness, j_{NM} is the electrical current density in the NM layer, μ_0 is the vacuum permeability, γ is the gyromagnetic ratio, \hbar is the reduced Planck constant, M_s is the saturation magnetization of FM, M_{eff} is the effective magnetization which deviates from the M_s due to out-of-plane magnetic anisotropy induced in the FM. The ratio $\Delta H_{\text{SHE}}/j_{\text{NM}}$ is in fact the linear coefficient B from the fits of linewidth ΔH (Tables 5.5, 5.6 and 5.7) multiplied with the NM cross-section area A_{NM} . Areas A_{NM} are presented in Table 5.8.

Sample	Area A_{NM} , m ²
Py(5)/Pt _{0.98} Mn _{0.02} (10) and Py(5)/Pt(10)	$8 \cdot 10^{-14}$
Py(10)/Cu _{0.98} Au _{0.02} (5)	$4 \cdot 10^{-14}$

Table 5.8: Cross-section areas of NM for SNE samples

The highest applied current densities j_{NM} for the studied membrane samples were $0.4 - 1.2 \cdot 10^{11}$, which is only a few times smaller than the highest applicable current densities for bulk substrate samples, due to interdiffusion and electromigration limit. Smaller than the maximal values are used intentionally, as the suspended parts of FM/NM stack are subjected to significantly higher temperatures due to worse cooling capability of the membrane. Thus, those are more vulnerable towards the interdiffusion and electromigration processes.

Calculated effective SHAs are listed in Table 5.9. A relatively large contribution to the error comes from uncertainty in d_{FM} thickness (5 %), which is used in calculation of the A_{NM} . The difference in the SHA values between Pt(10)/Py(5) and Pt_{0.98}Mn_{0.02}(5)/Py(10) samples exceeds 1σ error bars, meaning that 2% additive of Mn in Pt can lead to an enhancement of the SHE.

Sample	$\eta_{\text{DL}} \theta_{\text{SH}}$
Pt(10)/Py(5)	0.024 ± 0.005
Pt _{0.98} Mn _{0.02} (10)/Py(5)	0.036 ± 0.006

Table 5.9: Effective SHA values for studied samples

To find actual the SHA values θ_{SH} one needs to know the spin injection efficiency η_{DL} . For its estimation we need to know the spin diffusion length of NM. The values for the used samples are presented in Table 5.10.

Material	λ (nm)	Reference
Pt(10)	5 ± 3	averaged value from SHE review [122]
Py(5)	3	[4]

Table 5.10: Spin diffusion lengths for the studied samples

Using Eq.(2.41) and values from Tables 5.10 and 5.9 we obtain $\eta_{\text{DL}} = 0.34$. Knowing it, we finally calculate the actual SHA values θ_{SH} , see Table 5.11.

Sample	θ_{SH}
Pt(10)/Py(5)	0.089 ± 0.019
Pt _{0.98} Mn _{0.02} (10)/Py(5)	0.13 ± 0.022

Table 5.11: Actual SHA for studied samples

Conclusion on the SHE measurements

In the SHE review [122] the average SHA for Pt amounts to 0.04 ± 0.03 , whereas the maximal reported value is 0.12. A large deviation in the SHA values is related to the difference in measuring and sample production techniques. For example, the authors in [33] have shown, that the SHA values evaluated in SHE and ISHE experiments with magnetization dynamics induced by FMR are not completely the same. This is mostly due to the details (differences) of the charge current distribution. Our measurements for Pt show SHA larger than average in literature, but not larger than the maximal reported. Interestingly, the SHA for Pt_{0.98}Mn_{0.02} is 46% larger and even exceeds the maximal reported value for Pt. Based on this fact, we conclude that the Mn small additive to Pt leads to enhancement of the SHE.

We have observed signatures of the SHE in Pt_{0.98}Mn_{0.02}(5)/Py(10) and Pt(5)/Py(10) samples, while for the Py(10)/Cu_{0.98}Au_{0.02}(5) sample we see no measurable effect.

5.4 Check of SNE

According to the conducted SHE measurements, we can detect spin injection for electrical currents j_{NM} starting from $5 \cdot 10^{10}$ A/m² for the Pt(10)/Py(5) sample and $2.5 \cdot 10^{10}$ A/m² for the Pt_{0.98}Mn_{0.02}(10)/Py(5) one. Using the effective SHA values from Table 5.9, those electrical current values translate to spin current densities j_s of $1, 2 \cdot 10^9$ A/m² and $0, 9 \cdot 10^9$ A/m², respectively. This gives us the lowest sensitivity limit in SNE measurements for the mentioned samples.

The Cu_{0.98}Au_{0.02}(5)/Py(10) sample does not show any SHE, but we expect its sensitivity threshold to be about $2 \cdot 10^9$ A/m² (according to the theoretical model in [150]), which is somewhat higher than for Pt-based samples.

Cu_{0.98}Au_{0.02}(5)/Py(10) sample (geometry 2)

The experimental data sets are presented in Fig. 5.11 and the corresponding fit parameters are presented in Table 5.12.

The extracted slope B of the resonant field H_r for the SNE configurations shows a negative value for the field direction $-\mathbf{H}$ and a positive value for the field direction $+\mathbf{H}$. However, both values are in the range of 1σ error bars and are actually expected to be equal to zero for sample geometry 2, because the heater produces only an insignificant out-of-plane bias field, see H_z^{Oe}/I value in Table 5.1.

No difference within the error bars is observed in the parabolic coefficient C of ΔH between the $+\mathbf{H}$ and $-\mathbf{H}$ measurements. The dependence of ΔH on the applied

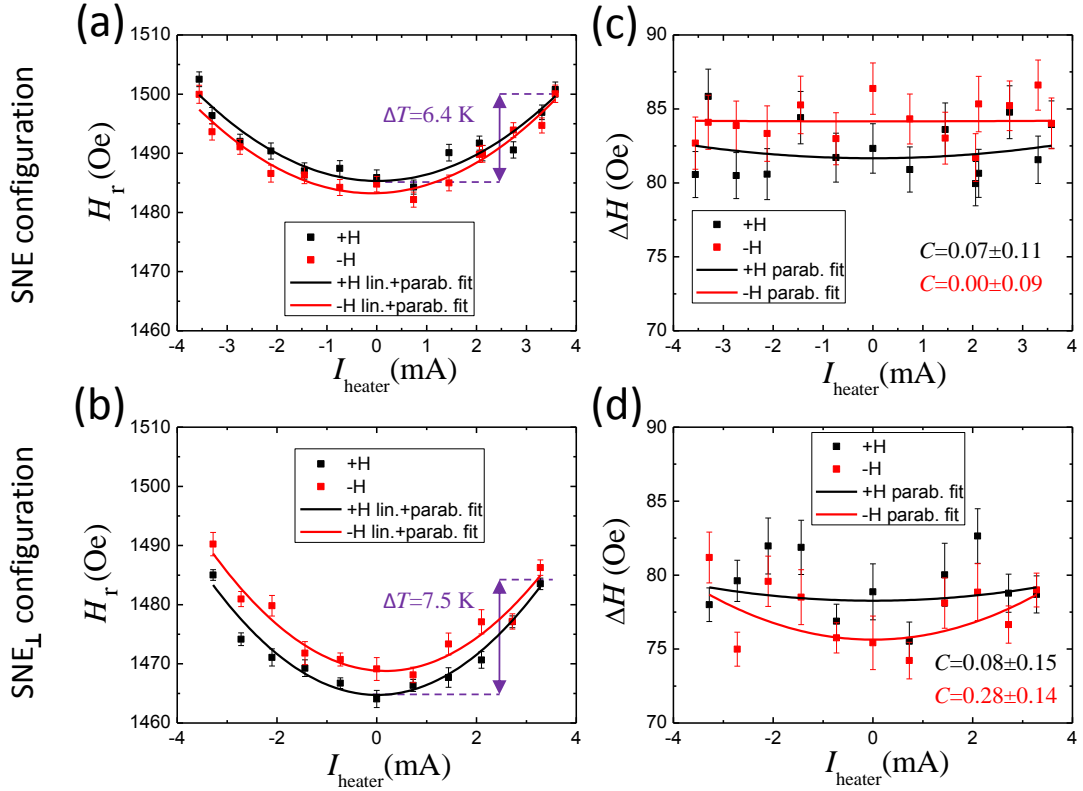


Figure 5.11: SNE measurements for the $\text{Cu}_{0.98}\text{Au}_{0.02}(5)/\text{Py}(10)$ sample, geometry 2. The maximal reached current density $j_{\text{heater}} = 2.1 \cdot 10^{11} \text{ A/m}^2$. (a) and (c) SNE configuration of the experiment. The maximal reached temperature enhancement is 6.4 K (temperature gradient $\nabla T = 4.3 \cdot 10^6 \text{ K/m}$) in the SNE measurement point, and the overall maximal temperature enhancement ΔT over the heater is about 24 K. (b) and (d) SNE_{\perp} configuration of experiment. The maximal reached temperature enhancement is 7.5 K ($\nabla T = 5.1 \cdot 10^6 \text{ K/m}$) in the SNE measurement point. The overall maximal temperature over the heater is about 28 K. All fit parameters are collected in Table 5.12. In (c) and (d) the extracted parabolic coefficients C are also shown as numbers.

SNE configuration

Measured value	Field direction	A (Oe)	B (Oe/mA)	C (Oe/mA ²)
Resonant field H_r	-H	1483.3 ± 0.7	0.22 ± 0.18	1.18 ± 0.10
	+H	1485.3 ± 0.8	-0.1 ± 0.2	1.13 ± 0.11
Linewidth ΔH	-H	84.2 ± 0.7	0	0.00 ± 0.10
	+H	81.7 ± 0.8	0	0.07 ± 0.11

SNE_⊥ configuration

Measured value	Field direction	A (Oe)	B (Oe/mA)	C (Oe/mA ²)
Resonant field H_r	-H	1468.8 ± 0.9	-0.6 ± 0.3	1.67 ± 0.15
	+H	1464.7 ± 0.8	0.00 ± 0.2	1.67 ± 0.15
Linewidth ΔH	-H	75.6 ± 0.9	0	0.28 ± 0.14
	+H	78.3 ± 1.0	0	0.08 ± 0.15

Table 5.12: SNE data. Fit parameters for the Cu_{0.98}Au_{0.02}(5)/Py(10) sample

current I_{heater} is barely visible. From these facts we conclude that we do not detect any influence of the SNE.

From the enhanced temperature ΔT in the SNE_⊥ configuration compared to the SNE configuration it is evident, that the heater conductivity is reduced due to a certain deterioration. Surprisingly, the offset value A of H_r for the SNE_⊥ configuration is lower than for the SNE configuration, meaning an enhancement of the effective magnetization M_{eff} . The enhancement can occur via the heating-induced relaxation of the mechanical tensions in the vicinity of the FM/NM interface.

The offset value A for ΔH in the SNE_⊥ configuration is smaller than in the SNE configuration, which means a reduction of the dissipation in the magnetic system. This statement also coincides with the assumption of mechanical stress relaxation, if one additionally assumes a reduction of the magnetic inhomogeneity in FM. Another possible explanation is an influence of standing waves: in the SNE configuration the film is more confined in the H_{ext} -field direction than in the SNE_⊥ configuration, edge modes appear and affect the damping in FM [33]. MOKE measurements conducted along the middle line of FM significantly reduce the influence of edge modes, but not completely.

The B value of H_r in both SNE and SNE_⊥ configurations lies mostly inside the error bars. It might be that the stray-field component H_z^{Oe} of the heater does influence B , however $H_z^{\text{Oe}}/I = 0, 14$ Oe and it is smaller than the error bars.

The parabolic coefficient C of H_r for the SNE_⊥ configuration is on average higher than for the SNE configuration due to higher temperatures.

Pt_{0.98}Mn_{0.02}(10)/Py(5) sample (geometry 1)

The measured SNE data is shown in Fig. 5.12. In the same manner as for the previous sample we fit the data with the quadratic function, fixing the linear coefficient B for ΔH to 0. The fit parameters can be found in Table 5.13.

For the SNE configuration the ΔH parabolic coefficient C is a constant within error bars between the **+H** and **-H** directions, implying absence of SNE. The linear coefficient B of H_r is slightly larger than the error bars. The average $|B|$ for the H_r coefficient is 0.26 ± 0.13 , while simulations for geometry 1 provide $H_y^{\text{Oe}}/I = 0.62$ Oe/mA. This value is about two times larger being well above the

SNE configuration				
Measured value	Field direction	A (Oe)	B (Oe/mA)	C (Oe/mA ²)
Resonant field H_r	-H	1276.3 ± 0.7	-0.32 ± 0.17	1.02 ± 0.07
	+H	1274.5 ± 0.9	0.2 ± 0.2	0.98 ± 0.09
Linewidth ΔH	-H	73.5 ± 0.8	0	0.32 ± 0.08
	+H	75.9 ± 1.0	0	0.26 ± 0.10
SNE_⊥ configuration				
Measured value	Field direction	A (Oe)	B (Oe/mA)	C (Oe/mA ²)
Resonant field H_r	-H	1290.2 ± 0.9	-0.18 ± 0.18	1.24 ± 0.08
	+H	1290.2 ± 1.2	0.3 ± 0.3	1.19 ± 0.10
Linewidth ΔH	-H	80.3 ± 0.7	0	0.2 ± 0.06
	+H	78.7 ± 0.9	0	0.33 ± 0.08

Table 5.13: SNE data fit parameters for the Pt_{0.98}Mn_{0.02}(10)/Py(5) sample

error bars and the reason for such a divergence is unclear. The earlier thermal simulations are in good agreement with the experiment, which means that the simulation parameters are not far from reality. As a possible explanation, one can assume a contribution of the field-like TSOT, but it contradicts the results for the parabolic coefficient C of ΔH . Thus, the SNE is not detected for this sample.

For the SNE_⊥ configuration the offset value A for H_r is higher compared to the SNE configuration, which is very likely due to a deterioration of the FM/NM stack resulting in a reduced effective magnetization M_{eff} . The parabolic coefficient C for the resonant field H_r is higher than for the SNE configuration, implying higher temperatures, again due to the deterioration of the FM/NM stack. The linewidth's ΔH offset level A is higher than for the SNE configuration due to the deterioration of the FM/NM. The average $|B|$ for H_r amounts to 0.24 ± 0.17 Oe/mA. From simulations we get 0.62 Oe/mA $\cdot 1/2 = 0.31$ Oe/mA. We halve the value, because the vector sum of the applied magnetic field H_{ext} with the magnetic field H_y^{Oe} induced by the I_{heater} is twice as small in the SNE_⊥ configuration than in the SNE configuration. This time the calculated value is in good agreement with the experiment.

The slope B for ΔH in both SNE and SNE_⊥ configurations changes sign when the field direction is changed, which is consistent with the assumed influence of the magnetic field produced by I_{heater} . A similar behavior is observed for all samples of geometry 1.

Pt(10)/Py(5) sample (geometry 1)

The measured SNE data is shown in Fig. 5.13. The fit parameters are collected in Table 5.14.

For the SNE configuration the linear coefficient B of the resonant field H_r is significantly outside the error bars. This fact implies an influence of the stray field H_y^{Oe} produced by I_{heater} . The sign change is consistent with the change of field direction in relation to the current-induced field of the heater. The averaged $|B|$ amounts to 0.6 ± 0.18 Oe/mA, which is in very good agreement with the simulated value of 0.62 Oe/mA unlike for the previous sample. The parabolic coefficient C for ΔH is unchanged as the applied field direction is switched, meaning no measurable

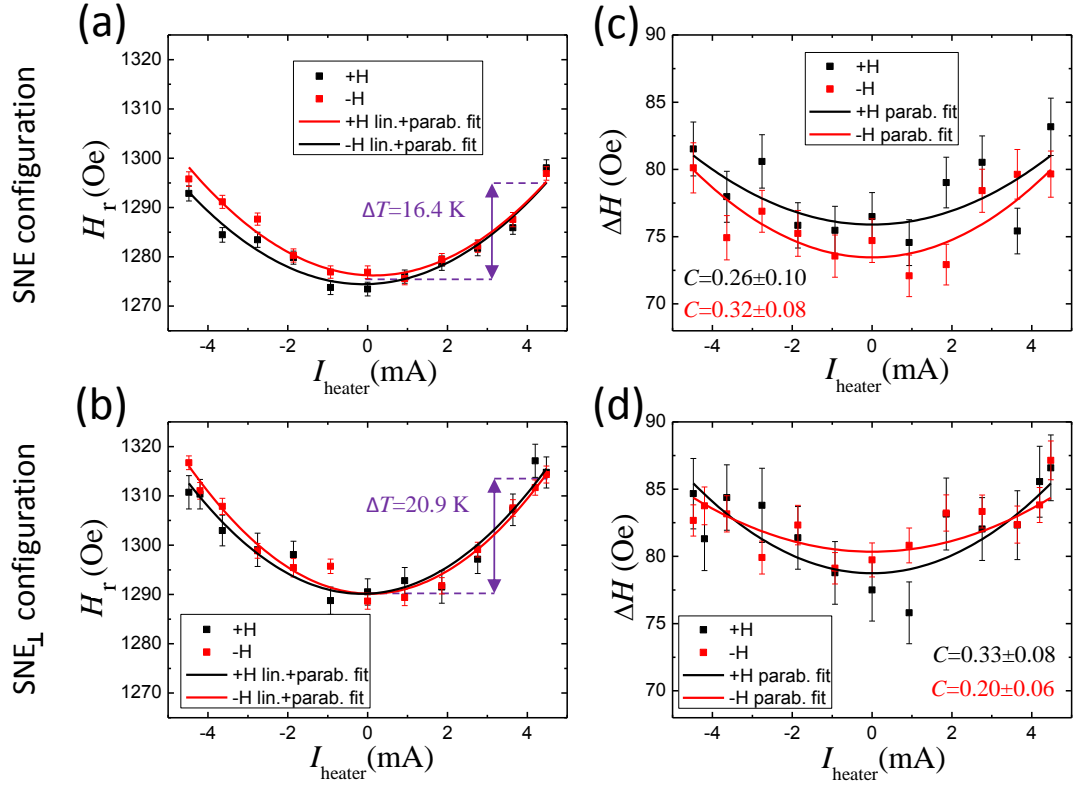


Figure 5.12: SNE measurements for the Py(5)/Pt_{0.98}Mn_{0.02}(10) sample, geometry 1. The maximal reached current density is $j_{\text{heater}} = 3.70 \cdot 10^{10}$ A/m². (a) and (c) SNE configurations of experiment. The maximal reached temperature enhancement is 16.4 K (temperature gradient $\nabla T = 1.6 \cdot 10^7$ K/m) in the SNE measurement point, the overall maximal temperature enhancement ΔT over the heater is about 32.3 K. (b) and (d) SNE_⊥ configuration of experiment. The maximal reached temperature enhancement is 20.9 K ($\nabla T = 2.0 \cdot 10^7$ K/m) in the SNE measurement point. The overall maximal temperature over the heater is about 41 K. All fit parameters are collected in Table 5.13. In (c) and (d) the extracted parabolic coefficients C are also shown.

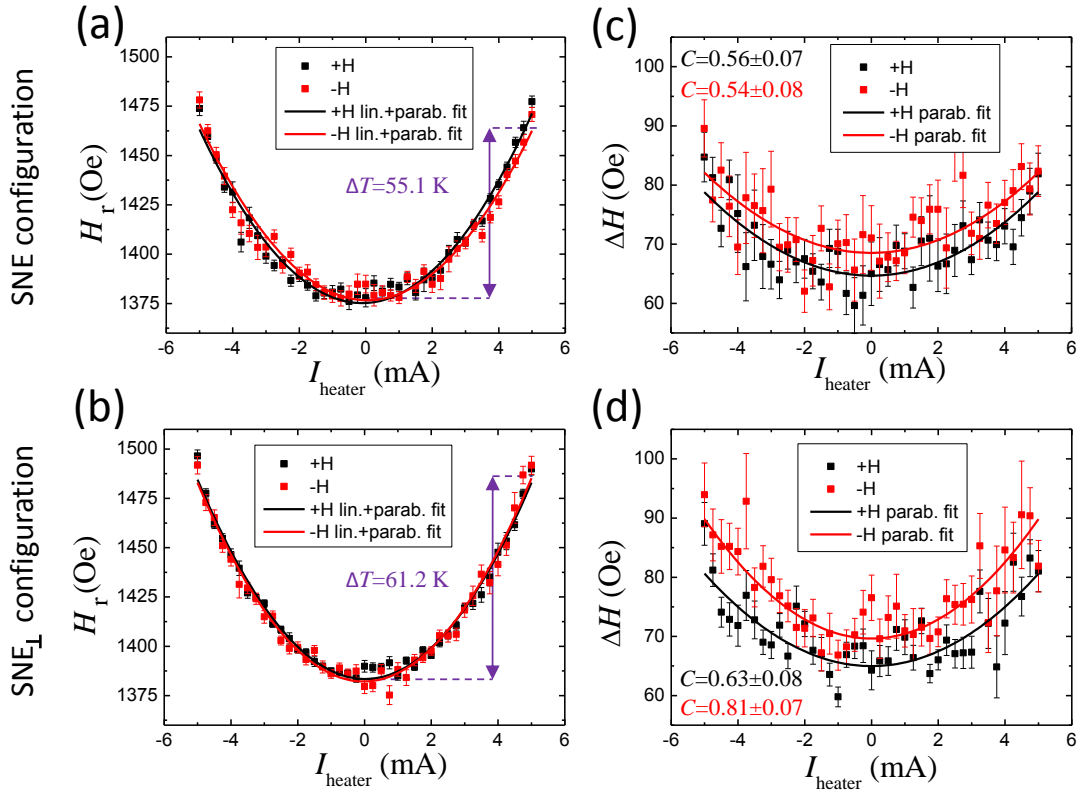


Figure 5.13: SNE measurements for the Pt(10)/Py(5) sample, geometry 1. The maximal reached current density is $j_{\text{heater}} = 4.2 \cdot 10^{10} \text{ A/m}^2$. (a) and (c) SNE configuration of experiment. The maximal reached temperature enhancement is 55.1 K ($\nabla T = 1.8 \cdot 10^7 \text{ K/m}$) in the SNE measurement point, the overall maximal temperature enhancement ΔT over the heater is about 115 K. (b) and (d) SNE $_{\perp}$ configuration of experiment. The maximal reached temperature enhancement is 61.2 K ($\nabla T = 2.0 \cdot 10^7 \text{ K/m}$) in the SNE measurement point. The overall maximal temperature over the heater is about 128 K. All fit parameters are collected in Table 5.14. In (c) and (d) the extracted parabolic coefficients C are also shown.

SNE contribution.

For the SNE $_{\perp}$ configuration. The H_r offset A is somewhat higher than for the SNE configuration. A possible reason is a reduction of M_{eff} due to deterioration of the FM/NM stack. The averaged $|B|$ coefficient for H_r amounts to $0.2 \pm 0.18 \text{ Oe/mA}$ compared to $0.62 \text{ Oe/mA} \cdot 1/2 = 0.31 \text{ Oe/mA}$ from the COMSOL simulations. And again the experimental value is in good agreement with the simulated one. The parabolic coefficient C for H_r is larger than in the SNE configuration due to higher temperatures of the heater at the given current value. The higher temperatures are related to the increased resistivity of the heater induced by the deterioration of the FN/NM stack. The difference between the parabolic coefficients C for ΔH is slightly outside 1σ error bars, but this is definitely an artifact, since in this configuration an influence of the SNE on the linewidth ΔH is not expected from theory.

Note for all measured samples. The offset value A of ΔH (ΔH is value related to dissipation of the magnetic system) in different directions of the magnetic

SNE configuration

Measured value	Field direction	A (Oe)	B (Oe/mA)	C (Oe/mA ²)
Resonant field H_r	-H	1376.7 ± 1.2	-0.4 ± 0.3	3.51 ± 0.11
	+H	1375.3 ± 1.2	0.8 ± 0.2	3.68 ± 0.10
Linewidth ΔH	-H	68.5 ± 1.0	0	0.54 ± 0.08
	+H	64.7 ± 0.8	0	0.56 ± 0.07

SNE_⊥ configuration

Measured value	Field direction	A (Oe)	B (Oe/mA)	C (Oe/mA ²)
Resonant field H_r	-H	1382.2 ± 0.9	0.2 ± 0.3	4.07 ± 0.10
	+H	1383.4 ± 0.7	-0.2 ± 0.2	4.01 ± 0.07
Linewidth ΔH	-H	69.6 ± 0.6	0	0.81 ± 0.07
	+H	65.0 ± 0.8	0	0.63 ± 0.08

Table 5.14: SNE data fit parameters for the Pt(10)/Py(5) sample

field \vec{H}_{ext} (**+H**/**-H**) differs by 2–6% for all samples. The reason, presumably, is the RF line impedance dependence on the direction of \vec{H}_{ext} due to magneto-mechanical coupling of parts of the RF line to the electromagnet. The coefficient C for ΔH shows a constant behavior within error bars meaning absence of a measurable SNE signal.

5.4.1 Conclusion and outlook on the SNE

For all samples we observe higher temperatures in the SNE_⊥ configuration compared to the SNE configuration. This is related to a degradation of heaters and the fact, that the SNE_⊥ measurements were performed after the SNE configuration measurements. According to the interdiffusion research on Pt(10)/Py(5) and Pt_{0.98}Mn_{0.02}(10)/Py(5) samples (described in the Appendix A.1), the sample's deterioration comes rather from an electromigration phenomenon than from interdiffusion alone. We make such a statement based on the fact that the interdiffusion for the mentioned samples starts from about 450 K, while in the SNE measurements 430 K is barely reached. For the Au heater (geometry 2) the maximal applied current densities j are $2 \cdot 10^{11}$ A/m² and for the Pt heater (geometry 1) samples are $3 - 4 \cdot 10^{10}$ A/m². These values are sufficient to lead to electromigration in these materials, especially in thin films, which have high atom mobility due to a very large surface-to-volume ratio [63].

Generally, the simulated temperature and stray magnetic field distributions in the samples are in a good agreement with the experiment. We showed, that a quadratic fit for temperature dependence on the heater current is reasonable at RT of surroundings and temperatures of FM under the interdiffusion limit.

At least Py(5)/Pt(10) and Py(5)/Pt_{0.98}Mn_{0.02}(10) interfaces show sufficient detection capability of the spin currents in SHE experiments. The extracted SHA value for Pt is somewhat larger than the average value from literature, but not larger than the maximal value published, whereas the Pt_{0.98}Mn_{0.02} shows 46% larger SHA than the Pt and its absolute value exceeds the maximal reported value for Pt. On the base of this we conclude, that a small addition of Mn in Pt enhances the SHE.

No SNE signature is detected in our experiments, however we can at least give an upper limit for the spin current that was reached in the experiments. Based

on the conducted SHE measurements, for Py(5)/Pt(10) and Py(5)/Pt_{0.98}Mn_{0.02}(10) samples this value amounts to $1.2 \cdot 10^9$ and $0.9 \cdot 10^9$ A/m², respectively. For the Py(10)/Cu_{0.98}Au_{0.02}(5) sample we assume a similar value of $2 \cdot 10^9$ A/m² based on the theoretical work of [136].

In the experiments we reach thermal gradients of $5 \cdot 10^6$ K/m for Cu-based sample and $2 \cdot 10^7$ K/m for Pt-based samples. The theoretical limit of the MOKE-based SNE measurements amounts to $2 \cdot 10^8$ K/m. However, technical problems such as the homogeneity of the thermal gradient and the interdiffusion of the FM/NM stack reduce this limit, and actually the thermal gradient can not be larger than what we got in our experiments by more than two times. Improvements can be done by making the suspended part of the FM/NM stack as short as possible, i.e. 3-4 μ m.

Additionally, a thermal gradient 2-3 times stronger in MOKE experiments can be achieved by reduction of the base temperature down to cryogenic temperatures. In our lab a cryogenic set-up with blue laser light is available. We have conducted some test measurements, but unfortunately, the photon energy of the blue laser is too high and it leads to destruction of our samples after a certain exposure time.

As a matter of speculation, it might be that some thermal analogon of the ISGE reduces the amplitude of the SNE in experiments, similarly as the ISGE makes it in some SHE experiments. Thus, even larger thermal gradients might be needed for SNE experiments.

We believe that for MOKE-based experiments another NM materials with SNE strength larger by an order of magnitude as for the NMs used in this work are necessary. A Ag(111) layer with 1% adatoms on its surface was offered by Long et al. [87] as a candidate for gigantic SNE strength. Theoretically, the system has the highest SNE strength ever reported, about an order of magnitude stronger than for the Cu_{0.99}Au_{0.01} system. However, its production is technically challenging. The gigantic effect in this work is based on resonant impurity scattering of the surface adatoms. This idea can be translated on resonant scattering of impurity adatoms in the NM volume and also the Kondo effect might be a key for such an SNE strength improvement. To the current date, such material compositions need to be modeled and found.

Appendix A

Interdiffusion in FM/NM bilayer systems

A.1 General

Stability of spintronic devices is an important question, especially in the subfield of spincalorics, where degradation of the devices caused by side effects as electromigration [63, 11, 84], interdiffusion [93], thermal-induced stresses [22], reduction of saturation magnetisation due to high temperatures [28] (and other) might occur. In the case of interdiffusion, not only exposure to high temperatures is a source of degradation ($\exp(-\frac{const}{T})$ dependance), but also prolonged exposure to lower temperatures (\sqrt{t} dependence).

Interdiffusion (also known as chemical diffusion) is a phenomenon of mutual diffusion of heterogeneous structure components, for example, bilayers composed of two different materials A and B. Interdiffusion of metals in macroscopic-scale devices is usually supposed to be insignificant at temperatures below 60% of the melting temperature T_m (for most of the widely used metals this value is above 600 K) and particularly at room temperature (RT). The interdiffusion in diffusion-couples of monocrystalline bulk metals is usually driven by defects of the crystal structure, namely vacancies [Ch. 6.3 in 93], while for semiconductors the main mechanism is the interstitial mechanism [Ch. 6.1 in 93]. In addition, other interdiffusion mechanisms (called high-diffusivity paths [Ch. 31 in 93] accelerating diffusion rates by orders of magnitude) might be involved. Grain boundaries in polycrystalline samples, free surfaces, and dislocations are among them (see Fig. A.1(a)). All these mechanisms become increasingly important for nanoscale multilayer structures, since the ratio of inner volume to surface drops, roughness and inhomogeneities of the substrate favor defect formation, and lattice parameter mismatch above 15% or amorphous substrate both can lead to polycrystalline growth with typical grain-boundaries width of $\delta \approx 0.5$ nm [p.559 in 93]. For grain size of, say, 5-10 nm this means that 20 – 50% of atoms are located in boundaries. A comparison of the diffusivities for all cases (D is for monocrystalline bulk diffusivity, D_{gb} - grain-boundary diffusivity, D_d - dislocation pipe diffusivity, D_s - diffusivity at surfaces) is shown in Fig. A.1(b). One can easily see, that these additional mechanisms enhance interdiffusion by many orders and can cause significant interdiffusion of multilayer structures even at RT.

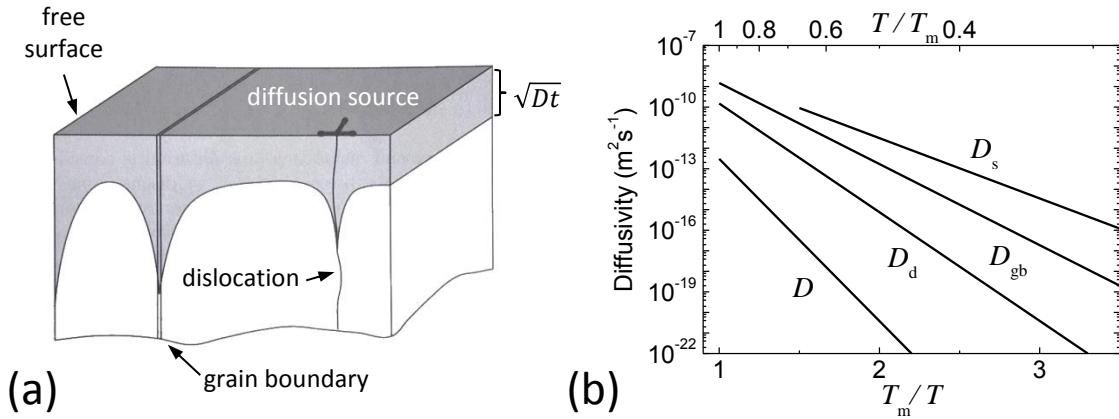


Figure A.1: (a) Schematic illustration of high-diffusivity paths in a solid [from 93, p.547]. (b) Schematic illustration of the diffusion spectrum for metals in reduced temperature scale [from 93, p.549]; T_m denotes the melting temperature

A.2 Solution of Fick's second equation for a bilayer stack

We consider a bilayer structure composed of ferromagnetic and non-magnetic (FM/NM) metals. Interdiffusion is expressed mathematically by Fick's second equation:

$$\frac{\partial C}{\partial t} = D(C) \frac{\partial^2 C}{\partial x^2} + \frac{dD(C)}{dC} \left(\frac{\partial C}{\partial x} \right)^2, \quad (\text{A.1})$$

where C is the concentration of the FM atoms along x -axis, where the x -axis is perpendicular to the interface of the FM and NM layers, D is the interdiffusion coefficient and t is the time. In general, the diffusivity D depends on concentrations of surrounding chemical elements. As Eq. (A.1) is a non-linear partial differential equation, it can not be solved analytically for arbitrary $D(C)$ dependences. If we neglect the concentration dependence of D , which is often justified, the solution of Eq. (A.1) according to [93] is expressed as:

$$\frac{C(x)}{C_0} = \frac{1}{2} \operatorname{erfc} \left(\frac{x}{2\sqrt{Dt}} \right), \quad (\text{A.2})$$

where C_0 is the initial concentration of FM atoms, the value $2\sqrt{Dt} \equiv l_{\text{diff}}$ is the characteristic diffusion length, which occurs frequently in diffusion problems, erfc is the complementary error function.

A plot of the error function is presented in Fig. A.2 (red curve) along with a linear approximation of this solution (black dashed line), which deviates from the exact solution by less than 8%. In the following we use the linear approximation for simplicity, because its deviation from the exact solution has even smaller impact on the averaged magnetic moment m_{av} of thin films, which we use in the analysis.

The diffusivity D almost always obeys the famous Arrhenius equation:

$$D = D_0 e^{-\frac{\Delta H_a}{k_B T}}, \quad (\text{A.3})$$

where D_0 is the pre-exponential factor, ΔH_a is the activation enthalpy, k_B is the Boltzmann constant, and T is the temperature. Typical exceptions from the Arrhenius behavior are cases of phase transitions. The pre-exponential factor D_0 for

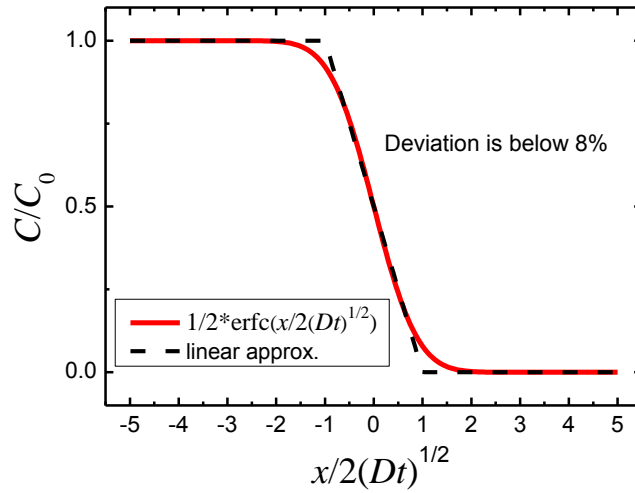


Figure A.2: Solution of the second Fick's law (red line) and its approximation by linear functions (black dashed line). The difference between the approximation and the exact solution does not exceed 8%. The value $2\sqrt{Dt} \equiv l_{\text{diff}}$ is the characteristic diffusion length.

grain-boundary interdiffusion in polycrystals is usually similar to those in single crystals (lattice diffusion). However, according to [93] the activation enthalpy of grain-boundary interdiffusion usually amounts to 0.4-0.6 of lattice diffusion.

A.3 Magnetic valence model for 3d-FM-containing alloys

In order to describe the magnetic moment per atom m (and subsequently the saturation magnetization M_S) of alloys of 3d FM with other metals we use the magnetic valence model [28, 110]:

$$m(x) = \left(\frac{C(x)}{C_0} (Z_m^{\text{FM}} + 2N_s^\uparrow) + \left(1 - \frac{C(x)}{C_0} \right) (Z_m^{\text{NM}} + 2N_s^\uparrow) \right) \mu_B, \quad (\text{A.4})$$

where m is the magnetic moment per atom, Z_m^i is the magnetic valence of a substance i , $2N_s^\uparrow \approx 0.6 - 0.7$ is the number of electrons in the unpolarised $4sp$ -band (for further calculations we take it equal 0.6), and μ_B is the Bohr magneton. Some of the magnetic valences are presented in Table A.1.

Substance	Z_m
Fe ^I	2
Co	1
Ni	0
Cu	-1

Table A.1: Magnetic valences Z_m for different materials [28, 110]

For a homogeneous alloy of known stoichiometry containing 3d FM metals (Fe,

Co, Ni), one can estimate m via Eq. (A.4). According to Table A.1, the effective Z_m for Py of $\text{Fe}_{0.2}\text{Ni}_{0.8}$ composition is 0.4.

Magnetic valence model is a generalization of the rigid-band model for 3d FM and proved to be reliable for "strong" FM (Co and Ni) and somewhat less reliable for Fe. The most famous manifestation of this fact is the Slater-Pauling curve [125, 110, 10].

A.4 Dependence of sample magnetization on diffusion length

In the following we are focused on the calculation of an averaged magnetic moment m_{av} in order to compare it with values known from the experiment. The geometry of the calculation model is shown in Fig. A.3. We consider a case of a bilayer stack composed of a ferromagnetic metal and a nonmagnetic metal (FM/NM). For normalized concentrations $C(x)/C_0$ of the FM below a critical value p_{cr} the magnetic moment per atom m is zero. Thus, for the averaged m the following equation fulfills:

$$m_{\text{av}}(l_{\text{diff}}) = \frac{1}{d_1 + d'} \int_0^{d_1+d'} m(x) dx, \quad (\text{A.5})$$

where integration goes over a "magnetically active" region $d_1 + d'$, d_1 is the thickness of FM layer, d' is the "magnetically active" part of the diffusing FM front in the NM.

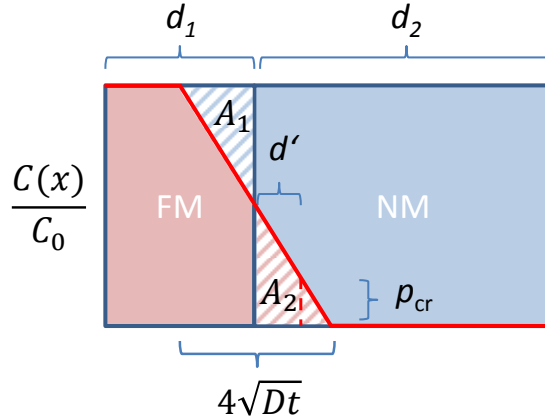


Figure A.3: Interdiffusion in a FM/NM bilayer stack. The red line is the normalized concentration $C(x)/C_0$ of FM atoms, which varies in the range of 0 to 1. d_1 and d_2 are thicknesses of the FM and NM layers before diffusion, respectively; p_{cr} is a critical normalized concentration, below which $m = 0$; d' is the length of the diffused FM front for which the magnetic moment $m > 0$; A_1 and A_2 (blue and red shaded areas) are diffused "volumes" of NM and FM, respectively.

¹for *bcc* αFe (thermodynamically stable structure of bulk Fe at normal conditions). *fcc* γFe is notoriously known for its magnetic moment (thus its Z_m as well) being very sensitive to the lattice parameter. Depending on it Fe crystal might be ferromagnetic, antiferromagnetic or nonmagnetic at all. γFe can be stabilized at RT by alloy addition or on an *fcc* substrate. Fe is often called "weak" ferromagnet.

If m_{av} , corresponding to the experimental saturation magnetization M_S , is measured with the help of CPW-FMR (like in our case), one might need to multiply the integrand in (A.5) by a factor of $\exp(-\frac{x}{\delta})$, where δ is some logarithmic decrement. The reason is the phenomenon of the RF magnetic field shielding by metallic films [9], which occurs for film thickness much smaller than the relevant skin depth [28, 46]². At 50 GHz one should add the exponential factor starting from thickness of ≈ 45 nm for Py, ≈ 10 nm for Cu and ≈ 65 nm for Pt. In our measurements, the samples are sufficiently thinner than this threshold thicknesses and therefore we neglect the exponential factor. SQUID and VSM measuring techniques [Ch. 10.5.1 in 28] are free from the magnetic shielding problem (magnetic field frequencies are in the acoustic range).

Because the number of atoms has to be conserved in the described system, equality $A_1 = A_2$ (see Fig. A.3) must always hold during the interdiffusion process. This is the key moment to calculate d' .

In the following we use next designations:

$$\begin{aligned} m_{\text{FM}} &= (Z_{\text{m}}^{\text{FM}} + 2N_{\text{s}}^{\uparrow})\mu_{\text{B}}, \\ m_{\text{NM}} &= (Z_{\text{m}}^{\text{NM}} + 2N_{\text{s}}^{\uparrow})\mu_{\text{B}}, \\ m_2 &= m_{\text{FM}}(1 + p_{\text{cr}})/2 + m_{\text{NM}}(1 - p_{\text{cr}})/2. \end{aligned} \tag{A.6}$$

$$l_{\text{diff}} = 2\sqrt{Dt}$$

Depending on whether the FM layer is thinner or thicker than the NM layer two cases with slightly different solutions arise:

1. Case $d_1 < d_2$ (FM layer is thinner than NM). The interdiffusion process can be separated into 4 stages:
 - (a) For the first stage $l_{\text{diff}} \leq d_1$ diffusion fronts equally spread in both directions, into the FM and NM. d' and average magnetic moment $m_{\text{av},1}$ are equal to:

$$\begin{aligned} d' &= l_{\text{diff}}(1 - 2p_{\text{cr}}), \\ m_{\text{av},1} &= \frac{m_{\text{FM}}(d_1 - l_{\text{diff}}) + m_2(d' + l_{\text{diff}})}{d_1 + d'}. \end{aligned} \tag{A.7}$$

- (b) As the diffusion front reaches the left border of the FM, the red line in Fig. A.3 shifts down in order to keep equality $A_1 = A_2$. Diffusion fronts into the FM and NM are not symmetric with respect to the initial bilayer interface any more. For $\frac{(d_1+d_2)^2}{4d_1} \geq l_{\text{diff}} > d_1$ (the second stage condition) we have:

$$\begin{aligned} d' &= 2\sqrt{l_{\text{diff}}d_1} - d_1 - 2p_{\text{cr}}l_{\text{diff}}, \\ m_{\text{av},2} &= m_{\text{FM}} \left(\frac{1}{1 + l_{\text{diff}}/d_1} + p_{\text{cr}}/2 \right) + \\ &+ m_{\text{NM}} \left(1 - \frac{1}{1 + l_{\text{diff}}/d_1} - p_{\text{cr}}/2 \right). \end{aligned} \tag{A.8}$$

²in the range of 5 – 50 GHz the skin depth δ_{skin} is 0.6 – 1.9 μm for Py

- (c) The diffusion front has already reached the right border d_2 of the NM ($l_{\text{diff}} > \frac{(d_1+d_2)^2}{4d_1}$), but the edge of the magnetically active zone d' has not reached the right border of the NM ($d' < d_2$):

$$\begin{aligned} p_{\text{av},3} &= 1/2 \left(\frac{d_1}{d_1 + d_2} + \frac{d_1 + d_2}{4l_{\text{diff}}} + p_{\text{cr}} \right), \\ d' &= (d_2 - d_1)/2 + 2l_{\text{diff}} \left(\frac{d_1}{d_1 + d_2} - p_{\text{cr}} \right), \\ m_{\text{av},3} &= m_{\text{FM}}p_{\text{av},3} + m_{\text{NM}}(1 - p_{\text{av},3}). \end{aligned} \quad (\text{A.9})$$

- (d) Once d' reaches the length of d_2 ($d' \geq d_2$), m_{av} is constant:

$$m_{\text{av},4} = \frac{d_1}{d_2}m_{\text{FM}} + \left(1 - \frac{d_1}{d_2}\right)m_{\text{NM}}, \quad (\text{A.10})$$

though interdiffusion continues.

The situation of d' having negative and decreasing values (border of p_{cr} shifts towards the left boundary of the FM region) is possible as well, when the thickness d_1 of the FM is very small in comparison to d_2 of the NM and/or the magnetic valence Z_{m}^{NM} of the NM has very large negative values. Once $-d' = d_1$ (the position of p_{cr} reaches the left boundary of the FM region), the average magnetic moment m_{av} is 0.

2. Case $d_1 > d_2$ (FM is thicker than NM)

- (a) Solution for the first stage is the same as (A.7), but the stage finishes when diffusion front l_{diff} reaches border d_2 instead of d_1 as in the first case.
- (b) For the second stage ($\frac{(d_1+d_2)^2}{4d_2} \geq l_{\text{diff}} > d_2$) the red line in Fig. A.3 will go up. The solution for this region is different from (A.8) and equals:

$$\begin{aligned} d' &= d_2 - 2l_{\text{diff}}(1 - p_{\text{cr}}) - 2\sqrt{l_{\text{diff}}d_2}, \\ m_{\text{av},2,2} &= \frac{m_{\text{FM}}(d_1 + d_2 - 2\sqrt{l_{\text{diff}}d_2}) + m_2(d' - d_2 + 2\sqrt{l_{\text{diff}}d_2})}{d_1 + d'}. \end{aligned} \quad (\text{A.11})$$

- (c) The solution for the third stage coincides with the case of thin FM presented in (A.9).
- (d) After d' reaches d_2 , m_{av} is a constant and equals (A.10).

Note that dilute alloys or compounds which contain less than 10% magnetic atoms cannot be expected to order magnetically at RT, if at all [Ch. 11.1 from 28]. Thus, p_{cr} extracted from (A.4) might slightly underestimate resulting m_{av} for materials with small Z_{m} .

It is worth noting that owing to different chemical surrounding, the magnetic moment m of atoms of the FM layer which are in direct contact to the NM should rather be estimated as the magnetic moment for the bulk composition $\text{FM}_{0.5}\text{NM}_{0.5}$ than for the pure FM. This should reduce m_{av} and might be significant for ultra-thin films (below 1-2 nm). However, here we omit the discrete character of the FM. Other problems influencing m in thin films will be discussed in the following subsections.

A.5 Experimental interdiffusion in FM/NM bilayers

Samples of composition Al(3)/Py(5)/Alumina(20)/Si₃N₄ and Al(3)/Py(5)/Pt_{0.98}Mn_{0.02}(10)/Alumina(20)/Si₃N₄ (in the following referred as Py(5)/Pt_{0.98}Mn_{0.02}(10)) are examined. The first sample is prepared *in situ* in an evaporation chamber with a vacuum level of $5 \cdot 10^{-6}$ mbar. For the second sample the Pt_{0.98}Mn_{0.02} layer is deposited in an MBE chamber (vacuum level of $\approx 10^{-10}$ mbar), then the sample is installed into the evaporation chamber with higher vacuum pressure $5 \cdot 10^{-6}$ mbar to deposit other layers. The Al capping layer of each stack is exposed to air and oxidized to ≈ 4 nm of Alumina. The samples are magnetically characterized at RT by CPW-FMR allowing for the determination of the saturation magnetization M_S , the damping factor α and the intercept value of the line-width ΔH_{interc} . Then each sample is annealed at different temperatures in the range of 450-800 K for a certain period of time (mostly 70 min) and further characterized by CPW-FMR at RT. To countercheck the interdiffusion data extrapolated from the magnetic measurements, we additionally measure concentration-profiles of the Py(5)/Pt_{0.98}Mn_{0.02}(10) sample with X-ray Photoelectron Spectroscopy (XPS) before annealing and after the last step of annealing.

The calculated dependence of m_{av} on the diffusion length l_{diff} for Py/Pt_{0.98}Mn_{0.02} is shown in Fig. A.4. The presence of Mn is not considered in the calculation, as concentration in the NM layer of only 2% does not give any significant contribution. The calculated curve has a plateau region after a sufficiently large diffusion length is reached. Theoretical plateau-level is $0.4 \mu_B$. Magnetic valences Z_m used in calculations are 0.4 for Py (composition Fe_{0.2}Ni_{0.8}, calculated according to the data in Table A.1) and -0.50 ± 0.15 for Pt (average value extrapolated from [30, 21]). The critical level p_{cr} used in calculation is 0 (extracted from (A.4) for known Z_m).

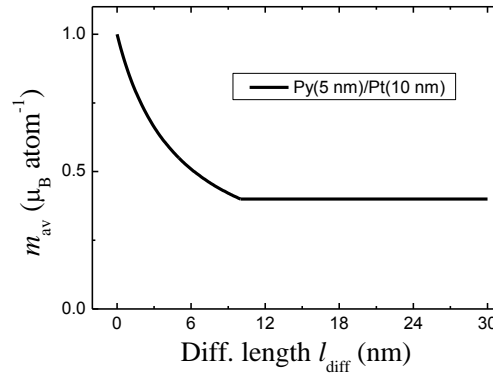


Figure A.4: Theoretical dependence of m_{av} on the diffusion length l_{diff} for a Py(5)/Pt(10) bilayer. The calculated curve has a plateau region after a diffusion length of 10 nm is reached. Theoretical plateau-level is $0.4 \mu_B$.

Fig. A.5 shows FMR-data and the m_{av} values estimated from them. The expected m_{av} value for bulk Py is $1 \mu_B$ corresponding to $\mu_0 M_S = 1.04$ T. Experimental values of M_S in the plot are effective in-plane magnetization values extracted from raw FMR data by using Eq. (??). These effective values for M_S do not contain an out-of-plane anisotropy contribution, which in some bilayer systems might lead

to significant underestimation of the actual magnetization of the sample. M_S of not annealed Al(3)/Py(5)/Alumina(20) and Py(5)/Pt_{0.98}Mn_{0.02}(10) samples (300 K point in Fig. A.5(a)) deviate by less than 9% from bulk M_S of Py and therefore we omit this difference in following.

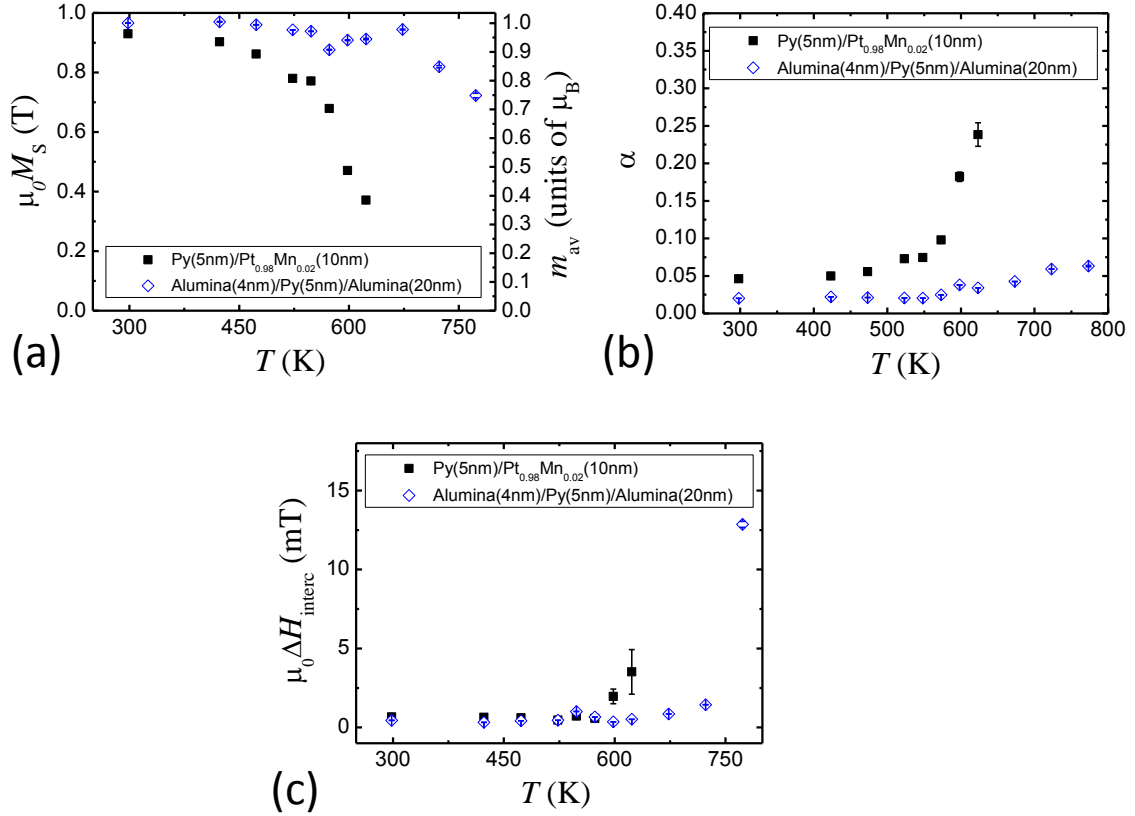


Figure A.5: FMR parameters of Al(3)/Py(5)/Alumina(20) and Py/Pt_{0.98}Mn_{0.02} samples after annealing at a certain temperature T . (a) Saturation magnetisation M_S and average magnetic moment m_{av} . (b) Gilbert damping constant α . (c) Intercept value of the line-width ΔH_{interc} .

For simplicity, experimental m_{av} values are calculated as $1.0\mu_B \cdot \mu_0 M_S(T)/0.97$ T, where 0.97 T is the magnetization of the Al(3)/Py(5)/Alumina(20) sample before annealing.

The $M_S(T)$ dependence for the Al(3)/Py(5)/Alumina(20) sample indicates no interdiffusion of Alumina and Py layers up to 650 K. Based on these data, we are safe to say, that all changes in M_S of the Py/Pt_{0.98}Mn_{0.02} sample up to 650 K are caused by the intermixture of the metallic layers. The Py/Pt_{0.98}Mn_{0.02} sample shows strong interdiffusion already at a moderate temperature of 500 K and reaches closely the predicted level of $0.4 \mu_B$ (experimental value is $0.38 \mu_B$). The plateau region is not observed, because the SNR of the FMR-signal was too small to continue the experiment (due to the rapid enhancement of the damping parameter α after the annealing step at 570 K).

From experimental m_{av} values we estimate the effective accumulated diffusion length l_Σ via formulae reciprocal to (A.7),(A.8),(A.9) and (A.11). This effective diffusion length l_Σ sums up all preceding annealing steps and equals to:

$$l_{\Sigma}^2(n) = \sum_{i=1}^n 4D(T_i)t_i, \quad (\text{A.12})$$

where n is the number of annealing steps, T_i and t_i are annealing temperature and time of the i -th annealing step, respectively. Knowing this dependence one can extract individual values $D(T_i)$ from the accumulated diffusion length l_{Σ} .

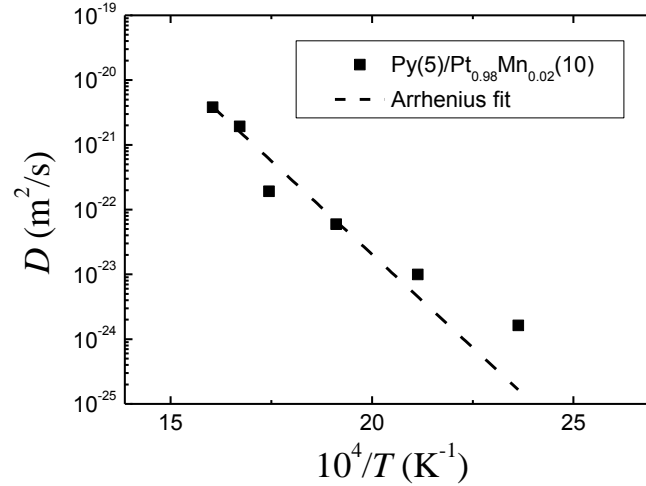


Figure A.6: Extracted diffusivities of the Py(5)/Pt_{0.98}Mn_{0.02}(10) sample. The points are experimental data and the dashed line its fit with Arrhenius equation (A.3)

The extracted diffusivities are shown in Fig. A.6. Table A.2 summarizes the activation parameters. From empirical data it is well known that close-packed crystal structures (e.g. *fcc* or *hcp*) are usually less diffusive than structures with a lower packing efficiency, like *bcc* [93]. Bulk Ni and Pt have *fcc* crystal structure at normal conditions, while Fe has *bcc* structure. Py of the composition Fe_{0.2}Ni_{0.8} is a random solid solution with a tendency to L₁₂ (γ' FeNi₃-type, also close-packed) order [28]. Thus, we do not expect structural phase transitions (from close-packed to less dense) in the investigated intermixing bilayer and as consequences the Arrhenius dependence of the diffusivity shown in (A.3) should hold well, and the interdiffusion coefficient $D(C)$ should not vary significantly with concentration (which proved at least for Ni/Pt in [35, 55]). This makes the assumptions of our calculation model legitimate.

Sample	D_0 (m 2 /s)	ΔH_a (eV)	T range (K)
Py(5)/Pt _{0.98} Mn _{0.02} (10)	$(0.1 - 2.7)10^{-11}$	1.14 ± 0.2	300-625

Table A.2: Extracted interdiffusion activation parameters of the Py(5)/Pt_{0.98}Mn_{0.02}(10) sample. Fit with Arrhenius equation (A.3)

To check the appropriateness of the extracted activation parameters we compare these with data from literature for Pt/Ni, Table A.3. These data should be applicable for our study, because Py consists 80% of Ni and, the concentration of Mn in the Pt_{0.98}Mn_{0.02} alloy is negligible and all components of the mentioned stacks (ours and from literature) have *fcc*-like crystal structures.

Sample, mono/polycrystalline, investigation method, reference	D_0 (m ² /s)	ΔH_a (eV)	T range (K)
(Pt(25 μ m)/Ni(25 μ m)) ₉ multifoil stack, monocrystalline, energy-dispersive spectroscopy, [35]	10 ⁻⁶	2.33	1570
Pt/Ni semi-infinite diffusion couples, monocrystalline, Electron Probe Micro-Analysis, [55]	–	3.21	1420-1570

Table A.3: Interdiffusion activation parameters of Pt/Ni from literature

For the Py/Pt_{0.98}Mn_{0.02} sample the activation enthalpy ΔH_a is 2-3 times lower than for a monocrystalline Pt/Ni bilayer. This implies low quality and high polycrystallinity. No contradiction here, since Py never (except composition Ni_{0.75}Fe_{0.25}) grows as single crystal, and the Pt_{0.98}Mn_{0.02} layer is grown on an amorphous substrate. The extracted pre-exponential factor is 5 orders smaller than in literature.

A.6 XPS concentration depth-profiling

For concentration-profile measurements we exploit X-ray photoelectron spectroscopy (XPS), also known as Electron Spectroscopy for Chemical Analysis (ESCA) [149, 156, 98, 64]. XPS is a surface analysis technique with an information depth of 1-10 nm. During a concentration measurement we remove sample material by Ar-ion bombardment (sputtering). The error on the concentrations determined in our measurements is 5%. A monochromatic Al K α X-ray source ($E_{\text{photon}} = 1486.7$ eV) is used for the XPS analysis.

Measured XPS concentration-profiles are shown in Fig. A.7 (25 min of Ar-etching time t correspond to ≈ 5 nm). The concentration of Mn in the Pt_{0.98}Mn_{0.02} alloy is not measured, since its concentration of 2% is below the detectivity of XPS measurements. One can see from Fig. A.7(a) for the unannealed Py(5)/Pt_{0.98}Mn_{0.02}(10) sample, that no step-like concentration change is visible on each of the interfaces (alumina/Py, Py/Pt, Pt/alumina). Smearing of a sharp interface is caused by presence of a surface roughness σ , partial interdiffusion of the layers at the interfaces, and due to the fact, that the analysis depth λ is never zero. According to Hofmann *et al.* [65], two most common models are used for the depth-profile description, namely: MRI model (atomic Mixing, Roughness and Information depth, see also [66]) and UDS model (up- and downslope, see also [36]). Both approaches are based on a convolution integral, where the measured normalized concentration $C_{\text{meas}}(x)$ as a function of the sputter-depth x is given by the convolution between the actual depth-profile $C(x)$ and the depth resolution function (DRF) $g(x)$:

$$C_{\text{meas}}(x) = (C * g)(x) = \int_{-\infty}^{+\infty} C(x')g(x - x')dx'. \quad (\text{A.13})$$

We base our next estimations on ideas of the MRI model, because its parameters have clearer physical meaning. For the MRI model the DRF is itself a convolution of the next functions:

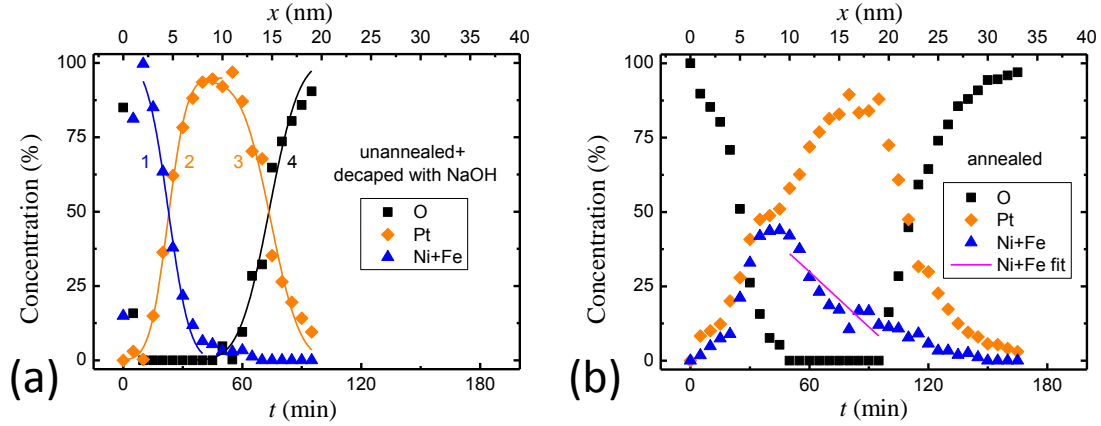


Figure A.7: Concentration profiles of the chemical elements obtained from XPS depth profiling. t is the Ar-etching time (current $3 \mu\text{A}$, acceleration voltage 1.2 kV), 5 nm of the sample are removed in $\approx 25 \text{ min}$. In the figures Ni+Fe denotes Py and the O data points originate from alumina. (a) unannealed Py(5)/Pt_{0.98}Mn_{0.02}(10) sample with the top alumina layer removed by NaOH prior to the XPS measurements. The points are experimental data and the lines are fits of the concentration profiles at the interfaces with Eq. (A.17). (b) shows the same sample after the last annealing step. Concentration resolution is 5%. The magenta line is a fit of the Py concentration profile in middle part with Eq. (A.16)

$$\begin{aligned}
g_w(x) &= \frac{1}{w} e^{\frac{x+w}{w}}, \quad \text{for } x < -w; \\
g_\sigma(x) &= \frac{1}{\sqrt{2\pi}\sigma} e^{-\left(\frac{x}{\sigma}\right)^2}, \quad \text{for } x \in (-\infty, +\infty); \\
g_\lambda(x) &= \frac{1}{\lambda} e^{-\frac{x}{\lambda}}, \quad \text{for } x > 0;
\end{aligned} \tag{A.14}$$

where w is the mixing length, σ is the roughness parameter, and λ is the information depth parameter. Function $g_w(x)$ takes into account the influence of unintended layer mixing at the interface, $g_\sigma(x)$ takes into account surface roughness (modeled by a Gaussian function), $g_\lambda(x)$ takes into account the finite analysis depth. λ is in fact an attenuation length of the electrons, which is related to the inelastic mean free path (IMFP) [149, 156, 98, 119] and depends on the electron's kinetic energy. Depth resolution of XPS experiments δ_{XPS} (not to confuse it with the information/analysis depth λ) is usually defined as 2σ [64, 149], however this is not always quite precise. If σ is smaller than $\lambda/2$ or $w/2$ then the mentioned definition will give understated numbers.

The mixing function $g_w(x)$ described above is an exponential function, which is usually applied for delta layers (one-atomic layer). But the actual diffused concentration profile in our experiments (solution of the interdiffusion problem for semi-infinite half-spaces) is an error function, which we approximate by a linear function (in subsection A.2). We assume an idealized concentration profile $C_{\text{ideal}}(x)$ of the following form:

$$C_{\text{ideal}}(x) = \begin{cases} 0 & , \text{ for } x \in (-\infty, 0); \\ kx & , \text{ for } x \in [0, 1/k]; \\ 1 & , \text{ for } x \in (1/k, +\infty); \end{cases}$$

where k is an arbitrary real positive constant. This concentration profile already includes diffusion at an interface, thus we omit the mixing function $g_w(x)$ of the MRI model. Our final goal is to determine from an experimental $C_{\text{meas}}(x)$ the slope k of the actual (idealized) concentration profile $C_{\text{ideal}}(x)$. Function $g_\sigma(x)$ significantly changes the slope k of the actual concentration distribution in the whole region of concentration change, especially for concentration changes with high k (sharp interfaces). Function $g_\lambda(x)$ in turn influences the slope k significantly only at the edges of the concentration change region ($(-2.3\lambda, 0)$ and $(1/k - 2.3\lambda, 1/k)$). For metals in the energy range of our measurements we have $\lambda = 1 - 2$ nm. For our final goal it is sufficient to use only the middle part of the concentration-transition region of annealed sample. Based on this, we omit the influence of $g_\lambda(x)$ and do not use it in our DRF $g(x)$. Finally, $g(x) = g_\sigma(x)$.

Note that the surface roughness σ is not a constant during Ar-etching, but rises with etching time (in the Appendix of [65] and in [64] a dependence $\sigma = c_1 + c_2\sqrt{x}$ is suggested, where c_i is some positive constant). Enhancement of σ can be lowered if one uses a rotating sample holder, however it was not the case for our study. Performed AFM measurements show that the initial surface roughness of our samples lies in a range of 1.1 – 1.5 nm.

With all discussed corrections to the MRI model we can finally calculate an expected concentration profile:

$$(C_{\text{XPS,ideal}} * g)(x) = \frac{1}{\sigma\sqrt{2\pi}} \left(\int_0^{1/k} (kx') e^{-\frac{1}{2}\left(\frac{x-x'}{\sigma}\right)^2} dx' + \int_{1/k}^{\infty} e^{-\frac{1}{2}\left(\frac{x-x'}{\sigma}\right)^2} dx' \right). \quad (\text{A.15})$$

Taking into account that

$$\begin{aligned} \frac{2}{\sqrt{\pi}} \int_{x_1}^{x_2} e^{-x'^2} dx' &= \text{erf}(x_2) - \text{erf}(x_1), \\ \text{erf}(0) &= 0, \\ \text{erf}(\infty) &= 1, \end{aligned}$$

we get next formula:

$$\begin{aligned} (C_{\text{XPS,ideal}} * g)(x) &= \frac{1}{2} \left[\frac{\sqrt{2}k\sigma}{\sqrt{\pi}} \left(e^{-\frac{1}{2}\left(\frac{x}{\sigma}\right)^2} - e^{-\frac{1}{2}\left(\frac{1/k-x}{\sigma}\right)^2} \right) + \right. \\ &\quad \left. + kx \left(\text{erf} \left(\frac{1/k-x}{\sqrt{2}\sigma} \right) - \text{erf} \left(-\frac{x}{\sqrt{2}\sigma} \right) \right) + \left(1 - \text{erf} \left(\frac{1/k-x}{\sqrt{2}\sigma} \right) \right) \right]. \quad (\text{A.16}) \end{aligned}$$

Even with all simplifications of the MRI model, this formula is not trivial. For the case of a sharp interface ($k = \infty$) we get the simple equation:

$$(C_{\text{XPS,ideal}} * g)(x) = \frac{1}{2} \left(1 - \operatorname{erf} \left(\frac{-x}{\sqrt{2}\sigma} \right) \right). \quad (\text{A.17})$$

As was mentioned above, the $g_\lambda(x)$ function significantly influences the slope of a concentration profile at the edges of the concentration transition zone, thus Eq. (A.17) does not reproduce precisely the concentration profiles of the sharp interfaces. However, Eq. (A.17) is sufficient to extract σ of the sharp interface, because $g_\lambda(x)$ makes the concentration profile asymmetric, while $g_\sigma(x)$ makes it symmetric. Thus, the influence of $g_\lambda(x)$ on σ extracted via Eq. (A.17) is strongly suppressed.

We use Eq. (A.17) to fit the concentration profiles of the unannealed sample in Fig. A.7(a). Each profile is marked with an index and the extracted parameters are collected in Table A.4. The roughness parameters σ for the solid lines 1 and 2 (for Py(5)/Pt_{0.98}Mn_{0.02} interface) are slightly higher than the initial value of the surface roughness. Moreover, σ for lines 3 and 4 are higher, than for lines 1 and 2. These facts are in agreement with the assumption of a σ enhancement during the Ar-etching.

Fit line number	σ (nm)
initial (AFM data)	1.3 ± 0.2
1	1.6 ± 0.2
2	1.42 ± 0.08
3	2.3 ± 0.3
4	2.4 ± 0.2

Table A.4: Extracted convolution parameters of Eq. (A.17) for the unannealed Py(5)/Pt_{0.98}Mn_{0.02}(10) sample. The numbers correspond to those in Fig. A.7(a).

The right end of the Py fit line 1 is lower than the experimental data points. This indicates a partial diffusion of Py into the Pt_{0.98}Mn_{0.02} alloy through the narrow grain boundary channels.

Next we extract the slope k from the Py concentration profile for the annealed sample in Fig. A.7(a). The fit is made with Eq. (A.16) in the t -range of 50-95 min (magenta line in the figure), where the O-concentration is 0%. We fixed σ at the level of 1.95 nm, which is an average of σ for lines 1,2,3,4 in Fig. A.7(a) and added an amplitude factor of 43% in Eq. (A.16). Other parameters are kept free. As the result we get $k = -0.072 \pm 0.015 \text{ nm}^{-1}$. From this we can easily calculate the "virtual" interdiffusion zone $\alpha = 1/k = 14 \pm 3 \text{ nm}$. Finally, we find the diffusion length $l_{\text{diff,XPS}}$ via the formula that we get during the development of the magnetic interdiffusion model in the section A.4 for diffusion stages (c)-(d) (development of formula is not explicitly described):

$$l_{\text{diff,XPS}} = \frac{(\alpha + d_i)^2}{4d_i}, \quad (\text{A.18})$$

where d_i is the thickness of the thinner layer of the FM/NM bilayer.

The diffusion length $l_{\text{diff,FMR}}$ is extrapolated from (A.12), where $D(T_i)$ is calculated via Eq. (A.3) with activation parameters from Table A.2. FMR-extracted diffusivity and XPS data are in a fair agreement within the error bars, see Table A.5.

Sample	$l_{\text{diff,FMR}}$ (nm)	$l_{\text{diff,XPS}}$ (nm)
Py(5)/Pt _{0.98} Mn _{0.02} (10)	22 ± 0.4	18 ± 4

Table A.5: Comparison of the diffusion lengths l_{diff} (after all annealing steps) extracted from FMR data and from XPS data

A.7 Conclusion on interdiffusion model

In principle, the described "magnetic" interdiffusion model works quite well and the extracted value of the activation enthalpy is reliable within 18% range. Not many techniques give an access to the interdiffusion process in structures of 1-10 nm thickness range and at relatively low annealing temperatures. To the best of the authors knowledge, no comparable magnetic models for FM/NM pairs are developed. The model might be extended on the case of a FM/FM bilayer without any change in calculation procedure. Generally, it is well applicable for most of the 3d-FM metal/any metal interfaces (Mn is one of the exceptions, as it introduces antiferromagnetic order).

However, our experiments on Al(3)/Py(10)/Cu_{0.98}Au_{0.02}(5)/Alumina(20)/Si₃N₄ sample (experimental data are not included here) grown in MBE show, that strains induced in the FM/NM interface produce inhomogeneous canting of the magnetization in out-of-plane direction and cracking of the sample surface during annealing with subsequent partial oxidation of the FM/NM. Both facts make an interpretation of the $M_S(T)$ evolution during annealing difficult.

List of other possible problems of the model (also in relation to other systems):

1. in the very beginning we have implicitly assumed that interdiffusion process is homogeneous, making it possible to describe the problem with the effective diffusivity in spatial-1D Fick's eq. (A.1). However, a numerical simulation with 2D Fick's equation [93], where grain-boundary channels (with D different than the volume diffusivity) are introduced, show that the 1D description is not always sufficiently precise. Cases with an average spacing between grain boundaries either extremely large (vanishing amount of grain boundaries) or very small (10 nm and smaller, also depend on T) can be well described with the 1D model. Polycrystalline thin films usually have grain sizes comparable with their thickness, thus 1D Fick's model is usually applicable for structures with layer thicknesses below 20 nm.
2. for oxygen-containing materials the calculation of the magnetization and its dependence on the concentrations of the constituents needs to be modified, because oxygen tends to form antiferromagnetic order;
3. if the initial stack consists of materials with different density of packing, one should consider violation of the Arrhenius law (A.3);
4. interstitial diffusion (dilution into FM crystal) of elements with small atomic radii (below 100 pm): H, B, C, N. These elements disturb the average distances between the FM atoms, thus leading to a change of the exchange integrals. A classical example is the striking change of the magnetic properties of iron alloys when H is diluted in it [p.379 in 28];

5. one might need to use SQUID or VSM to estimate M_S of relatively thick samples (≈ 45 nm for Py, ≈ 10 nm for Cu and ≈ 65 nm for Pt), since CPW-FMR has limited depth-sensitivity because of aforementioned RF magnetic field shielding. However, CPW-FMR gives an insight into the change of magnetic damping due to diffusion. In principle, some interdiffusion model based on the magnetic damping might be developed (for a detailed discussion of damping mechanisms see [Ch. 5 in 16]), but magnetic damping is far more sample-dependent and more difficult to interpret than M_S . CPW-FMR is also a tool to get a qualitative picture of magnetic inhomogeneities of different kind, like pores in a FM material, polycrystalline grains, pinning of magnetization direction at interfaces and others (all derived from contribution to line-width because of two-magnon processes [16]).
6. in some FM systems, which constituents are not 3d-FM. For example Heusler compounds, particularly Cu_2MnAl : models based on findings of Slater and Pauling (magnetic valence model, rigid band model) fail to estimate M_S of this material [10].

Bibliography

- [1] Hiroto Adachi et al. “Gigantic enhancement of spin Seebeck effect by phonon drag”. In: *Applied Physics Letters* 97.25 (2010), pp. 2012–2015. DOI: [10.1063/1.3529944](https://doi.org/10.1063/1.3529944).
- [2] A. Aharoni. “Demagnetizing factors for rectangular ferromagnetic prisms”. In: *J. Appl. Phys.* 83.1998 (1998), pp. 3432–3434. DOI: [10.1063/1.367113](https://doi.org/10.1063/1.367113).
- [3] V. P. Amin and M. D. Stiles. “Spin transport at interfaces with spin-orbit coupling: Formalism”. In: *Phys. Rev. B* 94 (10 2016), p. 104419. DOI: [10.1103/PhysRevB.94.104419](https://doi.org/10.1103/PhysRevB.94.104419).
- [4] K. Ando et al. “Electric Manipulation of Spin Relaxation Using the Spin Hall Effect”. In: *Phys. Rev. Lett.* 101 (3 2008), p. 036601. DOI: [10.1103/PhysRevLett.101.036601](https://doi.org/10.1103/PhysRevLett.101.036601).
- [5] N.W. Ashcroft and N. Mermin. *Solid state physics*. Cengage Learning, Inc, 1976.
- [6] A. D. Avery, M. R. Pufall, and B. L. Zink. “Observation of the planar nernst effect in permalloy and Nickel thin films with in-plane thermal gradients”. In: *Physical Review Letters* 109.19 (2012), pp. 1–5. DOI: [10.1103/PhysRevLett.109.196602](https://doi.org/10.1103/PhysRevLett.109.196602).
- [7] S.D. Bader. “SMOKE”. In: *Journal of Magnetism and Magnetic Materials* 100.1 (1991), pp. 440–454. DOI: [https://doi.org/10.1016/0304-8853\(91\)90833-V](https://doi.org/10.1016/0304-8853(91)90833-V).
- [8] M. N. Baibich et al. “Giant Magnetoresistance of (001)Fe/(001)Cr Magnetic Superlattices”. In: *Phys. Rev. Lett.* 61 (21 1988), pp. 2472–2475. DOI: [10.1103/PhysRevLett.61.2472](https://doi.org/10.1103/PhysRevLett.61.2472).
- [9] Matthieu Bailleul. “Shielding of the electromagnetic field of a coplanar waveguide by a metal film: Implications for broadband ferromagnetic resonance measurements”. In: *Applied Physics Letters* 103.19 (2013), p. 192405. DOI: [10.1063/1.4829367](https://doi.org/10.1063/1.4829367).
- [10] Benjamin Balke et al. “Rational design of new materials for spintronics: Co₂FeZ (Z=Al, Ga, Si, Ge)”. In: *Science and Technology of Advanced Materials* 9.1 (2008). DOI: <https://doi.org/10.1088/1468-6996/9/1/014102>.
- [11] Cemal Basaran, Minghui Lin, and Hua Ye. “A thermodynamic model for electrical current induced damage”. In: *International Journal of Solids and Structures* 40.26 (2003), pp. 7315–7327. DOI: <http://dx.doi.org/10.1016/j.ijsolstr.2003.08.018>.
- [12] Gerrit E. W. Bauer, Eiji Saitoh, and Bart J. van Wees. “Spin caloritronics”. In: *Nature Materials* 11.5 (Apr. 2012), pp. 391–399. DOI: [10.1038/nmat3301](https://doi.org/10.1038/nmat3301).

-
- [13] Gerrit E. W. Bauer et al. “Nanoscale magnetic heat pumps and engines”. In: *Phys. Rev. B* 81 (2 2010), p. 024427. DOI: [10.1103/PhysRevB.81.024427](https://doi.org/10.1103/PhysRevB.81.024427).
- [14] L. Berger. “Influence of spin-orbit interaction on the transport processes in ferromagnetic nickel alloys, in the presence of a degeneracy of the 3d band”. In: *Physica* 30.6 (1964), pp. 1141–1159. DOI: [https://doi.org/10.1016/0031-8914\(64\)90105-3](https://doi.org/10.1016/0031-8914(64)90105-3).
- [15] G. Binasch et al. “Enhanced magnetoresistance in layered magnetic structures with antiferromagnetic interlayer exchange”. In: *Phys. Rev. B* 39 (7 1989), pp. 4828–4830. DOI: [10.1103/PhysRevB.39.4828](https://doi.org/10.1103/PhysRevB.39.4828).
- [16] J.A.C. Bland and B. Heinrich. *Ultrathin Magnetic Structures III: Fundamentals of Nanomagnetism*. 1st ed. Springer-Verlag Berlin Heidelberg, 2005.
- [17] S. Bosu et al. “Spin Seebeck effect in thin films of the Heusler compound Co₂MnSi”. In: *Physical Review B - Condensed Matter and Materials Physics* 83.22 (2011), pp. 1–6. DOI: [10.1103/PhysRevB.83.224401](https://doi.org/10.1103/PhysRevB.83.224401).
- [18] Olivier Bourgeois et al. “Reduction of phonon mean free path: From low-temperature physics to room temperature applications in thermoelectricity”. In: *Comptes Rendus Physique* 17.10 (2016). Mesoscopic thermoelectric phenomena / Phénomènes thermoélectriques mésoscopiques, pp. 1154–1160. DOI: <https://doi.org/10.1016/j.crhy.2016.08.008>.
- [19] Arne Brataas, Gerrit E.W. Bauer, and Paul J. Kelly. “Non-collinear magnetoelectronics”. In: *Physics Reports* 427.4 (2006), pp. 157–255. DOI: <https://doi.org/10.1016/j.physrep.2006.01.001>.
- [20] P. Bruno. “Berry phase effects in magnetism”. In: *eprint arXiv:cond-mat/0506270* (June 2005).
- [21] K.H.J. Buschow. *Handbook of Magnetic Materials, Volume 19*. Handbook of Magnetic Materials. North Holland, 2011.
- [22] Win-Jin Chang, Te-Hua Fang, and Chao-Ming Lin. “Thermally induced viscoelastic stresses in multilayer thin films”. In: *Journal of Applied Physics* 97.10 (2005), p. 103521. DOI: [10.1063/1.1905797](https://doi.org/10.1063/1.1905797).
- [23] Claude Chappert, Albert Fert, and Frédéric Nguyen Van Dau. “The emergence of spin electronics in data storage”. In: *Nature Materials* 6.11 (2007), pp. 813–823. DOI: [10.1038/nmat2024](https://doi.org/10.1038/nmat2024).
- [24] Jian Chen and J. L. Erskine. “Surface-step-induced magnetic anisotropy in thin epitaxial Fe films on W(001)”. In: *Phys. Rev. Lett.* 68 (8 1992), pp. 1212–1215. DOI: [10.1103/PhysRevLett.68.1212](https://doi.org/10.1103/PhysRevLett.68.1212).
- [25] Yan-Ting Chen et al. “Theory of spin Hall magnetoresistance”. In: *Phys. Rev. B* 87 (14 2013), p. 144411. DOI: [10.1103/PhysRevB.87.144411](https://doi.org/10.1103/PhysRevB.87.144411).
- [26] Shu-guang Cheng et al. “Spin Nernst effect and Nernst effect in two-dimensional electron systems”. In: *Phys. Rev. B* 78 (4 2008), p. 045302. DOI: [10.1103/PhysRevB.78.045302](https://doi.org/10.1103/PhysRevB.78.045302).
- [27] D. B. Chrisey and G. K. Hubler. *Pulsed Laser Deposition of Thin Films*. May 2003, p. 648.
- [28] J. M. D. Coey. *Magnetism and magnetic materials*. Cambridge University Press, 2009.
-

- [29] G Council et al. “Temperature Dependences of the Resistivity and the Ferromagnetic Resonance Linewidth in Permalloy Thin Films”. In: 42 (Nov. 2006), pp. 3323–3325.
- [30] J. Crangle and D. Parsons. “The magnetization of ferromagnetic binary alloys of cobalt or nickel with elements of the palladium and platinum groups”. In: *Proceedings of the Royal Society of London A: Mathematical, Physical and Engineering Sciences* 255.1283 (1960), pp. 509–519. DOI: [10.1098/rspa.1960.0083](https://doi.org/10.1098/rspa.1960.0083).
- [31] Melvin Cutler and N. F. Mott. “Observation of Anderson Localization in an Electron Gas”. In: *Phys. Rev.* 181 (3 1969), pp. 1336–1340. DOI: [10.1103/PhysRev.181.1336](https://doi.org/10.1103/PhysRev.181.1336).
- [32] C. Daboo et al. “Anisotropy and orientational dependence of magnetization reversal processes in epitaxial ferromagnetic thin films”. In: *Phys. Rev. B* 51 (22 1995), pp. 15964–15973. DOI: [10.1103/PhysRevB.51.15964](https://doi.org/10.1103/PhysRevB.51.15964).
- [33] Martin M. Decker. “Spin current induced control of magnetization dynamics”. PhD thesis. University of Regensburg, 2017.
- [34] F. K. Dejene, J. Flipse, and B. J. van Wees. “Spin-dependent Seebeck coefficients of Ni₈₀Fe₂₀ and Co in nanopillar spin valves”. In: *Phys. Rev. B* 86.2, 024436 (July 2012), p. 024436. DOI: [10.1103/PhysRevB.86.024436](https://doi.org/10.1103/PhysRevB.86.024436).
- [35] Vadegadde Duggappa Divya, Upadrasta Ramamurty, and Alope Paul. “Interdiffusion and the vacancy wind effect in Ni–Pt and Co–Pt systems”. In: *Journal of Materials Research* 26.18 (2011), 2384–2393. DOI: [10.1557/jmr.2011.203](https://doi.org/10.1557/jmr.2011.203).
- [36] M. G. Dowsett et al. “An analytic form for the SIMS response function measured from ultra-thin impurity layers”. In: *Surface and Interface Analysis* 21.5 (1994), pp. 310–315. DOI: [10.1002/sia.740210508](https://doi.org/10.1002/sia.740210508).
- [37] G. Dresselhaus. “Spin-Orbit Coupling Effects in Zinc Blende Structures”. In: *Phys. Rev.* 100 (2 1955), pp. 580–586. DOI: [10.1103/PhysRev.100.580](https://doi.org/10.1103/PhysRev.100.580).
- [38] M. I. Dyakonov. “Spin Hall Effect”. In: *Spintronics*. Ed. by Manijeh Razeghi, Henri-Jean M. Drouhin, and Jean-Eric Wegrowe. Vol. 7036. International Society for Optics and Photonics. SPIE, 2008, pp. 105–118. DOI: [10.1117/12.798110](https://doi.org/10.1117/12.798110).
- [39] M.I. Dyakonov and V.I. Perel. “Current-induced spin orientation of electrons in semiconductors”. In: *Physics Letters A* 35.6 (1971), pp. 459–460. DOI: [https://doi.org/10.1016/0375-9601\(71\)90196-4](https://doi.org/10.1016/0375-9601(71)90196-4).
- [40] M.I. D’yakonov and V.I. Perel’. “Possibility of Orienting Electron Spins with Current”. In: *ZhETF Pis ma Redaktsiiu* 13.11 (1971), pp. 467–469.
- [41] Anna Dyrdał and J Barnaś. “Intrinsic contribution to spin Hall and spin Nernst effects in a bilayer graphene”. In: *Journal of physics. Condensed matter : an Institute of Physics journal* 24 (June 2012), p. 275302. DOI: [10.1088/0953-8984/24/27/275302](https://doi.org/10.1088/0953-8984/24/27/275302).
- [42] R. J. Elliott. “Theory of the Effect of Spin-Orbit Coupling on Magnetic Resonance in Some Semiconductors”. In: *Phys. Rev.* 96 (2 1954), pp. 266–279. DOI: [10.1103/PhysRev.96.266](https://doi.org/10.1103/PhysRev.96.266).

-
- [43] A. v. Etingshausen and W. Nernst. “Ueber das Auftreten electromotorischer Kräfte in Metallplatten, welche von einem Wärmestrome durchflossen werden und sich im magnetischen Felde befinden.” In: *Annalen der Physik* 10 (1886), pp. 343–347. DOI: [10.1002/andp.18862651010](https://doi.org/10.1002/andp.18862651010).
- [44] A. Fert, A. Friederich, and A. Hamzic. “Hall effect in dilute magnetic alloys”. In: *Journal of Magnetism and Magnetic Materials* 24.3 (1981), pp. 231–257. DOI: [https://doi.org/10.1016/0304-8853\(81\)90079-2](https://doi.org/10.1016/0304-8853(81)90079-2).
- [45] Albert Fert and Peter M. Levy. “Spin Hall Effect Induced by Resonant Scattering on Impurities in Metals”. In: *Phys. Rev. Lett.* 106 (15 2011), p. 157208. DOI: [10.1103/PhysRevLett.106.157208](https://doi.org/10.1103/PhysRevLett.106.157208).
- [46] Richard P. Feynman, Robert B. Leighton, and Matthew Sands. *The Feynman lectures on physics, Volume II*. Addison-Wesley publishing company inc., 2011.
- [47] Z. Frait et al. “On the effective magnetization and uniaxial anisotropy of permalloy films”. In: *Czechoslovakij fiziceskij zurnal B* 13.4 (1963), pp. 279–285. DOI: [10.1007/BF01688466](https://doi.org/10.1007/BF01688466).
- [48] Frank Freimuth, Stefan Blügel, and Yuriy Mokrousov. “Anisotropic Spin Hall Effect from First Principles”. In: *Phys. Rev. Lett.* 105 (24 2010), p. 246602. DOI: [10.1103/PhysRevLett.105.246602](https://doi.org/10.1103/PhysRevLett.105.246602).
- [49] K. Fuchs. “The conductivity of thin metallic films according to the electron theory of metals”. In: *Mathematical Proceedings of the Cambridge Philosophical Society* 34.1 (1938), 100–108. DOI: [10.1017/S0305004100019952](https://doi.org/10.1017/S0305004100019952).
- [50] Parag Gadkari. “Effect of Annealing on Copper Thin Films: the Classical Size Effect And Agglomeration”. MA thesis. University of Central Florida, 2005.
- [51] Daniel Gall. “Electron mean free path in elemental metals”. In: *Journal of Applied Physics* 119.8 (2016), p. 085101. DOI: [10.1063/1.4942216](https://doi.org/10.1063/1.4942216).
- [52] S. D. Ganichev et al. “Spin-galvanic effect”. In: *Nature* 417 (2002), 153 EP –.
- [53] Stephan Geprägs et al. “Investigation of induced Pt magnetic polarization in Pt/Y3Fe5O12 bilayers”. In: *Applied Physics Letters* 101.26 (2012), p. 262407. DOI: [10.1063/1.4773509](https://doi.org/10.1063/1.4773509).
- [54] Guillaume Géranton et al. “Spin-orbit torques in $L1_0$ – FePt/Pt thin films driven by electrical and thermal currents”. In: *Phys. Rev. B* 91 (1 2015), p. 014417. DOI: [10.1103/PhysRevB.91.014417](https://doi.org/10.1103/PhysRevB.91.014417).
- [55] Weiyan Gong et al. “Diffusivities and atomic mobilities in fcc Ni–Pt alloys”. In: *Scripta Materialia* 61.1 (2009), pp. 100–103. DOI: <http://dx.doi.org/10.1016/j.scriptamat.2009.03.010>.
- [56] Martin Gradhand et al. “Extrinsic Spin Hall Effect from First Principles”. In: *Phys. Rev. Lett.* 104 (18 2010), p. 186403. DOI: [10.1103/PhysRevLett.104.186403](https://doi.org/10.1103/PhysRevLett.104.186403).
- [57] G. Gubbiotti et al. “Perpendicular and in-plane magnetic anisotropy in epitaxial Cu/Ni/Cu/Si(111) ultrathin films”. In: *Phys. Rev. B* 56 (17 1997), pp. 11073–11083. DOI: [10.1103/PhysRevB.56.11073](https://doi.org/10.1103/PhysRevB.56.11073).
-

- [58] A.G. Gurevich and G.A. Melkov. *Magnetization oscillations and waves*. CRC Press, 1996.
- [59] E. H. Hall. “On a New Action of the Magnet on Electric Currents”. In: *American Journal of Mathematics* 2.3 (1879), pp. 287–292.
- [60] E.H. Hall. “XVIII. On the “Rotational Coefficient” in nickel and cobalt”. In: *The London, Edinburgh, and Dublin Philosophical Magazine and Journal of Science* 12.74 (1881), pp. 157–172. DOI: [10.1080/14786448108627086](https://doi.org/10.1080/14786448108627086).
- [61] Paul M. Haney et al. “Current induced torques and interfacial spin-orbit coupling: Semiclassical modeling”. In: *Phys. Rev. B* 87 (17 2013), p. 174411. DOI: [10.1103/PhysRevB.87.174411](https://doi.org/10.1103/PhysRevB.87.174411).
- [62] Christoph Hauser et al. “Yttrium Iron Garnet Thin Films with Very Low Damping Obtained by Recrystallization of Amorphous Material”. In: *Scientific Reports* 6 (2016). Article, 20827 EP –.
- [63] Paul S. Ho and Thomas Kwok. “Electromigration in metals”. In: *Reports on Progress in Physics* 52.3 (1989), p. 301.
- [64] S. Hofmann. “Sputter depth profiling: past, present, and future”. In: *Surface and Interface Analysis* 46.10-11 (2014). SIA-13-0581, pp. 654–662. DOI: [10.1002/sia.5489](https://doi.org/10.1002/sia.5489).
- [65] S. Hofmann et al. “Comparison of Analytical and Numerical Resolution Functions in Sputter Depth Profiling”. In: *ArXiv e-prints* (Jan. 2014).
- [66] Siegfried Hofmann. “Atomic mixing, surface roughness and information depth in high-resolution AES depth profiling of a GaAs/AlAs superlattice structure”. In: *Surface and Interface Analysis* 21.9 (1994), pp. 673–678. DOI: [10.1002/sia.740210912](https://doi.org/10.1002/sia.740210912).
- [67] <https://www.comsol.com/>. *Introduction to COMSOL Multiphysics*. <https://cdn.comsol.com/documentation/5.4.0.225/IntroductionToCOMSOLMultiphysics.pdf>.
- [68] S. Y. Huang et al. “Intrinsic spin-dependent thermal transport”. In: *Physical Review Letters* 107.21 (2011), pp. 1–4. DOI: [10.1103/PhysRevLett.107.216604](https://doi.org/10.1103/PhysRevLett.107.216604).
- [69] S. Y. Huang et al. “Transport Magnetic Proximity Effects in Platinum”. In: *Phys. Rev. Lett.* 109 (10 2012), p. 107204. DOI: [10.1103/PhysRevLett.109.107204](https://doi.org/10.1103/PhysRevLett.109.107204).
- [70] C M Jaworski et al. “Observation of the spin-Seebeck effect in a ferromagnetic semiconductor.” In: *Nature materials* 9.11 (2010), pp. 898–903. DOI: [10.1038/nmat2860](https://doi.org/10.1038/nmat2860).
- [71] C. M. Jaworski et al. “Spin-seebeck effect: A phonon driven spin distribution”. In: *Physical Review Letters* 106.18 (2011). DOI: [10.1103/PhysRevLett.106.186601](https://doi.org/10.1103/PhysRevLett.106.186601).
- [72] M. B. Jungfleisch et al. “Improvement of the yttrium iron garnet/platinum interface for spin pumping-based applications”. In: *Applied Physics Letters* 103.2 (2013), p. 022411. DOI: [10.1063/1.4813315](https://doi.org/10.1063/1.4813315).

-
- [73] A. Kaibi et al. “Structure, microstructure and magnetic properties of Ni₇₅Fe₂₅ films elaborated by evaporation from nanostructured powder”. In: *Applied Surface Science* 350 (2015). SATF2014 : Science and Applications of Thin Films, Conference & Exhibition, pp. 50–56. DOI: <https://doi.org/10.1016/j.apsusc.2015.02.050>.
- [74] Y. K. Kato et al. “Observation of the Spin Hall Effect in Semiconductors”. In: *Science* 306.5703 (2004), pp. 1910–1913. DOI: [10.1126/science.1105514](https://doi.org/10.1126/science.1105514).
- [75] Andreas Kehlberger et al. “Length Scale of the Spin Seebeck Effect”. In: *Phys. Rev. Lett.* 115 (9 2015), p. 096602. DOI: [10.1103/PhysRevLett.115.096602](https://doi.org/10.1103/PhysRevLett.115.096602).
- [76] T. Kimura et al. “Room-temperature reversible spin hall effect”. In: *Physical Review Letters* 98.15 (2007), pp. 1–4. DOI: [10.1103/PhysRevLett.98.156601](https://doi.org/10.1103/PhysRevLett.98.156601).
- [77] C. Kittel. *Introduction to Solid State Physics*. Wiley, 2004.
- [78] Ling Bing Kong et al. *Waste Energy Harvesting: Mechanical and Thermal Energies*. 1st ed. Lecture Notes in Energy 24. Springer-Verlag Berlin Heidelberg, 2014.
- [79] T. Kuschel et al. “Uniaxial magnetic anisotropy for thin Co films on glass studied by magneto-optic Kerr effect”. In: *Journal of Applied Physics* 109.9 (2011), p. 093907. DOI: [10.1063/1.3576135](https://doi.org/10.1063/1.3576135).
- [80] Vu Dinh Ky. “Planar Hall and Nernst Effect in Ferromagnetic Metals”. In: *Physica Status Solidi (B)* 22.2 (1967), pp. 729–736. DOI: [10.1002/pssb.19670220242](https://doi.org/10.1002/pssb.19670220242).
- [81] Clemens J. M. Lasance. *The Seebeck Coefficient*. Online; accessed 1-Feb-2013. 2006.
- [82] Xiaoyu Li et al. “Magnetic properties of permalloy films with different thicknesses deposited onto obliquely sputtered Cu underlayers”. In: *Journal of Magnetism and Magnetic Materials* 377 (2015), pp. 142–146. DOI: <https://doi.org/10.1016/j.jmmm.2014.10.029>.
- [83] Xiao Liang et al. “Influence of Interface Structure on Magnetic Proximity Effect in Pt/Y₃Fe₅O₁₂ Heterostructures”. In: *ACS Applied Materials & Interfaces* 8.12 (2016). PMID: 26967756, pp. 8175–8183. DOI: [10.1021/acsami.5b11173](https://doi.org/10.1021/acsami.5b11173).
- [84] Jens Lienig. “Introduction to Electromigration-aware Physical Design”. In: *Proceedings of the 2006 International Symposium on Physical Design*. ISPD '06. San Jose, California, USA: ACM, 2006, pp. 39–46. DOI: [10.1145/1123008.1123017](https://doi.org/10.1145/1123008.1123017).
- [85] Luqiao Liu et al. “Spin-Torque Ferromagnetic Resonance Induced by the Spin Hall Effect”. In: *Phys. Rev. Lett.* 106 (3 2011), p. 036601. DOI: [10.1103/PhysRevLett.106.036601](https://doi.org/10.1103/PhysRevLett.106.036601).
- [86] Xuele Liu and X.C. Xie. “Spin Nernst effect in the absence of a magnetic field”. In: *Solid State Communications* 150.11 (2010). Spin Caloritronics, pp. 471–474. DOI: <https://doi.org/10.1016/j.ssc.2009.12.017>.
-

- [87] Nguyen H. Long et al. “Giant spin Nernst effect induced by resonant scattering at surfaces of metallic films”. In: *Phys. Rev. B* 93 (18 2016), p. 180406. DOI: [10.1103/PhysRevB.93.180406](https://doi.org/10.1103/PhysRevB.93.180406).
- [88] Y. M. Lu et al. “Hybrid magnetoresistance in the proximity of a ferromagnet”. In: *Phys. Rev. B* 87 (22 2013), p. 220409. DOI: [10.1103/PhysRevB.87.220409](https://doi.org/10.1103/PhysRevB.87.220409).
- [89] Y. M. Lu et al. “Pt Magnetic Polarization on $\text{Y}_3\text{Fe}_5\text{O}_{12}$ and Magnetotransport Characteristics”. In: *Phys. Rev. Lett.* 110 (14 2013), p. 147207. DOI: [10.1103/PhysRevLett.110.147207](https://doi.org/10.1103/PhysRevLett.110.147207).
- [90] G. D. Mahan, L. Lindsay, and D. A. Broido. “The Seebeck coefficient and phonon drag in silicon”. In: *Journal of Applied Physics* 116.24 (2014), p. 245102. DOI: [10.1063/1.4904925](https://doi.org/10.1063/1.4904925).
- [91] A. Manchon and S. Zhang. “Theory of spin torque due to spin-orbit coupling”. In: *Phys. Rev. B* 79 (9 2009), p. 094422. DOI: [10.1103/PhysRevB.79.094422](https://doi.org/10.1103/PhysRevB.79.094422).
- [92] A. F. Mayadas and M. Shatzkes. “Electrical-Resistivity Model for Polycrystalline Films: the Case of Arbitrary Reflection at External Surfaces”. In: *Phys. Rev. B* 1 (4 1970), pp. 1382–1389. DOI: [10.1103/PhysRevB.1.1382](https://doi.org/10.1103/PhysRevB.1.1382).
- [93] Helmut Mehrer. *Diffusion in Solids*. Springer series in Solid State science 155. Springer, 2007.
- [94] D. Meier et al. “Influence of heat flow directions on Nernst effects in Py/Pt bilayers”. In: *Physical Review B - Condensed Matter and Materials Physics* 88.18 (2013), pp. 1–6. DOI: [10.1103/PhysRevB.88.184425](https://doi.org/10.1103/PhysRevB.88.184425).
- [95] D. Meier et al. “Thermally driven spin and charge currents in thin $\text{NiFe}_2\text{O}_4/\text{Pt}$ films”. In: *Phys. Rev. B* 87 (5 2013), p. 054421. DOI: [10.1103/PhysRevB.87.054421](https://doi.org/10.1103/PhysRevB.87.054421).
- [96] Daniel Meier et al. “Longitudinal spin Seebeck effect contribution in transverse spin Seebeck effect experiments in Pt/YIG and Pt/NFO”. In: *Nature Communications* 6 (2015). Article, 8211 EP –.
- [97] J. Mendil et al. “Magnetic properties and domain structure of ultrathin yttrium iron garnet/Pt bilayers”. In: *Phys. Rev. Materials* 3 (3 2019), p. 034403. DOI: [10.1103/PhysRevMaterials.3.034403](https://doi.org/10.1103/PhysRevMaterials.3.034403).
- [98] Sergiy Merzlikin. “Depth Profiling by X-ray Photoelectron Spectroscopy”. PhD thesis. Ruhr-Universität Bochum, 2007.
- [99] S. Meyer et al. “Observation of the spin Nernst effect”. In: *Nature Materials* 16 (2017), 977 EP –.
- [100] T. Miyazaki and N. Tezuka. “Giant magnetic tunneling effect in Fe/ Al_2O_3 /Fe junction”. In: *Journal of Magnetism and Magnetic Materials* 139.3 (1995), pp. L231 –L234. DOI: [https://doi.org/10.1016/0304-8853\(95\)90001-2](https://doi.org/10.1016/0304-8853(95)90001-2).
- [101] S Mizukami, Y Ando, and T Miyazaki. “Ferromagnetic resonance linewidth for NM/80NiFe/NM films (NM=Cu, Ta, Pd and Pt)”. In: *Journal of Magnetism and Magnetic Materials* 226-230 (2001). Proceedings of the International Conference on Magnetism (ICM 2000), pp. 1640 –1642. DOI: [https://doi.org/10.1016/S0304-8853\(00\)01097-0](https://doi.org/10.1016/S0304-8853(00)01097-0).

-
- [102] J. S. Moodera et al. “Large Magnetoresistance at Room Temperature in Ferromagnetic Thin Film Tunnel Junctions”. In: *Phys. Rev. Lett.* 74 (16 1995), pp. 3273–3276. DOI: [10.1103/PhysRevLett.74.3273](https://doi.org/10.1103/PhysRevLett.74.3273).
- [103] Nevill Francis Mott and Niels Henrik David Bohr. “The scattering of fast electrons by atomic nuclei”. In: *Proceedings of the Royal Society of London. Series A, Containing Papers of a Mathematical and Physical Character* 124.794 (1929), pp. 425–442. DOI: [10.1098/rspa.1929.0127](https://doi.org/10.1098/rspa.1929.0127).
- [104] Nevill Francis Mott and Ralph Howard Fowler. “The electrical conductivity of transition metals”. In: *Proceedings of the Royal Society of London. Series A - Mathematical and Physical Sciences* 153.880 (1936), pp. 699–717. DOI: [10.1098/rspa.1936.0031](https://doi.org/10.1098/rspa.1936.0031).
- [105] Nevill Francis Mott and Ralph Howard Fowler. “The polarisation of electrons by double scattering”. In: *Proceedings of the Royal Society of London. Series A, Containing Papers of a Mathematical and Physical Character* 135.827 (1932), pp. 429–458. DOI: [10.1098/rspa.1932.0044](https://doi.org/10.1098/rspa.1932.0044).
- [106] Naoto Nagaosa et al. “Anomalous Hall effect”. In: *Rev. Mod. Phys.* 82 (2 2010), pp. 1539–1592. DOI: [10.1103/RevModPhys.82.1539](https://doi.org/10.1103/RevModPhys.82.1539).
- [107] N. Nakajima et al. “Perpendicular Magnetic Anisotropy Caused by Interfacial Hybridization via Enhanced Orbital Moment in Co/Pt Multilayers: Magnetic Circular X-Ray Dichroism Study”. In: *Phys. Rev. Lett.* 81 (23 1998), pp. 5229–5232. DOI: [10.1103/PhysRevLett.81.5229](https://doi.org/10.1103/PhysRevLett.81.5229).
- [108] Peter Ozaveshe Oviroh et al. “New development of atomic layer deposition: processes, methods and applications”. In: *Science and Technology of Advanced Materials* 20.1 (2019). PMID: 31164953, pp. 465–496. DOI: [10.1080/14686996.2019.1599694](https://doi.org/10.1080/14686996.2019.1599694).
- [109] Yongsup Park, Eric E. Fullerton, and S. D. Bader. “Growth-induced uniaxial in-plane magnetic anisotropy for ultrathin Fe deposited on MgO(001) by oblique-incidence molecular beam epitaxy”. In: *Applied Physics Letters* 66.16 (1995), pp. 2140–2142. DOI: [10.1063/1.113929](https://doi.org/10.1063/1.113929).
- [110] Linus Pauling. “The Nature of the Interatomic Forces in Metals”. In: *Phys. Rev.* 54 (11 1938), pp. 899–904. DOI: [10.1103/PhysRev.54.899](https://doi.org/10.1103/PhysRev.54.899).
- [111] Yong Pu et al. “Anisotropic thermopower and planar Nernst effect in Ga_{1-x}Mn_xAs ferromagnetic semiconductors”. In: *Physical Review Letters* 97.3 (2006), pp. 1–4. DOI: [10.1103/PhysRevLett.97.036601](https://doi.org/10.1103/PhysRevLett.97.036601).
- [112] E. Rashba. “Properties of semiconductors with an extremum loop. I. Cyclotron and combinational resonance in a magnetic field perpendicular to the plane of the loop”. In: *Sov. Phys. Solid State* 2 (1960), pp. 1109–1122.
- [113] Oliver Reimer et al. “Quantitative separation of the anisotropic magnetothermopower and planar Nernst effect by the rotation of an in-plane thermal gradient”. In: *Scientific Reports* 7 (2017). Article, 40586 EP –.
- [114] E. Saitoh et al. “Conversion of spin current into charge current at room temperature: Inverse spin-Hall effect”. In: *Applied Physics Letters* 88.18 (2006), pp. 1–4. DOI: [10.1063/1.2199473](https://doi.org/10.1063/1.2199473).
-

- [115] M.C. Salvadori et al. “Measurement of Electrical Resistivity of Nanostructured Platinum Thin Films and Quantum Mechanical Estimates”. In: *Metastable, Mechanically Alloyed and Nanocrystalline Materials 2003*. Vol. 20. Journal of Metastable and Nanocrystalline Materials. Trans Tech Publications, July 2004, pp. 775–780. DOI: [10.4028/www.scientific.net/JMMN.20-21.775](https://doi.org/10.4028/www.scientific.net/JMMN.20-21.775).
- [116] J.R. Sambles. “The resistivity of thin metal films—Some critical remarks”. In: *Thin Solid Films* 106.4 (1983), pp. 321–331. DOI: [https://doi.org/10.1016/0040-6090\(83\)90344-9](https://doi.org/10.1016/0040-6090(83)90344-9).
- [117] M. Schmid et al. “Transverse spin seebeck effect versus anomalous and planar nernst effects in permalloy thin films”. In: *Physical Review Letters* 111.18 (2013), pp. 1–5. DOI: [10.1103/PhysRevLett.111.187201](https://doi.org/10.1103/PhysRevLett.111.187201).
- [118] Michael Schreier et al. “Magnon, phonon, and electron temperature profiles and the spin Seebeck effect in magnetic insulator/normal metal hybrid structures”. In: *Phys. Rev. B* 88 (9 2013), p. 094410. DOI: [10.1103/PhysRevB.88.094410](https://doi.org/10.1103/PhysRevB.88.094410).
- [119] M. P. Seah and W. A. Dench. “Quantitative electron spectroscopy of surfaces: A standard data base for electron inelastic mean free paths in solids”. In: *Surface and Interface Analysis* 1.1 (1979), pp. 2–11. DOI: [10.1002/sia.740010103](https://doi.org/10.1002/sia.740010103).
- [120] A. S. Shestakov et al. “Dependence of transverse magnetothermoelectric effects on inhomogeneous magnetic fields”. In: *Phys. Rev. B* 92 (22 2015), p. 224425. DOI: [10.1103/PhysRevB.92.224425](https://doi.org/10.1103/PhysRevB.92.224425).
- [121] Gene Siegel et al. “Robust longitudinal spin-Seebeck effect in Bi-YIG thin films”. In: *Scientific Reports* 4 (2014). Article, 4429 EP –.
- [122] J. Sinova et al. “Spin Hall effects”. In: *Reviews of Modern Physics* 87 (Oct. 2015), pp. 1213–1260. DOI: [10.1103/RevModPhys.87.1213](https://doi.org/10.1103/RevModPhys.87.1213).
- [123] T. D. Skinner et al. “Spin-orbit torque opposing the Oersted torque in ultrathin Co/Pt bilayers”. In: *Applied Physics Letters* 104.6 (2014), p. 062401. DOI: [10.1063/1.4864399](https://doi.org/10.1063/1.4864399).
- [124] A. Slachter et al. “Thermally driven spin injection from a ferromagnet into a non-magnetic metal”. In: *Nature Physics* 6 (2010), 879 EP –.
- [125] J. C. Slater. “The Ferromagnetism of Nickel. II. Temperature Effects”. In: *Phys. Rev.* 49 (12 1936), pp. 931–937. DOI: [10.1103/PhysRev.49.931](https://doi.org/10.1103/PhysRev.49.931).
- [126] J.C. Slonczewski. “Current-driven excitation of magnetic multilayers”. In: *Journal of Magnetism and Magnetic Materials* 159.1 (1996), pp. L1–L7. DOI: [https://doi.org/10.1016/0304-8853\(96\)00062-5](https://doi.org/10.1016/0304-8853(96)00062-5).
- [127] John C. Slonczewski. “Initiation of spin-transfer torque by thermal transport from magnons”. In: *Phys. Rev. B* 82 (5 2010), p. 054403. DOI: [10.1103/PhysRevB.82.054403](https://doi.org/10.1103/PhysRevB.82.054403).
- [128] J. Smit. “The spontaneous hall effect in ferromagnetics I”. In: *Physica* 21.6 (1955), pp. 877–887. DOI: [https://doi.org/10.1016/S0031-8914\(55\)92596-9](https://doi.org/10.1016/S0031-8914(55)92596-9).

-
- [129] J. Smit. “The spontaneous hall effect in ferromagnetics II”. In: *Physica* 24.1 (1958), pp. 39–51. DOI: [https://doi.org/10.1016/S0031-8914\(58\)93541-9](https://doi.org/10.1016/S0031-8914(58)93541-9).
- [130] Stephen B. Soffer. “Statistical Model for the Size Effect in Electrical Conduction”. In: *Journal of Applied Physics* 38.4 (1967), pp. 1710–1715. DOI: [10.1063/1.1709746](https://doi.org/10.1063/1.1709746).
- [131] I. V. Soldatov et al. “Thermoelectric effects and magnetic anisotropy of Ga_{1-x}MnxAs thin films”. In: *Physical Review B - Condensed Matter and Materials Physics* 90.10 (2014), pp. 1–9. DOI: [10.1103/PhysRevB.90.104423](https://doi.org/10.1103/PhysRevB.90.104423).
- [132] E.H. Sondheimer. “The mean free path of electrons in metals”. In: *Advances in Physics* 1.1 (1952), pp. 1–42. DOI: [10.1080/00018735200101151](https://doi.org/10.1080/00018735200101151).
- [133] M. D. Stiles and A. Zangwill. “Anatomy of spin-transfer torque”. In: *Phys. Rev. B* 66 (1 2002), p. 014407. DOI: [10.1103/PhysRevB.66.014407](https://doi.org/10.1103/PhysRevB.66.014407).
- [134] Stanford Research Systems. *About Lock-In Amplifiers*. <https://www.thinksrs.com/downloads/pdfs/applicationnotes/AboutLIAs.pdf>. [Online]. n.d.
- [135] Oleksandr Talalaevskyy. “Dynamical measurements of the Spin Hall angle”. PhD thesis. University of Regensburg, 2017.
- [136] Katarina Tauber et al. “Extrinsic Spin Nernst Effect from First Principles”. In: *Phys. Rev. Lett.* 109 (2 2012), p. 026601. DOI: [10.1103/PhysRevLett.109.026601](https://doi.org/10.1103/PhysRevLett.109.026601).
- [137] D. Thompson, L. Romankiw, and A. Mayadas. “Thin film magnetoresistors in memory, storage, and related applications”. In: *IEEE Transactions on Magnetism* 11.4 (1975), pp. 1039–1050. DOI: [10.1109/TMAG.1975.1058786](https://doi.org/10.1109/TMAG.1975.1058786).
- [138] W. Thomson. “On the electro-dynamic qualities of metals:—Effects of magnetization on the electric conductivity of nickel and of iron”. In: *Proc. Royal Soc. London* 8 (1857), p. 546. DOI: [10.1098/rspl.1856.0144](https://doi.org/10.1098/rspl.1856.0144).
- [139] Yaroslav Tserkovnyak, Arne Brataas, and Gerrit E. W. Bauer. “Enhanced Gilbert Damping in Thin Ferromagnetic Films”. In: *Phys. Rev. Lett.* 88 (11 2002), p. 117601. DOI: [10.1103/PhysRevLett.88.117601](https://doi.org/10.1103/PhysRevLett.88.117601).
- [140] Yaroslav Tserkovnyak et al. “Nonlocal magnetization dynamics in ferromagnetic heterostructures”. In: *Rev. Mod. Phys.* 77 (4 2005), pp. 1375–1421. DOI: [10.1103/RevModPhys.77.1375](https://doi.org/10.1103/RevModPhys.77.1375).
- [141] K. Uchida et al. “Acoustic spin pumping: Direct generation of spin currents from sound waves in Pt/Y₃Fe₅O₁₂ hybrid structures”. In: *Journal of Applied Physics* 111.5 (2012), p. 053903. DOI: [10.1063/1.3688332](https://doi.org/10.1063/1.3688332).
- [142] K. Uchida et al. “Long-range spin Seebeck effect and acoustic spin?pumping”. In: *Nature Materials* 10 (2011), 737 EP –.
- [143] K. Uchida et al. “Longitudinal spin Seebeck effect in various garnet ferrites”. In: *Phys. Rev. B* 87 (10 2013), p. 104412. DOI: [10.1103/PhysRevB.87.104412](https://doi.org/10.1103/PhysRevB.87.104412).
- [144] K. Uchida et al. “Observation of the spin Seebeck effect.” In: *Nature* 455.7214 (2008), pp. 778–81. DOI: [10.1038/nature07321](https://doi.org/10.1038/nature07321).
-

- [145] K. Uchida et al. “Spin-Seebeck effects in Ni₈₁Fe₁₉/Pt films”. In: *Solid State Communications* 150.11 (2010). Spin Caloritronics, pp. 524–528. DOI: <https://doi.org/10.1016/j.ssc.2009.10.045>.
- [146] K Uchida et al. “Spin Seebeck insulator.” In: *Nature materials* 9.11 (2010), pp. 894–897. DOI: [10.1038/NMAT2856](https://doi.org/10.1038/NMAT2856).
- [147] Ken-ichi Uchida et al. “Observation of longitudinal spin-Seebeck effect in magnetic insulators”. In: *Applied Physics Letters* 97.17 (2010), p. 172505. DOI: [10.1063/1.3507386](https://doi.org/10.1063/1.3507386).
- [148] Arne Vansteenkiste et al. “The design and verification of MuMax3”. In: *AIP Advances* 4.10 (2014), p. 107133. DOI: [10.1063/1.4899186](https://doi.org/10.1063/1.4899186).
- [149] J. F. Watts and J Wolstenholme. *An Introduction to Surface Analysis by XPS and AES*. John Wiley & Sons Ltd., 2003. DOI: [10.1002/0470867930](https://doi.org/10.1002/0470867930).
- [150] S. Wimmer et al. “First-principles linear response description of the spin Nernst effect”. In: *Phys. Rev. B* 88 (20 2013), p. 201108. DOI: [10.1103/PhysRevB.88.201108](https://doi.org/10.1103/PhysRevB.88.201108).
- [151] [www.filmetrics.com. Reflectance Calculator.](https://www.filmetrics.com/reflectance-calculator) <https://www.filmetrics.com/reflectance-calculator>.
- [152] [www.madur.com. Thermoelectric effect.](https://www.madur.com/pdf/article/en/Thermocouples_EN.pdf) https://www.madur.com/pdf/article/en/Thermocouples_EN.pdf.
- [153] Jiang Xiao et al. “Theory of magnon-driven spin Seebeck effect”. In: *Phys. Rev. B* 81 (21 2010), p. 214418. DOI: [10.1103/PhysRevB.81.214418](https://doi.org/10.1103/PhysRevB.81.214418).
- [154] Y. Yafet. “g Factors and Spin-Lattice Relaxation of Conduction Electrons”. In: ed. by Frederick Seitz and David Turnbull. Vol. 14. *Solid State Physics*. Academic Press, 1963, pp. 1–98. DOI: [https://doi.org/10.1016/S0081-1947\(08\)60259-3](https://doi.org/10.1016/S0081-1947(08)60259-3).
- [155] L. F. Yin et al. “Magnetocrystalline Anisotropy in Permalloy Revisited”. In: *Phys. Rev. Lett.* 97 (6 2006), p. 067203. DOI: [10.1103/PhysRevLett.97.067203](https://doi.org/10.1103/PhysRevLett.97.067203).
- [156] Andrew Zangwill. *Physics at Surfaces*. Cambridge University Press, 1988. DOI: [10.1017/CB09780511622564](https://doi.org/10.1017/CB09780511622564).
- [157] Qing-feng Zhan et al. “Magnetic anisotropies of epitaxial Fe/MgO(001) films with varying thickness and grown under different conditions”. In: *New Journal of Physics* 11.6 (2009), p. 063003.
- [158] Qing-feng Zhan et al. “Manipulation of in-plane uniaxial anisotropy in Fe/MgO(001) films by ion sputtering”. In: *Applied Physics Letters* 91.12 (2007), p. 122510. DOI: [10.1063/1.2789396](https://doi.org/10.1063/1.2789396).
- [159] Maciej Zwierzycki et al. “First-principles study of magnetization relaxation enhancement and spin transfer in thin magnetic films”. In: *Phys. Rev. B* 71 (6 2005), p. 064420. DOI: [10.1103/PhysRevB.71.064420](https://doi.org/10.1103/PhysRevB.71.064420).

List of abbreviations

AES	Auger electron spectroscopy
AFM	Atomic force microscopy
AHE	Anomalous Hall effect
ALD	Atomic layer deposition
AMR	Anisotropic magnetoresistance
AMTP/AMTEP	Anisotropic magnetothermopower
ANE	Anomalous Nernst effect
<i>bcc</i>	body-centered cubic (crystal packing)
CCD	Charge-coupled device
CMA	cubic magnetic anisotropy
CPU	Central processing unit
CPW	Coplanar waveguide
DAC	Digital-to-analog converter
DOS	Density of states
DRF	depth resolution function
DFT	density functional theory
<i>fcc</i>	face-centered cubic (crystal packing)
F-D	Fermi-Dirac (distribution)
FM	ferromagnetic metal/ferromagnet
FMI	ferromagnetic insulator
FMR	Ferromagnetic resonance
GGG	Gadolinium gallium garnet
GMR	Giant magnetoresistance
GPU	Graphics processing unit

IMFP	inelastic mean free path
ISGE	inverse spin galvanic effect
ISHE	inverse spin Hall effect
<i>hcp</i>	hexagonal close packed (crystal structure)
HF	High frequency
HDD	Hard disk drive
LED	Light-emitting diode
LLE	Landau-Lifshitz equation
LSSE	Longitudinal spin Seebeck effect
MBE	Molecular beam epitaxy
MFP	mean free path
MOD	Modulation of damping
MOKE	Magneto-optic Kerr effect
MPE	Magnetic proximity effect
MRAM	Magnetoresistive random-access memory
MRI	atomic <u>M</u> ixing, <u>R</u> oughness and <u>I</u> nformation depth
NM	non-magnetic/normal material/metal
PC	Personal computer
PHE	Planar Hall effect
PLD	pulsed laser deposition
PMMA	Poly(methyl methacrylate)
PNE	Planar Nernst effect
Py	Permalloy
RF	Radio frequency
REE	Rashba-Edelstein effect
RT	Room temperature
SHA	Spin Hall angle
SHC	Spin Hall conductivity
SHE	Spin Hall effect

SMC	Spin mixing conductance
SMR	Spin Hall magnetoresistance
SNA	Spin Nernst angle
SNR or S/N	Signal-to-noise ratio
SNC	Spin Nernst conductivity
SNE	Spin Nernst effect
SNMTP	spin Nernst magmeto-thermopower
SOC	Spin-orbit coupling
SOT	Spin-orbit torque
SP	Spin pumping
STT	Spin transfer torque
SQUID	Superconducting quantum interference device
SSE	Spin Seebeck effect
TCR	Temperature coefficient of resistivity
Ti:Sa	Titan sapphire
TMR	Tunnel magnetoresistance
TRMOKE	Time resolved magneto-optical Kerr effect
TSOT	Thermal spin orbit torque
TSSE	Transverse spin Seebeck effect
UMA	uniaxial magnetic anisotropy
VSM	Vibrating sample magnetometer
XMCD	X-ray magnetic circular dichroism
XPS	X-ray photoelectron spectroscopy
XRD	X-ray diffraction
YIG	Yttrium iron garnet

Acknowledgments

I would like to thank the following people for helping throughout my PhD time:

Christian H. Back for a kind supervision of the PhD thesis.

Erick R. J. Edwards for information about the PhD position and SpinIcur Research Project, and also for a great help with accommodation in Regensburg in first days.

Bryan J. Hickey, Trish Grant and all participants of the SpinIcur project for nice meetings, offered opportunities and discussions.

Rolf Allenspach and Ricardo Ferreira for help with planning of secondments and accommodations by IBM and INL.

Martin Decker and Johannes Stigloher for introduction to TRMOKE setup. Also a huge thanks to Martin for discussions of the SNE samples design and explanation of clean room techniques.

Michael Müller for presentation of the group mini-clean room and its equipment.

Michael Vogel for hints regarding handling thin membrane films and discussions of heat transport and thermal simulations.

Alexander Talalaevsky for frequent physics-related discussions and help with the clean-room machines.

Max Schmidt for an initial introduction in the TSSE topic and a nice set-up left after him.

Timo Kuschel and Oliver Reimer for a comprehensive discussion of the TSSE-related questions and thermal gradient generation methods, and also for co-writing of a joint article.

Polina Bougiatioti for production and provision of the YIG samples for TSSE measurements.

Silvia Hrdina, Magdalena Pflieger, Claudia Zange for help with documents and organizational questions.

Thomas N. G. Meier for a massive help with XPS measurements and proofreading of Appendix of the thesis.

Yuriy Mokrousov and Nguyen H. Long for a fruitful discussion of the Spin Nernst Effect and offer of theoretically promising materials for experimental investigations.

Helmut Körner for SQUID measurements of SNE samples.

Matthias Kronseder for production of CuAu/Py samples in MBE chamber.

Group of prof. C.H. Back for a friendly atmosphere and support in scientific sphere.

Peresyphkina Eugenia for proofreading of the thesis and advises regarding English and scientific writing.

Arpita Mitra for temperature-dependent magnetization measurements of the SNE samples.

The largest gratitude I want to address to Galina Dorofeeva for an inspiration to start the PhD work in foreign land.